Optical monitoring of OH radical using Cavity-enhanced Faraday Rotation Spectroscopy (CEAS-FRS)

Minh Nhut Ngo

Thèse de Doctorat

Discipline : PHYSIQUE

Spécialité : MILIEUX DILUÉS ET OPTIQUE

présentée à ***l'Ecole Doctorale en Sciences Technologie et Santé (ED 585)***

de l'Université du Littoral Côte d'Opale

par

Minh Nhut NGO

pour obtenir le grade de Docteur de l'Université du Littoral Côte d'Opale

Optical monitoring of OH radical using Cavity-enhanced Faraday Rotation Spectroscopy (CEAS-FRS)

Soutenue le 30 septembre 2022, après avis des rapporteurs, devant le jury d'examen :

M. Andy RUTH, Professeur, University of Cork	**Rapporteur**
M$^{me.}$ Christa FITTSCHEN, Directrice de Recherche, Université de Lille 1	**Rapporteur**
M$^{me.}$ Ha TRAN, Directrice de Recherche, Sorbonne Université	**Présidente**
M$^{me.}$ Irène VENTRILLARD, Maître de Conférences HDR, Université Grenoble Alpes	**Examinateur**
M$^{me.}$ Mélanie GHYSELS-DUBOIS, Ingénieur de Recherche, Université de Reims	**Examinateur**
M. Weidong CHEN, Professeur, ULCO	**Directeur de thèse**
M. Tong NGUYEN-BA, Maître de Conférences, ULCO	**Encadrant**

Acknowledgments

This work was realized at the Laboratoire de Physico-Chimie de l'Atmosphère (LPCA) at the Université du Littoral Côte d'Opale (ULCO).

First of all, I would like to express my deepest appreciation to my thesis director Prof. Weidong Chen, and my supervisor Dr. Tong Nguyen-Ba, for giving me the opportunity to do my PhD in the LPCA. To Prof. Weidong Chen, thanks for his guidance and encouragement during three years of work. My PhD progress would not have been possible without his insight and advice, including his attention to the little details in my scientific results. That allowed me to grow academically as well as intellectually. To Tong, thank you all for your support and boundless patience. I wouldn't get anything done without your continuous presence in laboratory.

I would like to give my sincere acknowledgment to the members of the jury who have accepted to evaluate my thesis work.

When working on HONO absorption measurement, it is not easy for me to produce a constant concentration of HONO. I would like to extend my sincere thanks to Mr. Nicolas Houzel and Dr. Cécile Coeur for your support and discussions on chemical experiments. I am also thankful to my colleague Jonas Bruckhuisen and Prof. Arnaud Cuisset for discussing the simulation of HONO spectra in my thesis. To Mr. Eric Fertein and my colleague Jean Decker, thank you for advising me to solve some technical problems in the lab. Thanks to Pierre Kulinski for his help in 3D printing.

A special thanks to my colleague, Mr. An Tran Dang Bao, at University of Education, Ho Chi Minh City, Viet Nam, for discussing spectroscopic experiments and optical alignment. He always helps me when I have problems.

I would like to acknowledge Prof. Qian Gou at School of Chemistry and Chemical Engineering, Chongqing University, China, for giving me valuable comments and advice on line parameters of HONO.

Thanks to my team members, including Ruyue Cui, Tingting Wei, Marie-Hélène Mammez, Sama Molaie, Anastasia Pienkeina, Zhen Liu. Thanks to my friends in LPCA, including Bao-Anh Phung-Ngoc, Thien Le-Phu, Bouthayna Alrifai, Fatima Al Ali, and Ghoufrane Abichou.

I would also like to thank my colleagues at Faculty of Physics, HCMC University of Education, Vietnam, who have shared the teaching work during my PhD period.

Finally, I would like to thank my wife and my family in Vietnam for all your love and support.

Abstract

Hydroxyl free radicals (OH) and nitrous acid (HONO) are short-lived reactive species that play a central role in atmospheric chemistry. Real-time monitoring of their concentrations is crucial for studying their related chemical processes, understanding chemical cycles and the oxidation capacity of the atmosphere. Absorption spectroscopy is an efficient tool to measure molecule concentrations in the gas phase. According to the Beer-Lambert law, increasing light-matter interaction paths, which are achieved by means of multi-pass cells or optical cavities, is one of the effective ways to enhance detection sensitivity. Meanwhile, the uncertainty of such measurements depends strongly on the accuracy of spectral line parameters (line position, line intensity, or cross-section) used for the quantification.

This PhD thesis is on the development and application of optical instruments for accurate measurements of OH radical mixing ratios and for the study of the OH oxidation capacity in the laboratory, as well as for investigations of spectral line parameters of HONO. The PhD work is divided into 3 parts:

(1) A robust and compact instrument for direct measurement of OH concentration was developed based on **off-axis integrated cavity output spectroscopy (OA-ICOS)** operating at 2.8 μm. This OA-ICOS system is simple to align and robust, it does not require high-speed electronic devices to real-time match laser frequencies to cavity modes during laser frequency scan (as in the case of cavity ring-down spectroscopy). Performance of the OA-ICOS approach was evaluated by measuring OH radicals generated from a microwave discharge of water vapor at low pressure. Wavelength modulation was applied to OA-ICOS in order to further enhance the detection sensitivity which resulted in a gain factor of 3.4, giving a limit of detection (LoD) of 2.5×10^{10} molecules.cm^{-3} (1σ) for an integration time of 20 s.

(2) Faraday rotation spectroscopy (FRS), which is a highly selective measurement method relying on the magneto-optical effect for paramagnetic species (such as OH), was combined with the OA-ICOS setup to establish a **cavity-enhanced Faraday rotation** instrument (CE-FRS) for interference-free monitoring of OH radicals. By applying an external magnetic field along the optical cavity axis and performing a differential detection approach for two polarizations of the light leaking out the cavity, a LoD for OH of 1×10^{10} molecules.cm^{-3} was achieved for an averaging time of 20 s. The CE-FRS setup was tested by measuring the reaction rate constant of OH with CH_4 on a milliseconds timescale.

(3) Line parameters of HONO in the mid-IR near 6 μm were investigated. A **quantum cascade laser (QCL) based direct absorption spectrometer using a multi-pass cell** and custom-made control software were developed and employed to determine about 60 new line positions and their effective line intensities of the ν_2 band (N=O stretch) of *cis*-HONO in the range of 1659.2 - 1662.2 cm^{-1} (*R*-branch). The absorption line frequencies were in real-time measured during laser frequency scans using a wavelength meter. The *cis*-HONO spectra were simulated using PGOPHER code to identify line positions and to validate the present experimental results.

Keywords: OH radicals, off-axis integrated cavity output spectroscopy, Faraday rotation spectroscopy, wavelength modulation spectroscopy, quantum cascade laser spectroscopy, ν_2 band *cis*-HONO, effective line intensity.

Résumé

Les radicaux hydroxyles (OH) et l'acide nitreux (HONO) sont des espèces réactives à courte durée de vie et ils jouent un rôle clé dans la chimie atmosphérique. La surveillance en temps réel de leurs concentrations est cruciale pour étudier la capacité d'oxydation atmosphérique. La spectroscopie d'absorption est un outil efficace pour l'analyse qualitative et quantitative des espèces gazeux à l'état de trace. Selon la loi de Beer-Lambert, l'augmentation de la longueur du chemin optique à travers l'échantillon via une cellule multi-passage ou une cavité optique est l'un des moyens plus efficaces d'améliorer la sensibilité de détection. Quant à l'incertitude de mesure, elle dépend fortement de la précision des paramètres de raie spectrale (telles que la position, l'intensité de la raie ou la section efficace) utilisée pour la quantification.

Les travaux de ma thèse portent sur le développement et l'application d'instruments optiques pour la mesure précise des radicaux OH en laboratoire et pour l'étude spectroscopique des raies spectrales de HONO.

(1) Un spectromètre compact, basé sur la spectroscopie en cavité résonante hors d'axe (OA-ICOS) fonctionnant à 2,8μm, a été développé pour la mesure de la concentration des radicaux OH. L'approche OA-ICOS consiste à mesurer l'intensité lumineuse intégrée dans le temps à

la sortie d'une cavité optique lorsque le faisceau laser est injecté hors axe. Ce système est simple à aligner et il ne nécessite pas de dispositifs électroniques à haute vitesse pour verrouiller en temps réel la fréquence du laser aux modes de la cavité pendant le balayage de fréquence laser (c'est le cas pour le dispositif Cavity Ring-Down Spectroscopy – CRDS). La performance du spectromètre OA-ICOS a été évaluée en mesurant les radicaux OH générés par la décharge micro-onde de vapeur d'eau à basse pression. Modulation de longueur d'onde a été ensuite appliquée afin d'améliorer davantage la sensibilité de détection, ce qui nous a permis d'obtenir un facteur d'amélioration de 3,4 et une limite de détection de 2.5×10^{10} molecule.cm^{-3} pour un temps d'intégration de 20 s.

(2) Dans l'étape suivante, la spectroscopie de rotation de Faraday (FRS), qui est une méthode de mesure hautement sélective basé sur l'effet magnéto-optique pour les espèces paramagnétiques (telle que OH), a été couplée à la configuration OA-ICOS pour établir un instrument de rotation de Faraday amélioré par cavité (CE-FRS) pour la mesure sans interférence des radicaux OH. En appliquant un champ magnétique externe le long de l'axe de la cavité et en effectuant une détection différentielle pour les deux polarisations de la lumière s'échappant de la cavité, une limite de détection de 10^{10} OH.cm^{-3} a été obtenue pour une durée moyenne de 20 s. Cet instrument développé a été utilisé ensuite pour l'étude cinétique chimique en mesurant la constante de vitesse de réaction de OH et CH_4 avec une échelle de temps de millisecondes afin de valider la performance de l'instrument.

(3) Un spectromètre à absorption directe, utilisant un laser à cascade quantique (QCL) couplé à une cellule multi-passage, et un logiciel d'interface dédié ont été développés et utilisés pour déterminer des paramètres spectraux d'environ 60 nouvelles raies de la bande ν_2 (étirement N = O) de cis-HONO dans la gamme de 1659,2 – 1662,2 cm^{-1} (*R*-branche). Les fréquences des raies d'absorption ont été mesurées en temps réel lors du balayage de fréquence laser à l'aide d'un lambdamètre. Les spectres de cis-HONO ont été également simulés à l'aide du code PGOPHER pour identifier et valider les résultats expérimentaux obtenus.

Mots-clés : radicaux OH, OA-ICOS, spectroscopie de rotation de Faraday, spectroscopie de modulation de longueur d'onde, cis-HONO ν_2 bandes, intensité de raie efficace, spectroscopie laser à cascade quantique.

Contents

List of Figures

List of Tables

List of Abbreviation

A

AC	Alternating current
ADC	Analog-to-digital converter
AI	Analog input
AO	Analog output
AOM	Acousto-optical modulator
APJs	Atmospheric plasma jets
ASE	Amplified spontaneous emission

B

BW	Bandwidth
BD	Balanced detection

C

CEAS	Cavity-enhanced absorption spectroscopy
CE-FRS	Cavity-enhanced Faraday rotation spectroscopy
CRDS	Cavity ring-down spectroscopy
CW	Continuous wave

D

DAQ	Data acquisition card
DAS	Direct absorption spectroscopy
DBD	Dielectric barrier discharge
DC	Direct current
DFB	Distributed feedback
DOAS	Differential optical absorption spectroscopy

F

FAGE	Fluorescence assay by gas expansion
FRS	Faraday rotation spectroscopy
FSR	Free spectral range
FT	Fourier Transform
FWHM	Full width at haft maximum
HRM	High reflectivity mirror

H

HV	High voltage
HWHM	Haft width at haft maximum

I

IBBCEAS	Incoherent broadband cavity-enhanced absorption spectroscopy
ICL	Interband cascade laser
ICOS	Integrated cavity output spectroscopy
IR	Infrared

L

LDC	Laser diode controller
LHCP, RHCP	Left- and right-hand circularly polarized waves
LIA	Lock-in amplifier
LIF	Laser-induced fluorescence
LoD	Limit of detection

M

MCB	Magnetic circular birefringence
MCD	Magnetic circular dichroism
MDA	Minimum detectable absorption
MDAC	Minimum detectable absorption coefficient
mid-IR	mid-infrared
MW	Microwave

N

NEAS	Noise equivalent absorption sensitivity
NTC	Negative temperature coefficient

O

OA-ICOS	Off-axis integrated cavity output spectroscopy
OAPM	Off-axis parabolic mirrors
OF-CEAS	Optical-feedback cavity-enhanced absorption spectroscopy

P

PCI	Peripheral Component Interconnect
PS-CRDS	Phase-shift cavity ring-down spectroscopy
PZT	Piezoelectric transducer

Q

QCL	Quantum cascade laser
QEPAS	Quartz-enhanced photoacoustic spectroscopy

R

RAM	Residual amplitude modulation
RMS	Root-mean-square

S

SNR	Signal-to-noise ratio

T

TEC	Thermo-electric cooler

TLAS	Tunable laser absorption spectroscopy
TTL	Transistor-Transistor Logic

U

UV	Ultra-violet

V

VOCs	Volatile organic compounds

W

WM	Wavelength modulation
WM-CE-FRS	Wavelength modulated Cavity-enhanced Faraday rotation spectroscopy
WM-OA-ICOS	Wavelength modulation enhanced off-axis integrated cavity output spectroscopy
WMS	Wavelength modulation spectroscopy

Chapter 1 Introduction

1.1 Role of OH radicals in the atmosphere

The atmosphere is a chemically complex and dynamic system that consists of various chemical compounds emitted from natural processes and human activity. In recent times, concentrations of CO_2, CH_4 and other air pollutants have increased due to industrial activities, livestock and traffic, causing a negative impact on the global climate by warming the Earth's surface and troposphere (greenhouse effect) [1]. Due to atmospheric photochemical cycles, most trace gases emitted into the atmosphere are removed through oxidizing chemical reactions by atmospheric oxidants including ozone (O_3), nitrate (NO_3) and hydroxyl (OH) free radicals [2]. This ability of the atmosphere to "clean" itself strongly depends upon the atmospheric oxidation capacity. In 1952, Bates and Witherspoon identified OH as the major atmospheric sink for CO and CH_4 [3]. Since then laboratory experiments and model calculations have firmly established the central role of the OH molecule in tropospheric chemistry and have led to the suggestion that the OH radical is the main initiator of oxidation processes in the troposphere [4].

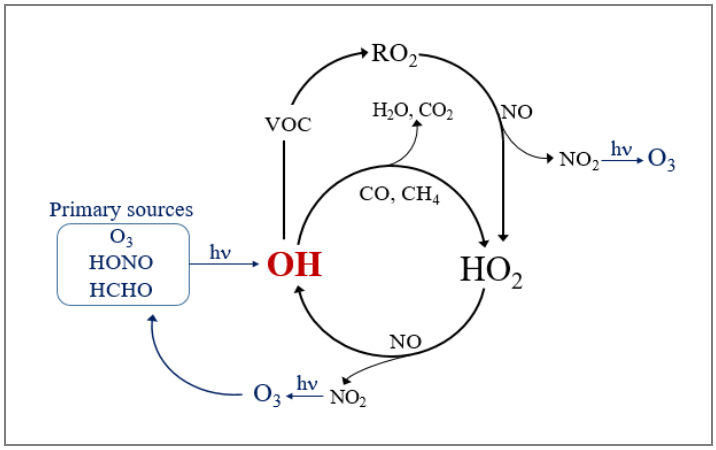

Figure 1.1 Main interaction cycle of atmospheric OH and HO_2 radicals which can be considered to be essentially in photochemical equilibrium.

Figure 1.1 illustrates the main interaction cycle of atmospheric OH radicals which are intimately linked to hydroperoxyl radicals (HO_2). OH is the principal component playing a central role in the metabolism of pollutants. It is produced by the solar photolysis cycle of various sources and destroyed predominantly by reaction with CH_4 and CO. The balance

between production and removal rates leads to estimates of a chemical lifetime of about <1 s and daytime concentration levels of 10^6 molecules.cm^{-3} in the troposphere [5,6]. Oxidation of primary pollutants by OH leads to the formation of HO_2 and organic peroxyl radicals (RO_2, R = organic group) which are important intermediates in the photochemical formation of ozone and organic aerosols [7]. A good understanding of OH and its related chemistry is therefore indispensable for reliable prediction of atmospheric oxidation and the formation of secondary atmospheric pollutants.

1.1.1 Primary source of OH production

Photochemical processes mainly produce the OH radical. Many studies attempt to characterize the contributions of the different production sources of atmospheric OH radicals under environmental influences [8,9]. Simulation models, including pollution parameters in urban and rural environments as well as the influence of the seasons and sunshine (air temperature, wind direction), distinguished several significant sources contributing to OH production and showed a reasonable agreement with the variation of measured OH concentration [8]. These results were partly confirmed by field studies [7,10]. Whereby, there are three primary sources for atmospheric OH production: (1) ozone (O_3), (2) nitrous acid (HONO), and (3) formaldehyde (HCHO).

(1) Photolysis of ozone by solar radiation in the presence of water vapor is the primary source of hydroxyl radicals in the troposphere. When O_3 absorbs UV light at wavelengths less than 310 nm, it produces excited oxygen atoms O(^{1}D) that can attack water vapor to produce OH [11]:

$$O_3 + h\nu(\lambda < 310nm) \rightarrow O(^1D) + O_2(^1\Delta, {}^3\textstyle\sum) \quad (1.1)$$

$$O(^1D) + H_2O \rightarrow 2OH \quad (1.2)$$

In addition, OH can be reformed from HO_2 via the reaction with O_3:

$$HO_2 + O_3 \rightarrow OH + 2O_2 \quad (1.3)$$

(2) Photolysis of nitrous acid has long been recognized as a potentially important production mechanism for OH radicals in the polluted urban atmosphere [12–14]. In the early morning, the photolysis of HONO, accumulated to ppbv levels [15,16] during night time, makes a large contribution to OH radical concentrations [9]:

$$HONO + h\nu(300nm < \lambda < 405nm) \rightarrow OH + NO \quad (1.4)$$

Several atmospheric field measurements reported that photolysis of HONO at its ambient concentration contributed between 20 % and 40 % to the overall HO_x radical budget (OH + HO_2) [17–19] during daytime. According to a study by *X. Zhou et al.* [17] in 1998, the investigation of the summertime HONO chemistry in the atmospheric boundary layer at a rural site in New York State showed that photolysis of HONO accounted for 24% of the total production from photolysis of the primary sources including HONO, O_3, and HCHO. *X. Ren et al.* [18] reported the observation of OH and HO_2 chemistry in the urban atmosphere of New York City in 2001. Data in [18] showed that about 56 % of the average daily HO_x production was formed from photolysis of HONO, while its nighttime production was mainly from the O_3 reactions with alkenes. Specifically, the contribution of HONO photolysis to daily OH production can reach 60% [20,21].

(3) Formaldehyde (HCHO) is formed through the oxidation of most biogenic and anthropogenic hydrocarbons and is also present in primary emissions from combustion sources such as motor vehicles [22]. The photolysis of formaldehyde can form RO_2 radicals, which are converted to OH radicals in the presence of NO. The following reactions show these mechanisms [9]:

$$HCHO + hv(\lambda < 370nm) \rightarrow H + HCO \quad (1.5)$$

$$HCO + O_2 \rightarrow HO_2 + CO \quad (1.6)$$

$$HO_2 + NO \rightarrow OH + NO_2 \quad (1.7)$$

Atmospheric oxidation of alkenes by ozone and reactions of RO_2 and HO_2 with NO is a secondary source of OH radicals.

1.1.2 Removal of air pollutants by OH oxidation

Hydroxyl radicals are involved in the degradation processes of many air pollutants whose concentration is mainly determined by the reaction rates with OH radicals. Calculations indicate that the reactions of OH with NO_2, hydrocarbons, CO, NO, and carbonyls accounted for about 32%, 25%, 12%, 10% and 7% of total OH loss, respectively, in an urban area [18]. Figure 1.2 shows the global emissions and the corresponding approximate percentage of each emitted gas destroyed by reaction with OH [23].

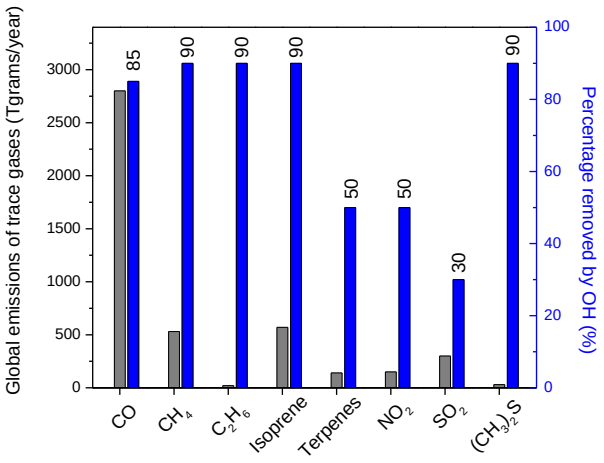

Figure 1.2 Estimates of the global emission rates of tropospheric trace gases and their removal by reaction with OH refer to 1990, according to [23]. 1 Tgrams = 10^{12} g

The two most crucial loss routes for the OH radical in the clean troposphere are the reactions with carbon monoxide and methane [22]:

$$OH + CH_4 \rightarrow H_2O + CH_3 \tag{1.8}$$

$$OH + CO \rightarrow H + CO_2 \tag{1.9}$$

Under most atmospheric conditions, the removal of VOCs is dominated by their reaction with OH (where RH is a VOC and R is an alkyl group)

$$OH + RH \rightarrow R + H_2O \tag{1.10}$$

The other mechanisms involving OH are reactions with nitrogen oxides (nitrogen monoxide (NO) and nitrogen dioxide (NO_2)):

$$OH + NO_2 \xrightarrow{M} HNO_3 \tag{1.11}$$

$$OH + NO \xrightarrow{M} HONO \tag{1.12}$$

where M is a third body that acts only to collisionally stabilize the association complex [24,25].

Although ozone is one of the primary sources of OH production, it is also likely to react with the latter under conditions where NO concentrations are low:

$$OH + O_3 \rightarrow HO_2 + O_2 \tag{1.13}$$

1.2 Spectroscopic techniques for detection of OH radicals

OH can be detected using absorption spectroscopy. The sensitivity of absorption spectroscopy depends on the line intensity (or cross-section) used for the quantification of OH and the optical path length. The number of well-established techniques for detecting OH in the gas phase is limited due to its low concentration (~10^6 molecules.cm^{-3}) and short lifetime (<1 s). It was shown that only long-path differential optical absorption spectroscopy (DOAS) and laser-induced fluorescence (LIF) at low pressure (known as fluorescence assay by gas expansion - FAGE) have been utilized successfully for field monitoring of OH concentration at ambient concentration levels [26–29].

1.2.1 Differential optical absorption spectroscopy (DOAS)

DOAS is a direct, absolute and in-situ analytical technique that measures the integrated absorption of a laser beam traveling over a long path length in the atmosphere (typically several km). The laser beam is directed over the absorption path by a transmitter telescope. The light is usually reflected by a retro-reflector into a receiver telescope, providing the absorption of OH. Figure 1.3 shows a scheme of a basic DOAS setup [27]. Compared with other existing techniques, the most crucial advantage of the DOAS method is self-calibration via the Beer-Lambert law and high sensitivity, allowing a reliable identification of OH radicals at the ambient level. The accuracy depends on the uncertainty in the line intensity (or cross-section) of the OH transition exploited and the optical path length. Most measurements employed the strong rovibronic absorption lines of the $A^2\Sigma$ (v' = 0) ← $X^2\Pi$ (v" = 0) transition in the UV range at 306.0–309.5 nm. An early measurement of tropospheric OH based on the DOAS method was reported in 1976 by *D. Perner* [27]. By exploiting the strongest OH $Q_1(2)$ line located at 307.9951 nm, an LoD for OH of 2×10^6 molecules.cm^{-3} was obtained with an optical path length of 7.8 km. Some DOAS approaches realized long path lengths by multiple-reflections of the laser beam (typically several hundred round-trip passes) between three mirrors separated by a distance of a few tens of meters [30–33]. This White-type multi-pass arrangement operating in an open-path configuration provided an LoD in the range of 10^6 molecules.cm^{-3}.

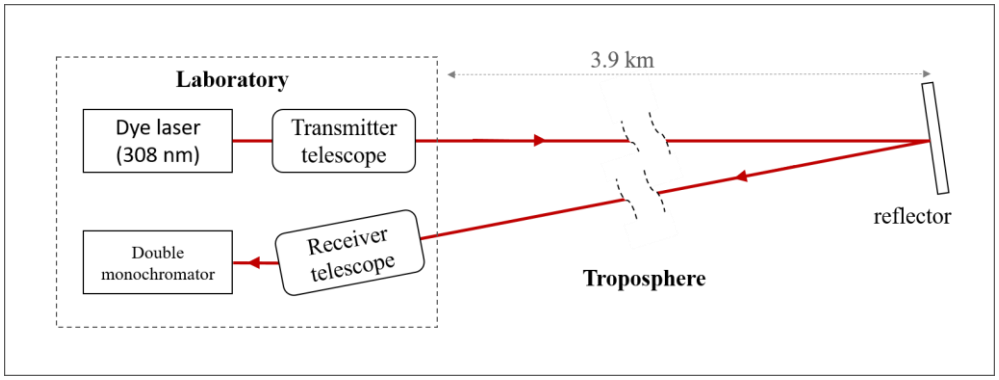

Figure 1.3 OH detection system by DOAS [27].

Due to the size and difficulty of implementation (positioning of the mirrors, the influence of the environment on optical alignment), the DOAS system is difficult to transport and it has a low spatial resolution (as the measurement of concentrations is integrated over the long optical path). The LoD of the DOAS method for OH detection is essentially limited by wavelength-dependent interfering structures from atmospheric species. Random fluctuations of the atmosphere due to light scattering through dust and aerosol lead to an unknown time-dependent attenuation of the laser radiation along the absorption path should be carefully addressed [31].

1.2.2 Laser-induced fluorescence (LIF) and Fluorescence assay by gas expansion (FAGE)

Laser-induced fluorescence is a spectroscopic method that measures the light emission of an atom or molecule from its excited higher energy level by absorption of excitation light to its ground state. Figure 1.4 shows the principle of laser-induced fluorescence. High energy photons (UV) will be absorbed by the molecule (red). This absorption will excite the molecule to the electronic excitation state. Several relaxation mechanisms may then take place, including non-radiative vibrational relaxation (blue), non-radiative: quenching (violet) which is a transfer of energy non-radiative by collisions or other mechanisms (vibration) and radiative fluorescence (green). The early version of LIF used the excitation of OH $A^2\sum$ (ν' = 1) ← $X^2\Pi_i$ (ν" = 0) at 282 nm, with collection of red-shifted fluorescence near 308 nm [34,35]. However, this approach faced the problem of O_3 interference resulting in artificially produced OH due to the photolysis of ambient ozone by the 282 nm laser [6]. Thus later LIF systems referred both laser-excitation and fluorescence collection in the $A^2\sum$ (ν' = 0) ← $X^2\Pi_i$

(v" = 0) band at about 308 nm [36–39]. In order to limit collisions (quenching) and extend the lifetime of OH fluorescence beyond the duration of the excitation laser pulse [40], the LIF instruments are working at low pressure (1–5 mbar) conditions in which ambient air is expanded through a 1 mm nozzle into a fluorescence cell [22]. This technique is known as Fluorescence Assay by Gas Expansion (FAGE), first developed in 1984 by *Hard et al.* [41].

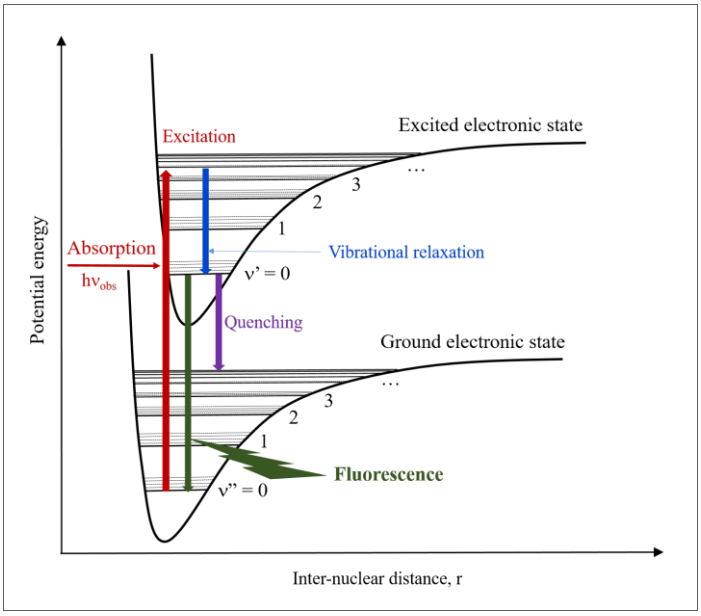

Figure 1.4 An energy level diagram indicates the principle of laser-induced fluorescence.

Nowadays FAGE is widely used for studying the reactivity of OH [42,43], as well as field and airborne measurements of OH with excellent sensitivity [44]. However, it is a non-absolute detection method and needs careful calibration [43,45]. The FAGE system is rather complex with large size and weight, high electrical power usage, and high-cost.

1.2.3 Other spectroscopic techniques

Besides DOAS and FAGE, cavity ring-down spectroscopy (CRDS) and Faraday rotation spectroscopy (FRS) have been developed to detect higher OH concentration. The principle of CRDS and FRS are explained in section **3.1** and **4.1**, respectively.

CRDS, employing high reflectivity mirrors to form a high finesse optical cavity to realize an effective optical length of up to several kilometers, provides high sensitivity [46]. Several CRDS setups were applied to measure OH density profiles in flames [47,48] and in plasmas jet [49,50]. For example, the UV-CRDS systems were applied to quantify OH radicals in the far downstream part of an atmospheric microwave plasma jets [49,50]. By probing the $R_2(4)$

line of the OH A-X（0–0) band, a detection limit of 1.3×10^{11} molecules.cm^{-3} was achieved [49].

In contrast to other spectroscopic approaches, FRS measures the optical dispersion instead of molecular absorption. FRS relies on the magneto-optics effect (Faraday effect) that causes a rotation of the polarization plane of a linearly polarized light propagating through a paramagnetic sample (OH, HO_2, NO_x, …) permeated by a longitudinal magnetic field. Since the Faraday effect is only observed for paramagnetic species, the major advantage of the FRS method is removing or significantly reducing the spectral interference of most major atmospheric species, such as H_2O and CO_2. In addition, the sensitivity can reach the shot noise level thanks to the internal modulation of the molecule [51,52]. The first observation of OH radical by FRS was reported by *Litfin et al*. [53] in 1980 by exploiting the R(3) F_1 transition of the fundamental vibrational band of the OH radical at 2.69 μm (~3708 cm^{-1}) with a signal path length of ~20 cm. One year later, *Pfeiffer et al*. [54] made further improvements in a similar FRS approach and reported a detection limit of 1×10^{11} molecules.cm^{-3} by probing the two Λ-components of the $^2\Pi F_1$ R(3.5) OH (v=1←0) transition. Recently, *Zhao et al.* reported a FRS systems operating near 2.8 μm based on single pass cell [51,52], and then coupled a multi-pass arrangement to FRS [55,56] to provide an LoD of 10^7-10^8 molecules.cm^{-3} by probing the OH Q (1.5e) line at ~3568.52 cm^{-1}.

Table 1.1 Performance and qualities of the reported spectroscopic techniques for OH detection.

Techniques	**Sensitivity** (molecules.cm^{-3})	**Advantages**	**Disadvantages**
DOAS [27,31–33]	10^5-10^6	absolute measurement of integrated concentration at ambient level	low spatial resolution (integrated concentration); large dimension; untransportable
LIF-FAGE [28,36,39]	10^5	excellent sensitivity; high spatial resolution (local concentration)	potential interferences, requirement of calibration; complex system
CRDS [47–50]	10^{11}-10^{12}	long path length achieved by optical cavity; high spatial resolution	low sensitivity; servo of optical cavity
FRS [51,52,55,56]	10^7-10^8	spectral selectivity; high spatial resolution	low sensitivity, paramagnetic species limited

Table 1.1 lists the sensitivities, advantages and disadvantages of the techniques outlined above. Although both CRDS and FRS cannot provide the sensitivity to permit measurements

of OH at ambient levels in comparison with DOAS and FAGE, they are potential techniques for developing less complicated, compact and transportable instruments. Combining the advantages of cavity-enhanced absorption spectroscopy (CEAS) and Faraday Rotation Spectroscopy (FRS), a Cavity enhanced Faraday rotation spectroscopy instrument (CE-FRS) is developed in the present work. The instrument performance is benefited from two advantages. First, the sensitivity of the spectroscopic detection system can be improved via increasing optical absorption path length achieved by the CEAS techniques. Second, the use of FRS avoids interferences from non-paramagnetic species, providing significant selectivity.

1.3 Aim of this work

The objective of the present PhD work is to develop and apply optical instruments for accurate measurements of OH radicals in laboratory, and for investigation of spectral line parameters of HONO. Two experimental setups were developed for these purposes: (1) a CE-FRS for interference-free and high sensitivity detection of OH radical, and (2) a multi-pass cell based direct absorption spectroscopy for the determination of line parameters of HONO (line positions and line intensity) in the mid-infrared.

The dissertation is organized as follows:

Chapter 2 provides an overview of absorption spectroscopy applied to gas sensing, as well as the analytical methods currently used for the measurements of molecular concentration and absorption line intensity.

Chapter 3 is devoted to the principle of the CEAS technique and the development of an off-axis CEAS (so-called Off-axis integrated cavity output spectroscopy, OA-ICOS) setup for direct measurements of OH concentrations at 2.8 μm. The OH radicals were produced in a continuous microwave discharge of water vapor at low pressure to evaluate the performance of the developed system. Two detection schemes were used and compared. First, the OA-ICOS setup was developed to determine the absolute concentration of OH. Then a wavelength modulation scheme was applied to improve the sensitivity (WM-OA-ICOS).

Chapter 4 presents the coupling of FRS to the OA-ICOS setup to establish a CE-FRS approach for interference-free measurement of OH radicals. The Faraday signal was obtained using a differential detection scheme of two polarizations of the cavity output within an axial magnetic field. By applying wavelength modulation and performing demodulation of the differential signal using a phase-sensitivity lock-in detection, the OH concentration was

determined on a millisecond time scale based on tracking the harmonic signal at the resonance frequency of an OH line. In conjunction with a pulsed microwave discharge device, the WM-CE-FRS was tested and validated by measuring the reaction rate constant of OH with methane.

Chapter 5 describes the development of a quantum cascade laser (QCL) based direct absorption spectrometer to determine the line positions and their effective line intensities of the ν_2 band (N=O stretch) of *cis*-HONO in the range of 1659.2-1662.2 cm^{-1} (*R*-branch). The cis-HONO spectra were simulated using PGOPHER to identify and validate the present experimental results.

Finally, chapter 6 summarizes the major achievements in this PhD work and outlines potential future work, i.e. further improvements of instrumental performances to meet the demands for measuring OH concentrations with higher sensitivity, higher precision and higher accuracy.

Chapter 2 Trace gas detection by absorption spectroscopy

Absorption spectroscopy provide an extremely effective non-invasive approach for the identification and quantification of molecular traces gas [1–3]. This method is based on the Beer-Lambert law and consists of an optical measurement of the light-matter interaction when a light beam propagates through the medium to be analyzed. This chapter will overview the principles of gas-phase absorption spectroscopy for optical detection of trace gases as well as spectral analysis of the molecular features. In addition, concepts and characteristics of the instrumental performance of a spectroscopic measurement system will be presented.

2.1 Principle of absorption spectroscopy for trace gas sensing

Absorption spectroscopy detects and characterizes a medium based on studying the attenuation of the incident light radiation propagating through a sample, resulting in an interaction between the light and molecules, particles, or any other form of matter in the sample. The amount of absorption can be used to infer the concentration of the absorber in the sample based on the Beer-Lambert Law under specific conditions.

2.1.1 Beer-Lambert law

The attenuation of the frequency-dependent intensity $I(\nu)$ of radiation transmitted through a medium uniform distributed along a path length L follows the Beer-Lambert law:

$$I(\nu) = I_0(\nu)\exp\left[-\alpha(\nu)L\right] = I_0(\nu)\exp\left[-A(\nu)\right] \tag{2.1}$$

where $I(\nu)$ is the radiation intensity at frequency ν; measured in the presence of the absorber of number density n (molecules.cm^{-3}). $I_0(\nu)$ is the light intensity of the incident radiation in the absence of the absorber; $\alpha(\nu) = n\sigma(\nu)$ is the absorption coefficient of the sample, $\sigma(\nu)$ is the frequency-dependent absorption cross–section (cm^2.molecule^{-1}). The dimensionless exponential component in the Beer-Lambert law, $A(\nu) = n\sigma(\nu)L$, is often called absorbance, and the exponent is denoted as sample optical thickness, optical depth, or simply absorption. A medium is called optically thin in case $A(\nu) \ll 1$, and optically thick whenever $A(\nu) \gg 1$.

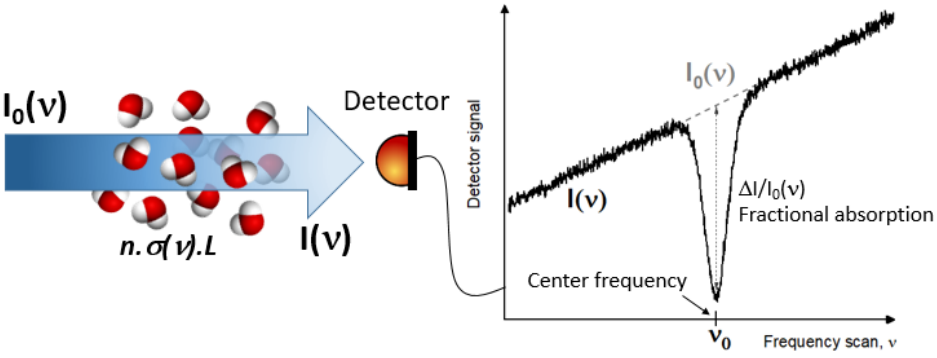

Figure 2.1 Illustration of the parameters involved in the Beer-Lambert law.

The frequency-dependent absorption cross-section is dependent on the experimental conditions and the available spectral parameters:

$$\sigma(\nu) = S.\overline{\chi}(\nu) = \sigma_0 \overline{\chi}^{abs}(\nu) \tag{2.2}$$

where S is the integrated line intensity of a transition (cm^{-1}/molecule.cm^{-2}), $\overline{\chi}(\nu)$ is the frequency-dependent area-normalized absorption lineshape function ($1/cm^{-1}$) which is characterized by various enlargement contributions such as sample pressure and temperature, σ_0 is the cross–section on resonance (at center frequency ν_0) and $\overline{\chi}^{abs}(\nu)$ is a peak-normalized absorption lineshape function (dimensionless). The normalization requirement is:

$$\int_0^{\infty} \overline{\chi}(\nu)\, d\nu = 1 \tag{2.3}$$

with ν is the frequency in cm^{-1}. The attenuation of selected radiation is measured by a detector, providing the absorption spectrum of a particular transition. Combined with some spectral parameters (S, ν_0) from the common databases (HITRAN, or GEISA) [4,5], the concentration of the target species can be determined.

2.1.2 Aspect of applied spectroscopy : absorption profile and line parameters

Absorption spectroscopy is not only for quantitative determination of concentrations of interested species but also for characterization of their spectroscopic properties if their concentrations are well known. These properties are the position of the transition lines (also called center frequency), the intensities, and the phenomena that impact the absorption profile of the compounds including line broadening by air and its temperature dependence, self-

broadening, the influence of air pressure on the frequency of the transition, Einstein coefficient, and energy levels. The remainder of this section is to devote various broadening mechanisms which affect the line profiles under different experimental conditions.

2.1.2.1 Absorption profile

Due to various broadening processes, absorption has a frequency distribution around the center frequency of the transition that defines a certain linewidth. The shape of the absorption feature is described by the lineshape function $\bar{\chi}(v)$ depending on the experimental conditions (essentially on the temperature and pressure of the sample) and normalized according to equation (2.3). The absorption linewidth can be impacted by line broadening due to three different phenomena : natural broadening, broadening by the Doppler effect, and collisional broadening [6] that causes the lineshape to be represented by a Gaussian, Lorentzian, or Voigt function.

If the lineshape originates from an inhomogeneously (Doppler) broadened transition (usually at low-pressure conditions of less than one mbar), the lineshape function has a Gaussian form, and its area-normalized function can be expressed as:

$$\bar{\chi}_D = \frac{\sqrt{\ln 2}}{\Delta v_D \sqrt{\pi}} \exp\left(-\ln 2 \left(\frac{v - v_0}{\Delta v_D} \right)^2 \right) \tag{2.4}$$

with the Doppler half width at half maximum (HWHM), Δv_D, is given by:

$$\Delta v_D = v_0 \sqrt{\frac{2kTN_A \ln 2}{Mc^2}} \approx 3.58 \times 10^{-7} v_0 \sqrt{\frac{T}{M}} \tag{2.5}$$

where v_0 is the center frequency, N_A is the Avogadro's number (=6.022×10^{23} molecules/mole), M is the molecular weight (g/mol) of the species, k is the Boltzmann's constant (J/K), and T is the temperature in [K].

In the case of homogeneously broadened transition media mainly due to collision broadening (occurring predominantly at high pressures where the molecular density is more significant and the collision rates are high, usually at P > 100 mbar), the area-normalized lineshape function has a Lorentzian form and can be expressed as:

$$\bar{\chi}_L = \frac{1}{\pi} \left(\frac{(\Delta v_L)}{(v - v_0)^2 + (\Delta v_L)^2} \right) \tag{2.6}$$

with

$$\Delta\nu_L = \gamma_{self}(T).P_p + \sum_i \gamma_i(T).P_i \tag{2.7}$$

where the HWHM, $\Delta\nu_L$, is a sum of different broadening contributions, including the self-broadening (with coefficient γ_{self}) of the considered gas at its partial pressure P_p and the pressure broadening (with coefficient γ_i) with other gases species "*i*" at the partial pressure P_i. The parameters γ_{self} and γ_i are listed in the HITRAN and GEISA databases for a number of common trace gases.

If neither of these two broadening mechanisms are dominant (the pressure is in a range of 1-100 mbar), the line shape function is described by a Voigt function, which is a convolution of the Gaussian and Lorentzian functions. There is no explicit analytic formula for the Voigt function, it is necessary to numerically calculate the Voigt profile; several iteration procedures exist [7,8]. In section **5.3.3** of this thesis, the spectral analysis of the HONO spectra was performed with the "Fityk" fitting tool [9], which has the advantage of modeling the data with multiple peaks with a built-in function type (such as Gaussian, Voigt, Lorentzian, sigmoid, polynomial and dozens of others) and to be under GNU General Public License. An illustration of absorption profiles dominated by the three different lineshapes is shown in Figure 2.2.

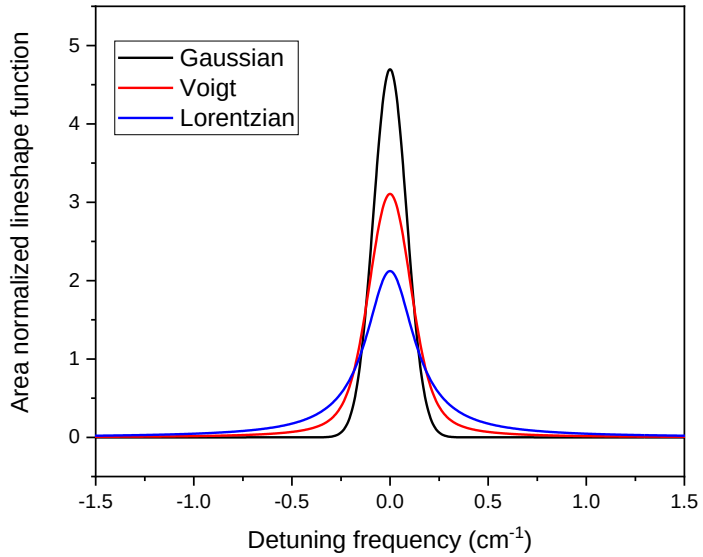

Figure 2.2 Absorption profiles dominated by different area-normalized lineshape functions.

2.1.2.2 Determination of line parameters

The integrated line intensity *S* and the center frequency are the essential line parameters for quantitative trace gas sensing based on absorption spectroscopy. Based on Eq. (2.1) & (2.2), line intensity of a specific transition can be determined at a given temperature *T* by integrating the absorption spectrum with the knowledge of the media concentration and the optical path length.

$$S(T) = \frac{\int \sigma(\nu)\, d\nu}{\int \bar{\chi} d\nu} = \frac{1}{nL} \int \ln\left(\frac{I_0(\nu)}{I(\nu)}\right) d\nu \tag{2.8}$$

dν is in cm^{-1}. In addition, the center frequency ν_0 of a transition can be extracted from the fit of the lineshape function to the experimental spectrum. For example in **Chapter 5**, the line positions of transitions of *cis*-HONO were determined from the Voigt fit of the absorbance spectra recorded simultaneously with direct measurement of laser frequency by a wavelength meter. The frequency metrology will be explained in detail in section **5.2.3**.

2.1.3 Trace gas quantification

In direct absorption spectroscopy, number density of the target species can be determined after digital processing of the absorption signal from the detector in the following way:

According to Eq. (2.1), the absorbance spectrum $A(\nu)$ can be obtained by the ratio between the light intensities without ($I(\nu)$) and with ($I_0(\nu)$) the presence of the target species in the absorption cell:

$$A(\nu) = \ln\left(\frac{I_0(\nu)}{I(\nu)}\right) = n.\sigma(\nu).L = n.S.\bar{\chi}(\nu).L \tag{2.9}$$

By integrating the absorbance spectrum around the center frequency of a single transition line described by the normalized absorption profile, the integrated absorbance A_I (the area under the absorption profile) with the unit cm^{-1} is introduced:

$$A_I = \int A(\nu) d\nu = n.S.L. \int_0^{\infty} \bar{\chi}(\nu) d\nu = n.S.L \tag{2.10}$$

Since the integrated lineshape is defined as $\int_0^{\infty} \bar{\chi}(\nu)\, d\nu = 1$. Eq. (2.10) takes advantage of independent of the lineshape function which is affected by the broadening mechanisms, i.e.,

the environment where the species is detected. Therefore, the absolute number of density of the medium (number of molecules per cm^3), *n*, can be determined:

$$n = A_I / (S.L) \tag{2.11}$$

In general, the concentration of gas-phase molecules in the atmosphere is represented by a dimensionless mixing ratio which is expressed in pptv (particles per trillion, or 10^{-12}), ppbv (parts per trillion, or 10^{-9}), or ppmv (parts per million, or 10^{-6}). The mixing ratio C is the abundance of one component (the medium under investigation) of a mixture relative to that of all other elements and is defined by:

$$C = n / N(T, P) \tag{2.12}$$

where $N(T,P) = N_L \dfrac{P.T_0}{P_0.T}$ is the number of global molecules per unit of volume under experimental conditions of pressure *P* and temperature *T*. N_L = 2.68678×10^{19} molecules.cm^{-3} is the Loschmidt number representing the number of molecules of an ideal gas at reference pressure P_0 (1013.25 mbar) and at reference temperature T_0 (273.15 K).

The concentration in ppm, C_{ppm}, is obtained from:

$$C_{ppm} = \frac{A_I}{S.L.N(T,P)} \times 10^6 \tag{2.13}$$

2.2 Instrumental characteristic performance consideration

2.2.1 Measurement accuracy and precision

The accuracy of a measurement, usually presented by the uncertainty, is known as the degree of closeness of the measured analyte concentration to its true value. According to Eq. (2.13), the total relative uncertainty of the concentration determined by absorption spectroscopy is:

$$\delta_C = \sqrt{\sum (\delta_i)^2} \tag{2.14}$$

with the element δ_i presents the relative uncertainty in the absorption path length *L*, in the line intensity *S*, in the integrated absorbance A_I, in the pressure *P*, and in the temperature *T*, respectively. The accuracy of the concentration from absorption spectroscopic measurement is mainly limited by the uncertainties in the absorption path length *L*, in the integrated area A_I, and in the absorption line intensity *S* (provided by the database [4] and usually δ_s ~ 5% or even more). The calibration of the path length is thus essential for accurate determination of analyte concentration. In this work, the optical path length is calibrated using a standard

reference gas with an accurate well-known concentration (section **3.2.3**). We also note the fact that in the case of cavities, there is no unique path length and that this aspect will be discussed later.

The precision of a measurement is the degree to which repeated measurements under unchanged conditions show the same results. In simpler terms, with a given set of data points from repeated measures of the same quantity, the sample set is considered precise if their standard deviation is relatively small (by an accepted value) compared to their average value, and is considered accurate if the average value is close to the true value. Generally, the measurement precision is mainly limited by the system stability (see **3.3.5.1**). In a *white* noise (see **2.2.2.1**) dominant regime, the measurement precision can be improved by data averaging within an optimal integration time, which can reduce the noise by a factor of $N^{1/2}$ (with N being the average number of measurements). The optimal integration time can be characterized using Allan variance analysis introduced by David W. Allan [10] in 1966 for a characterization of frequency standards.

2.2.2 Signal to noise ratio (SNR) and limit of detection (LoD)

2.2.2.1 Noise characterization

In general, the detection limit of an analytic instrument is limited by noises affecting the absorption signal, which can be divided into three kinds of noises:

(1) *White* noise coming from the shot noise and thermal noise linked to the electronic detection systems, respectively. It is independent of the frequency. The thermal noise arises from the random fluctuation of the velocity of the charge carriers in resistive material and consistently contributes to the total noise, regardless of the laser power impinging on the detector. Typically, white noise of the electronic system can be effectively reduced by averaging spectra. On the other hand, the shot noise originates from the quantum nature of the light or from the discrete nature of electric charge that occurs in photon counting in the photodetectors, causing the random electronic emission. This type of noise is thus unavoidable and constitutes the fundamental noise limit. The shot noise current from a photodetector is given by [11],

$$i_{shot} = \sqrt{2e.i_{dc}.BW} = \sqrt{2e.\eta.P_D.BW} \tag{2.15}$$

where e is the electron charge (C), BW is the detection bandwidth (Hz), $i_{dc} = \eta P_D$ represents the average photon current, η is the detector responsivity (A/W), P_D is the incident optical power impinging on the detector (W).

In direct absorption spectroscopy, the shot noise related detection limit can be expressed as [12]:

$$(\alpha_0)_{\min} = \frac{1}{L_{eff}} \sqrt{\frac{2e.BW}{\eta P_D}} \tag{2.16}$$

with $(\alpha_0)_{\min}$ being the minimum detectable absorption coefficient, and L_{eff} being the effective path length (m).

(2) ***Flicker noise***, often referred to as "1/f" noise or "pink" noise. It is the most common type of noise that has a power density maximum around the frequency f = 0 Hz. Its origin is usually the power fluctuation of the light source. In direct absorption spectroscopy, spectral signals are measured with a bandwidth from 0 Hz up to high cutoff frequencies which depend on the bandwidth of the detector or the pre-amplifier. This type of noise is a significant issue that usually limits the LoD. An effective way to eliminate 1/f-noise is to shift the absorption signal away from the low frequency regime and perform the detection in a relatively high-frequency domain to eliminate the 1/*f* noise by using modulation techniques, such as phase-sensitive detection, wavelength modulation or frequency modulation [13–15]. The concept of modulation techniques will be discussed in more detail in section **3.3**.

(3) ***Residual amplitude modulation*** (RAM). The RAM [16] is raised from variation of the wavelength-dependent laser power associated to the wavelength modulation of the semiconductor laser by modulation of the laser injection current. It also occurs when the optical setup has a frequency-dependent transmission (especially in an optical cavity), causing optical noise which contribute to the total noise in the detection system.

(4) ***Interference fringes*** (etalon effect) is related to multiple reflections inside or between optical components, causing unwanted periodic signals [17] which cannot be removed by spectral average.

RAM and etalon effects are the most common optical noise sources [18,19] that could not be eliminated entirely, although several approaches have been applied, i.e., adequate alignment, avoiding beam retro reflections using anti-reflection coated or wedged optical components, and polarization [20], or using a digital filter to suppress the etalon fringes [21–23].

The limit of detection is enhanced if and only if the noise issues are solved by using either one or a combination of several techniques. A well-constructed detection system is thus considered when it has the LoD close to the shot noise level.

2.2.2.2 Signal to Noise Ratio

The SNR can be defined as the ratio of the signal amplitude $Peak\_ampl$ of the absorption line to the standard deviation σ_N of the noise *Np-p* (peak-to-peak) in the baseline. Alternatively, the peak amplitude can be returned from a fit of the absorption lineshape to the experimental data and σ_N is the 1σ residual (the standard deviation between the measured absorption line and its fitted profile). An example is shown in Figure 2.3, where an absorbance spectrum of H_2O in air (mixing ratio of 22000 ppmv) at 1660.46 cm^{-1} in an interaction length of 100 m was recorded at a pressure of 9.2 mbar with 1 s integration time. The SNR was 32.2.

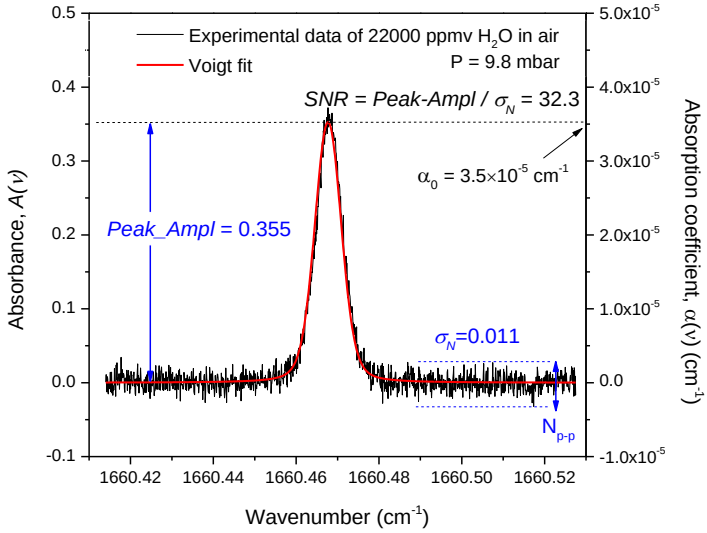

Figure 2.3 An example for calculating the limit of detection. The left hand axis refers to an absorbance spectrum (dimensionless) of an H_2O line near 6.0 μm recorded over an optical path length of 100 m within an integration time of 1 s, while the right hand axis represents the absorption coefficient spectrum calculated by dividing $A(\nu)$ by the path length.

2.2.2.3 Limit of detection

Minimum detectable quantity, called also the limit of detection (LoD) is usually used to characterize the measurement capacity of a spectroscopic instrument for a specific species. There are several ways to define the LoD of absorption spectroscopy [24–28].

Experimentally, the LoD is mainly determined by the SNR of a spectral signal used to infer the concentration. The 1σ (SNR=1) LoD can be expressed as follows:

$$LoD = C_{ppm} / SNR \tag{2.17}$$

where C_{ppm} is the concentration inferred from the spectral signal that exhibits a SNR being used in Eq. (2.17).

Sometimes the detection limit can be expressed in terms of minimum detectable absorption coefficient (MDAC), $(\alpha_0)_{\min}$ with units of cm^{-1}, as defined as:

$$(\alpha_0)_{\min} = \alpha_0 / SNR \tag{2.18}$$

where α_0 is the absorption coefficient at the center frequency of the target line used to quantify the molecular concentration. In the case of absolute $\alpha(\nu)$ being provided by a spectroscopic approach (for example DAS, cavity ring-down spectroscopy CRDS (see **3.1.2.1**), ….) this value is calculated based on the experimental spectrum. For instance, the right axis in Figure 2.3 shows the absorption coefficient spectrum $\alpha(\nu)$, obtained by dividing $A(\nu)$ to the path length, L_{eff} = 1000 cm. By fitting the calculated $\alpha(\nu)$ spectrum, α_0 = 3.5×10^{-5} cm^{-1} is determined from the fitted value at the line center. With SNR = 32.2, the minimum detectable absorption coefficient is $(\alpha_0)_{\min} = 1.09\times10^{-6}$ cm^{-1}.

In contrast, some methods cannot provide absolute $\alpha(\nu)$ such as wavelength modulation spectroscopy (WMS) and Quartz-enhanced photoacoustic absorption spectroscopy (QEPAS), $\alpha_0 = \sigma_0$. N is determined via the simulated cross-section σ_0 from the databases, taking into the experimental conditions such as sample pressure, temperature, laser linewidth, and the determined concentration *n*.

2.2.2.4 Minimum detectable absorption (MDA) and Noise Equivalent Absorption Sensitivity (NEAS)

The detection limit calculated by Eq. (2.17) only provides the minimum detectable quantity for a particular integration time used to obtain the spectral signal. Minimum detectable absorption (MDA with units of $Hz^{-1/2}$) is defined to describe the minimum detectable absorption normalized by the detection bandwidth [27]:

$$MDA = \left(\frac{\Delta P}{P}\right)_N \cdot \sqrt{\tau_{opt}} = \left(\frac{\Delta P}{P}\right)_N / \sqrt{BW} \tag{2.19}$$

where N is the number of averaged spectra measured within an integration time $\tau_{opt} = N * T_s$ (normally optimized based on the Allan deviation analysis), $BW = 1/\tau_{opt}$ is the detection bandwidth, ΔP is the minimum variation in intensity measurable by the instrument due to absorption, while P is the intensity of the signal. T_s is the period of the laser scanning (spectral sweep). We can consider $\Delta P/P$ as the 1σ residual of the fitted spectrum. It can also be taken as the standard deviation of individual data measured over time. The MDA is sometimes cited with units of ppmv.$Hz^{-1/2}$ [25] or molecules.cm^{-3}. $Hz^{-1/2}$ [28] for LoD normalized to the detection bandwidth.

With a spectroscopic technique using resonators to increase interaction path length, the minimum detectable absorption can be normalized by the interaction length L_{eff}, which is called "Noise Equivalent Absorption Sensitivity" (NEAS) in [cm^{-1}. $Hz^{-1/2}$]:

$$NEAS = MDA / L_{eff} = \left(\frac{\Delta P}{P} \right)_N . \frac{1}{L_{eff}} . \frac{1}{\sqrt{BW}} \tag{2.20}$$

NEAS indicates the smallest absorption coefficient that can be measured for a 1 s integration time. The calculation of the NEAS allows comparing the performance of instruments that are based on different measurement approaches.

Note that the definitions of the MDA and the NEAS used in this thesis is scaled to "per scan" values that considers the noise fluctuation of a full scanned spectrum over multiple absorption lines. Consider that a full spectrum is measured at a scan rate of f_s. Each spectrum is acquired by an interval time equaled to $T_s = 1/f_s$. The detection bandwidth used to calculate those two values is the bandwidth corresponding to an integration time needed to average N spectra to achieve the specific SNR (integration time = $N.T_s$), rather than the bandwidth of the detector, nor the bandwidth of the instrument (cavity), nor the acquisition rate.

2.2.3 Measurement specificity (spectral selectivity)

In case of gas sensing by spectroscopy, spectral overlapping of absorptions from various species, called spectral interference, might cause a serious issue that should be carefully addressed. Spectral selectivity is thus an important parameter to characterize the instrument ability to correctly retrieve the target gas concentration in the presence of concomitant species. A high selectivity thus means that the measurement is relatively insensitive to spectral interference effects. There are several ways to improve the selectivity, such as selection of spectral lines well isolated from interfering lines from other gases (Figure 2.4-a),

performing the measurement at a reduced pressure to avoid spectral line overlapping due to pressure-broadening (Figure 2.4-b), removing the Doppler broadening using saturation absorption spectroscopy [29], and interference-free detection of paramagnetic species based on the magneto effect using Faraday rotation spectroscopy [30] (being discussed in **Chapter 4**). Figure 2.4 shows a simulation of absorption spectra based on the HITRAN database that illustrates the spectral overlap of absorption lines of common atmospheric target molecules, N_2O and OH in panel (a) and (b), respectively. It demonstrates that the interference issue needs to be carefully considered when choosing the spectroscopic parameters (i.e., the absorption line, the working pressure) for optical monitoring of the target molecules. For example, the chosen N_2O (a) and OH (b) lines are well isolated to absorption lines of other species.

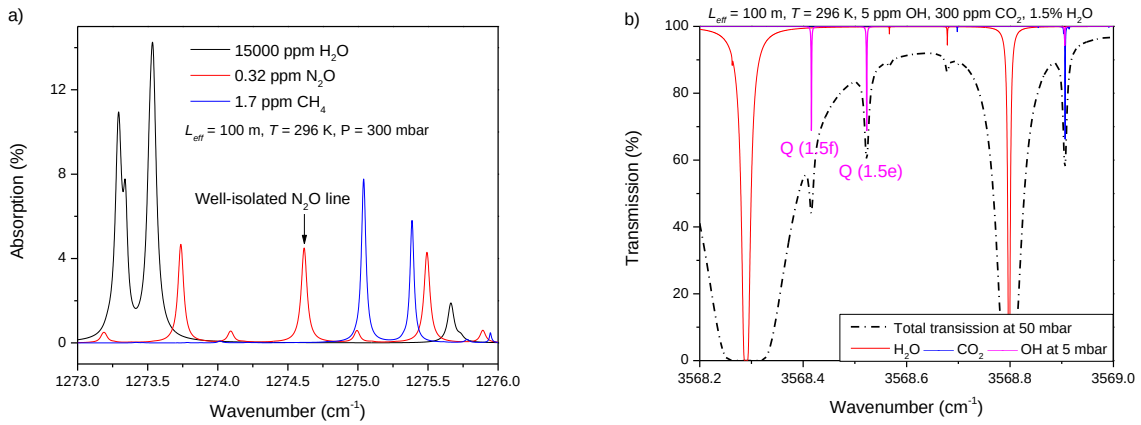

Figure 2.4 a – Simulated absorption spectra for the atmospheric concentration of N_2O in the presence of H_2O and CH_4. A well-isolated N_2O line can be used for high selective monitoring concentration in the atmosphere. b – Simulated absorption spectra of double lines transition Q(1.5f) and Q(1.5e) of OH at 2.8 µm. The spectral overlap with strong H_2O lines can be avoided by working at a reduced pressure.

2.3 Conclusion

As discussed above, absorption spectroscopy can be used for identifying and quantifying molecules in the gas phase. Development of a spectrometer needs consideration of detectability, selectivity, precision, and accuracy. According to the Beer-Lambert law, there are two ways to improve the detectability of an analytical instrument: enhancing the absorption signal and decreasing the noise. A more significant absorption signal can be obtained by selecting a different transition with a larger cross-section or line intensity, and increasing optical absorption path length. The long interaction path length between light and

absorbing medium can be realized by using either a multi-pass absorption cell or an optical cavity, while the choice of a transition with higher intensity needs to be considered in the context spectral interference. Noise reduction, on the other hand, is usually achieved by spectral averaging and modulation techniques. The combination of several approaches thus may further improve the measurement sensitivity of a system.

Chapter 3 Development of an instrument based on cavity-enhanced absorption spectroscopy (CEAS) for OH radical detection

Increasing light-matter interaction path lengths is one of the effective ways to improve the sensitivity of trace gas detection by absorption spectroscopy. This can be achieved by using an optical cavity in which the photons are trapped and make a large number of round trips within the probed medium, enhancing thus the effective absorption path length. The most common cavities are made up of two high-reflectivity mirrors. Spectroscopy techniques using such an optical resonator are grouped under the generic term of CEAS, Cavity-enhanced absorption spectroscopy [82]. Among various laser-based cavity techniques, off-axis integrated cavity output spectroscopy (OA-ICOS) [83–86] is a good candidate for trace gas detections. Using the un resonant coupling of a narrow bandwidth laser source into a cavity, this approach has advantages of simple optical alignment [80] and robustness. In particular OA-ICOS determines the molecular absorption based on the measurement of time-integrated light leaking out of the cavity, rather than the time-decay of the light intensity inside the cavity like in CRDS; it does not require high bandwidth detection [87].

This chapter will present the development of an optical instrument for OH detection at 2.8 μm based on the OA-ICOS approach. First, the principle of the CEAS technique and several approaches based on cavity-enhanced absorption method are briefly recalled in section **3.1**. Then the implementation of the OA-ICOS device will be explained in detail in section **3.2**.

In section **3.3**, a wavelength modulation scheme was applied to the OA-ICOS setup to shift the detection to a higher frequency regime where 1/f noise is reduced (WM-OA-ICOS). The LoD was improved by a factor of 4 compared to that obtained by OA-ICOS.

3.1 Cavity-enhanced absorption spectroscopy

Multi-pass cells provided an increase in the interaction length L [88–90] typically up to ~ 200 m. Their implementation turns out to be technically complex when hundreds of passes are desired inside a gas cell using planar or specifically designed mirrors [91]. First, optical alignment of the mirrors in a multi-pass cell requires highly stable mechanics. Second, large mirror sizes, and consequently, a large sample volume, are required in order to reduce optical interference effects [92] resulting from light beam overlap between adjacent reflections. Longer pathlengths can be achieved with the help of optical cavities providing thousands of

passes inside the cavity. Moreover, the mirror size is much smaller than in the multi-pass cell as it only depends on the laser beam size propagating along the optical axis of the cavity. The cell volume is thus reduced significantly. In contrast to the traditional multi-pass absorption cells, where a long path is achieved by multiple-reflections of the laser beam between two (or more) mirrors, the coupling of the laser beam into a high-finesse cavity to get thousands of number round-trips in a cavity is complicated. It requires mode-matching of the laser beam to the cavity mode which will be discussed in section **3.1.1**.

3.1.1 Properties of optical cavity

An optical cavity acts as a resonator that amplifies the light trapped in it and can be characterized by several parameters. A brief introduction is provided below which concentrates on the fundamental aspects which are to be considered to design a linear cavity (consisting of two spherical mirrors), as well as on the physical behavior of the cavity response in the spectral domain.

First, light beam propagation within a resonator must meet the criteria of stability for resonance. The stability condition of a cavity is obtained from g-Parameters, which are based on the choice of an adequate length of the cavity L for the non-destructive propagation of the beam between two mirrors (M_1 and M_2) with radius of curvature r_1 and r_2, as defined as:

$$0 < g_1 g_2 < 1 \tag{3.1}$$

with $g_i = 1 - L / r_i$. So for two identical mirrors ($r_1 = r_2 = r$), the cavity is optically stable if:

$$0 < L < r \quad \text{or} \quad r < L < 2r \tag{3.2}$$

Second, light transmission through an optical cavity has a frequency-dependent resonance. This function can be described by an Airy function establishing a “comb-like” transmission pattern. The light can only pass through the cavity with maximum transmission if the cavity length is equal to an integer number of half wavelength of the injected light. The peak pattern is called cavity mode structure. For a cavity constructed from two spherical mirrors, the mode structure is given by [93]:

$$\nu_{qmn} = \frac{c}{2L}\left(q + \frac{(n+m+1)}{\pi} \arccos\sqrt{r_1 r_2} \right) \tag{3.3}$$

Each set of values of the three integers q, m and n, defines cavity modes, where q, m and n are the mode indices that characterize the electromagnetic field in the cavity. Specifically, q presents the low order modes – longitudinal modes (usually called the Gaussian TEM00

mode), while *m* and *n* describe the high order modes – transverse modes, corresponding to the variation of the electric field in the plane perpendicular to the cavity axis. The transverse mode structure is described by the standard TEM_{mn} mode labeling.

The frequency spacing between two adjacent longitudinal modes (labeled by *q* and *q* + 1), but with the same values of *m* and *n*, is the *free spectral range* (FSR) of the cavity (see Figure 3.1 – right).

$$FSR = c/(2n_r L) \tag{3.4}$$

where n_r is the refractive index of the medium in the cavity. A perturbation applied to either the frequency of the laser radiation illuminating the cavity or to the length of the cavity is converted to the small deviations around the cavity modes, having Lorentzian profile with a FWHM of $\Gamma = FSR/F$. F is called the cavity finesse, depending on the mirror reflectivity, that determines the maximum possible circulating power inside the cavity and is usually expressed as:

$$F = FSR/\Gamma = \pi\sqrt{R}/(1-R) \tag{3.5}$$

where R is the geometric mean of the mirror reflectivity.

Finally, to successfully couple a light beam mode of a laser into and transmit through the cavity, the laser beam mode and the cavity mode should be mode-matched. The mode-matching is required to convert the properties of the incoming laser beam into those best supported by the cavity in order to ensure a high laser coupling efficiency and high laser power building-up in the cavity. For a Gaussian-profile beam [94] and a linear cavity with identical mirrors (g_1=g_2=g), mode-matching can be achieved by matching the laser beam waist size to the cavity waist size at its center and matching the radius of curvature (RoC) of the laser wavefront with the RoC of the cavity mirror at the mirror's surface. A simple mode-matching arrangement of a signal mode collimated laser beam to the cavity using a signal lens is shown in Figure 3.1 – left. The cavity waist size is determined by [95]:

$$w_0^2 = \frac{L\lambda}{\pi}\sqrt{\frac{1+g}{4(1-g)}} \tag{3.6}$$

The lens focal length *f*, the distance *d* from the lens to the first mirror and the incident beam radius w_i are important parameters for mode-matching [96]. In practical work, two or more lenses are required to give more flexibility to experimental configuration.

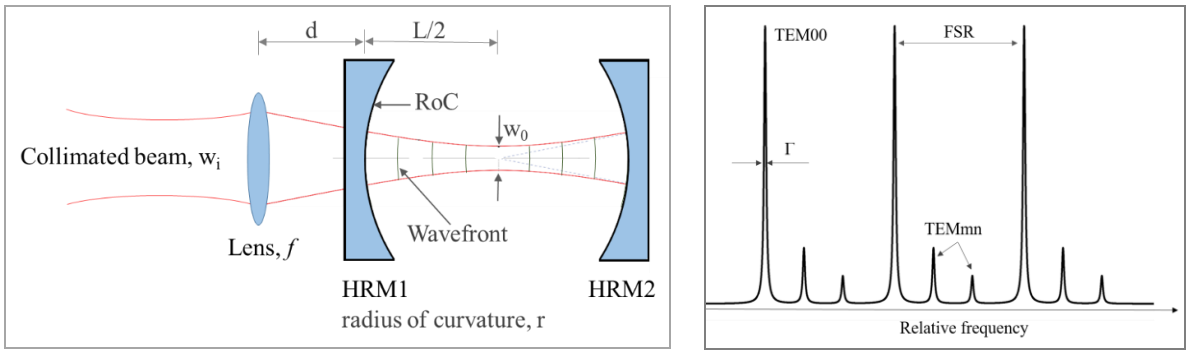

Figure 3.1 Left – simple mode-matching setup with a single lens at a distance d from the cavity transforming a collimated incident beam of spot size w_i to match the spatial characteristics of the lowest order mode of the cavity. Right – an example of cavity transmission (Finesse = 50) consisting of the fundamental modes TEM00 and transverse modes TEM_{mn}. Mode-matching maximizes the power that builds up in the lowest order cavity modes, thus reducing significantly the transverse modes.

3.1.2 Various CEAS approaches

CEAS techniques usually measure the power transmitted through the cavity and benefit from the enhanced signal contrast. The absorption can be detected in the time domain i.e. CRDS [97,98] based upon the comparison of the cavity decay times in empty and filled cavities (time-decay measurement), or in amplitude domains (time-integrated output measurement) such as OA-ICOS [83] and OF-CEAS [99]. This section summarizes the basic equations which are necessary to analyze and retrieve the recorded data in different CEAS approaches.

3.1.2.1 Cavity ring-down spectroscopy (CRDS)

CRDS is based on measuring the decay time of the light intensity leaking out of a cavity. It can be performed with pulsed [100,101] or continuous-wave (CW) [102,103] laser sources. In both cases, the best sensitivity is achieved when a single longitudinal cavity mode is excited. This condition is difficult to obtain for pulsed lasers because of their relatively large emission bandwidth. With CW lasers, the bandwidth is typically narrow (a few MHz) and thus single longitudinal modes can be achieved. To obtain a ring down event in CW-CRDS, the cavity length is tuned (by scanning a PZT installed on one cavity mirror) in resonance with the laser frequency. When the light is built up with the cavity mode, the light on the detector exceeds the set threshold value, and a trigger signal is generated to turn off the laser beam via an acousto-optical modulator (AOM). The ring-down signal is recorded and then an exponential function is fitted to the ring-down decay to determine the decay time [34]. When the laser

frequency is scanned, the frequency-dependent absorption coefficient can be obtained from the decay times measured without and with absorber in the cavity $\tau_0(\nu)$ and $\tau(\nu)$:

$$\alpha(\nu) = n.\sigma(\nu) = \frac{1}{c}\left(\frac{1}{\tau(\nu)} - \frac{1}{\tau_0(\nu)}\right) \tag{3.7}$$

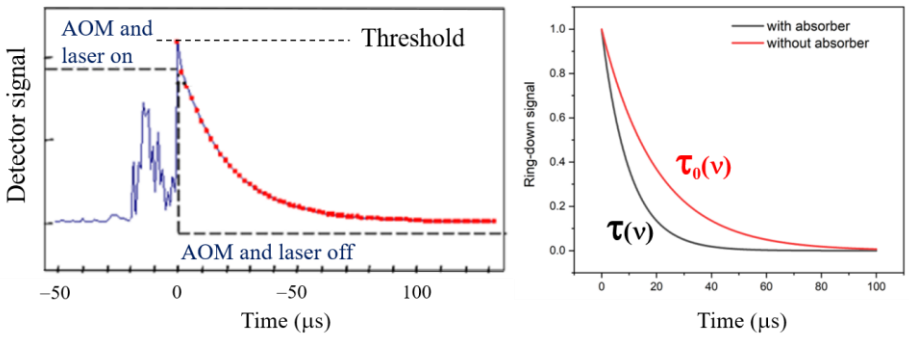

Figure 3.2 Left – illustration of ring-down signal recording with laser turned on/off by an AOM [97]. Right – ring-down time with and without absorber, $\tau(\nu)$ and $\tau_0(\nu)$, respectively.

CRDS is a direct absorption technique that provides the absorption coefficient on an absolute scale with high sensitivity. CRDS measurements are independent of the amplitude of the light intensity transmitted through a cavity, but they are susceptible to various types of low-frequency noise that affect the decay rate measurement. The minimum detectable absorption coefficient in CRDS is proportional to the mirror loss (1-*R*) divided by the cavity length:

$$\alpha(\nu)_{\min-CRDS} = \frac{1-R}{L}\left(\frac{\Delta\tau}{\tau_0}\right)_{\min} \tag{3.8}$$

where $\Delta\tau$ is the standard deviation of the measured ring-down times. As can be seen, the sensitivity depends on the uncertainty of decay time measurement which is affected by the vertical (intensity) and horizontal (time) resolution of a digitizer used for recording the ring-down signal, and the performance of the fitting routine used to extract the decay rate. For example, considering a cavity constructed with two identical mirrors with reflectivity of R = 0.9999, separated by L = 50 cm, and assuming that the decay times are measured with high accuracy $\left(\Delta\tau/\tau_0\right)_{\min} = 0.1\%$, the minimum detectable absorption coefficient can reach 2×10^{-9} cm^{-1}.

Disadvantage of CRDS, though it is not a real challenge, is the requirement of a fast switch on/off the laser and high-speed electronics devices to capture ring-down signals. According to equations (2.9), (2.10) and (3.7), concentration determination requires a whole spectrum

$\alpha(\nu)$ for a particular transition. Therefore, in many cases, the laser frequency needs to be scanned across a spectral region. At each laser frequency, the laser is switched off for measuring the ring-down decay. Thus, the data collection over the investigated wavelength range is thus not continuous.

3.1.2.2 Phase-shift cavity ring-down spectroscopy (PS-CRDS)

A different version of CRDS is phase shift cavity ring-down spectroscopy (PS-CRDS), in which the absorption is measured in terms of the phase shift between the modulated CW light beams entering the cavity and the light transmitted through the optical cavity, using a lock-in amplifier [104,105]. A sinusoidally intensity-modulated light beam (with an angular modulation frequency, ω) passes through a high-finesse optically stable cavity, the light undergoes a phase shift $\phi(\nu)$ related to the ring-down time of the cavity, $\tau(\nu)$:

$$\tan\left[\phi(\nu)\right] = -\omega\tau(\nu) \tag{3.9}$$

By measuring the magnitude of the phase shift with and without absorbers in the cavity, the frequency-dependent absorption coefficient can be determined by rewriting equation (3.7) with $\tau(\nu)$ taken from equation (3.9).

$$\alpha(\nu) = \frac{\omega}{c}\left(\frac{1}{\tan\phi(\nu)} - \frac{1}{\tan\phi_0(\nu)}\right) \tag{3.10}$$

The absorption spectrum is extracted from the measured frequency-dependent phase-shift angle which is independent of the intensity fluctuation of the light source, and measurements of the ring-down time are not needed in PS-CRDS.

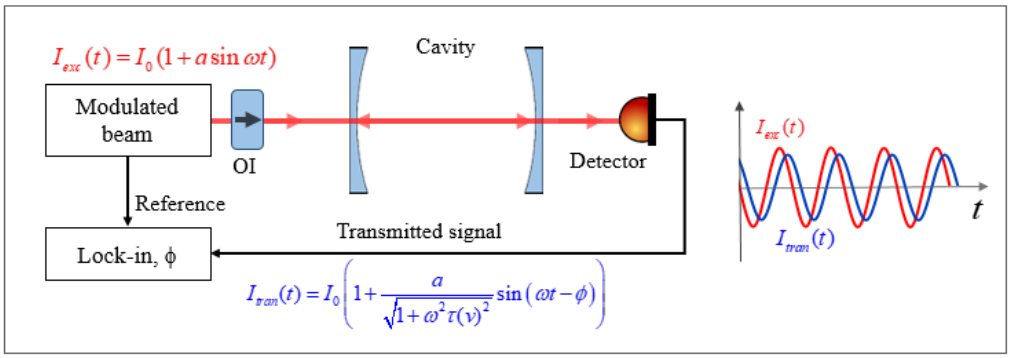

Figure 3.3 Principle of PS-CRDS. OI – optical isolator.

3.1.2.3 Optical feedback cavity-enhanced absorption spectroscopy (OF-CEAS)

Optical-feedback cavity-enhanced absorption spectroscopy (OF-CEAS) relies on a self-locking of a laser beam to the TEM00 mode of the cavity. This process is carried out by allowing optical feedback (OF) from the high finesse cavity to the laser. If the optical feedback is at the correct phase (resonance within the cavity), it 'seeds' the laser, stimulating it to emit a narrower bandwidth below the mode linewidth. Normally, a V-shape cavity (constructed from three cavity mirrors) is used as it is perhaps the simplest configuration producing frequency selected OF when the laser frequency enters in resonance with one of the cavity mode [106]. The OF-CEAS is performed by scanning the laser wavelength through many cavity modes. The laser emission is locked to each resonance frequency by OF, thus enabling efficient injection of the laser into the cavity to achieve strong and stable cavity transmission and reduction of amplitude noise.

By recording the cavity transmission when the laser frequency is scanned across an absorption feature, the molecule's absorption spectrum can be obtained. In the case of V-shape cavity, the absorption coefficient $\alpha(\nu)$ of an intra-cavity sample can be written in the form [107]:

$$\alpha(\nu) = \frac{1-R}{d}\left(\sqrt{\frac{I_0(\nu)}{I(\nu)}} - 1\right) \tag{3.11}$$

where $I_0(\nu)$ being the amplitude of the cavity modes represents the baseline. d is the sum of the two arms of the V-shape cavity. The mirror reflectivity R needs to be calibrated to extract the absolute absorption coefficient, typically by measuring the integrated absorption of a known concentration gas [108]. Such a set-up has the advantage over conventional ICOS (discussed in the next section) because it is not plagued by low signal levels and it minimizes problems associated with intensity and laser linewidth fluctuations. On the other hand, the absorption coefficient data are extracted from the peak value of TEM00 modes which are equally separated by the FSR of the cavity. This technique is limited when the absorption linewidth is less than or comparable to the cavity FSR, especially with experiments performed at low pressure.

3.1.2.4 Integrated cavity output spectroscopy (ICOS)

Unlike CRDS, integrated cavity output spectroscopy (ICOS) is based on measuring the time-integrated light intensity leaking out of a high finesse cavity. The absorption spectrum as a function of laser wavelength is obtained by continuously sweeping the frequency of the used

CW laser around the transitions to be studied. The first description of the ICOS experiment was introduced by *O'Keefe* in 1998 for a pulsed laser [109] and then was applied for CW lasers [83,110]. The characteristic of the light intensity leaking out the linear cavity formed by two identical mirrors $\left(R_1 = R_2 = R\right)$ is described with considerations that the mode structure of the cavity intensity is neglected, and the cavity transmission is determined only by the mirror reflectivity *R* and the one-pass absorption $e^{-\alpha L}$ by the medium inside the cavity.

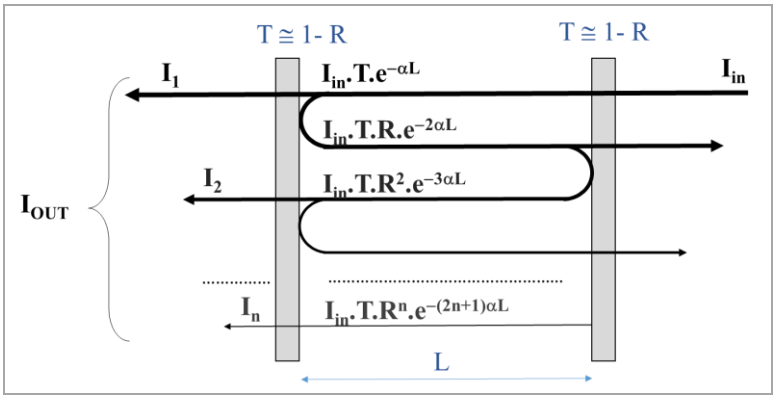

Figure 3.4 A schematic diagram for calculating the integrated intensity output of a beam leaking out of a cavity of length L in ICOS experiments. I_{in} is the incident intensity of the laser, and I_{out} is the time-integrated output intensity.

Assumes that non-absorbing and non-scattering mirrors are used (so the mirrors transmission is $T \cong 1-R$) and the cavity is optically stable, the first pass of the laser light through the cavity gives the transmitted signal (detected behind the second mirror) related to the incident pulse, I_{in}, by:

$$I_1 = I_{in}.T.T.e^{-\alpha L} \tag{3.12}$$

where α is the absorption coefficient due to the presence of the absorber over the cavity length *L*. The next transmission to the detector follows a round-trip cycle in the cavity where the intra-cavity power is reduced by two reflections and two-pass absorption:

$$I_2 = I_{in}.T.T.R^2.e^{-3\alpha L} \tag{3.13}$$

The total (integrated) transmitted signal is a summation over an infinite number of round-trip cycles, *n*, in the cavity:

$$I_{out} = \sum_{n=0}^{\infty} I_n = I_{in} T^2 \sum_{n=0}^{\infty} R^{2n} e^{-(2n+1)\alpha L} = I_{in} \left(1-R\right)^2 e^{-\alpha L} \sum_{n=0}^{\infty} \left(Re^{-\alpha L}\right)^{2n} \tag{3.14}$$

Because $Re^{-\alpha L} < 1$, equation (3.14) is rewritten:

$$I_{out} = I_{in} \frac{(1-R)^2 e^{-\alpha L}}{1-R^2 e^{-2\alpha L}} \tag{3.15}$$

Consider the case in which there is no absorption ($\alpha = 0$), the output intensity is:

$$I_{out}^0 = I_{in}(1-R)/(1+R) \tag{3.16}$$

The ratio of intensities measured without and with absorption is:

$$\frac{I_{out}^0}{I_{out}} = \frac{1-\mathrm{R}^2 \mathrm{e}^{-2\alpha L}}{(1-R^2)\mathrm{e}^{-\alpha L}} \tag{3.17}$$

The absorption coefficient is determined by solving equation (3.17) with measured integrated signals with and without the medium filled in the cavity. There are, however, several approximated formulas used to analyze the absorption in ICOS experiments [83,110,111]. Commonly, with a very low absorption coefficient $(\alpha \to 0)$, we have $e^{-2\alpha L} \approx 1-2\alpha L$ and $e^{-\alpha L} \approx 1$. Equation (3.17) can be re-written by:

$$\frac{I_{out}^0}{I_{out}} = \frac{1-\mathrm{R}^2(1-2\alpha L)}{(1-R^2)} = \frac{1-\mathrm{R}^2+\mathrm{R}^2 2\alpha L}{(1-R^2)} = 1+\frac{2\alpha L \mathrm{R}^2}{(1+R)(1-R)} \tag{3.18}$$

Consider high reflectivity ($R \to 1$ and $1+R \approx 2$), a transmission describing the change of the power in a cavity pumped by a CW laser can be derived as:

$$\frac{I_{out}^0}{I_{out}} = 1+\frac{\alpha L}{1-R} \tag{3.19}$$

Compared to traditional absorption spectroscopy (single pass) where $I_{out}^0 / I_{out} = e^{\alpha L} \approx 1+\alpha L$ according to Beer-Lambert law, ICOS shows an effective enhancement of the absorption by a factor:

$$G = (1-R)^{-1} \tag{3.20}$$

That makes ICOS suitable for use as direct absorption method for quantitative measurement of weak molecular absorption. Here the effective path length enhanced by the cavity is introduced:

$$L_{eff} = L/(1-R) \approx \frac{F}{\pi} L \tag{3.21}$$

The use of higher reflectivity mirrors can further improve the enhancement factor, however, the resultant very low cavity transmission becomes a serious limitation to sensitivity.

According to equation **(3.16)**, the transmitted power intensity through the cavity without absorption is approximated by:

$$P_{out} = C_p P_{in} \frac{1-R}{1+R} \cong C_p \frac{T}{2} P_{in} \tag{3.22}$$

where a factor C_p (in a range between 0 and 1, depending on the optical arrangement) is added to correct for the spatial coupling efficiency of the laser beam injection into the cavity [111]. Consider a cavity formed from the mirrors with R = 0.9999 and a CW laser power of 5 mW. Assuming perfect coupling of the laser to the cavity (C_p = 1) yields a transmitted power of only 250 nW! The non-resonant coupling ICOS technique results in low output signal [112]. Accurate measurement of the integrated signal requires very high sensitivity detectors, relatively high input laser power and extensive averaging of the time-integrated cavity output.

Rewriting Eq. (3.19), the frequency-dependent absorption coefficients around a molecular transition can be expressed as follows:

$$\alpha(\nu) = \frac{1-R}{L}\left(\frac{I_{out}^{0}(\nu)}{I_{out}(\nu)} - 1\right) \tag{3.23}$$

with $I_{out}^{0}(\nu)$ represents the baseline which is in many cases determined from the nth order polynomial fit for spectral retrieval. It can be seen that ICOS is a multi-pass like high finesses cavity technique that allows continuously sampling cavity output while not requiring any optical switching or fast electronics devices to analyze ring-down transients as in CRDS. However, the mirror reflectivity must be calibrated beforehand in order to determine the absolute magnitude of $\alpha(\nu)$ using Eq. (3.20), which is a disadvantage of ICOS compared to CRDS. Because ICOS relies on intensity measurement as opposed to time-decay measurement in CRDS, residual mode structure and laser frequency noise can cause the intensity fluctuation in the cavity transmission which is directly converted into the noise in the integrated signal on the detector. They are the main noise sources which limits ICOS's sensitivity to less than CRDS [111,112]. From Eq. **(3.23)**, the minimum detectable absorption coefficient for the ICOS system is:

$$\alpha(\nu)_{\min-ICOS} = \frac{(1-R)}{L}\left(\frac{\Delta I}{I_{out}^{0}}\right)_{\min} \tag{3.24}$$

where ΔI represents the intensity fluctuation due to cavity mode fluctuations and fluctuations of the light source. The MDAC under the shot noise limit is provided by [65]:

$$\alpha_{\min-shotnoise} = \frac{\pi}{L.F}\sqrt{\frac{2eB}{\eta P_D}} \approx \frac{1-R}{L}\sqrt{\frac{2eB}{\eta P_D}} \tag{3.25}$$

where e is the electron charge, η is the photodetector responsivity, and P_D is the incident power on the detector, L is the cavity length, F is the cavity finesse and B is detector bandwidth. From Eq. (3.24) and (3.25), it can be seen that the MDAC in ICOS is mainly dependent on variations of the transmitted signal.

The measurement accuracy is mainly dependent on the error in the mirror reflectivity R and noise of the light impinging on the detector:

$$\left(\frac{\Delta\alpha}{\alpha}\right)_{ICOS} = \sqrt{\left(\frac{\Delta R}{R}\right)^2 + \left(\frac{\Delta I}{I_{out}^0}\right)^2} \tag{3.26}$$

In general, ICOS technique has a higher detectability only by virtue of the cavity enhancement factor (Eq. (3.19)). The cavity not only enhances the absorption but also amplifies the amplitude variations related to the laser-frequency noise, thus causing amplitude noises. In addition, the fluctuation of the cavity transmitted intensity due to the mode structure cause a significantly higher optical noise compared to the continuous transmission in the conventional single and multi-pass approaches [113]. To reduce noise, ICOS can be combined with cavity length modulation (via PZT), signal averaging or using off-axis configuration [114].

3.1.2.5 Off-axis integrated cavity output spectroscopy (OA-ICOS)

The cavity mode noise is absolutely crucial and limits the sensitivity of the ICOS system. An extension to ICOS, termed off-axis ICOS, uses off-axis alignment of the incident laser beam. The laser beam is coupled off-axis to the cavity, resulting in a Herriott and Lissajous type pattern in the spherical and astigmatic cavity mirror, respectively [111]. In this technique, a non-mode matched condition is recommended to excite higher-order transverses modes, thus creating a dense cavity mode structure. Combined with rapid laser scanning and averaging spectra, the fluctuation of cavity-mode based transmitted intensity is reduced. The absorption signal is “smooth” in much the same fashion as in conventional absorption measurements using a multi-pass cell. The absorption coefficient spectrum is determined using the same formula as ICOS – equation (3.23).

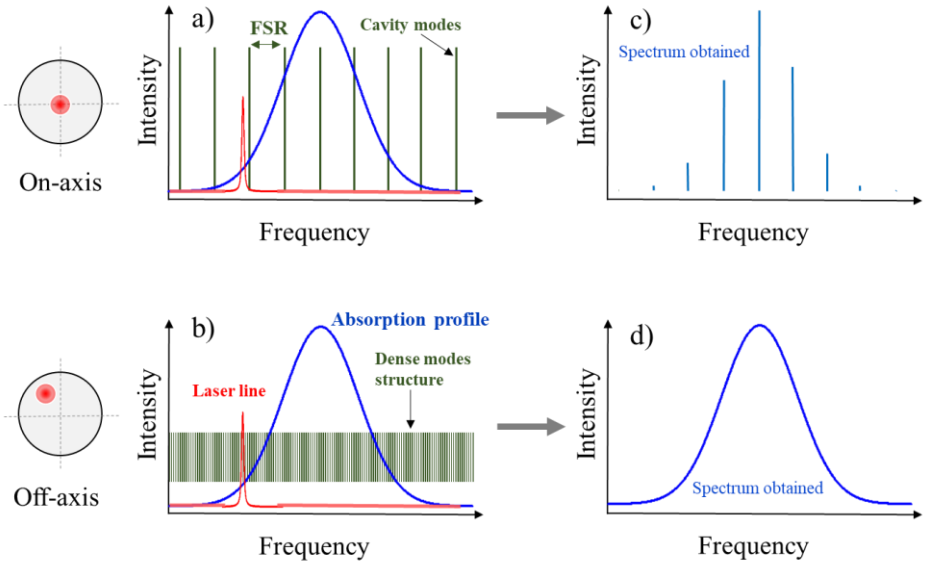

Figure 3.5 Demonstration of the mode structure between on-axis (a) and off-axis (b) alignment within the scan of a narrow bandwidth laser across a molecular transition. In a successful off-axis alignment, a dense mode structure is excited, resulting in the continuous cavity transmission in the absorption spectrum (d), compared to the on-axis configuration (c). [114]

A comparison of the cavity mode structure and the noise in the transmitted intensities using on- and off-axis coupling of the laser into the cavity is shown in Figure 3.5 and Figure 3.6, respectively.

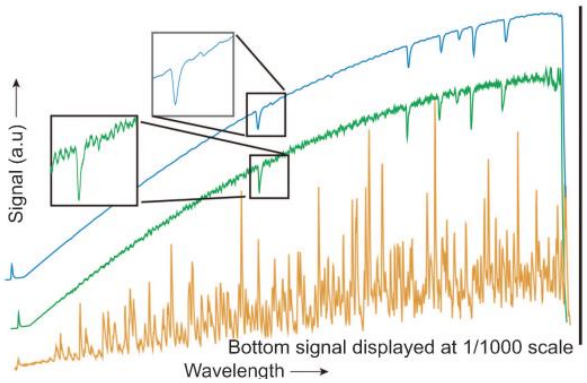

Figure 3.6 An example demonstrating three different levels of the noise of the cavity transmitted signal resulting from the coupling of laser to optical cavity on-axis (orange), near ideal off-axis (green) and ideal off-axis alignment (blue) [114].

As discussed above, each laser-based cavity technique has its advantages and disadvantages, in terms of system complexity and measurement sensitivity. In the consideration of the need of a compact and robust instrument for continuous and in-situ measurement of gases, the OA-ICOS approach is chosen to develop a detection system for monitoring OH radical. The sensitivity of OA-ICOS is then further improved by combining it with a wavelength

modulation technique. The detail of those experiments is described in the next sections **3.2** & **3.3**.

3.2 Development of an OA-ICOS instrument for OH radical detection

An OA-ICOS instrument operating at 2.8 μm was developed based on off-axis coupling an Interband Cascade Laser (ICL) beam to a high finesse cavity. The instrument performance was investigated by measuring OH radicals that were produced in a microwave discharge of water vapor. This section will present the experimental procedures for the development of the instrument and the characterization of its performance.

3.2.1 Choice of absorption transition lines and OH production method

To achieve high sensitivity of a spectroscopic instrument, careful choice of the exploitable transition line(s) is essential. The consideration includes the spectral parameters of the investigated molecule, such as line intensities and the transition frequencies. Higher line intensity provides higher absorption signal, while well-isolated absorption lines allow avoiding interference from other atmospheric species. Second is the material constraints, including the availability of laser sources, their characteristics (power, spectral range, and linewidth), and the optical components (depends on laser wavelength) used for the system assembly. Finally, the cost for building the setup should be reasonable.

In the earlier works, the long path absorption spectroscopy has been applied to measure OH concentrations in the UV region [26,33,115] since the highest line intensity is from its electronic transitions located near 308 nm [116]. Due to the broadband absorptions of some molecules such as HONO [117], O_3 [118], and NO_2 [119,120] in the same spectral range, the use of UV sources makes the measurement facing potential spectral overlaps. Meanwhile, the infrared provides rich rovibrational transitions which are suitable for optical detections. The employment of those transitions, with the availability of various commercially compact, and narrow bandwidth laser sources (i.e., ICL), will provide high spectral resolution of absorption spectra for concentration retrieval. In this work, the OH lines originating from rovibrational transitions in the infrared were chosen for OH monitoring. The line intensities and line frequencies of OH and other atmospheric molecules are listed in the HITRAN database. Possible interferences with absorption lines of other species have been identified. Figure 3.7 shows the transitions of OH, H_2O, and CO_2 in the visible and the mid-infrared region. We can see that OH transitions located near 2.8 μm have higher intensities compared to other regions.

Among the available OH transitions in this frequency range, the highest and well-isolated OH (Q1.5e) line at 3568.5238 cm^{-1} (intensity of 9.032×10^{-20} cm^{-1}/molecules.cm^{-2}) has been chosen for monitoring the concentration (see the inserted graph). The CO_2 line addressed at 3568.6982 cm^{-1} (noted by *) will be used later for calibration of the developed OA-ICOS system – section **3.2.3**.

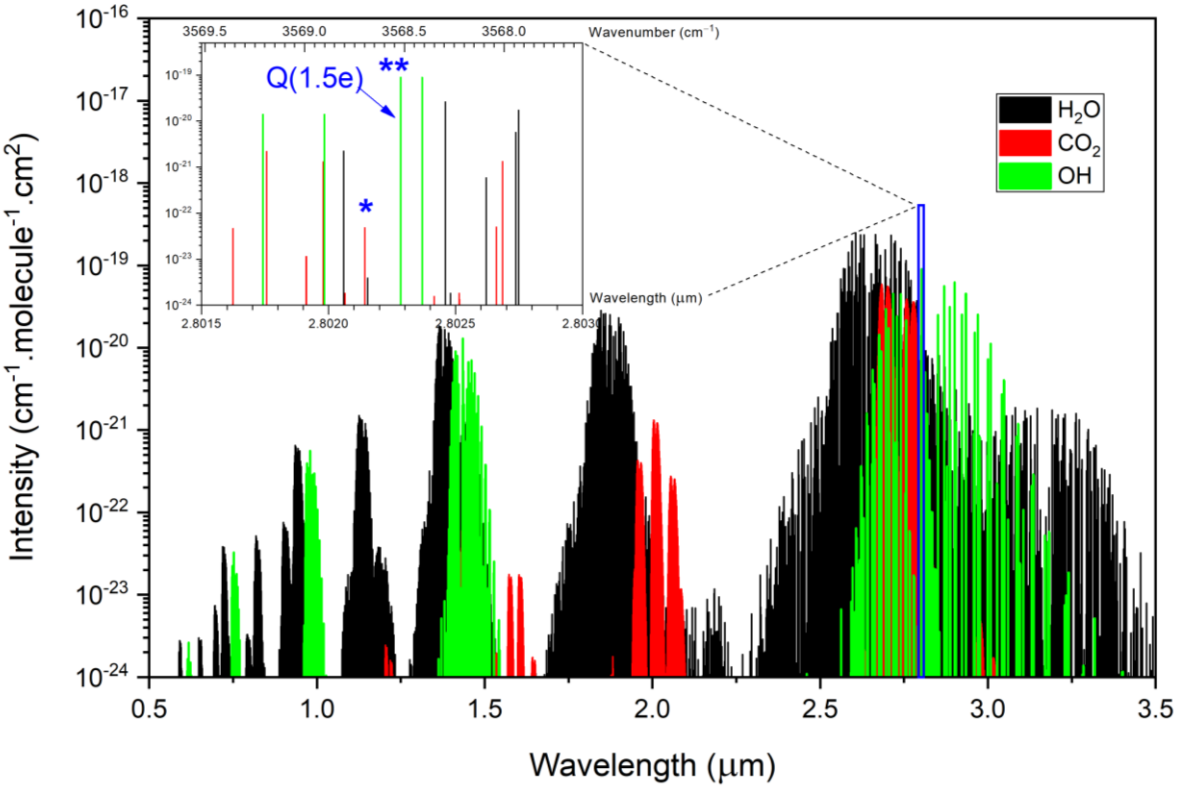

Figure 3.7 Transitions of OH (green), H_2O (black) and CO_2 (red) from the visible to the mid-infrared region. The inserted graph shows the selected OH Q(1.5e) line and a CO_2 line noted by (*) for calibration of the cavity mirror reflectivity.

3.2.2 Implementation of an OA-ICOS system

Figure 3.8 shows the scheme of an OA-ICOS system, consisting of three parts which are the laser sources, the optical cavity, and the detection system. The laser source includes a 2.8 µm distributed feedback interband cascade laser (DFB-ICL), controlled with a laser diode controller (LDC501, Stanford Research System), and a red He-Ne laser for optical alignment. During the work for this thesis, two DFB-ICLs with different optical powers were used: the first one with lower power (5 mW) was accidently broken and then replaced by the second one with higher power (10 mW). In this chapter, both the OA-ICOS (section **3.2**) and WM-OA-ICOS (section **3.3**) setups utilized the first laser. The second laser was used to for the CE-

FRS (in **Chapter 4**). The free-space collimated DFB-ICL beam is co-aligned with the red laser beam via a CaF_2 beam-splitter for optical alignment. The emerging beam from the beam splitter is off-axis coupled into the ICOS cavity with the help of mirrors M_1 and M_2. The incident laser beam made angle of about 2^o with respect to the optical axis of the cavity. The light leaking out of the cavity was focused onto a VIGO detector (PVI-TE-3.4/MIPDC-F-1.0) with a 7.5 cm focal length lens. The ICOS signal is then recorded and digitized by a data acquisition card (PCI 6620, National Instrument) connected to a custom-made Labview interface for data analysis and saving. The details of those components are described in the next section.

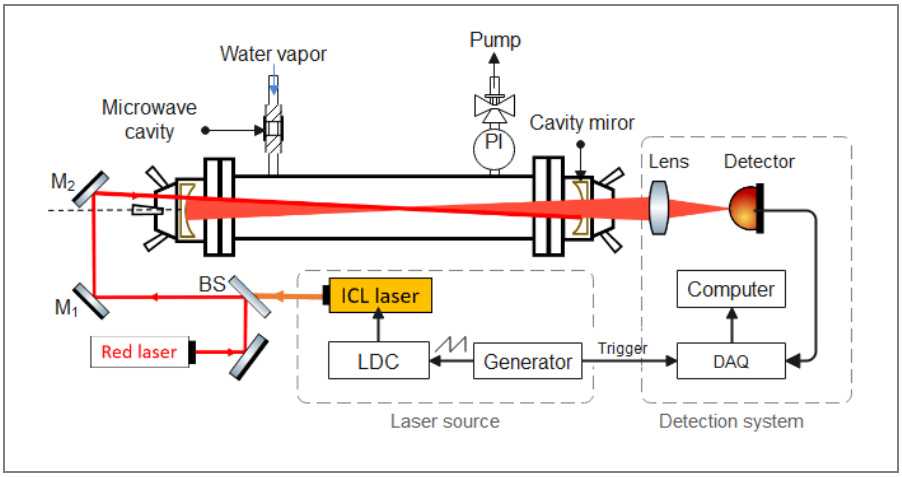

Figure 3.8 Scheme of an OA-ICOS system for detection of OH radical. LDC – Laser diode controller, DAQ – Data acquisition card.

3.2.2.1 Laser source

The used laser source is a single-mode DFB ICL (Nanoplus) integrated together with a TEC[1] and an NTC[2] thermistor in a TO66 package. The laser package is mounted on a cube heatsink and equipped with a collimating lens (Figure 3.9-a). The central wavelength of the laser emission is 2803.2 nm with a maximum continuous output power of ~5 mW. Its frequency is tunable over a spectral range of ~14 cm^{-1} (Figure 3.9-c) by tuning either the temperature (0.36 cm^{-1}/K) or the laser current (0.24 cm^{-1}/mA). A fast tuning laser frequency is performed via current modulation by applying a waveform voltage from a signal generator to the modulation input of the laser controller (the estimated conversion function is about 25 mA/V). The electrical modulation bandwidth is up to 1 MHz.

[1] Thermo-electric cooler
[2] Negative temperature coefficient

a.

b.

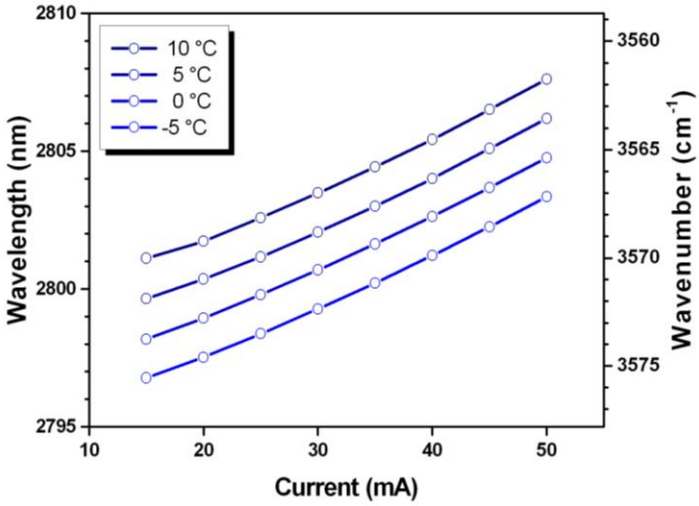

c.

Figure 3.9 a – DFB-ICL mounted on a cube heat sink with a collimating lens. b – Laser controller – LDC501. c – Mode hope free tuning of the DFB-ICL at 2800 nm by current and temperature.

3.2.2.2 Detection systems

The detection system consists of a mid-infrared detector and a data acquisition card (DAQ). The performances of the photodetector were characterized by several intrinsic parameters, including the detector bandwidth, f_{BW}, the spectral response, $\Re(\lambda)$, (the sensitivity of the response at a given wavelength [A/W]), and output noise density (overall noise per unit of bandwidth). The choice of the detector needs to carefully address those parameters so that it can measure very low laser power transmitted through the cavity with a reasonable response time. High measurement sensitivity requires high responsivity and detectivity with low noise density. Meanwhile, a higher bandwidth can provide a faster response time for detecting variations in the intensity of the modes transmitted by the cavity.

An HgCdTe photovoltaic detector (PVI-4TE-3.4, VIGO System S.A.) equipped with a four-stage thermoelectrical cooler and integrated with a preamplifier (MIPDC-F-1) was used for the OA-ICOS setup. The output current, resulting from the impact of photons on the surface of the photodetector, is converted into the voltage signal and amplified by the preamplifier, providing a voltage responsivity (at 3.4 μm) of 1.8×10^6 V/W with a maximum DC output of 2

V and 1 MHz bandwidth. The main specification of the detector and the preamplifier module are given in Table 4.3 in **Chapter 4**.

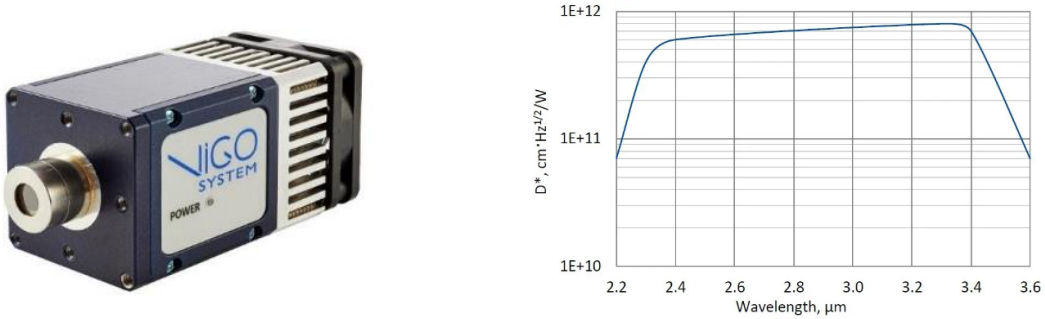

Figure 3.10 Left – PVI-4TE-3.4 VIGO detector. Right – detectivity vs. wavelength (at 293 K)

The acquisition system, i.e., the DAQ card, digitizes the analog signal from the photodetector based on an analog-to-digital converter (ADC). The acquisition system is therefore characterized by its bandwidth and sample rate, indicating how it succeeds in digitizing analog signal. In addition, the precision of the voltage measurement depends on the resolution (bits) and the voltage range of the ADC which affects the noise level in the recorded spectrum. Another critical parameter is the memory writing speed, indicating how fast the data can be transferred from the DAQ memory to the computer. Primarily when a fast scan is performed, simultaneous recording and averaging of the spectra are required. In this work, the NI-DAQ card (NI PCI-6251, National Instrument) is used to measure the absorption spectrum. The card has a bandwidth of 1.7 MHz (at -3 dB) for an input impedance of > 10 GΩ and a sampling rate of up to 1.25 MS/s (for a single analog input channel, AI) with an input FIFO size of 4095 data samples. The PCI bus allows fast sending of data to a Labview's interface in the computer. The DC-coupling AI channels have an ADC resolution of 16 bits with different input ranges (±0.1 V, ±0.2 V, ±0.5 V, ±1 V, ±2 V, ±5 V, ±10 V), providing a random noise of 15 μVrms and an absolute accuracy at full scale of 52 μV.

For example, in the current OA-ICOS approach, the laser wavelength was swept at a scan rate of 50 Hz for the measurements of OH spectra. Each individual spectrum, consisting of 9000 data points, was recorded at a sample rate of 500 kS/s and transferred immediately to the interface for data computing and saving. The absorption spectrum thus could be averaged 50 times within 1 s, meaning 450000 data points were processed. This DAQ card allows direct visualization of the spectrum for the system's settings and to recover the data on removable media to carry out the computer processing and analysis.

3.2.2.3 Optical cavity & optical alignment

The optical cavity is constructed using a 50-cm long and 3-cm outer diameter stainless steel tube (Los Gatos Research, LGR) and two spherical mirrors arranged on either sides of the cell, providing an FSR of about 300 MHz. The interior walls of the tube body have a quartz coating in order to limit the wall reaction with the target molecule samples. Each mirror is mounted on a support equipped with three tripod adjustment screws for cavity alignment. The mirror supports are connected to the cavity body via CF40 flanges, and one of those is equipped with PZT[3] screws to allow micrometric dithering of the cavity mirror.

The spherical mirrors (Layertec GmbH) used for the experiments in this thesis have a diameter of 1 inch and a radius of curvature of 0.4 m which are adapted with the cavity length for a stable optical cavity, according to the equation (3.1). The manufacturer's guaranteed reflectivity is larger than 99.8% for a spectral range from 2500 nm to 3100 nm (Figure 3.11-right). Calibration is performed in section **3.2.3** to determine the exact mirror reflectivity of a specific wavelength.

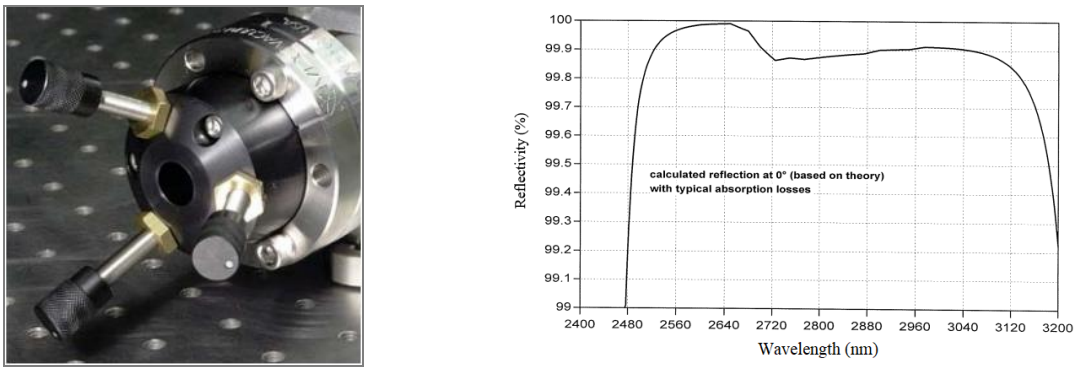

Figure 3.11 Left – cavity mirror support, LGR. Right – mirror reflectivity vs. wavelength (provided by Layertec)

The alignment of the cavity is crucial before implementing the OA-ICOS setup. The initial step, as for CRDS measurements, is to align the laser beam to the cavity axis within two cavity mirrors parallel. The procedure has been described in a reference [121]. In this work, it was done by following three major steps.

[3] Piezoelectric transducer

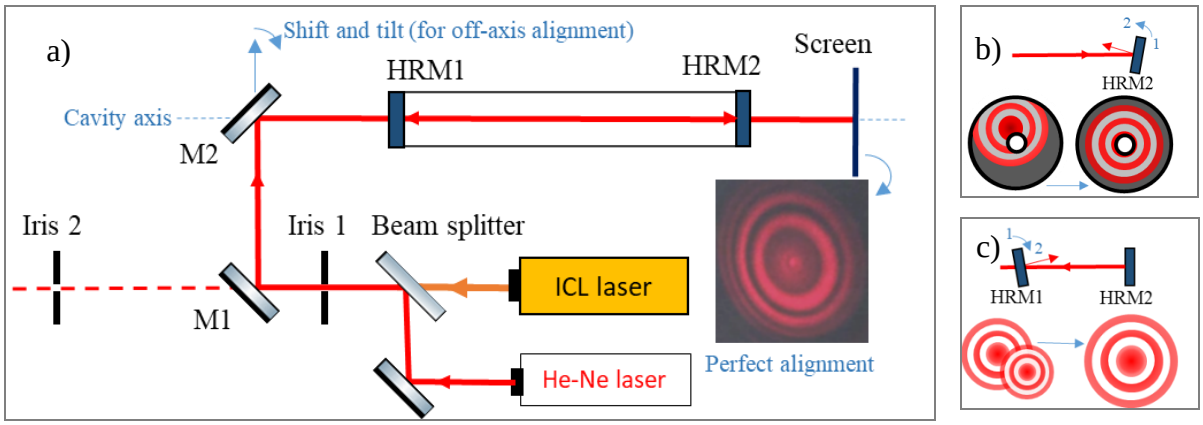

Figure 3.12 a – Experimental setup for cavity alignment. b – The spot pattern due to the reflected laser beam from HRM2 (without HRM1 installed) on Iris 1. The left and the right spot patterns correspond to an adjustment of HRM2 position from 1 to 2, respectively. c – Interference pattern (transmitted through the cavity) due to multi reflections of the laser beams back and fold between two mirrors is observed on the screen (with HRM1 installed). The left and the right interference patterns correspond to an adjustment of HRM1 position from 1 to 2 (parallel with HRM2), respectively. HMR: high reflectivity mirror.

Step 1. Alignment laser beam (He-Ne laser) was co-aligned with the mid-infrared beam via a beam splitter by adjusting two beams to pass through the center of two irises (1 & 2) separated > 1 m. Mirrors M1 and M2 were removed in this step. Their overlapping was rechecked using an IR detector card. A minor adjustment of the beam splitter may be necessary to get a perfect emerging beam. Then, the He-Ne beam could be used for optical alignment in the following steps.

Step 2. The He-Ne laser was aligned to the cavity with the help of mirrors M_1 and M_2. In this step, the cavity axis was determined by placing two mirror holders (without cavity mirrors installed – see Figure 3.11-left) at two ends of the cavity body. Each holder's aperture of 15 mm was glued with a printed circle paper with a drilled pin hole (diameter is smaller than the laser beam) at its center. The laser beam was adjusted to pass through two pin holes on the cavity axis.

Step 3. Aligning the cavity:

- Iris 1 was rechecked to ensure its hole is centered in the laser beam cross-section and allows the passing of the laser beam to the cavity.
- The first entire mirror holder was removed, and the rear cavity mirror (HRM2) mounted on the second holder was installed.

- HMR2 was adjusted to steer the reflection of the He – Ne laser beam back to the center hole of iris 1. The reflection spots should be perfectly centered around the hole so one can see diffraction rings around it (see Figure 3.12-b).
- A thin white paper was placed close to the He-Ne laser so that it cut half of the laser beam. In this case, the overlap between the incident beam and the reflected beam (with the ring interference pattern) could be easily observed. Then, a minor adjustment of the HMR2 to center the incident beam in the rings was necessary.
- Once the rear mirror (HRM2) was well-aligned, the front mirror (HRM1) mounted on the first holder could be installed. Because the mirror holders are designed to press the mirror on an O-ring which compresses upon evacuating the cavity. From this step, the cell was closed and pumped down to a measurement pressure (about 0.5 mbar) to avoid any movement of the two mirrors after alignment since they act as windows.
- The adjustment of the HRM1 was carried out by placing a screen far away from the rear mirror and observing the transmitted interference patterns through the cavity. Carefully adjust HRM1 so that its spot pattern (which looks smaller than the other) is centered on the first pattern caused by HRM1 (see Figure 3.12-c). When two mirrors were perfectly aligned, a concentric ring interference pattern could be observed (see the inserted picture in Figure 3.12-a).

3.2.2.4 Off-axis coupling of laser light into optical cavity

When two cavity mirrors were adjusted perfectly parallel to each other and perpendicular to the laser beam propagating along the cavity's axis, the laser beam was then shifted by a distance from the mirror center to achieve a multi-reflections covering the whole mirror surface [122].

In the present work, the off-axis alignment was arranged by shifting (~6 mm) mirror M2 (placed in a translational stage) perpendicularly to the cavity axis. Then this mirror was tilted at a slight angle so that the light pattern could exist the rear mirror. Finally, the screen was replaced by the detector to measure the cavity transmitted signal. With OA-ICOS alignment, the cavity mode structure was reduced significantly, and the transmitted signal was "smoothed" as a normal transmission from a multi-pass cell, however, at lower voltage level (Figure 3.13-left). The OA-ICOS signal was improved by continuously adjusting mirror M2 to reduce the cavity mode noise while scanning the laser.

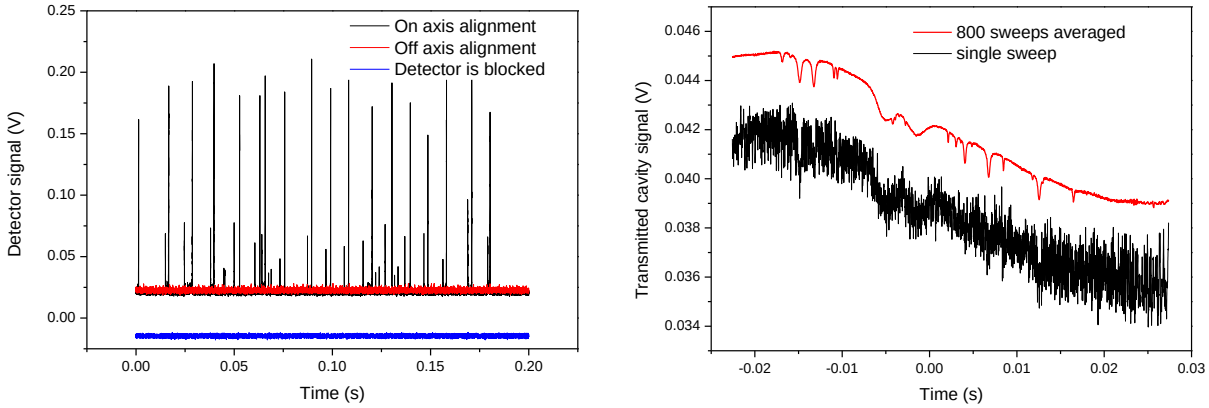

Figure 3.13 Left – time series of detector signal of the light intensity transmitted through the cavity in the case of on-axis laser coupling (black) and off-axis coupling (red) to the cavity. The laser frequency was fixed and the on-axis signal was related to a drift of the mirrors due to (thermal) instabilities. The blue is detector signal without laser incidence providing information on detector noise. Right – single scan (black) and 800 averaged (red) spectra recorded with a well-alignment of the OA-ICOS setup. The red line was manually shifted from the black line for clearly displaying two spectra.

3.2.3 Calibration of cavity mirror reflectivity

According to equation (3.23), quantitative measurement based on the OA-ICOS approach requires the knowledge of the cavity reflectivity *R*, which can be found by either measuring the ring down-time of the empty cavity (like CRDS) or recording a spectrum of a known amount of a specific gas. Although a good approximation for *R* can result from CRDS measurements, it usually requires good cavity alignment, fast optical switching, and digitization of ring-down trace [95]. In the case of off-axis alignment in the present work, the mirror reflectivity was calibrated via absorption measurements of well-known gas concentrations. An available calibrated gas cylinder, containing of a mixture of CO_2+CO+N_2, was used for the measurement of the mirror reflectivity with the help of a nearby CO_2 transition (R 21f) at 3568.6982 cm^{-1}. The concentration of the reference CO_2 in the mixture is $(19.3 \pm 0.3)\times10^4$ ppmv.

A 50 Hz ramping signal from a function generator (Vpp = 400 mV) was applied to the LDC to scan the laser current from 25 to 35 mA, which results in the laser frequency tuning over a spectral range of ~2 cm^{-1} which covers the position of theCO_2 line at 3568.6982 cm^{-1}. The turning rate was about 100 cm^{-1}/s. The laser temperature was set at 5 ^oC. The input range of the AI channel in the NI-DAQ card was set at ± 0.1 V in order to measure the cavity transmitted signal (in the order of a few mV).

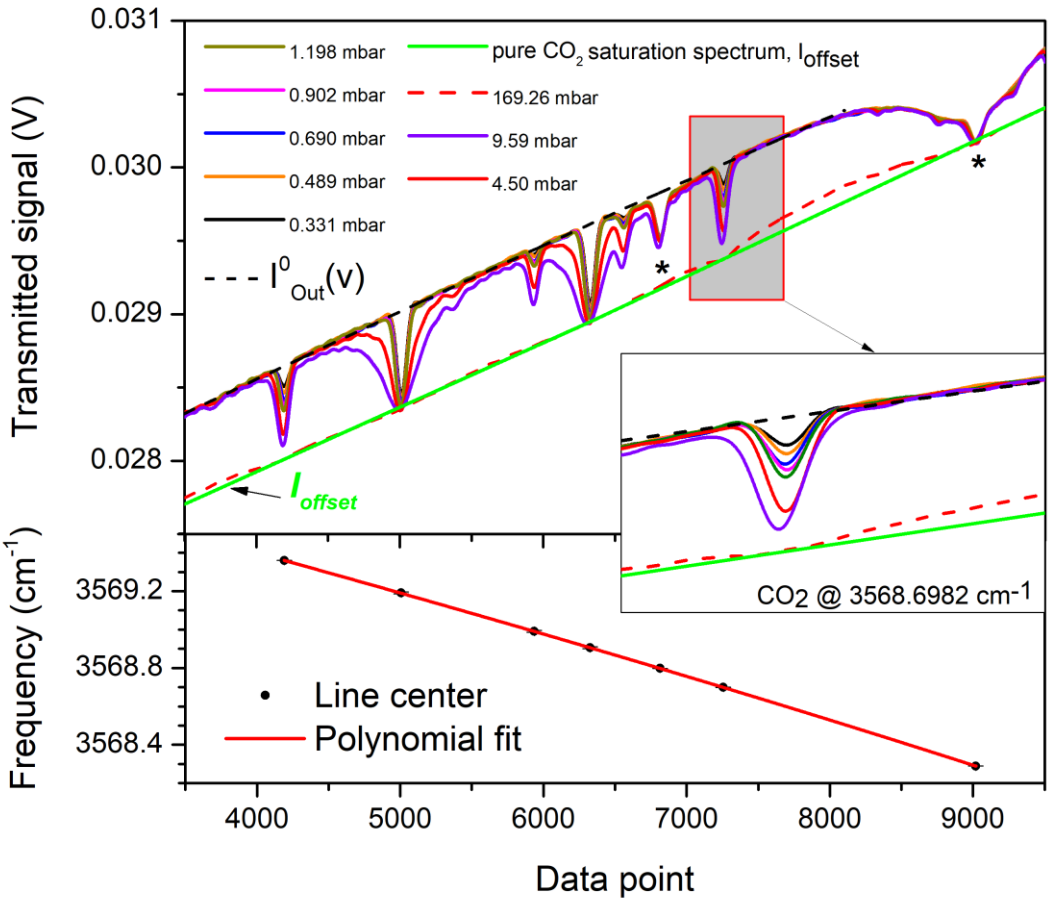

Figure 3.14 Upper – OA-ICOS signals of light intensities leaking out of the cavity recorded by scanning the laser frequency over a spectral range of 2 cm^{-1} at different sample pressure of 19.3 % CO_2. The green line I_{offset} indicates a fully saturation spectrum of pure CO_2 measured at 200 mbar. The lines noted by "*" are H_2O lines. The scanning rate was 50 Hz. Each spectrum was averaged 2000 times. Lower – polynomial fit (red) to the line-center frequencies (black dots) of the CO_2 and H_2O absorption lines. The absorption frequencies are taken from the HITRAN database.

The upper panel of Figure 3.14 shows the time-integrated signals measured at different pressures of the mixture sample as a function of scanning time (represented by data point). The direction from the left to the right of the x-axis corresponds to a decrease of laser frequency in wavenumber. Each spectrum consisting of 9000 data points (sample rate of 500 kHz) was averaged 2000 times by the data acquisition card within an integration time of 40 s. The inserted panel presents the separated CO_2 line located at 3568.6982 cm^{-1} (line intensity of 4.876×10^{-23} cm^{-1}/(molecule.cm^{-2})), which was chosen to determine the value of *R*. The lower panel is the plot of mid-infrared frequency vs. measured data point number corresponding to the CO_2 absorption peak, accompanied with a polynomial fit to determine a calibration curve of frequency vs. data number with the help of the center frequencies of the CO_2 and H_2O absorption lines (black dots) taken from the HITRAN database [59]. This calibration curve is

used for conversion of the recorded absorption signal in the time domain to an absorption spectrum in the frequency domain:

$$y = 3575.151\text{cm}^{-1} - \left(1.718\times10^{-4}\right)\frac{\text{cm}^{-1}}{\text{datapoint}}x - \left(4.21\times10^{-9}\right)\frac{\text{cm}^{-1}}{\text{datapoint}^2}x^2 + \left(4.03\times10^{-14}\right)\frac{\text{cm}^{-1}}{\text{datapoint}^3}x^3 \quad (3.27)$$

with y and x the laser wavenumber (cm^{-1}) and data point, respectively.

It can be seen that the increase of the sample pressure resulting in saturation of absorption lines. Especially at 169.26 mbar, stronger CO_2 transitions are saturated. To determine the saturation level $I_{offset}(v)$, pure CO_2 was then injected into the cell at 200 mbar and the $I_{offset}(v)$ was recorded with a laser scan. As shown by $I_{offset}(v)$ (green line) in the upper panel of Figure 3.14, a fully saturated spectrum was observed and the saturation level was not declined to zero. It demonstrated that there is a background signal (depended on laser frequency) contributing to the OA-IOCS signal $I_{out}(v)$ of the light intensity leaking out of the cavity. This phenomenon can be explained as a result of amplified spontaneous emission (ASE) from the diode laser which constitutes a relatively broadband signal transmitted through the optical cavity [122,123]. In this case, the $I_{offset}(v)$ should be taken into account and subtracted from the $I_{out}(v)$ and $I_{out}^0(v)$ term in equation **(3.23)**. The integrated absorbance for a single line, therefore, is expressed by:

$$A_I = \int A(v)dv = \int L_{eff}.\alpha(v)dv = \int\left(\frac{I_{out}^0(v) - I_{offset}(v)}{I_{out}(v) - I_{offset}(v)} - 1\right)dv \quad (3.28)$$

Figure 3.15-a indicates the absorption signal of the selected CO_2 line (black) after subtraction of $I_{offset}(v)$. The red line is a polynomial baseline with offset subtracted, $I_{out}^0(v) - I_{offset}(v)$, for calculating the absorbance spectra $A(v)$ in Figure 3.15-b. Since the OA-ICOS experiment is performed with an off-axis coupling configuration, as a result, the intra-cavity light is reflected at different regions of the mirror surfaces with different incident angles. It may result in an effective reflectivity which is different to the corresponding value obtained in on-axis alignment (incident angle = 0 degree). As the cavity alignment is affected by sample pressure. The measurement of the mirror reflectivity at different pressures may have different reflectivities [78], therefore, the calibration in this work should be performed under the same

experimental conditions as for the OH measurements. The absorbance spectra in a range of 0.331 – 1.196 mbar were chosen to determine R (shown in Figure 3.15-b).

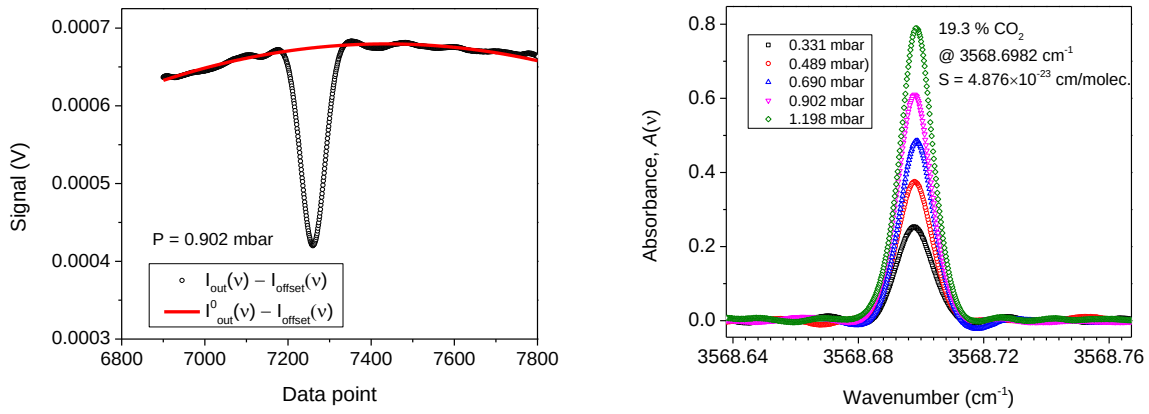

a b

Figure 3.15 a – Transmitted intensity spectrum (black) subtracted by the background signal $I_{offset}(\nu)$ and the polynomial baseline $I^0_{out}(\nu)$ (red) of the selected CO_2 line located at 3568.6982 cm^{-1} at P = 0.9 mbar. b – Absorbance spectra at a pressure approximately 1 mbar, used to determine the effective optical path length.

Absorbance A_I of the CO_2 line is extracted from a Gaussian fit to the absorbance spectra and the pressure-dependent integrated A_I is plotted in Figure 3.16. A good linear relation between A_I and sample pressure is observed according to equation (2.13). The effective path length was determined from the slope of the linear fit:

$$slope = C_{ppm}.S.L_{eff}.N_L.T_0.10^{-6}/(P_0.T) = C_{ppm}.S.\frac{L}{(1-R)}.N_L.T_0.10^{-6}/(P_0.T) \qquad (3.29)$$

with a *slope* = (8.57 ± 0.17)×10^{-3} cm^{-1}/mbar, the concentration of CO_2 in the mixture sample C_{ppm} = 193000 ppm, the line intensity of the CO_2 line S = 4.876×10^{-23} cm^{-1}/(molecule.cm^{-2}) @ T_{ref} = 296 K, N_L = 2.68678×10^{19} molecule, T_0 = 273 K, P_0 = 1013.25 mbar, T ≈ 293 K, an effective path length about 368.6 ± 12.9 m was deduced, corresponding to a mirror reflectivity of (99.864 ± 0.005) % which resulted in an effective cavity finesse of about 2308. In the present experiment, the error of the determined effective path length is about 3.5%, given a 2% uncertainty in the line intensity (the dependence of S on the temperature was not taken in to account), a 2% uncertainty in the slope from the linear fit, a 0.3% uncertainty in the concentration of CO_2, and a 2% uncertainty in the gas temperature (considered as room temperature).

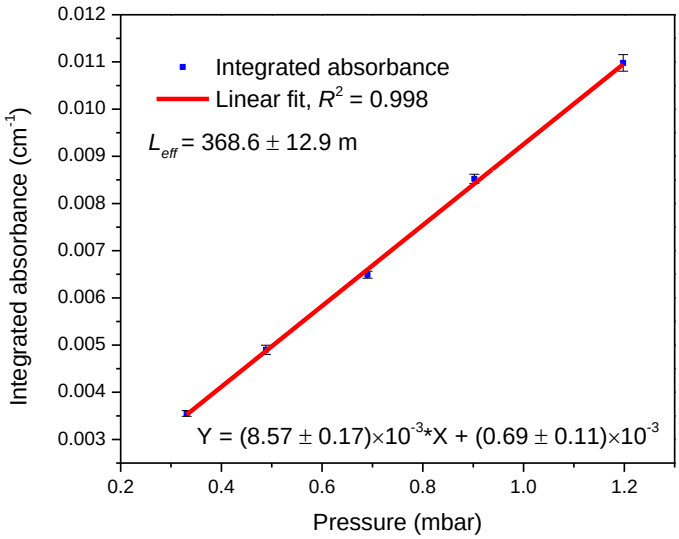

Figure 3.16 Measurement of the mirror reflectivity based on the measurement of absorption spectra of a CO_2 transition at 3568.6982 cm^{-1} as a function of pressure with the knowledge of the concentration and the line intensity, which allowed determination of the effective path length L_{eff}.

3.2.4 Performance of the developed OA-ICOS system

OH radical is a highly reactive species with a very short life time, no calibrated cylinder can be used as spectral reference standard. To evaluate the performance of the developed OA-ICOS instrument, OH radicals were generated by a microwave discharge of a pure H_2O vapor flow at P < 1 mbar in a 6 mm quartz tube inserted in a microwave cavity (Figure 3.17). Due to the lack of a flowmeter working at low pressures, the flow rate could not be determined and it was considered constant when the total sample pressure was stable.

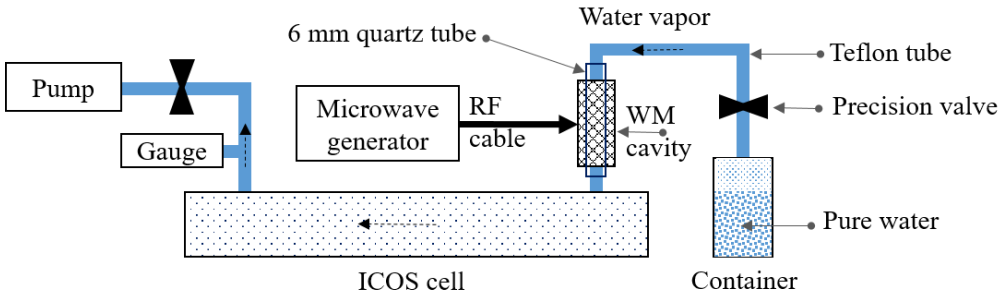

Figure 3.17 Scheme of OH production by microwave (MW) discharge of water vapor.

Pure water vapor was produced by creating a vacuum at the surface of the distilled water which was contained in a sealed container. Once the pressure in the container is lower than the saturated vapor pressure, the water evaporates into its gaseous form. Continuously

pumping the ICOS cell causes a pressure difference with the container, thus the water vapor was injected to the detection system. Before the generation of OH radicals, the whole system was pumped down to 0.04 mbar. Then a needle valve was slowly opened and adjusted to inject continuously water vapor from the container into the quartz tube. The microwave discharge ionizes water vapor and produces OH radicals that were flushed to the ICOS cell. The generation of OH radicals was carried out continuously by a 2.45 GHz microwave discharge (Sairem Inc.) at 75 W[4]. The concentration of OH was measured by the OA-ICOS approach downstream of the discharge.

3.2.4.1 Detection of OH radical by OA-ICOS approach

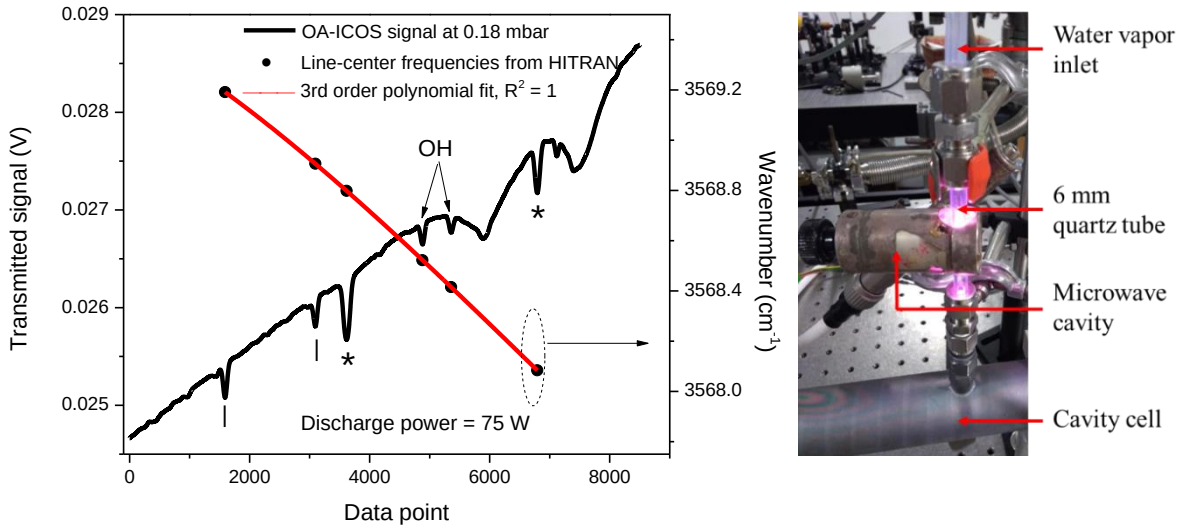

a b

Figure 3.18 a – 3000-averaged OA-ICOS spectrum (black line) showing the Q (1.5) double-line of the $^2\Pi_{3/2}$ state of OH transition in the presence of H_2O and CO_2 lines, noted by "*" and "|", respectively. The black dots represent the center frequencies of those absorption lines whose values are taken from the HITRAN database. The red line is the polynomial fit for the laser frequency calibration. b – Picture showing microwave discharge for OH production.

An experimental OA-ICOS signal is shown in Figure 3.18-a. The spectrum, consisting of OH, H_2O, and CO_2 lines, was averaged 3000 times at a scan rate of 50 Hz (experimental estimated from several scan rates to obtained less noise in the spectrum) corresponding to an integration time of 60 s. The spectral processing was performed as explained in section **3.2.3**. The red

[4] Due to the microwave source performance, the power of 75 W is chosen to maintain the production of OH stable.

curve shows a third-order polynomial fit to the center frequencies of all absorption lines recorded in order to obtain a calibration curve of frequency vs data point number such that the absorption signals can be converted to the absorbance spectrum as a function of laser wavenumber (Figure 3.19).

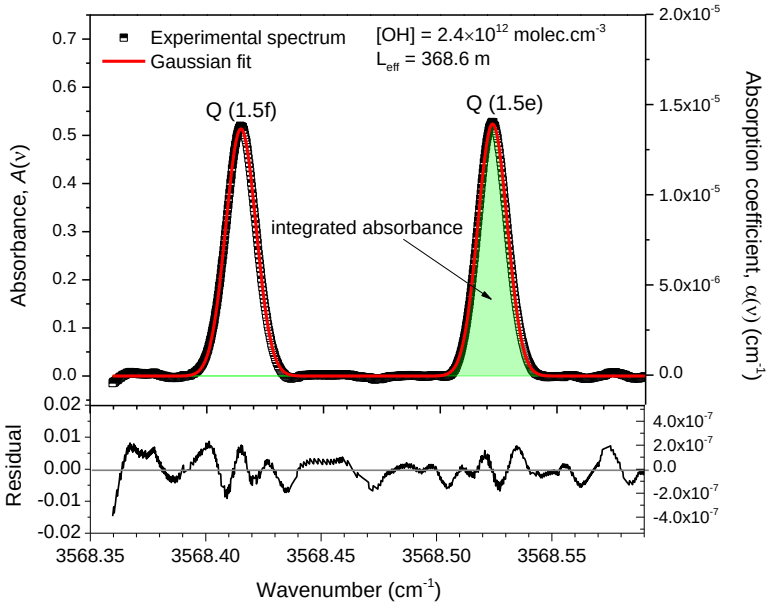

Figure 3.19 Upper – absorbance spectrum of the Q (1.5) double-line of the $^2\Pi_{3/2}$ state of OH transition (black) and its Gaussian fit (red). The right hand axis represents the absorption coefficient spectrum. Lower – residual of the fit.

OH concentration is calculated based on Eq. (2.11) using the integrated absorbance determined from a Gaussian fit to the OH Q(1.5e) transition spectrum centered at 3568.5238 cm^{-1} with S = 9.03×10^{-20} cm^{-1}/(molecule.cm^{-2}). As shown in the upper panel of Figure 3.19, the injection of a stream of pure water vapor for a pressure of 0.18 mbar associated with a microwave power of 75 W allows the generation of OH concentration of 2.4×10^{12} molecule.cm^{-3}. However, these specific conditions could not provide experimental conditions for well-controlled OH production by the discharge of H_2O vapor because the OH radical is detected downstream of the production source and its concentration decreases over the length of the quartz tube and the cavity. This setup was not able to distinguish the loss mechanisms due to wall reaction and recombination. For instance, *Pesce et al.* [124] generated OH radical by an RF discharge of H_2O vapor at low pressure. They investigated the OH concentration as a function of the main experimental parameters of the RF discharge system. It shows that the OH concentration is linearly proportional to the discharge current for the current values larger than 100 mA for fixed H_2O pressure. In contrast, at a fixed discharge current, OH

concentration had a linear behavior with the H_2O pressure in the range of 0 – 1 mbar. The OH density reached a plateau for pressure values between 1 and 6 mbar, probably due to an equilibrium between production and losses mechanisms. At higher pressures, the OH density decreased again. In section **3.3.4**, different OH concentrations are generated to calibrate the 2f signal (see section **3.3.1**) of the WM-OA-ICOS experiment by varying the H_2O pressure in a range of less than 1 mbar.

3.2.4.2 Detection limit of the developed OA-ICOS instrument

It is possible to determine the system's performance in terms of LoD and NEAS based on the SNR of the recorded spectrum and the integration time. The SNR is easily obtained from the absorbance spectrum in Figure 3.19 by calculating the ratio between the OH Q(1.5e) amplitude and the standard deviation of the noise in the spectral baseline (or from the residual from the fit). With 60 s integration time, the SNR is about 32, giving a $LoD_{(OA\text{-}ICOS)}$ of 7.5×10^{10} molecule.cm^{-3}. According to equation (3.24), the minimum detectable absorption coefficient MDAC can be determined from the baseline noise of the absorption spectrum and normalized by the effective path length. For this experiment, $MDAC_{(OA\text{-}ICOS)} = 5.8\times10^{-7}$ cm^{-1} in a 60 s integration time and based on R = 0.99864, L_{eff} = 368.6 m, ΔI = 0.18 mV and $I^0_{out} \approx$ 26.85 mV.

To investigate the noise effects on the detection sensitivity of the developed instrument, the detection limit in term minimum detectable absorption coefficient [cm^{-1}] versus the number of spectra averaged N (integration time) was analyzed. It is shown in Figure 3.20 (red dots). The $MDAC_{(OA\text{-}ICOS)}$ was calculated from the standard deviation of the noise in the baseline of the absorption spectra recorded at different averaging numbers (sampling interval time = 0.02 s) and normalized to the path length. As can be seen, the baseline noise was reduced with the following $1/N^{1/2}$ rule up to 20000 spectra averaged (corresponding to 300 s integration time), indicating a good agreement with the Fourier transform analysis (see **3.3.5.2**) of the cavity transmitted signal. Due to the intensity fluctuation of the cavity mode, noise in the integrated signal is dominated by the random noise which can be reduced by spectral averaging [123,125]. The OA-ICOS approach therefore requires a long integration time to reduce the white noise in the absorption spectrum. From a $\tau^{1/2}$ fit, a $NEAS_{(OA\text{-}ICOS)}$ of about 5.4×10^{-6} cm^{-1}.Hz$^{-1/2}$ was found. For 20000 averages, the $MDAC_{(OA\text{-}ICOS)}$ can reach 2.7×10^{-7} cm^{-1}, corresponding to a $LoD_{(OA\text{-}ICOS)}$ of 3.5×10^{10} molecule.cm^{-3} for OH concentration.

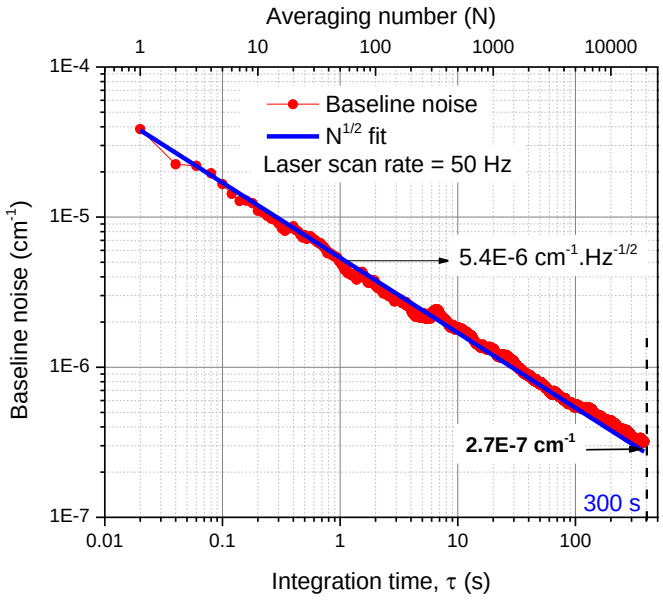

Figure 3.20 Baseline noise characterized by the standard deviation of the noise in the baseline (cm^{-1}) plot as a function of averaging number (integration time) for OA-ICOS performance.

Off-axis coupling results in a $NEAS_{(OA\text{-}ICOS)}$ of 5.4×10^{-6} $cm^{-1}.Hz^{-1/2}$ for the current OA-ICOS setup providing a detection limit of 7.5×10^{10} molecule.cm^{-3} for 60 seconds integration time (3000 averaged spectra). The detection of limit can be further improved by increasing the average time to reduce baseline noise in the absorption spectrum. The uncertainty of the measured concentration, depends on the uncertainty of the effective path length (3.5%), the line strength (2%), the measured absorption signal (5%), and was estimated to be 6.4%. A comparison of the instrument characteristics and performance in this work and various OA-ICOS studies is shown in Table 3.1.

Table 3.1 Experimental parameters for several OA-ICOS studies on different target species and resulting NEAS, taken from the published literature.

Ref	**λ** μ m	**$NEAS_{(OA\text{-}ICOS)}$** $cm^{-1}.Hz^{-1/2}$	**L_{eff}** m	**L** cm	**1 – R** ppm	**Power** mW	**fs** Hz	**Target species**
[81]	3.380	2.8×10^{-8}	1800	90	500	5.5	125	CH_4
[112]	0.687	3.0×10^{-8}	1300	100	800	20	16.7	O_2
[78]	1.573	4.3×10^{-7}	68	44	4400	20	30	CO_2
This work	2.803	5.4×10^{-6}	368	50	1360	5	50	OH

Note that some references prefer a definition of MDA that is independent on scan characteristics, i.e. sampling rate and use a “per point” MDA (MDA_{pp}). This notion considers

the minimum detectable absorption for an individual data point rather than sweeping over an actual scan as in this study, called "per scan" MDA (MDA_{ps}). In their case, the detection bandwidth is related to the sampling rate which corresponds to the number of points recorded per scan, *npts*, and the scan rate, f_s, and the number of average, N, for obtaining a spectrum [80]: $BW_{pp} = (npst * f_s) / N$. Compared our bandwidth determined from the integration time for averaging N spectra, $BW_{ps} = f_s / N$, the MDA_{pp} and MDA_{ps} can be linked through the following expression [80]:

$$MDA_{pp} = MDA_{ps} / \sqrt{npts} \tag{3.30}$$

Therefore, the NEAS calculated by dividing the MDA_{pp} to the effective path length (Eq. 2.24) is different by a factor of $\sqrt{npts}$ compared to our NEAS value. For reasonable comparison, the NEAS presented in Table 3.1 was derived from the published data by dividing the MDAC (provided or estimated from the recorded spectrum) to the square root of the BW_{ps} (is the invers of the total integration time used for spectral averaging).

A disadvantage of the OA-ICOS setup is the need to determine and subtraction the offset level due to the ASE contribution of the laser beam likely to be transmitted by the cavity without participating in absorption. In the next section, wavelength modulation will be applied to the OA-ICOS approach to further improve the sensitivity by reducing 1/f noise in the system. Moreover, the offset in the OA-ICOS signal can be removed thanks to the demodulation and detection at the second harmonic of the modulated signal.

3.3 OA-ICOS enhanced wavelength modulation technique (WM-OA-ICOS)

This section will present the improvement of the sensitivity of OH detection using wavelength modulation (WM) applied to the OA-ICOS system outlined in the previous section. The following parts will provide the details of the WM-OA-ICOS setup, including the principle of wavelength modulation spectroscopy (WMS), the optimizations of the experimental parameters, the calibration of the instrument as well as the instrument performance.

3.3.1 Principle of wavelength modulation spectroscopy (WMS)

WMS is also called *derivative spectroscopy* or *harmonic detection spectroscopy* which is applied largely to diode laser spectroscopy due to the lasers' narrow bandwidth and rapid frequency tuning capabilities [126]. In WMS, the detection of the absorption signal is shifted

to a higher frequency regime to reduce 1/f noise and suppress non-specific background in absorption measurements [68]. Its principle has been comprehensively reported in literature [66,68,127] and can be summarized into two processes.

- First, modulation of the laser wavelength at a modulation frequency f_m usually from a few kHz to a few tens of kHz, with an appropriate modulation amplitude, v_a (which commonly is of the order of the width of the absorption profile).
- Second, the modulated signal, resulting from the interaction of the modulated laser beam with the absorbing species, detected with a photodetector is fed to a lock-in amplifier where the i^{th} harmonic of the absorption signal is extracted at a demodulation frequency if_m (where i = 1,2, …) with a bandwidth given by the inverse of the integration time.

The in-phase component of the 2nd harmonic signal from the output of the lock-in amplifier (obtained for a user-chosen lock-in reference phase angle of $\theta_i = 0$) can be derived by [127]:

$$S_2^{in-phase}\left(\bar{v}_d,\bar{v}_a\right) \approx -\eta I_0 \frac{1}{4}\bar{v}_a^2 \bar{\chi}^{(2)}\left(\bar{v}_d\right) A_0 \tag{3.31}$$

where η is introduced as an instrumentation factor, I_0 is the power of the light impinging upon the detector in the absence of the absorber (I_0 is assumed to be frequency independent), $A_0 = n\sigma_0 L_{eff}$ is the absorbance at the center frequency, $\bar{v}_d$ is the HWHM width-normalized center detuning, $\bar{v}_a = v_a / \Delta v_{as-HWHM}$ is the HWHM width-normalized frequency modulation amplitude in which ν_a is the modulation amplitude and $\Delta\nu_{as\text{-}HWHM}$ is the HWHM of the target transition profile. $\bar{\chi}^{(2)}\left(\bar{v}_d\right)$ is the 2nd derivative of the lineshape function, derived from [127]:

$$\bar{\chi}_i\left(\bar{v}_d,\bar{v}_a\right) = \frac{2-\delta_{i0}}{\tau}\int_0^{\tau} \bar{\chi}\left(\bar{v}_d,\bar{v}_a,t\right)\cos(2\pi i f_m t)dt \tag{3.32}$$

with τ being integration time (time constant of the lock-in amplifier), δ_{n0} - the Kronecker delta, f_m - the modulation frequency, and i = 1, 2, … is the harmonic index.

From these expressions**,** it is possible to figure out some characterizations of the WMS. First, the WMS signal detected via the second harmonic output from the lock-in amplifier is directly proportional to A_0 which yields in a linear response to the concentration of a target molecule n. Second, the amplitude of the second harmonic WMS signal (2f signal) depends on the

width-normalized frequency modulation amplitude, $\bar{\nu}_a$, and the second derivative of the lineshape profile, $\bar{\chi}^{(2)}\left(\bar{\nu}_d\right)$. It is necessary to optimize the modulation amplitude, ν_a, via the current modulation amplitude of the laser so that it adapts with the lineshape function of the absorption line to obtain the largest 2f amplitude. Finally, due to the instrument factor η, the 2f signal needs to be calibrated.

In practical work, the laser wavelength is both scanned and modulated simultaneously by tuning the laser current with two waveforms [128–130]. The scan waveform allows sweeping the wavelength at low scan rate f_s (typically a few tens of Hz), across several transitions to acquire a full absorption feature. The modulation waveform at higher frequency f_m (typically in the kHz region) is used for harmonic detection, as indicated above. Generally, f_s is lower than f_m by a factor of a few hundred. The time constant is depended on how two frequencies are separated and needed to be optimized. The modulation amplitude should be optimized according to the absorption linewidth under specific experimental conditions to maximize the amplitude of the 2f signal.

3.3.2 Implementation of a WM-OA-ICOS system

In the WM-OA-ICOS approach, a ramp signal (amplitude of V_s = 0.4 Vpp in our case) from a function generator to sweep the laser frequency over ~ 2 cm^{-1} across the selected OH line and H_2O lines located around 3568.52 cm^{-1} at a scan rate of f_s = 50 Hz. Wavelength modulation of the DFB-ICL was carried out with a sinusoidal waveform signal (V_m – the voltage amplitude that is used to achieve a frequency shift of ν_a) provided by a lock-in amplifier (DSP 7270, Ametek). The sinusoidal waveform signal is combined with the ramping signal via a multiplier that is connected to Laser Diode Controller (LDC) to modulate the laser current with both signals simultaneously (Figure 3.21). Wavelength modulation was carried out at a higher frequency f_m = 15.5 kHz with a modulation amplitude of V_m = 5.0 mV_{rms}. The modulated signal emerging from the detector was fed to a lock-in amplifier for demodulation to extract second harmonic signal using an appropriate time constant. The 2f signal was digitized with an NI PCI-6251 data acquisition card.

A WM-switch shown in Figure 3.21 was introduced to allow the OA-ICOS setup to perform either wavelength modulation, or only direct absorption measurements (without modulation) in case of the absolute concentration of OH radicals needed to be measured for the calibration

of the 2f signal. The OH radicals were produced and measured with WM-OA--ICOS using the same experimental protocol as in the OA-ICOS approach.

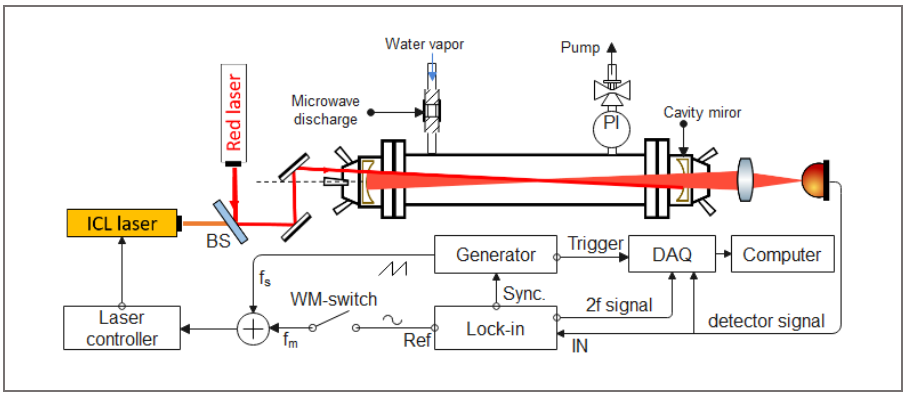

Figure 3.21 Scheme of the WM-OA-ICOS setup: f_m is the modulation frequency, f_s is the sweeping rate of laser frequency.

3.3.3 Optimization of modulation parameters

The most crucial experimental key parameter in WMS is the modulation amplitude, which must be adjusted according to the absorption line width to maximize the signal intensity. The determination of this parameter in the WM-OA-ICOS setup was carried out by comparing the 2f signal of the OH transition – Q (1.5e) at different modulation amplitudes V_m of the sinusoidal waveform modulation signal. The wavelength modulation amplitude is predicted from the theoretical modulation index $\bar{\nu}_a$. For a Gaussian profile under low pressure condition, the modulation index $\bar{\nu}_a$ equals 2.1 (according to a study by *P. Kluczynski et al.* [127]) times the HWHM of the Q (1.5e) OH lines (~ 0.0077 cm^{-1} at the working pressure of about 0.1 mbar), corresponding to an estimated modulation amplitude of :

$$\nu_a = \bar{\nu}_a . \Delta\nu_{as-HWHM} = 2.11 * 0.0077 \approx 0.016 \ cm^{-1} \qquad (3.33)$$

Given a linear response of the laser frequency to the injection current (0.24 cm^{-1}/mA) and the linear transfer factor of the LDC (25 mA/V), the amplitude of the wavelength modulation V_m of about 3.78 mV_{rms} was calculated using a converting factor, β = (0.24 cm^{-1}/mA)*(25 mA/V) = 6 cm^{-1}/V. For a 50 Hz laser sweeping frequency and using a 15.5 kHz wavelength modulation frequency (corresponding to a time constant of 50 µs for demodulation), the peak-to-peak of the 2f signal of the OH absorption line was measured for different V_m varying around its prediction value at 0.1 mbar (Figure 3.22 – Left). The optimum amplitude V_{rms} was fond to be about 5 mV_{rms}.

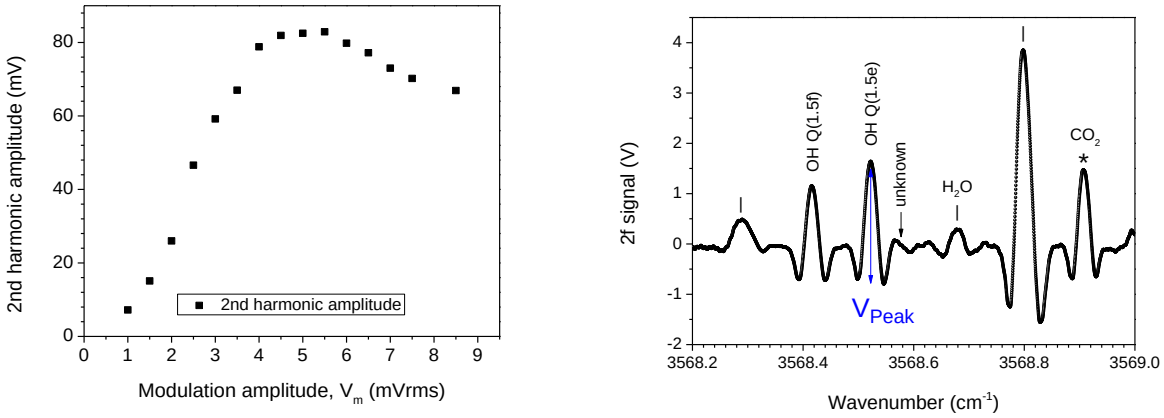

Figure 3.22 Left – peak amplitudes of 2f signal of the OH Q (1.5e) absorption line vs. wavelength modulation amplitudes. The optimum modulation amplitude V_m was about 5.0 mV_{rms}, in comparison with the estimated value of 3.78 mV_{rms}. Right – the 2f spectrum consisting of double lines OH transition obtained by WM-OA-ICOS with the parameters listed in Table 3.2.

The reference phase angle and the time constant were experimentally adjusted to maximize the WM-OA-ICOS signal and the SNR of the in-phase component of the 2f signal from the lock-in amplifier.

All parameters used in the present work for optimal operation of the WM-OA-ICOS are summarized in Table 3.2.

Table 3.2 Summary of the experimental parameters of the WM-OA-ICOS system

Parameter	**Value**	**Unit**
Laser scanning parameters		
Laser scan rate, f_s	50	Hz
Scanning amplitude, V_s	400	mV_{pp}
Laser tuning range	2	cm^{-1}
Modulation parameters		
Modulation frequency, f_m	15.5	kHz
Modulation amplitude, V_m	5.0	mV_{rms}
Lock-in settings		
Reference phase	217.8	degree
Time constant, τ	50	μs
Sensitivity	50	μV
Input limit (mV)	250	mV
Data acquisition		
Average	1000	spectra
Average time	20	s

The optimized modulation amplitude is higher than the theoretical value by a factor of 1.32. A reason may be due to the reduction of the WM amplitude at high modulation frequency [78,131] that can be explained by the following. The WM amplitude was calculated with

considerations that the laser wavelength has a linear response to the injection current, and the current modulation amplitude has a linear response to the modulation voltage signal (provided by the lock-in) applied to the LDC. In fact, the wavelength vs injection current curve was calibrated with a wavelength meter without modulation, and does not have a linear response (polynomial function – see the current tuning curve in Figure 3.9-c). Therefore at f_m = 15.5 kHz, the converting factors β might be different compared to the predicted values of 6 cm^{-1}/V. Another reason may be due to a decrease of the voltage level of the lock-in's waveform in the multiplier circuit that were connected to the external modulation input of the LDC.

3.3.4 Calibration

The 2f signal is proportional to the molecular concentration (the number density), but it is necessary to perform a calibration to find a conversion function. To do this, the protocol in section **3.2.4.1** was repeated to determine absolute OH concentrations using OA-ICOS measurement. Different OH concentrations were produced by varying the total pressure of H_2O vapor injected into the discharge cavity from 0.06 to 0.18 mbar.

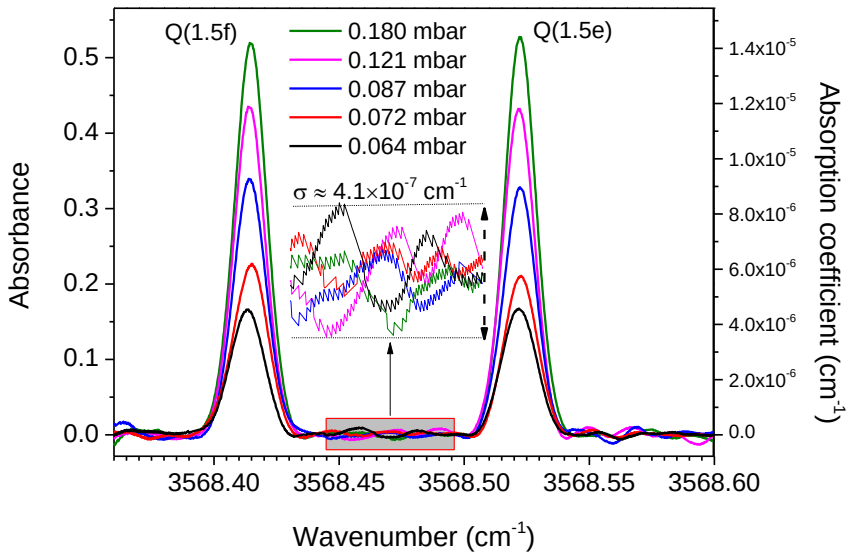

Figure 3.23 Absorbance spectra of OH at different pressures of H_2O vapor injection. Each spectrum is the result of the average of 3000 measurements (integration time 60 s). The linewidths at different pressures within the present working condition (0.06-0.18 mbar) is considered constant within the spectral fit uncertainties. The inserted graph shows a portion of the baseline fluctuation induced noise (in terms of absorption coefficient). The 1σ standard deviation of the noise is about $\sigma = 4.1\times10^{-7}$ cm^{-1}.

The corresponding absorbance spectra experimentally measured by OA-ICOS are shown in Figure 3.23. Each spectrum was averaged 3000 times at a scan rate of 50 Hz, corresponding to an integration time of 60 s. By fitting a Gaussian lineshape to the Q (1.5e) absorption transition, OH concentrations were retrieved from the integrated area of the fit. The increase of the H_2O pressure in the range of < 1 mbar results in an increase in the OH concentration generated by the microwave discharge, which is similar to the study by *Pesce et al.* [124].

As the modulation amplitude was optimized with a specific absorption linewidth to maximize the 2f signal, changing the total pressure can result in a variation in the absorption linewidth and affecting thus the 2f amplitude. However, under the present working pressure condition (0.06-0.18 mbar), pressure-induced line broadening at different pressures has been observed constant within the uncertainties of the fitted FWHM of the OH line. The calibration was thus performed with an assumption of no effect of the pressure broadening on the absorption linewidth.

Figure 3.24-right shows the 2f spectra of OH lines recorded at the same conditions as the OA-ICOS performed (Figure 3.23). Each spectrum was averaged over 1000 wavelength sweeps within 20 s. The peak-to-peak of the 2f signal of the Q (1.5e) transition versus the OH concentration retrieved by the OA-ICOS approach is plotted in Figure 3.24-left.

A linear relation has been found with R^2 = 0.995, and the sensitivity (slope) of 5.12×10^{11} molecule.cm^{-3}/volt. The linear fit did not go to zero due to an offset in the 2f signal from the lock-in amplifier's output.

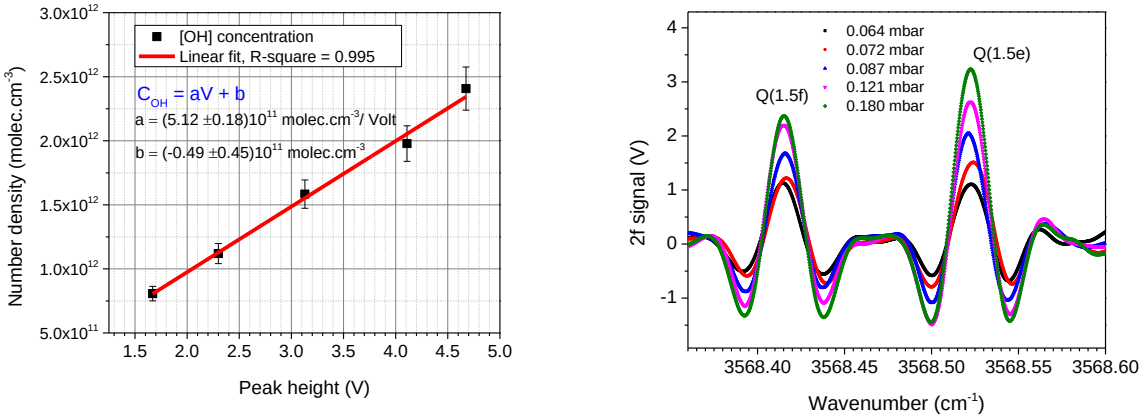

Figure 3.24 Left – calibration of 2f harmonic amplitude vs. number density of OH Q (1.5e) line for the WM-OA-ICOS system based on direct measurement of OH concentration using OA-ICOS. The error bars on the number density were calculated using the uncertainty of 3.5% of OH determined by the OA-ICOS approach. Linear response of the 2f amplitude to the OH concentration was observed. Right – the 2nd harmonic OH spectra measured under the same experimental conditions as OA-ICOS were carried out.

3.3.5 The WM-OA-ICOS performance

3.3.5.1 Detection limit (of the measurements using OH Q (1.5e) line)

At a pressure of 0.064 mbar (black line in Figure 3.24-right), the OH concentration determined by OA-ICOS is 8.0×10^{11} molecule.cm^{-3}. A signal-to-noise ratio SNR of ~ 32 was obtained for the 2f spectrum within 20 s integration time at this pressure, leading to a $LoD_{WM\text{-}OA\text{-}ICOS}$ of $n_{min} = 2.5\times10^{10}$ molecule.cm^{-3} for WM-OA-ICOS measurement. Using the relation:

$$\alpha_{min} = n_{min}.\sigma_0 \tag{3.34}$$

in which $\sigma_0 = 8.03\times10^{-18}$ cm^2.molecule^{-1} is the absorption cross-section at the center frequency of the Q(1.5e) OH transition derived (Figure 3.25) from the line intensity provided by the HITRAN database[5] taking into the experimental conditions (P ≈ 0.1 mbar, T ≈ 296 K, Gauss line shape). A minimum detectable absorption coefficient was estimated at $MDAC_{WM\text{-}OA\text{-}ICOS} = 2.0\times10^{-7}$ cm^{-1}.

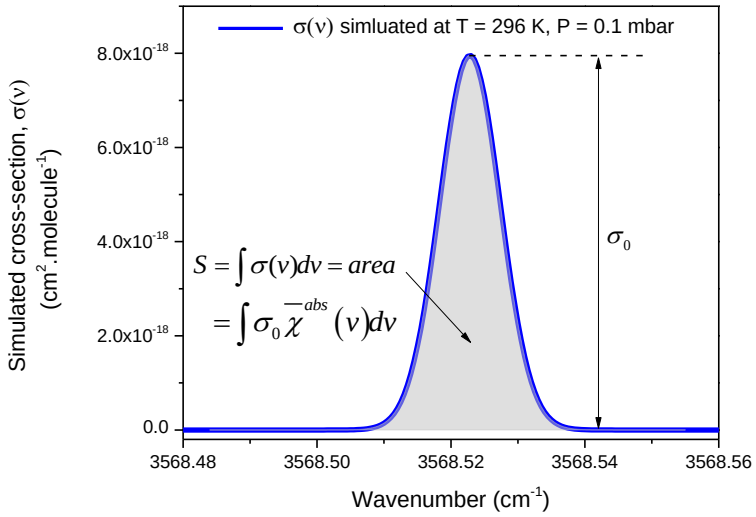

Figure 3.25 Simulation cross-section of the OH Q(1.5e) line using HITRAN database. $\bar{\chi}^{abs}(\nu)$ is the peak-normalized Gauss line shape function, S = 9.03×10^{-20} cm^{-1}/(molecule.cm^{-2}) is the line intensity. A calculation model are provided on the website[6]. The simulation was performed with the ignores of the laser linewidth and collision broadening since the experiments was carried out at low pressure.

To evaluate the stability of the developed WM-OA-ICOS, an Allan deviation analysis of the 2f signal was performed. Since the concentration of OH generated by the discharge of H_2O is not stable enough for measuring the 2f signal over a long time, the measurement of Allan

[5] The simulation was performed on https://spectra.iao.ru/molecules/simlaunch
[6] https://hitran.iao.ru/home.sim-theory

deviation was performed by recording the 2f signal of an H_2O line at 3568.0838 cm^{-1} over 5500 seconds when pure water vapor is injected into the cell without discharge. Each data point (shown in the upper panel of Figure 3.26) was calculated from 200 averages of the 2f spectrum of the H_2O line, corresponding to a sampling period of 4 s. The lower panel shows the Allan deviation of the 2f signal (left axis) versus integration time. The system is stable with an average time of up to 300 s, giving a corresponding detection limit for OH of 1.0×10^{10} molecules.cm^{-3}.

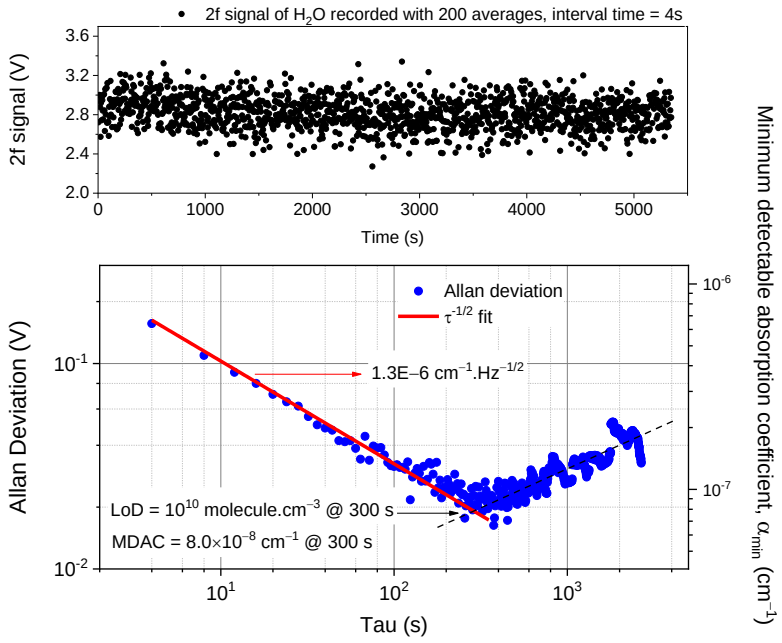

Figure 3.26 Upper – time series of the 2f signal of the H_2O line at 3568.0838 cm^{-1} recorded with an overall integration time of 4 s. Lower – Allan deviation of the 2f signal (left axis with units in V) and the corresponding minimum detectable absorption coefficient (right axis with units in cm^{-1})

It is possible to convert the Allan analysis in terms of the deviation of the 2f signal, ΔV (in [V]), to the minimum detectable absorption coefficient (in [cm^{-1}]) based on the slope of the calibration curve in Figure 3.24-left. First, we consider the Allan deviation of the concentration Δn_{Allan} = *Slope**ΔV. Then using equation (3.34), the Allan deviation of the minimum detectable absorption coefficient is determined by $\Delta\alpha_{min\text{-}Allan} = \Delta n_{Allan}*\sigma_0$ = *Slope**$\Delta V*\sigma_0$. With *Slope* = 5.12×10^{11} molecule.cm^{-3}/volt and $\sigma_0 = 8.03\times10^{-18}$ cm^2.$molecule^{-1}$, the minimum detectable absorption coefficient as a function of the integration time is shown on the right axis of the lower panel in Figure 3.26. For the integration time of 300 s, $\alpha_{\min-WM-OA-ICOS} = 8.0\times10^{-8}$ cm^{-1}. In the region of < 300 s where the

white noise dominates the performance of the system, the $\tau^{-1/2}$ fit (red line) provided an estimation of the $NEAS_{(WM\text{-}OA\text{-}ICOS)}$ of about 1.3×10^{-6} $cm^{-1}.Hz^{-1/2}$, which is ~4 times better than the corresponding value in the OA-ICOS approach.

3.3.5.2 Discussion of the dominant noises in CEAS

Several studies pointed out that the main limitation to the detection sensitivity of the cavity-enhanced technique (i.e., ICOS) is the optical noise, including etalon effects and cavity-mode noise, which is a result of relative intensity fluctuations due to mode injection noise [123,125]. (1) The mode-noise can be reduced by increasing the number of averaged spectra (integration time), and by introducing a dense mode structure via off-axis alignment (used in this work). A Fourier transform FT of the detector signal (see Figure 3.13-left) was performed to demonstrate the effect of the cavity-mode noise on the transmitted light intensity as well as to identify noise sources.

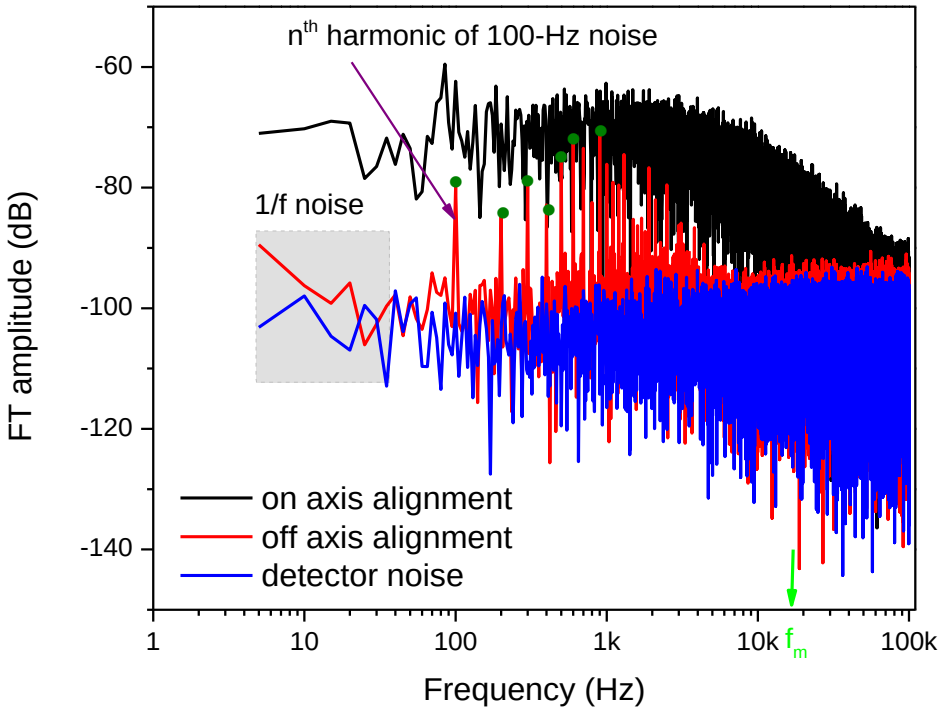

Figure 3.27 Amplitude spectra from Fourier transform analysis of the measured detector signal of the cavity transmission. The grey square indicates the 1/f noise contributing to the total noise in the detection system at low-frequency region.

Figure 3.27 shows the FT analysis of the detector signals recorded at 200 kS/s within 0.2 s at three conditions: laser turned off – consisting of only detector noise (blue), laser is turned on and on-axis (black) or off-axis (red) aligned to the cavity axis. In the case of the laser being turned on and aligned to the cavity axis (black), the FT amplitude (including the detector, laser, and cavity-mode noises) is higher than the detector noise (~30 dB) and mainly dominated in a region from a few Hertz to high frequency (10 kHz) due to the fluctuation of the cavity-modes. For off-axis alignment (red) the total noise was decreased significantly, although some clear amplitude spikes were observed at the n^{th} harmonic frequency of the 100-Hz noise (i.e., 100, 200, 300, 400, 500, 600 Hz) which may be caused by the electronic noise from the laser power supply. The cavity transmission showed a white-noise like behavior in a region from 30 Hz to 100 kHz, indicating the reduction in the cavity-mode fluctuation thanks to the non-resonance coupling laser beam to the optical cavity. The 1/f noise from the laser was also clearly observed at low frequencies < 30 Hz (indicated by a square region in Figure 3.27).

In the OA-ICOS approach, the absorption was measured with a detection bandwidth from DC to high frequency region. Therefore, the recorded absorption signal was affected by the 1/f noise, the n^{th} harmonic of the 100-Hz noise and the white noise. As can be seen in Figure 3.27, the total noise level in the region from 10 kHz to 100 kHz is less than its value in the low frequency regime. The WM technique was then applied to the OA-ICOS set-up (WM-OA-ICOS) to further reduce low-frequency fluctuations (1/f noise) in the laser intensity and in the detection chain. Modulation at f_m = 15.5 kHz and detecting the absorption signal at the second harmonic of the modulation frequency can reduce the 1/f noise by a factor of about 5 dB. An improvement factor of ~3.4 in the LoD has be experimentally obtained.

In WM schemes, residual amplitude modulation (RAM) [132] is the main limiting factor of the measurement detection limit. The RAM is raised from modulation of the wavelength-dependent laser power associated to the WM of the semiconductor laser by modulation of the laser injection current. Further RAM elimination in a WM-OA-ICOS instrument allowed *Lengigon et al*. [133] to achieve a NEAS[7] of 4.5×10^{-12} cm^{-1} $Hz^{-1/2}$ (compared to this work of 1.3×10^{-8} cm^{-1} $Hz^{-1/2}$)[8] with an SNR enhancement factor of about 10 compared to the WM-OA-ICOS configuration for OH detection near 6965.80 cm^{-1}.

[7] This value was obtained from the "per point" MDA with consideration that the detection bandwidth corresponds to the sampling rate and the number of data point per scan. (see Eq 3.30)

[8] This value was converted from our $NEAS_{(WM\text{-}OA\text{-}ICOS)}$ of 1.3×10^{-6} cm^{-1} $Hz^{-1/2}$ for comparison with definition of the detection bandwidth in the reference.

Regarding the optical noise resulting from etalon effects in the cavity mirrors can be further improved using oversized cavity mirror.

3.4 Chapter conclusion

This chapter presented the development of a compact and robust optical instrument for OH radicals detection at 2.8 μm based on the off-axis CEAS technique. Using a high finesse cavity (F = 2300), the optical path length is enhanced to 368.6 m compared to the physical length of 0.5 m. Two experimental schemes: OA-ICOS and WM-OA-ICOS, were introduced to detect OH radicals generated by a microwave discharge of water vapor at low pressure (~0.1 mbar).

By coupling the ICL beam off-axis to the cavity, the OA-ICOS approach allowed direct determining the absolute concentration of OH based on measuring the absorption spectra of the Q (1.5) double-line of the $^2\Pi_{3/2}$ state of OH transition. A $LoD_{(OA\text{-}ICOS)}$ of 7.5×10^{10} molecule.cm^{-3} within 60 s averaging time was achieved with a $NEAS_{(OA\text{-}ICOS)}$ of about 5.4×10^{-6} cm^{-1}.Hz$^{-1/2}$.

The OA-ICOS methodology relies on the measurement of the time-integrated light intensity leaking out of the cavity. It has some advantages over other laser-based-cavity techniques (i.e., CRDS measuring the absorption signal in the time domain) in simpler experimental alignment, immediately acquiring data for a complete spectral region by fast sweeping the laser, and not requiring the fast optical switching and digitization. However, the integrated transmitted intensity through the cavity is quite low (a few mV in this experiment) and the background signal correction is required. Consequently, the small amplitude of the absorption signals due to those issues, together with the noise level (usually dominated by residual cavity mode noise), makes it challenging to obtain a good signal-to-noise ratio in OA-ICOS signal. Therefore, more extensive averaging of the OA-ICOS signal to enhance the spectral SNR is required. For instance, the $MDAC_{OA\text{-}ICOS}$ could reach 2.7×10^{-7} cm^{-1} for 300 s integration time (15000 spectra averaged).

In order to increase the sensitivity of the OA-ICOS systems, wavelength modulation was applied to shift the detection scheme to a higher frequency regime where 1/f noise is reduced. The absorption was recorded by demodulation and detected at the 2nd harmonic modulation frequency. The WM-OA-ICOS system presented here is based on modulating the injection current of the diode laser at 15.5 kHz. Implementing the wavelength modulation and studying

the second harmonic of the modulated absorption signal allows an improvement of the LoD by a factor of 3.4 compared to the OA-ICOS system, with a $NEAS_{WM\text{-}OA\text{-}ICOS} = 1.3\times10^{-6}$ $cm^{-1}.Hz^{-1/2}$. The WMS shows the advantage in removing the background signal observed in the OA-ICOS spectra; however, it requires a calibration of the 2f signal from the lock-in amplifier. The WM-OA-ICOS system allows a detection limit of 2.5×10^{10} molecule.cm^{-3} for the integration time of 20 s and can be further improved by continuous averaging. At 300 s (15000 spectra averaged), the LoD is 1.0×10^{10} molecule.cm^{-3}, corresponding to a minimum detectable absorption coefficient of 8.0×10^{-8} cm^{-1}

The main limitation of the sensitivity of both approaches is the optical noise from the fluctuation of the transmitted light intensity due to the cavity-mode noise. The LoDs in both approaches could not reach the atmospheric level of OH radicals (10^6 to 10^7 molecules.cm^{-3}). However, the instrument can be used for combustion applications and laboratory studies where OH concentrations are high. In the next chapter, the Faraday Rotation Spectroscopy is coupled with the OA-ICOS in order to improve the sensitivity and the spectral selectivity of the apparatus thanks to the Faraday effect which is observed only for paramagnetic species such as OH or HO_2.

Chapter 4 Development of an instrument based on cavity-enhanced Faraday rotation spectroscopy for interference-free detection of OH radicals

This chapter presents the development of a cavity-enhanced Faraday rotation spectroscopy (CE-FRS) setup for OH detection. This method relies on measuring the time-integrated signals of two different polarizations resulting from the Faraday effect. This differential detection based CE-FRS scheme has the advantage of high selectivity by removing spectral interference from non-paramagnetic species (like H_2O and CO_2) in comparison with the previously presented OA-ICOS and WM-ICOS approaches. Application to the measurement of the reaction rate constant of OH with CH_4 was demonstrated to evaluate its performance.

4.1 Faraday Rotation Spectroscopy (FRS)

4.1.1 Principle of FRS

Faraday Rotation Spectroscopy (FRS) was first reported by *Litfin et al.* [134] in 1980 for the quantification of paramagnetic molecules with significantly higher selectivity compared to the direct absorption spectroscopic techniques (DAS) [134]. FRS relies on the magneto-optics effect (Faraday effect) that causes a rotation of the polarization plane of a linearly polarized light wave propagating through a paramagnetic sample permeated by a longitudinal magnetic field. Measurement of the rotation angle allows to infer the concentration of the target molecules. This Faraday effect based analytical method offers the advantage of eliminating interfering absorption from non-paramagnetic species, such as water and carbon dioxide. This makes FRS suitable for highly selective detection of paramagnetic atmospheric species such as NOx [135,136], O_2 [137,138], free radicals HO_2 [139–141] and OH [51,54,55,142].

Figure 4.1 illustrates a basic 90 degree cross analyzing FRS setup. The laser beam is first polarized fully through a linear polarizer placed in front of the absorption cell. An axial magnetic field is generated using a magnetic coil around the absorption cell. By placing a second polarizer (called the analyzer) after the cell, with a polarization perpendicular to the one in front of the gas cell, a small change in rotation angle θ can be converted to a change in the transmitted intensity that will be detected with a conventional detector.

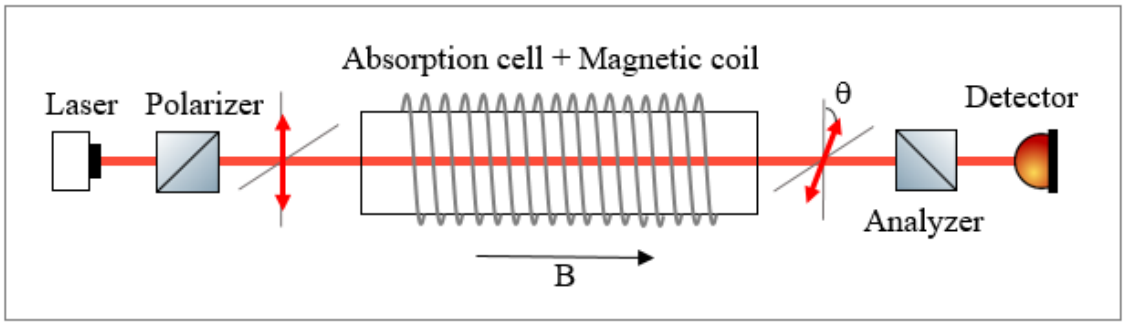

Figure 4.1 A scheme of the basic 90 degree cross analyzing FRS.

Zeeman effect and Faraday effect

In the presence of an external magnetic field, the Zeeman effect splits a single degenerate transition into multiple transitions with different energies and intensities [143]. Each molecular energy state with a given total angular momentum, J, is split into a multitude of sub-states with a corresponding frequency separation of $Mg\mu_B B$ where g is the g-factor, B is the magnetic field, μ_B is the Bohr magneton, and M is the magnetic quantum number. The line center frequency $\nu_{M'',M'}$ of an electric dipole transition induced M'' → M' transition is given by [143]:

$$\nu_{M''M'} = \nu_0 + (M'g' - M''g'')\mu_B B \tag{4.1}$$

According to the quantum selection rules, a linearly polarized light propagating along the direction of an external magnetic field can only induce transitions with the conditions $\Delta M = \pm 1$. Linearly polarized light can be considered as a superposition of two left- and right-handed circularly polarized waves, (LHCP and RHCP) respectively. When it propagates over a distance L through a paramagnetic species in the presence of an axial magnetic field. The RHCP and LHCP waves cause a transition between states whose energies are modified by Zeeman effect, involving $\Delta M = +1$ and $\Delta M = -1$ component, respectively. This results in different refractive indices (magnetic circular birefringence, MCB) and attenuation due to absorption (magnetic circular dichroism, MCD) for two circular polarizations. The MCB causes a difference in the phase-shift of LHCP and RHCP waves, ϕ_L and ϕ_R, providing the Faraday rotation angle θ [144],

$$\theta = (\phi_L - \phi_R)/2 = \Delta n L \pi / \lambda \tag{4.2}$$

with $\Delta n = n_R - n_L$ being the difference between the refractive index for RHCP and LHCP, respectively. Notice that the total phase-shifts of LHCP ϕ_L and RHCP ϕ_R are proportional to

the molecule density n, the absorption line strength S, and the path length L [144]. They can be expressed in terms of a dispersion lines shape function X (see supplementary material of reference [144] for details):

$$\phi_L = \sum_{M=-J}^{J} \phi_M^+ = \frac{nSL}{2} \sum_{M=-J}^{J} \overline{S}_M^+ \mathrm{X}\left(\psi_M^+, V\right) \tag{4.3}$$

$$\phi_R = \sum_{M=-J}^{J} \phi_M^- = \frac{nSL}{2} \sum_{M=-J}^{J} \overline{S}_M^- \mathrm{X}\left(\psi_M^-, V\right) \tag{4.4}$$

with ϕ_M^+ (ϕ_M^-) being the phase-shift of a LHCP (RHCP) wave due to the $M \to M+1$ ($M \to M-1$) sub-transition, $\overline{S}_M^+$ ($\overline{S}_M^-$) is the relative line strength of the transition $M \to M+1$ ($M \to M-1$). ψ_M^+ (ψ_M^-) is the Doppler-width normalized detuning of the laser frequency ν from the center of the Zeeman-shifted transition $M \to M+1$ ($M \to M-1$), $V = \left(\sqrt{\ln 2} / \Delta\nu_D\right)\Delta\nu_L$ is the Voigt parameter.

$$\psi_M^+ = \frac{\sqrt{\ln 2}}{\nu_D}\left\{\nu - \left[\nu_0 - \left(\left(M+1\right)g' - Mg\right)\mu_B B\right]\right\} \tag{4.5}$$

ν_0 is the center of the transition in zero-field case. For low molecule concentrations and short optical paths, magnetic circular dichroism is negligible, and only the MCB signal from the difference between two dispersion curves contributes to the FRS signal [135] (see Figure 4.2-b&c). The Zeeman split induced transitions of the OH $^2\Pi_{2/3}$ Q(1.5) line under a static magnetic field (DC field) are illustrated by the vertical arrows in Figure 4.2-a [145], where each group of arrows: red and green, correspond to transitions induced by the LHCP and RHCP light, respectively.

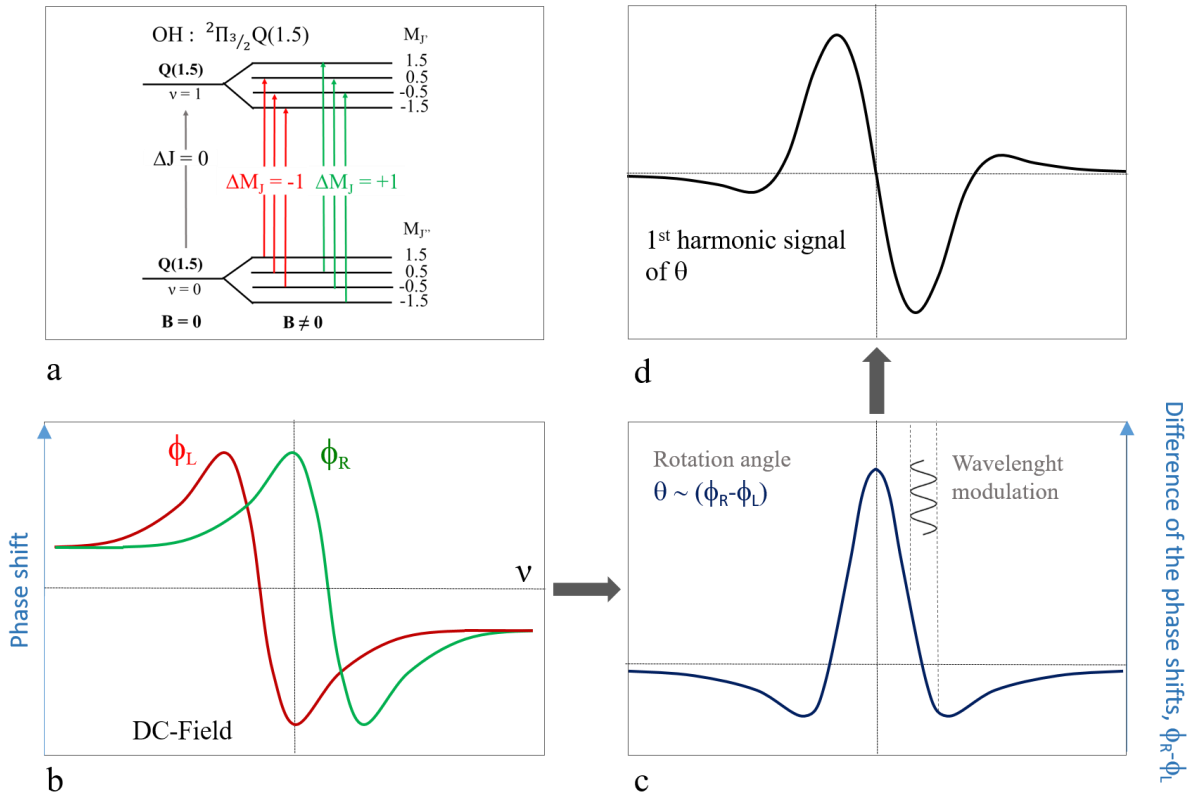

Figure 4.2 Schematic of the DC-FRS signal generation from the Zeeman-split dispersion lines under static magnetic field conditions using a wavelength modulation approach. a – Zeeman splitting energy pattern of the OH $^2\Pi_{2/3}$ Q(1.5) line and the associated transitions corresponding to ΔM = +1 and ΔM = -1 transitions. b – Total dispersion profiles of the phase shifts for the LHCP and the RHCP components. c – Difference of the two dispersion profiles ϕ_R-ϕ_L, to which the rotation angle θ is proportional. In 45-degree crossing-analysis method, the FRS spectrum can be obtained through laser scan across the transition or even combined with modulation technique to further improvement in sensitivity. The concept of rotation angle modulation created through wavelength modulation over the θ spectrum (see Eq. 4.2) is presented. d – 1st harmonic signal from lock-in detection after demodulation that is proportional to θ related to the molecular concentration (see Eqs. 4.2-4.4).

4.1.2 Different schemes of FRS for paramagnetic species detection

A variety of FRS techniques have been developed based on single pass [50,51] and multi-pass [54,140] absorption configurations (using multi-pass cell or optical cavity). Alternating (AC) and a static (DC) magnetic field [137] were exploited in combination with phase-sensitive lock-in detection, referred to as AC-FRS and DC-FRS.

4.1.2.1 AC-FRS and DC-FRS

For the AC-FRS approach [50,51,135,146,147], modulation of the magnetic field results in the modulation of the Zeeman splitting of the RHCP and LHCP transition components that are symmetrically around the absorption lines. This procedure modulates the polarization

rotation θ(t) of the transmitted light reaching the detector. By performing a slow scan of laser wavelength, the alternating polarization rotation signal as a function of optical frequency can be recorded and demodulated using a lock-in detection at the fundamental frequency of the magnetic field modulation. The first harmonic signal is proportional the rotation angle θ related to the molecular concentration.

In the DC-FRS approach [55,138,141], the Zeeman splitting is static. The Faraday rotation angle at each wavelength is proportional to the difference in the RHCP and LHCP dispersion spectra. Wavelength modulation is applied to produce a modulated polarization rotation signal as in the AC-FRS approach. Like WMS, this technique required an adjustment of the modulation depth related to the shape of the static dispersion profile to maximize the harmonic output signal amplitude. As shown in Figure 4.2-d, the signal shape resembles the first derivative of the static difference in the dispersion spectral envelopes for the LHCP and RHCP wave components (Figure 4.2-c).

Table 4.1 summarizes their potential and drawbacks.

Table 4.1 Comparison of FRS approaches based on AC and DC magnetic field

	Alternating magnetic field (AC-FRS)	**Static magnetic field with WMS (DC-FRS)**
Advantages	No modulation of laser frequency, the FRS signal is only produced from internal modulation (Zeeman-effect modulation) of the molecule and is less susceptible to optical interference and RAM effects; Higher sensitivity compared to using a DC field [137]; A zero baseline of the FRS spectrum.	higher WM frequency (a few ten kHz); time resolution enhancement [55]; low power consumption for generation of DC field; FRS based on permanent magnets, suitable for development of low-power consumption sensors [138].
Disadvantages	low magnetic field modulation frequency (typically less than 5 kHz) due to the size of the electromagnetic coils; limit of detection time resolution to the millisecond's timescale; high power consumption for production of the required AC magnetic field; Electromagnetic interference affecting the performance of the electric components.	laser frequency modulation converted into amplitude modulation of the light intensity on the detector; influence of optical fringing and other spectral interference on FRS signal.

4.1.2.2 90-degree- and 45-degree-crossed analyzing FRS

The FRS is also divided into two approaches based on the orientation of the analyzer with respect to the polarizer: 90-degree crossing or the 45-degree crossing.

In a nearly 90° crossing method, the linear polarizer, placed between the gas cell and the photodetector, is set at 90 + φ angle with respect to the polarization of the incident light to act as an analyzer. A small angle φ of a few degrees is introduced to minimize laser excess noise. The optimum offset angle φ_{opt} depends on the quality of the polarization, ξ, which is a factor representing the percentage of light penetrating a crossed pair of polarizers. For example, a decrease of polarization can cause an increase of φ_{opt} and this lowers the maximum achievable S/N ratio of the FRS signal [148]. As a single detector is used in this configuration, this approach requires a modulation in the phase-shifts of LHCP and RHCP, resulting in a modulation of the Faraday rotation angle which is demodulated using phase-sensitive lock-in detection to exhibit the FRS signal. The modulated polarization rotation signal can be introduced by applying an AC magnetic field [50,51], wavelength modulation [149], or dual modulations [150]. For a small φ and negligible power saturation, the FRS signal detected by a lock-in amplifier for a given modulation frequency can be expressed as [135]:

$$S_{lock-in} = \kappa\theta P_0 2\varphi \tag{4.6}$$

where P_0 is the intensity of the light incident at the analyzer, κ is the instrument factor including the detector response and the lock-in gain, and θ is the rotation angle resulting from the Faraday effect. The advantages and disadvantages of the 90-degree method are summarized in Table 4.2.

In the 45-degree crossing method, a Rochon or Wollaston type analyzer is oriented at 45° with respect to the incoming polarization to split the original beam into two parts of equal intensities but with opposite polarization. The two beams, therefore carry identical noise and are captured simultaneously by two identical (ideally) detectors or a balanced detector. A differential detection (BD) of the two channels allows to obtain a Faraday rotation signal minimizing common noises. The advantage of using the 45-degree configuration is that the FRS signal can be produced under the DC field by just scanning the laser wavelength across the molecule transition without applying high frequency modulation on the Faraday rotation angle, associated with demodulation. Therefore, the measurement of paramagnetic species' concentrations can be performed with a short timescale which is only limited by the laser wavelength scan and data acquisition rate, which is suitable for studying chemical reactivity

[140,151]. *B. Brumfield et al*. [152] demonstrated that the balanced signal with a DC field, $V_{signal\text{-}45^o}$, is proportional to the Faraday rotation angle θ, the laser power P_0, and the absorption path length L; it can be expressed as [138]:

$$V_{signal-45^o} = R_v \frac{\eta e}{h\nu} P_0 \exp\left(-\frac{1}{2}(\alpha_L + \alpha_R)L\right) \times 2\theta \tag{4.7}$$

where R_v is the transimpedance gain (in V/A), α_L and α_R describe the absorption coefficient of LHCP and RHCP lights by paramagnetic species, respectively, η is the quantum efficiency of the detector, and the photodiode responsivity (in A/W) is given by ($\eta e/h\nu$). In addition, the analyzer is set to 45° and the total laser power is divided into two orthogonal polarization beams. Balanced detection is then performed which makes the polarizer extinction of less important [140] and avoids the wasting of laser power as in the 90° crossing configuration in which only a small amount of the laser beam passes through the very small rotation angle for FRS signal detection. Therefore, this 45° crossing configuration is useful for applications involving low output power laser and low transmission optical system like multi-pass arrangements where degradation of polarization degree is substantial due to imperfections of the mirror surfaces [148].

Table 4.2 Comparison of two FRS approaches using 90°- and 45°-crossing methods

	90° crossing method	**45° crossing method**
Advantages	a single detector is needed, low-cost; significant laser excess noise reduction [51]	Total laser power is used for two polarizations, useful for low laser power and multi-pass arrangement.
Disadvantages	To achieve a good *SNR* the two polarizers have to be nearly crossed at 90°: the offset angle needs to be optimized and leads to the waste of laser intensity, thus unsuitable for use with weak laser power and low transmission of optical system Effects of depolarization due to mirror imperfections in the multi-pass experiment.	Requirement of two identical detectors or a balanced detector which is costly in the mid-infrared. The performance depends on differential signal processing.

4.1.3 Cavity enhanced Faraday rotation spectroscopy

The rotation angle by Faraday effect is proportional to the total optical path length, enhancement of the path length using optical cavities can further improve the detection limit

of the FRS system [153–155]. In a linear optical cavity with finesse F, the Faraday rotation angle can be enhanced by a factor of $2F/\pi$ due through the increased path length [156,157].

$$\theta_{cavity} = \frac{2F}{\pi}\theta \tag{4.8}$$

The common cavity-enhanced approaches combined successfully with FRS are CRDS and phase-shift CRDS [153,154], both were carried out with DC magnetic field, providing absolute Faraday rotation angle.

In the case of CRDS being combined with FRS, the rotation angle is determined by measuring the ring down times τ_s and τ_p for s and p polarizations, respectively [154].

$$\theta_{cavity}(\nu) = \frac{L}{2c}\left(\frac{1}{\tau_s(\nu)} - \frac{1}{\tau_p(\nu)}\right) \tag{4.9}$$

When PS-CRDS is combined with FRS, the rotation angle is calculated from the phase-shift of the modulated light (at an angular modulation frequency ω) that is transmitted by the cavity. The phase shifts for s and p polarizations, ϑ_s and ϑ_p respectively, are associated with the ring down time via [153]:

$$\begin{aligned}\tan\left[\vartheta_s(\nu)\right] &= -\omega.\tau_s(\nu)\\ \tan\left[\vartheta_p(\nu)\right] &= -\omega.\tau_p(\nu)\end{aligned} \tag{4.10}$$

In the next section, it will be outlined how FRS will be combined with the CEAS approach to improve the selectivity and sensitivity of the OH detection system. The idea is similar to the 45-degree FRS approach [138], which uses a multi-pass cell and balanced detection. In our case, the FRS signal is determined by measuring the integrated cavity transmission signal for two polarizations using a differential detection scheme (BD).

4.2 Implementation of an instrument based on cavity-enhanced Faraday rotation spectroscopy (CE-FRS)

4.2.1 Instrument components

The components used in the development of the CE-FRS instrument were inherited from the previous experimental system, such as the cavity cell, the laser controller, the detector, the lock-in amplifier, and the DAQ card. In order to perform FRS, some new components were installed, including a new continuous-wave (CW) DFB-ICL (nanoplus GmbH), a second

detector used for differential detection, magnetic coils for magnetic field production, and a new microwave generator allowing modulation of the OH production.

(1) CW DFB-ICL

The new laser source has the same packaging configuration as the last one used in **Chapter 3** but provides an output power of 11 mW, which is approximately three times higher than that of the laser described in **Chapter 3**. A frequency tuning range from 3565 to 3573 cm^{-1} over ~ 8 cm^{-1} can be achieved by tuning laser current (0.0163 cm^{-1}/mA) and temperature (0.3342 $cm^{-1}/^{o}C$). In order to probe the OH Q(1.5e) transition, the ICL was operated at 27°C with a current of 152.42 mA. Figure 4.3 depicts the spectral tuning range (left) and the ICL output power (right) at 27°C.

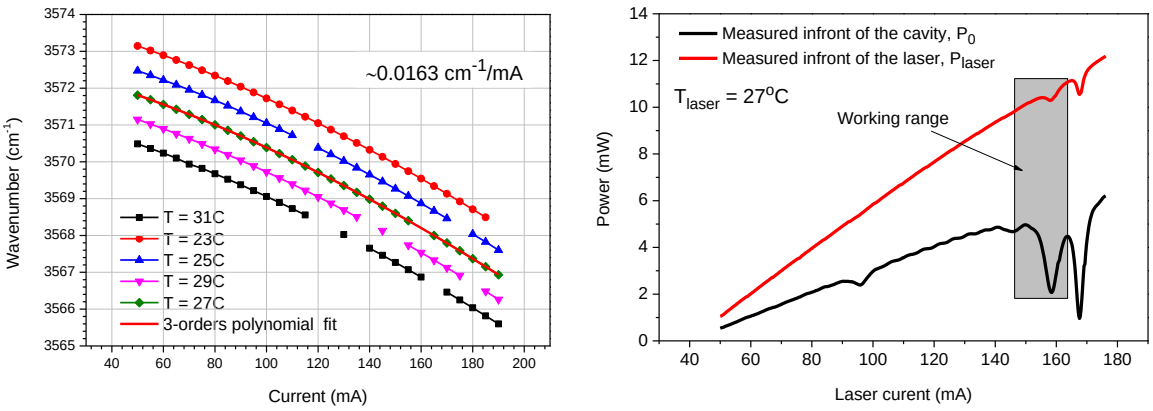

Figure 4.3 Characterization of a new CW DFB-ICL. Left – laser wavenumber versus its current and temperature. Right – output power vs laser current; the black curve is the power measured in front of the cavity (after passing through a polarizer and a beam splitter) which is half of the input laser power (red). The observed optical power drops are due to ambient water absorptions.

(2) Magnetic coils

The magnetic coils were incorporated around the cavity body to generate a magnetic field along the optical cavity axis. In this work, the cavity previously used for the OA-ICOS experiments was utilized for the CE-FRS setup (see Figure 4.4). Its body is constructed with a 0.5-m long stainless steel tube with an outer diameter of 30 mm, and equipped with three gas connections (1/4" male connection, Swagelok): one at the center and the others located at a distance of 160 mm from the center. At two ends of the body, CF-40 flanges with a diameter of 69 mm are installed in order to connect the mirror supports.

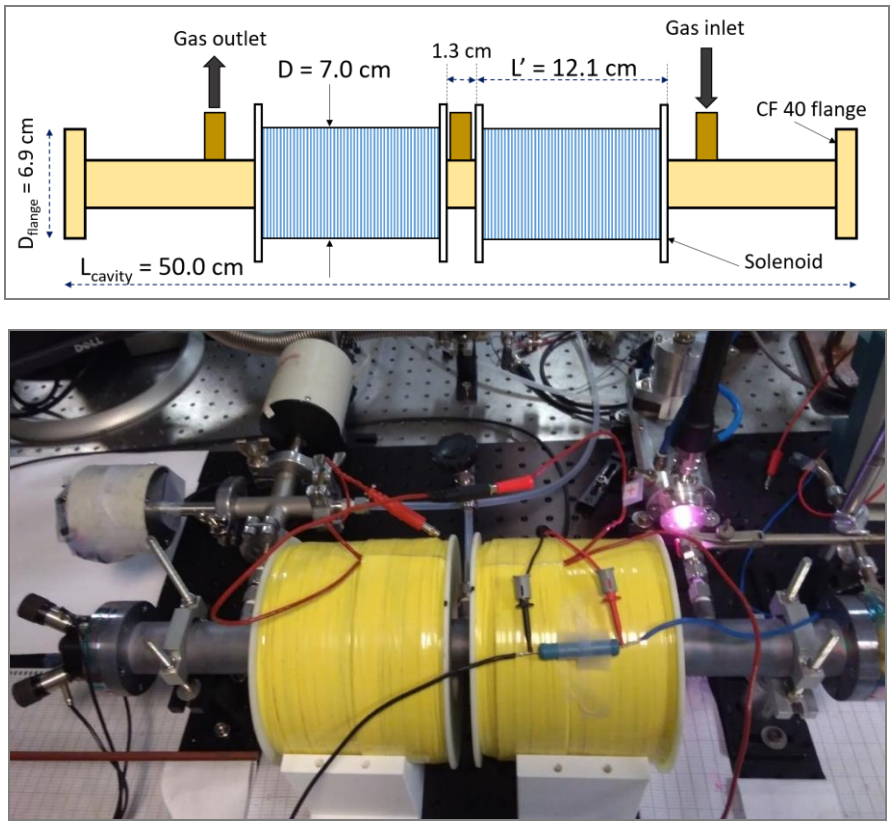

Figure 4.4 Schematic view (upper) and photo (lower) of the optical cavity equipped with a pair of magnetic coils.

The inner diameter of the magnetic coil is 70 mm so that the cavity body fits on the inside. Due to the gas connection at the center, two identical magnetic coils were installed to cover a sample length of 25 cm. The spacing between the two magnetic coils is 1.3 cm. Each coil was made of ~790 m (1115 turns) of a 16 gauge (d = 1.29 mm), enamel-coated copper wire wound around a 12.1-cm plastic cylinder in multiple-layers. Each coil has an inductance of 0.315 H and an ohmic resistance of 10.2 Ω.

(3) Detectors for balance detection

A second detector (PVI-4TE-3, VIGO System S.A.) integrated with a preamplifier (MIP-DC-1M-F-M4) was used together with the first detector (PVI-4TE-3.4) to perform a differential balance detection. The main specifications are given in Table 4.3. The PVI-4TE-3 has a higher output voltage noise density of 775 nV/Hz$^{-1/2}$, compared to the PVI-4TE-3.4 of 400 nV/Hz$^{-1/2}$, while the output voltage responsivity is smaller by a factor of 1.8.

Table 4.3 Characteristics of the detector, PVI-4TE-3/MIP-DC-1M-F-M4.

Detector characteristics		
Detectors	**PVI-4TE-3**	**PVI-4TE-3.4**
Active area (mm^2)	1×1	1×1
Wavelength range (μm)	2.1 to 3.4	2.2 to 3.6
Spectral responsibility (A/W), $\Re(\lambda)$ @ 3.0 μm	1.2	1.3
Time constant (ns), τ	< 200	< 200
Detectivity ± 20% @ 3.0 μm ($cm.Hz^{1/2}/W$)	1.6E12	4.5E11
Current noise density ($pA/ Hz^{1/2}$)	0.08	0.1
Preamplifiers:	**MIP-DC-1M-F-M4**	**MIPDC-F-1**
Transimpedance (V/A) @ R_{LOAD} = 1 MΩ	9.4E5	1.4E6
Detector bandwidth, f_{BW}	DC to 1 MHz	DC to 1 MHz
Voltage output (V), V_{out} @ R_{LOAD} = 1 MΩ	3	2
Voltage responsivity ± 20% @ 3.0 μm (V/W)	1.05E6	1.8E6
Output noise density @ 100 kHz ($nV.Hz^{-1/2}$)	775	400

4.2.2 Experimental setup

The layout of a complete cavity-enhanced Faraday rotation spectroscopy setup is shown in Figure 4.5. The principle of this approach is based on measuring integrated light intensity of two different polarizations at the cavity output. The OA-ICOS approach used in **Chapter 3** was modified to perform to couple FRS. Notice that the new OA-ICOS-FRS system could be also used to perform conventional OA-ICOS without alteration (in absence of the magnetic field). This capability is leveraged to calibrate the FRS signal and evaluate the CE-FRS detection in comparison to conventional OA-ICOS under the same experimental conditions.

The collimated ICL beam was passed through a Glan polarizer P1 (GLP8010, Focteck Photonics) in free-space to establish a polarization axis of the incident laser and then co-aligned with a He-Ne laser via a CaF_2 beam splitter for optical alignment. The beam leaking out of the cavity (spot pattern with diameter of ~1.5 cm at a distance of ~6 cm from the rear cavity mirror) was focused onto a Rochon prism polarizer P2 (RPM10, Thorlabs) using a focusing lens (75 mm focal length). The analyzer P2 was rotated at 45^0 with respect to the initial polarizer to convert laser polarization rotation into intensity changes that could be detected using photodetectors. Hence the existing beam was split into s and p orthogonal polarizations. The s polarization component makes an angle of 1.5^o with respect to the optical

propagation axis. The polarization extinction ratio (the ratio of maximum to minimum transmission of a sufficiently linearly polarized light input when it is rotated parallel and perpendicular to the transmission axis of a polarizer, respectively) of the two polarizers, P1, and P2, are $< 5\times10^{-6}$ and $< 10^{-5}$, respectively. A mirror was placed at a distance of 10 cm from P2 to separate the s from the p component of the transmitted light. The separated beams were then focused onto two detectors, D1 and D2 (PVI-4 TE-3.4 and PVI-4 TE-3, respectively), using two off-axis parabolic mirrors (OAPM), with a focal length of 5 mm and 3.5 mm, respectively. The parabolic mirrors were placed so that the distance from the second polarizer P2 to each detector was the same such that the common noise signals based on the absorption of water vapor outside the cavity are approximatively equal for the two channels. Therefore, the total noise, including the noises originating from the laser source and the optical noises (i.e. etalon effects and water absorption), will contribute to the two detection channels with the same characteristics that can be ideally suppressed as possible.

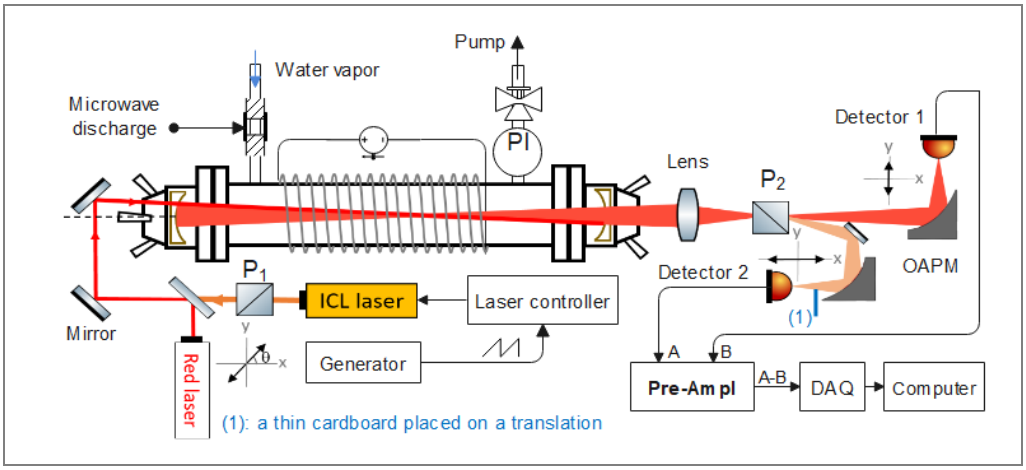

Figure 4.5 Scheme of the CE-FRS system. P1: linear polarizer; P2: Rochon Prims polarizer; OAPM: Off-axis parabolic mirror. A thin piece of cardboard was used to block a small amount of the laser beam on the second detector for manually balancing the signal levels on the two detectors.

The signal from detectors D1 and D2 were fed to a pre-amplifier (EG&G 5113, Signal Recovery) via inputs A and B.

The pre-amplifier output could be set at different modes: A or A-B with DC-coupling and AC-coupling. The amplifier provides an adjustable gain G and a band-pass electronic filter. Different fixed values of 5, 10, 20, 50, 100, 250, and 500 are available for coarse gain tuning. Lower and higher cutoff frequencies of the electronic filter can be adjusted with different fixed levels (0.03 Hz, 1 Hz, 3 Hz, 10 Hz, 100 Hz, 300 Hz, 1 kHz, 3 kHz, 10 kHz, 30 kHz, 100 kHz, and 300 kHz). The choice of amplifier mode and pass band of the filter depends on

experimental requirements. For example, DC-coupling, A-mode output, G = 250, and a bandwidth of 0.03 Hz to 3 kHz were used to measure direct absorption for 1 detector channel based on the OA-ICOS approach. AC-coupling, (A-B) mode, G = 250, and bandwidth 300 Hz-10 kHz were used for the measurement of differential signals. The amplified signal was sent to a DAQ card (PCI 6251) for recording the absorption spectra and the differential signal.

Laser frequency scanning was achieved by applying a triangle waveform (Vs = 0.8 Vpp at 510 Hz) from a function generator to the external modulation input of the laser controller (LDC 501, Stanford Research). It provided a tuning range of 20 mA around its center value of 152.42 mA, corresponding a frequency tuning of about ~ 0.33 cm^{-1} across the OH Q(1.5e) absorption line. The coils were driven with a DC power supply (72-13330, Tenma) providing a constant DC current up to 3 A. A new microwave generator (GMS200W, Sairem) with a maximum power of 200 W was applied to a microwave cavity (S-wave, Sairem) for OH generation (see Figure 4.15).

4.2.3 Distribution of magnetic field inside the optical cavity

Two magnetic coils were connected in series so that an equal electric current feeds the two coils to generate two identical magnetic fields. The total internal resistance was R_0 = 20.5 Ω. During the experiments, the power supply was driven in constant current mode to generate a static magnetic field with constant field strength.

The axial magnetic field distribution over the cavity length of 0.5 m was measured using a Gauss meter and is shown in Figure 4.6-left. The magnetic field inside the coils is non-uniform, as expected due to the large size of the coils. The magnetic field strength B is maximized at the centers of the two coils, reduced rapidly by 44.4 % at the edges of the coils, and declined to zero at the two ends of the cavity. Because the field strength distributed from the edges of the coils to the two ends of the cavity is much smaller than its center value, as well as the optimum value required for obtaining the FRS signal (see **4.2.5.1**). The physical interaction length of the beam with the magnetic field was considered of about 25 cm.

To evaluate the effect of the stainless steel tube on the magnetic field strength inside, measurements were performed where the magnetic field strength was determined at the coil's center with (field B_1) and without (field B_0) the stainless steel tube being present. Figure 4.6-right shows a linear relation between the static magnetic field strength and the coil current. Based on the slopes, the loss of about 1.3 % indicates that the stainless steel tube does not profoundly affect the field strength inside the cavity. The magnetic field increases by 186.8

Gauss per Ampere at each coil center. The field strength B mentioned in the following sections refers to the maximum field strength at the coil center.

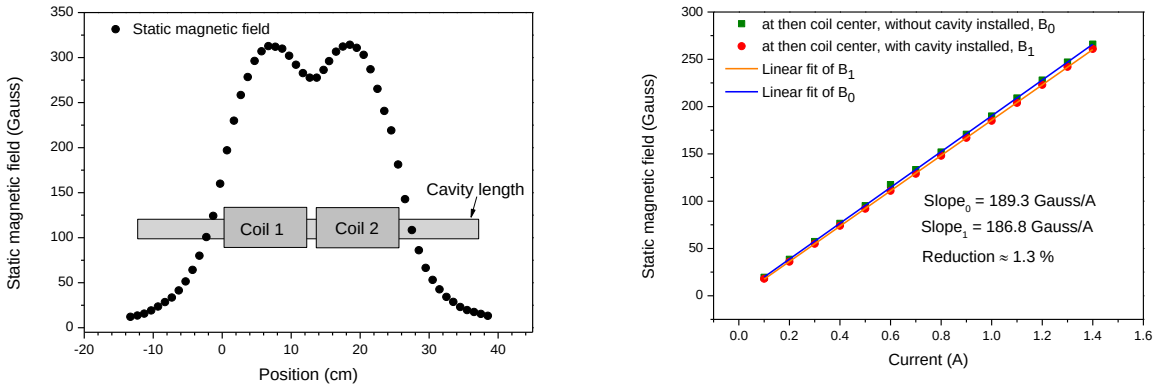

Figure 4.6 Left – axial distribution of magnetic field strength B inside two coils powered with I = 1.7 A. Right – magnetic field strength at coil's center vs coil current I.

4.2.4 Differential detection scheme (BD)

4.2.4.1 Balancing process

Measurement of the Faraday rotation signal is based on a differential detection scheme which can be achieved by employing an auto-balancing detector with a high common-mode suppression ratio [138,157]. As the availability of adequately balanced detectors in the mid-IR is quite limited and costly, two mid-IR photodetectors were used for balancing detection. The two detectors had different voltage responsivities and gains, the output signals converted from the received incident powers were $V_1(t)$ and $V_2(t)$, respectively. Manually balancing the detector signals is crucial for obtaining a line-scanned FRS spectrum. The balancing procedure was performed by adjusting the signal level of the second detector $V_2(t)$ to the reference value of the first detector $V_1(t)$. The process is summarized below:

- outputs of the two detectors are connected to an oscilloscope, via CH_1 and CH_2, respectively, using AC-coupling to remove the detector offset signals.
- laser is scanned over ~ 0.33 cm^{-1} across the OH Q(1.5e) line at a scan rate of 40 Hz. The detector signals, $V_1(t)$ and $V_2(t)$ are recorded simultaneously. In this step, the magnetic field is switched off.
- the oscilloscope is set to "x-y" display mode, in which x and y represent the $V_1(t)$ and $V_2(t)$, respectively. Once the two detectors are balanced, the AC signals from the two detectors have the same amplitude $V_2(t)=V_1(t)$, and a linear line made at an angle of 45^0 ($V_2(t)/V_1(t)$ =1) to the x-axis can be observed.

- as the pre-amplifiers of two detectors have their own fixed gain, $V_2(t)$ was adjusted optically by changing the laser intensity impinging on D2. A thin piece of cardboard was placed on a linear translation stage for that purple, and was slowly adjusted to block a small amount of the laser beam (see Figure 4.5). The adjustment was completed once the slope of the $V_2(t)/V_1(t)$ line reached 1.

Figure 4.7-a shows cavity transmitted signals of two polarizations after balancing, measured by detectors D1 and D2 at a full bandwidth of 1 MHz. The inserted panel is a zoom in the OH Q(1.5e) line region that clearly shows the cavity modes with the same amplitude and shapes for two channels, meaning a good balance of the detectors was achieved. Dividing the frequency space of the two OH lines (about 3210 GHz) by the number of cavity modes (~ 42 via counting in the spectrum) between two lines, the mode spacing of about 75 MHz was estimated. This spacing is four times smaller than the cavity FSR of 300 MHz, indicating an overlapping after 2 round trips of the laser beam in the cavity.

Figure 4.7-b plots $V_2(t)$ versus $V_1(t)$, giving a slope of 0.989. A significant deviation around the linear fit might be due to a difference in the noise densities between the two detectors.

A Fourier transform analysis of the detector background signals (D1 and D2 were blocked) was performed as shown in Figure 4.7-c. It can be seen that the detectors have different noise levels. Detector D2 has a like-white noise with a higher noise level, as expected from the manufacturer datasheet. On the other hand, the noise in D1 has some "spikes" with a much higher amplitude located at frequencies of 270, 530, 1060 Hz, … (maybe resulting from electronics perturbation). This causes a challenge for entirely suppressing detector noises using the differential detection scheme. In addition, the chaotic behavior of the cavity build-up power might contribute to noises in cavity transmitted lights. These optical noise could not be wholly suppressed via a differential detection scheme using analog electronic removal [153]. Those reasons (including electric noise from the detector itself and optical noise) caused some random noise in the balanced FRS signal (discussed in **4.2.5**) and limited the performance of the current CE-FRS approach. Moreover, weak cavity output intensities impinging on the detectors due to un-resonance coupling of the laser beam to the cavity also restrict the differential detection process. The signal level is a few mV (see Figure 4.7-b), comparable to the detector noises.

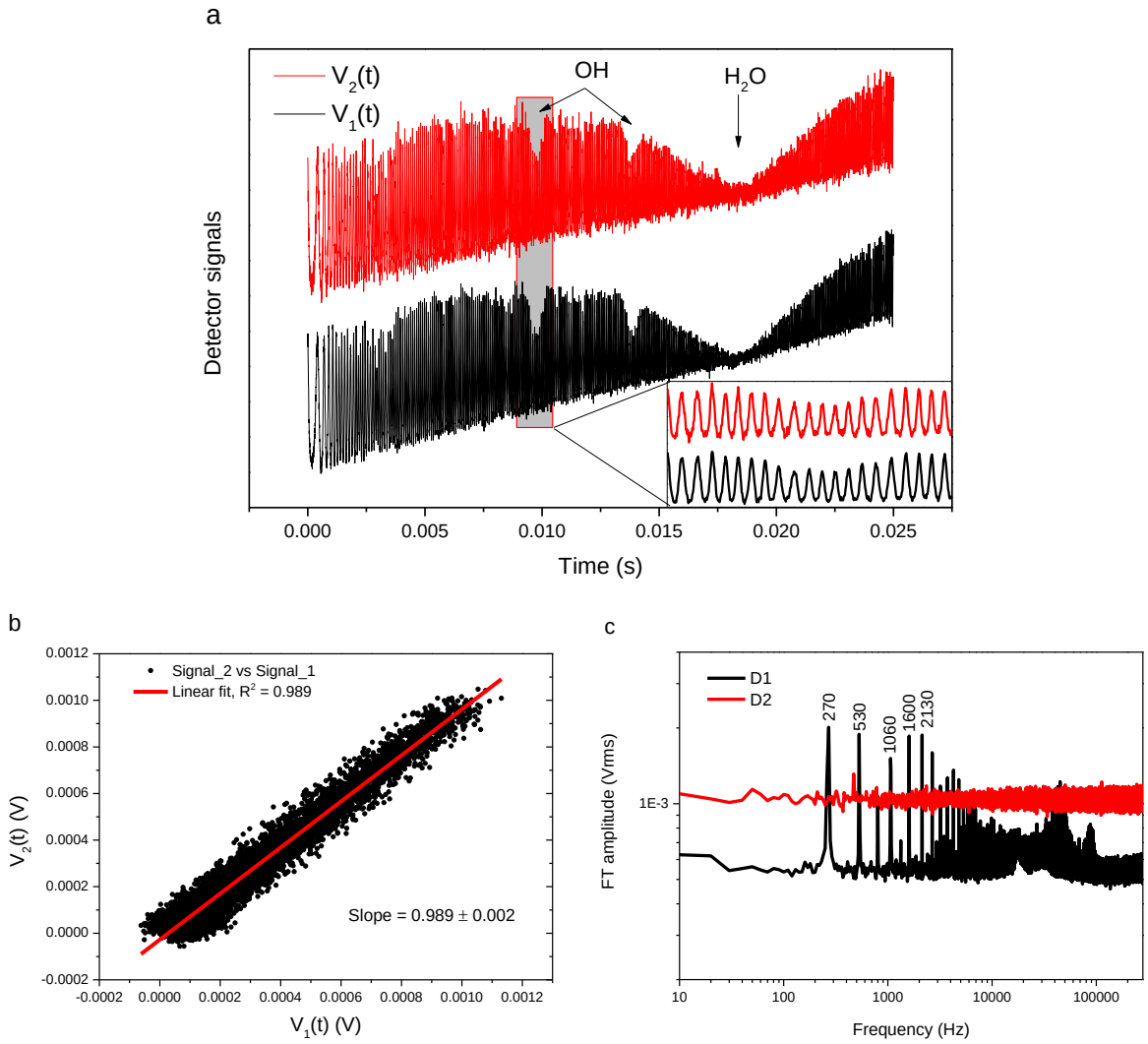

Figure 4.7 a – Detector signals (AC-coupling, 1 MHz bandwidth) of two polarization signals from cavity outputs after power balancing (laser scan rate = 40 Hz, sampling rate = 320 kS/s, average = 1000, I_{coil} = 0 A, P = 0.5 mbar); b – Plot of $V_2(t)$ vs. $V_1(t)$ with a slope of 0.989; c – Fourier transform analysis of detector noises.

4.2.4.2 Differential signal

Cavity output signals of two different polarizations emerging from the detectors were fed to two identical, homemade active low-pass filters (NE555 operational amplifier, Texas Instrument) with a cutoff frequency of 3 kHz and a gain of 80. Figure 4.8-left presents the integrated cavity output signals of two different polarizations during the laser frequency scanning across OH lines, without the application of the magnetic field. The spectral signals show similar line profiles for both detectors. The two spectral signals agreed well, including the region of OH and H_2O absorption. Also etalon effect and baselines seemed to match largely. Once a magnetic field of B = 260 Gauss was applied, the Faraday rotation effect

causes a difference in the transmitted signals of the two different polarizations only for the paramagnetic species OH (Figure 4.8-right). The FRS signal can be obtained by subtracting $V_1(t)$ to $V_2(t)$ while eliminating the effect of H_2O absorption and optical interferences.

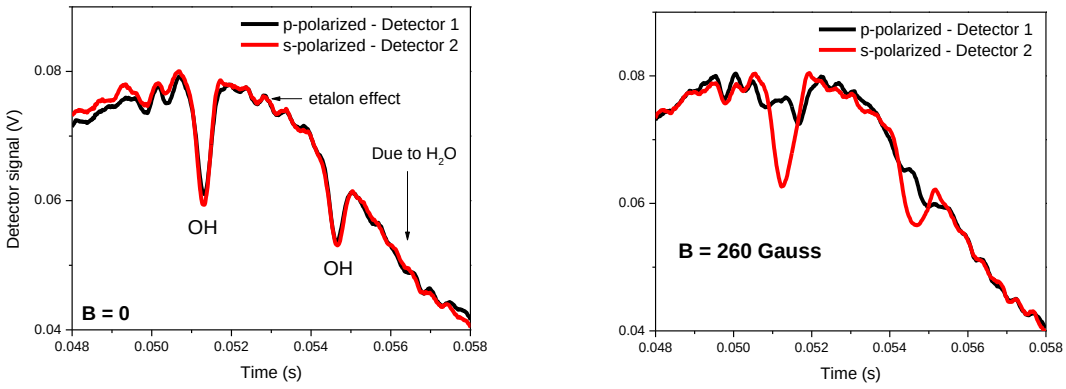

Figure 4.8 1000-averages cavity output signals of two polarizations recorded by detector D1 and D2 without (left) and with (right) magnetic field application. The laser was swept across the OH lines with a scan rate of 40 Hz.

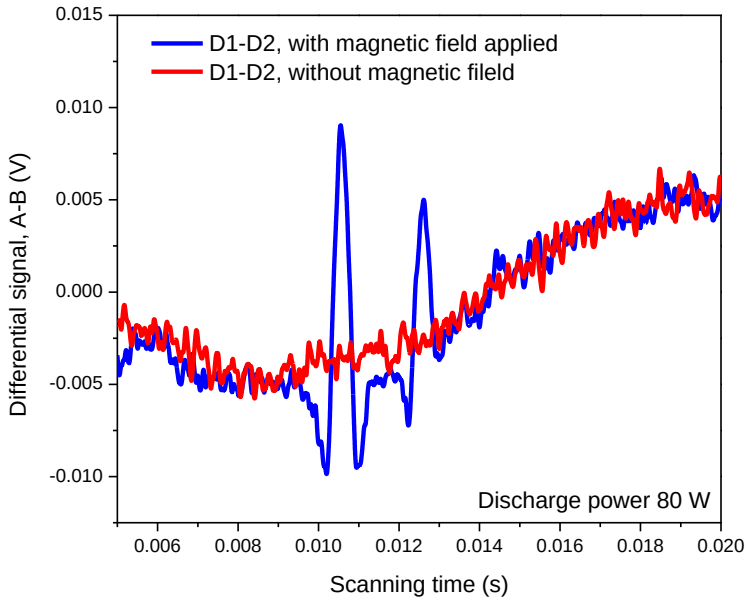

Figure 4.9 Differential signal (A-B) for balanced detectors with (blue trace) and without (red trace) magnetic field applied.

In practice, the signals $V_1(t)$ and $V_2(t)$ were fed to inputs A and B (AC-coupling) of the pre-amplifier, respectively, to extract the difference signal. The output A-B was amplified and filtered with a gain of 250 and a bandwidth of 10 Hz-3 kHz. As shown in Figure 4.9, by subtracting the two signals and measuring the difference signal (A-B), CE-FRS signal of OH

lines was achieved when a static magnetic field (260 G) was applied. It is obviously observed suppression of the etalon fringes and the absorptions of non-paramagnetic molecules by balancing detection in both with and without magnetic field application. That indicates the advantage of FRS in the improvement of the spectral selectivity. Notice that the settings of the laser scan rate (40 Hz), the filter bandwidth (10 Hz-3 kHz), and magnetic field strength used for this observation were the non-optimized parameters. In the next section, they are re-optimized.

4.2.5 Optimization and characterization of the FRS setup

4.2.5.1 Magnetic field strength

For maximizing the balanced FRS signal, the magnetic field strength B needs to be optimized so that the Zeeman splitting becomes comparable with the spectral line width of the transition at B = 0 [158]. Experiments were performed to determine experimentally the optimum magnetic field strength B_{opt}. The OH radicals were generated by 40 W continuous microwave discharge of H_2O vapor. In the current system, due to limitations imposed by the OH generation method (the microwave discharge system required working at low pressure), the pressure in the CE-FRS system was 0.6 mbar. The amplitude of the balanced FRS signal for the OH Q (1.5e) transition was measured with various B fields by changing the coil current in steps of 0.3 A. Each FRS spectrum consisting of 500 data points was averaged 1000 times at a laser scan rate of 80 Hz (see the inserted graph in Figure 4.10). The B-field strength was deduced from the linear relation between the field strength and the coil current (see Figure 4.6-right).

As can be seen in Figure 4.10, the peak-to-peak amplitude of the OH Q(1.5e) line increases approximately linearly with B for relatively low magnetic field strengths (< 170 Gauss). Continuous increase in the B-field strength cannot significantly increase the BD-FRS signal amplitude while the widths of the OH lines become larger and overlapping each other (see the inserted graph in Figure 4.10). The plateau of the A-B amplitude for I > 1.5 A may be due to the non-uniform of the magnetic field which maximizes at the coil's centers and significantly reduces at the two ends of the cavity (see Figure 4.6-left). A reason can be explained as following. The measured BD-FRS signal can be considered as the integral of the FRS signals at different positions over the axial length of 0.5 m. Because the amplitude of the FRS signal is maximized at the optimum B-field strength and then is reduced with the increase of B value. Therefore, continuous increase the B-field strength might increase the FRS signals

caused by OH distributed outside the coil's length, but saturate the FRS signals caused by OH inside the coil. As a result, the amplitude of the total BD-FRS signal was saturated at high B-field strength. A simulation of the impact of the axial magnetic field profile on the Faraday rotation spectrum is discussed on the supplementary of ref. [153]. In addition, use of higher currents can cause a faster self-heating of the coils. An optimum field strength $B_{opt} \approx 318$ Gauss (at $I_{coil} = 1.7$ A) was selected for the further characterization of the CE-FRS instrument. Since the absorption linewidth depends on the pressure which influences the B_{opt} value, all further experiments were carried out at the same pressure (0.6 mbar) under the same experimental condition.

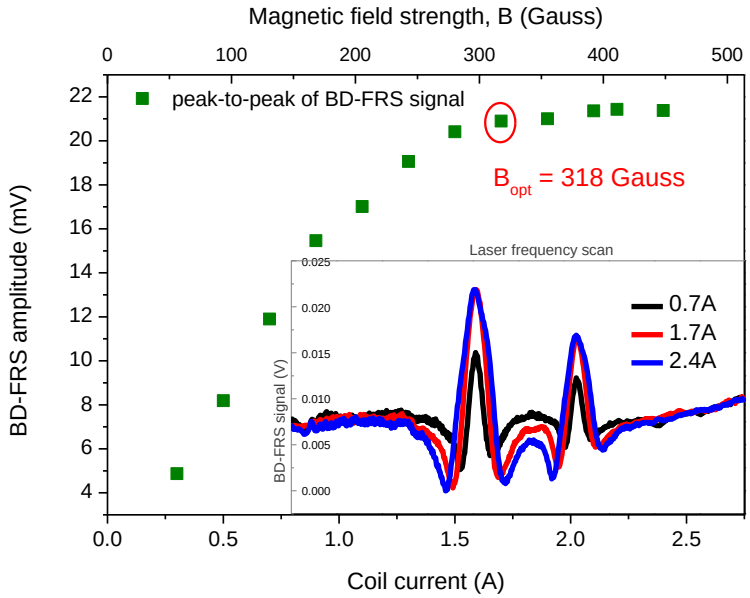

Figure 4.10 Plot of the peak-to-peak balanced FRS signal vs applied magnetic field. The inserted panel shows the balanced FRS spectra obtained from 1000 averages of laser scan at a rate of 80 Hz. Each spectrum consists of 500 data points.

4.2.5.2 Laser scan rate

In CE-FRS, balanced FRS signal is measured from the light leaking out of a high finesse optical cavity (ultralow cavity mirror transmission), in which optical noise (random of cavity mode) [125] dominates. Because the balanced detection using two non-identical detectors could not thoroughly eliminate those common noises, it is necessary to average the spectra to get a good SNR. Fast scanning of the laser wavelength allows increasing the averaging within a fixed integration time, while keeping a fast time response. The noise suppression as a function of the laser scan rate has therefore been investigated.

Figure 4.11-a shows FRS spectra recorded at different laser scan rates f_s. A band-pass filter of the pre-amplifier of 0.03 Hz-3 kHz was used. The laser scan rate was increased from 40 Hz to 320 Hz in steps of 40 Hz. As the number of data averaging in a fixed integration time increases with the laser scan rate, noise suppression efficiency is significantly improved with increasing of the laser scan rate. It indicates that the noise in the balanced CE-FRS signal was mainly dominated by the random noise which is reduced by averaging. Figure 4.11-b plots the corresponding SNR that increases with the laser scan rate. Higher laser scan rate is thus well desirable.

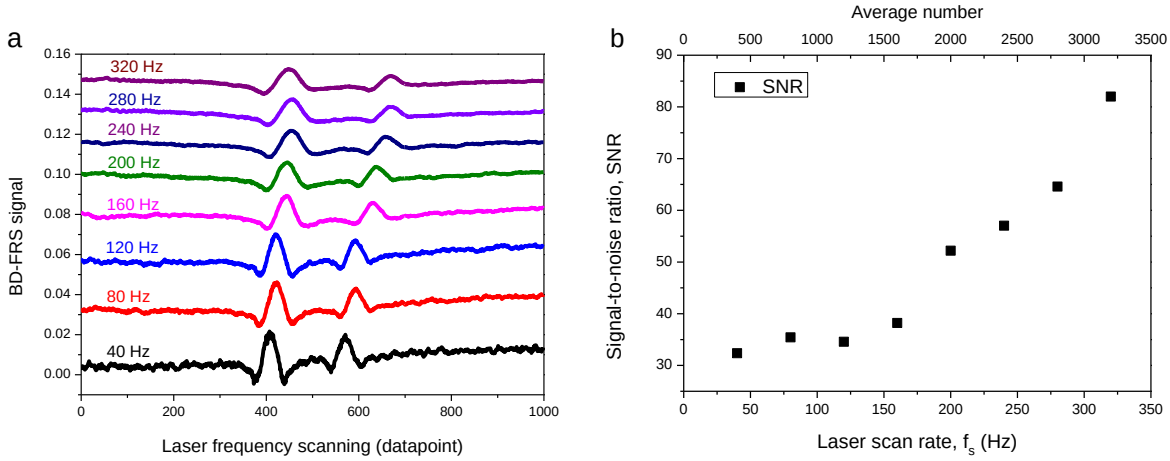

Figure 4.11 a – FRS spectra of OH lines were averaged within 10 s integration time at different laser scan rates. b – Signal-to-noise ratio vs laser scan rate.

In the present work, a triangular waveform was applied to sweep the laser current, those spectra were measured during the first half of the scan period (rising edge of the waveform). Each spectrum consists of 1000 data points, resulting in a sampling rate of $f_{sample} = 1000*2*f_s$ for the DAQ card. It means that the higher laser scan frequency requires the higher sampling rate of the DAQ card. For example, f_s = 320 Hz results in a sample rate of f_{sample} = 640 kS/s. Constrained by the sampling rate of the used DAQ card and the limit of the Labview's interface performance, the maximum scan rate achievable was limited to 510 Hz in the present experimental setup. Another issue related to fast laser scan is the "skew" effect due to the distorts in spectral line shapes by filtering. This effect should be taken into consideration. The filter bandwidth of the pre-amplifier was adjusted to 300 Hz - 10 kHz to minimize this effect when scanning laser at 510 Hz.

4.2.5.3 FRS signal versus laser power

Several studies pointed out that the SNR of the FRS signal is proportional to the incident power on the second polarizer P2 [135], which is the transmitted power through the cavity in the present setup. A study of the cavity transmitted power-dependent SNR of the FRS signal was carried out with different transmitted powers P_{out} by attenuating the incident power P_{in}. Experimentally, several optical filters (transmission of 0.49, 0.38, 0.27, and 0.21) were placed between the incident laser and the cavity input to reduce P_{in} from 4.8 mW to 2.3, 1.8, 1.3, and 1.0 mW, respectively. Notice that although the laser emits a power of P_{laser} = 10.2 mW at the target wavelength, due to the absorption of H_2O in air, the transmission of the linear polarizer P1 (~80%) and the losses from the beam splitter, the laser power at the cavity input was about 4.8 mW (see Figure 4.3-right).

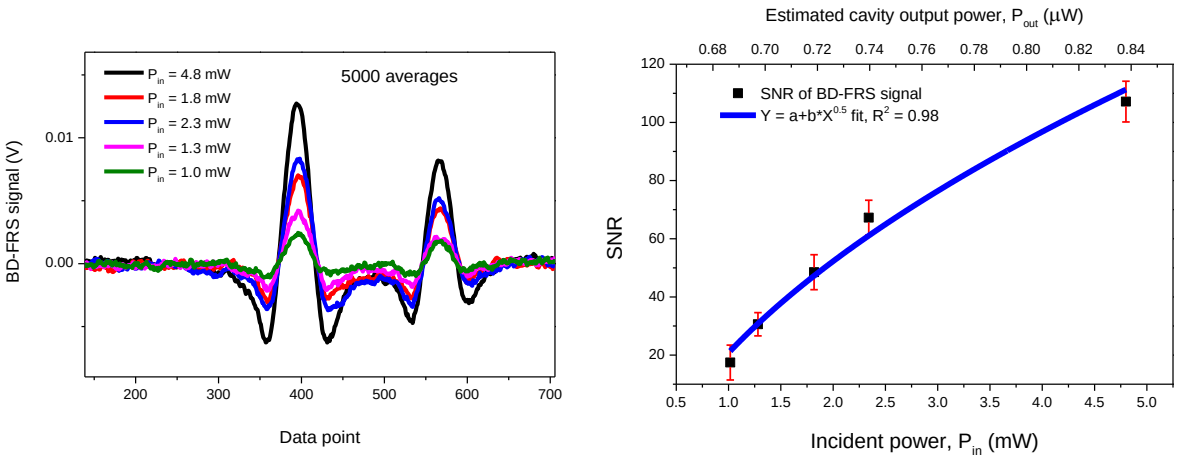

Figure 4.12 Left – FRS spectra measured with different incident power entering the cavity, P_{in}. Right – SNR of FRS signal vs P_{in} (and thus the estimated cavity output P_{out}).

The CE-FRS system was operated in a fast laser scan mode. A constant microwave discharge power of 40 W was used to produce constant OH concentrations at 0.6 mbar. A series of FRS spectra of OH absorption at different excitation powers P_{in} were recorded, as shown in Figure 4.12-left. A dependence of the FRS signal on the incident power P_{in} is obvious. For each SNR, the signal amplitude (peak-to-peak) at the OH Q(1.5e) line as well as the standard deviation of the noise in the baseline away from the line center were analyzed. Figure 4.12-right illustrates the calculated SNR arising as the root mean square of the input power or transmitted cavity power P_{out} estimated from the detector signal level:

$$SNR \approx P_{in}^{1/2} \tag{4.11}$$

Higher P_{out} means more light intensity impinging on the detectors, giving better SNR of the FRS signal. P_{out} can be improved by either using higher laser power or enhancing the coupling factor of the laser into the cavity. While the first ideal depends on the availability of laser, and the second solution is realizable using a re-coupling configuration [159].

In conclusion, the performance of the CE-FRS approach involving differential detection was impacted by weak transmitted power through the cavity.

4.2.5.4 Calibration of FRS signal

To calibrate FRS signal, the experimental procedure discussed in section **3.3.4**, **Chapter 3** was performed. Different OH concentrations were produced by changing the microwave discharge power while the pressure of H_2O injected was maintained at about 0.6 mbar. The concentration of OH radicals was determined based on the OA-ICOS approach by recording direct absorption signals from detector D2 without a B-field (see **3.2.4.1** for spectral processing).

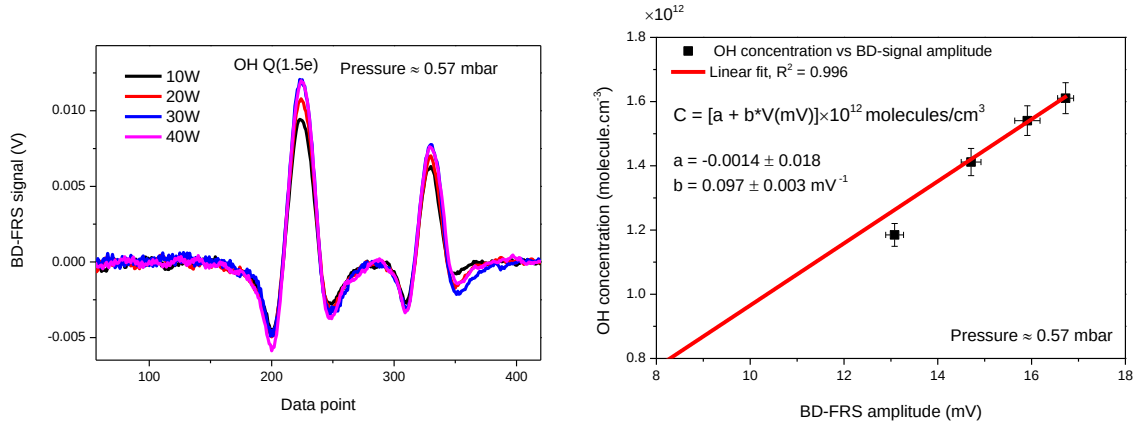

Figure 4.13 Left – FRS spectra recorded at 0.57 mbar at different discharge powers. Right – linear response of the peak-to-peak balanced-signal and the OH concentrations determined by the OA-ICOS approach.

FRS spectra measured at different microwave discharge powers (10, 20, 30, 40W) are shown in Figure 4.13-left. Each spectrum, consisting of 500 data points, was averaged over 10200 spectra (laser scan rate of 510 Hz) within 20 s integration time. Peak-to-peak of the FRS signal of the OH Q (1.5e) line versus the OH concentration retrieved by the OA-ICOS measurement is plotted in Figure 4.13-right. A linear relationship was found with a coefficient $R^2 = 0.996$ and a slope (sensitivity) of 9.7×10^{10} molecule.cm^{-3}/mV. Based on the SNR of the spectrum, a LoD of ~10^{10} molecule.cm^{-3} was achieved by the CE-FRS setup for a 20 s

averaging time, which is improved by a factor of ~2 compared to the corresponding value in the WM-OA-ICOS approach.

The FRS signal eliminated significantly the absorption of non-paramagnetic species affecting the OH Q(1.5e) line (see Figure 3.24-right for comparison) as well as the ASE perturbation to the absorption signal as observed in the OA-ICOS measurement. Moreover, the etalon noise, typically observed with the use of cavity, was also reduced thanks to the differential detection scheme.

4.2.6 MDAC versus integration time in the CE-FRS system operating in a fast scanning mode

The dependence of MDAC on measurement integration time, the measurement precision and stability of the CE-FRS system were evaluated using Allan deviation analysis. As the produced OH concentration was unstable over longer times (> 20 s) and H_2O absorption could not be observed in the FRS signal (unlike using H_2O absorption signal in a WM-OA-ICOS for its Allan analysis), a time series measurement (over 3.8 hours) of the "FRS signal" was performed using N_2 to fill up the system. The Allan analysis was thus carried out without OH generation and without any absorption, like in a BBCEAS (Broadband Cavity Enhanced Absorption Spectroscopy). As shown in Figure 4.14-a, each data point was averaged over 510 laser scans for an integration time of 1 s. Allan deviation in terms of the voltage signal was performed and converted to minimum detectable absorption coefficient vs. integration time using a slope of 9.7×10^{10} molecule.cm^{-3}/mV and the cross-section at the resonance of the OH Q(1.5e) line simulated at 0.6 mbar (see **3.3.5.1** for detail). The result is shown in Figure 4.14-b and compared to the OA-ICOS and WM-OA-ICOS approaches. The CE-FRS system exhibits random noise-dominated operation for averaging times up to 2000 s. At 20 s averaging time, the minimum detectable absorption coefficient is 1.5×10^{-7} cm^{-1} which is better than the OA-ICOS by a factor of ~9. The LoD, MDAC, and NEAS of the three approaches performed in this thesis are summarized in Table 4.4.

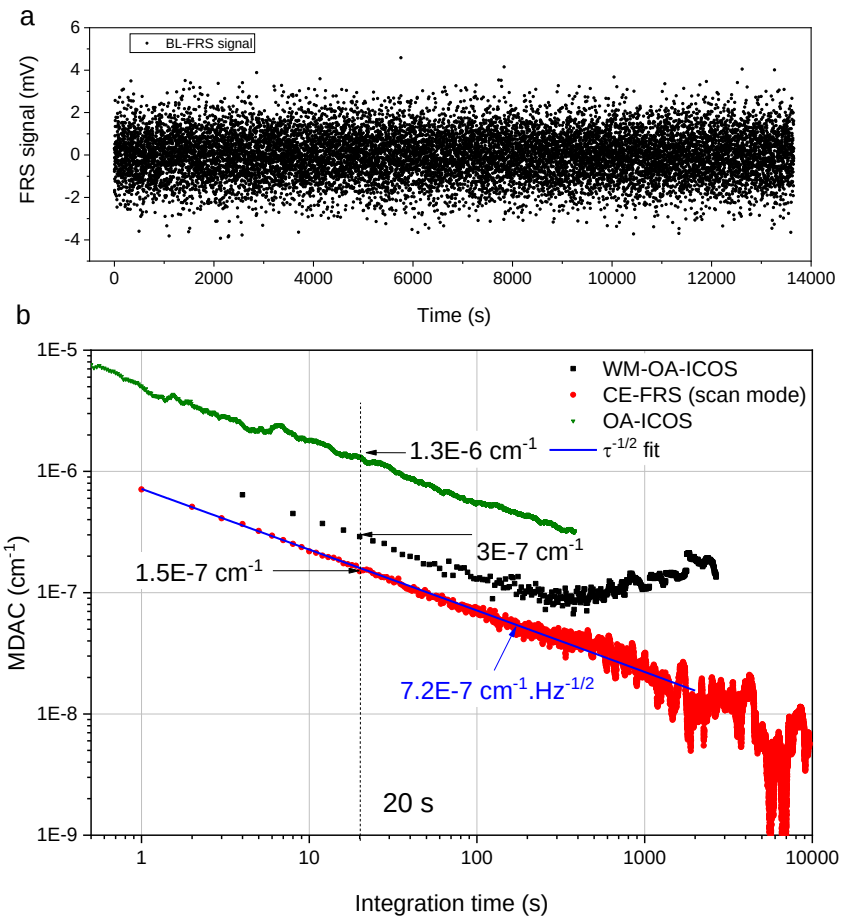

Figure 4.14 a – Time series of the FRS signal recorded with an interval time of 1 s. b – Allan deviation in terms of minimum detectable absorption coefficient (with units in cm^{-1}) in comparison with OA-ICOS and WM-OA-ICOS approaches. The vertical line shows the MDAC of the three approaches obtained with an integration time of 20 s.

Table 4.4 Comparison on LoD, MDAC and NEAS of the developed instruments for OH measurement in this work.

Technique	**LoD** ($OH.cm^{-3}$)	**MDAC** (cm^{-1})	**Integration time** (s)	**NEAS** ($cm^{-1}.H^{-1/2}$)
OA-ICOS	1.1×10^{11}	1.3×10^{-6}	20	5.4×10^{-6}
WM-OA-ICOS	2.5×10^{10}	3.0×10^{-7}	20	1.3×10^{-6}
CE-FRS (in fast laser scan mode)	10^{10}	1.5×10^{-7}	20	7.2×10^{-7}

In Table 4.5 the parameters characterizing the performances of some FRS systems from the literature are compared. All FRS setups were used to detect OH using the Q (1.5e) transition at 3568.52 cm^{-1}. The given LoD is normalized to its measurement bandwidth (inverse of

square root of integration time). Meanwhile, the value for L is the effective absorption length, estimated from the given data in the references.

Table 4.5 Performance comparison of several reported FRS systems operating at the same wavelength for OH detection.

References	FRS approach, magnetic field	L_{eff} (m)	Optical arrangement	B (Gauss)	Bandwidth-normalized LoD [OH.cm^{-3}].Hz$^{-1/2}$
This work	45^o method, DC	183	cavity	318	4.5×10^{10}
Zhao et al. [160]	90^o method, DC	0.46	signal pass	NA	6.2×10^{10}
Zhao et al. [51]	90^o method, AC	0.25	signal pass	177 rms	4.1×10^{9}
Wie et al. [55]	90^o method, DC	39	multi-pass	NA	3.0×10^{7}
Zhao et al. [54]	45^o method, DC	90	multi-pass	215	3.2×10^{6}

The values in Table 4.5 highlight an apparent improvement of the LoD with increasing L. The bandwidth-normalized LoD in the present work is less than that in the FRS enhanced multi-pass cell experiments (refs. [54] & [55]) a few orders of magnitude although we have longer path length. According to the analysis in section **4.2.5.3**, the SNR of the BD-FRS signal is proportional to the square root of the transmitted power through the cavity P_{out}, which is the optical power incident at the analyzer P2 in our case (see Figure 4.5). This result agreed well with the theoretical formula of the SNR of the FRS signal from ref. [135]:

$$SNR_{FRS} = \frac{\Delta n.L_{eff}.\sqrt{P_{inc}}}{\sqrt{2bd + c^2}} \tag{4.12}$$

where Δn is the difference of refractive indies of LHCP and RHCP wave; P_{inc} is the optical power incident at the analyzer; b is detector and system noise; c is related to the detector responsivity; and d is the proportionality coefficient specific for the particular laser source.

We believe that the main reason of less LoD in the cavity-enhanced FRS compared to the multi-pass experiments is due to the weak transmitted power through absorption cell. Therefore, we gave a calculation of P_{inc} for comparison with ref. [54] which used the same FRS approach (balanced detection within static B-field).

- In our setup, P_{inc}(cavity) = P_{out} can be calculated using Eq. (3.22). Consider T≈1-R =0.0014 and C_p=1 (perfect coupling), we have $P_{inc}(\text{cavity})\approx7\times10^{-4}*P_{in}$ (P_{in} is the optical power before entering the absorption cell).

- For the FRS enhanced multi-pass cell setup in ref. [54] using the same laser, $P_{inc}(multipass)=R_1^N*P_{in} \approx 0.112*P_{in}$ ($R_1=0.97$ is the reflectivity of the mirror in the multi-pass cell, N=72 is the number of passes)

We can see $P_{inc}(cavity)$ is less than $P_{inc}(multipass)$ two orders of magnitude. This reason made our bandwidth-normalized LoD is far away from the value obtained by FRS enhanced multi-pass cell. In addition, the use of non-identical detectors in the present work could not suppress fully the noises using balanced detection. That limited the SNR of the FRS signal according to Eq. (4.12).

Some remarks are also discussed below:

(1) The best bandwidth-normalized LoD in a range of 10^7-10^6 [OH.cm^{-3}].Hz$^{-1/2}$ [54,55] was achieved thanks to long path lengths using multi-pass arrangement. However, the multi-reflections require a larger mirror, consequently a bigger absorption cell is used. This made large dimension magnetic coils and high power consumption for generating the required field strength necessary. For example, the designed magnet coil in ref. [54] has an outer diameter of 0.55 m and it is 1.19 m long. The coil was sealed in a Dewar's vessel and cooled with a closed-cycle cryocooler below 5 K to generate a field strength of 215 Gauss (17.9 Gauss/A), compared to B = 318 Gauss (186.8 Gauss/A) in our system with much smaller coils. The mass of the whole magnetic system was about 700 kg which made the system untransportable. Moreover, the use of a large mirror can reduce the polarization (depolarization effect) due to the imperfect of the mirror surface, which decrease the SNR of the FRS signal [148].

(2) In our case, compared to OA-ICOS approach, the bandwidth-normalized LoD from the OA-ICOS enhanced FRS was improved by a factor of 9 by FRS. To our knowledge, there is no cavity-enhanced FRS system for OH detection as reference for comparison. *Wesberge and Wysoki* [154] reported a CRDS enhanced FRS system for detection of O_2 (cavity length = 0.5 m, Finesse = 47124, and 0.25 m in length of the coil), which provided an improvement in the bandwidth-normalized LoD by a factor of 4 in comparison with CRDS approach alone, using a similar balanced detection for FRS signal measurements, we might conclude that the FRS enhancement factor is in the range of ~ 10.

(3) Compared to our bandwidth-normalized LoD of 4.5×10^{10} [OH.cm^{-3}].Hz$^{-1/2}$, *Zhao et al.* [51] reported a LoD of 4.1×10^9 [OH.cm^{-3}].Hz$^{-1/2}$ achieved using a much shorter single path cell (L=0.25 m). In Ref. [154] using CRDS enhanced FRS for O_2 detection, an effective absorption path length (in the magnetic field) was enhanced to 3750 m. Although this path

length is about 550 times longer than that in a FRS enhanced 6.8-m multi-pass cell [138,161] operating at the same wavelength for detection of the same molecule, the bandwidth-normalized LoD for O_2 detection was only enhanced by a factor of ~6. *Gianella et al.* [150] reported an OF-CEAS enhanced FRS system for NO detection but it could not reach the shot-noise limited level as obtained using a short-pass FRS approach. They have highlighted the difficulties associated with the demodulation of the cavity output signal, which poses a challenge to achieve ultra-low sensitivity.

From the comparisons above, it can be seen that the use of cavity to increase the path length could not provide the expected LoD which is far away from the shot-noise limited detection as in signal-pass or multi-pass configurations [51,150,162]. So far there is no further study on the enhancement factor provided by cavities and multi-pass cells to FRS, nor the reason of higher LoD for cavity enhanced FRS. Detailed studies on the depolarization effects would be carried out in the future.

(4) Some studies showed that multi-pass based AC-FRS systems usually exhibited shot-noise limited performance. However, over longer acquisition times these systems are strongly affected by system drift effects, and allowed for averaging times only in a 10- to 30-s range [50,51]. In contrast, cavity based FRS system (using static BD-fields) was white noise dominated up to 10^3 s as shown in this work and another study [154], which allows a longer averaging time to lower LoD.

4.3 Application to OH reactivity measurement

The CE-FRS instrument was used for an OH reactivity study. In this study, the OH concentrations were monitored in real-time (see section **4.3.2**) [163] using the CE-FRS instrument. The decrease in the concentration of OH due to its reaction with the target chemical species can be experimentally determined which allows one to determine the reaction rate constant of OH with this target species.

The fast scan mode and measurement of the AC component of the differential signal yield a better sensitivity compared to the OA-ICOS and WM-OA-ICOS schemes. However, the scanning method with 20 s averaging time made real-time monitoring of OH concentrations challenging for study of OH reactivity. Thus it appeared to be simpler to fix the laser frequency to the peak of the FRS signal and merely track the signal magnitude as a function of time. However, the FRS detected in AC mode by the differential method cannot be used without laser scan. Wavelength modulation and demodulation using a lock-in amplifier was

therefore implemented. A fast observation of OH concentration during its reaction with other species can be achieved by measuring the WM-FRS signal from the lock-in amplifier. The next section will present an extension of the CE-FRS technique where wavelength modulation is included in the measurement approach (WM-CE-FRS).

4.3.1 OH decay rate measurements using a pulsed microwave discharge

Depending on the reaction rate constant, the concentrations of the molecules used, and other experimental conditions, the decay time can be on a time scale from hours to seconds or milliseconds [163,164]. In the case of the hour and minute time scale, measurements of concentration profile vs time can be easily observed. Due to its high reactivity and short lifetime, the measurement of OH decay rate is challenging. To perform the reaction rate constant measurement, it is crucial to produce OH with constant concentration in the reaction cell (in this work by microwave discharge of H_2O) and characterize the loss rate (due to wall losses) without any reactions with target species. With a continuous microwave discharge (CW-MW), OH can be easily generated and monitored by CE-FRS or even OA-ICOS or WM-ICOS if the concentration is high enough. However, this method cannot distinguish OH loss due to its reaction with some target species or due to other losses. Therefore, it is necessary to stop OH production and observe the OH decay without and with the presence of the target molecule. Unfortunately, the OH concentration quickly drops to zero after switching off the CW-MW power (less than 1 second). Determination of high time-resolution OH concentration profile in the order of millisecond timescale requires exact timing on generation and synchronized measurement of its concentration after the production switched off [35,43,55]. Therefore, a well-controlled pulsed generation of OH radical is crucial for OH decay rate measurements.

The experimental setup of the WM-CE-FRS instrument is shown in Figure 4.15. The instrument consists of two parts: the CE-FRS setup for real-time in-situ measurement of OH radicals and a pulsed microwave discharge device for pulsed generation of high concentrations of OH radicals.

The optical part was kept the same as described in **4.2.2,** while the electronics part was modified to perform WMS detection. The laser frequency was tuned by a point-by-point tuning method by applying a voltage signal from the analog output channel (AO0) of the NI-PCI 6251 card to the external modulation of the laser controller via an adding circuit. It allowed controlling the laser current to reach the target wavelength. For the WM detection, a

sinusoidal modulation with a frequency f_m of 17.5 kHz (modulation amplitude of 50 mVrms) from a lock-in amplifier was added to the laser current. The signals detected by two detectors were fed to a pre-amplifier to extract the differential signal (A-B) with a gain of 250 and filtered by a bandwidth filter between 10 kHz and 30 kHz. The AC component of the differential signal was then demodulated (second-harmonic, 2f detection) by the lock-in amplifier with a time constant of 200 μs to obtain the WM-FRS signal. The magnetic field strength was set at 318 Gauss.

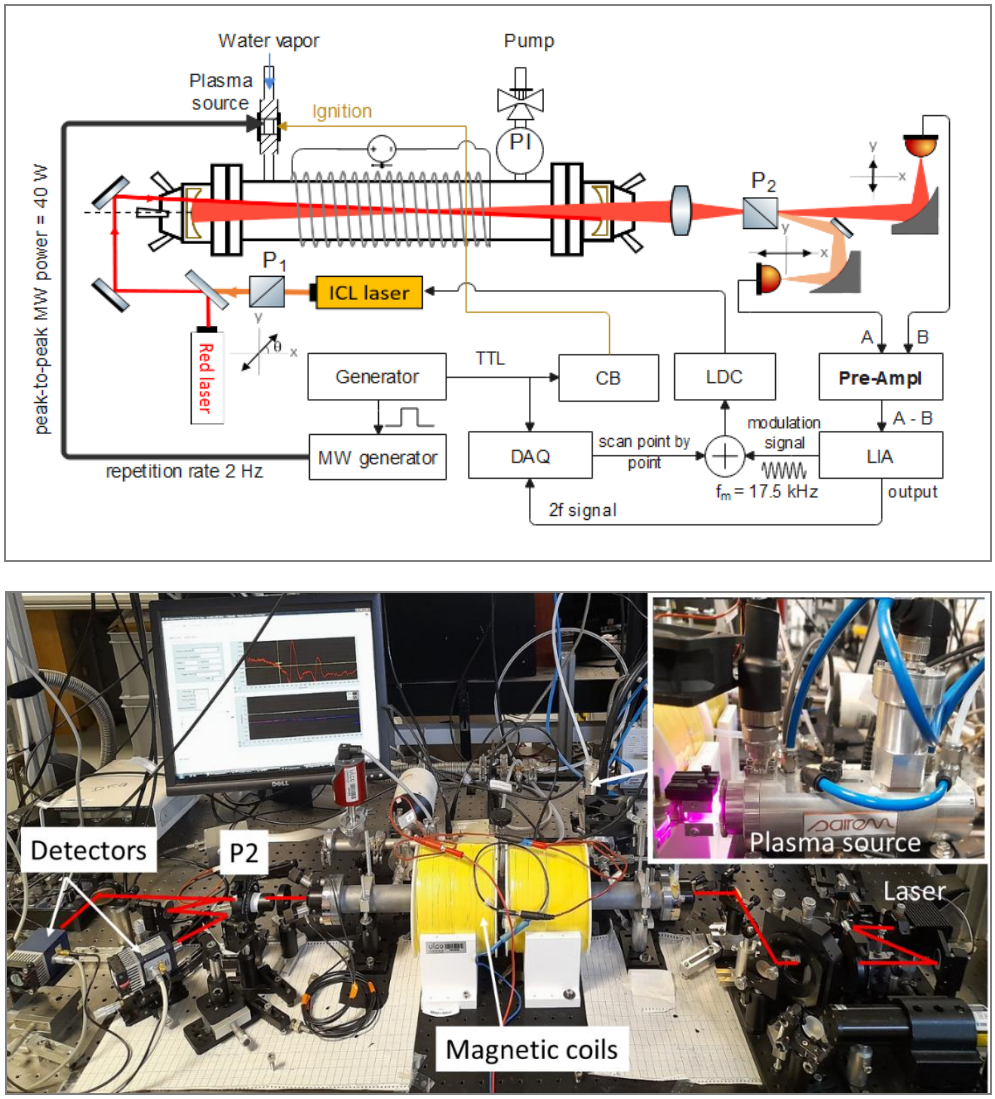

Figure 4.15 Upper – scheme of the WM-CE-FRS system. LIA: lock-in amplifier, CB: control box for the plasma source. Lower – photo of the setup. The inserted picture is the plasma source for producing OH radical.

To obtain a calibration curve of the 2f signal from the lock-in vs. OH concentration, a series of experiments was performed as in **4.2.5.4**. First, a whole 2f-WM-FRS spectrum was recoded to determine the peak amplitude at center frequency of the OH Q(1.5e) line. Then the OH

radical was determined based on OA-ICOS approach. Because these spectral measurements require more than 1 minute to complete, OH radicals for the calibration process were thus generated using continuous microwave power of 10–60 W at ~0.6 mbar. A point-by-point tuning of the laser current was applied to record the whole 2f-WM-FRS spectrum (consisting of 371 spectral data) for each MW power, as shown in Figure 4.16-left. In this case, the initial laser current was set by the LDC to about 152.45 mA (T_{laser}=27°C) near the center frequency of the OH Q(1.5e) line at 3568.52 cm^{-1}. By providing a voltage ramp in steps of 2 mV by the DAQ, the laser current was scanned from 150 mA to 157.5 mA with a resolution of 0.05 mA, resulting in a laser wavenumber tuning of ~0.4 cm^{-1} across two OH lines with a spectral resolution of 0.002 cm^{-1}. Each spectral point was an average of 2000 sample data acquired in 1 s acquisition time, yielding a full spectrum acquisition time of 371 s. Figure 4.16-right plots the OH concentration for each microwave power as a function of the peak amplitude of the OH Q(1.5e) signal. A linear response was found with a sensitivity of 2.54×10^{12} molecule.cm^{-3}/V. In practice, a full spectrum was recorded first with a continuous microwave discharge power to determine the laser current at the center frequency of the OH Q(1.5e) line. Then the laser was manually adjusted to the line center frequency for fast measuring the peak amplitude of the 2f-WM-FRS signal as a function of time with a pulsed microwave discharge.

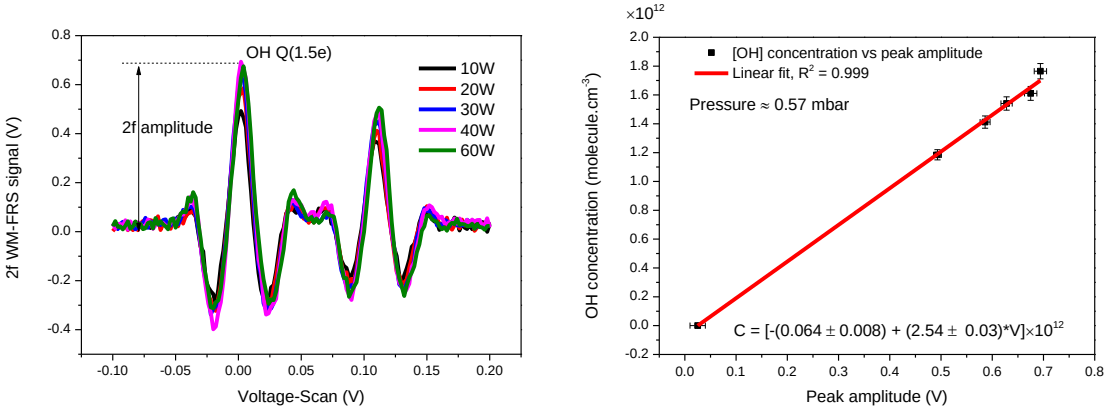

Figure 4.16 Left – second-harmonic WM-FRS spectra recorded at different MW powers at 0.6 mbar. Right – calibration of OH concentration determined by OA-ICOS as a function of peak amplitude of the OH Q(1.5e) line.

For a pulsed generation of OH radicals, a square waveform (Low level = 0 V, High level = 2 V) of frequency of 2 Hz from the output channel of a function generator was applied to the external modulation input of the microwave generator (GMS200W, Sairem) to provide a MW pulse (Low level = 0 W, High level = 40 W). The MW signal was sent to the plasma source

(S-wave, Sairem) via an N coaxial cable (see insert in Figure 4.15-lower). Meanwhile, the TTL signal (Low level = 0 V, High level = 5 V) from the synchronized channel of the function generator (in phase with the output square waveform) was sent to the S-wave control box to introduce a high voltage signal applied to the electrode for the discharge. Once the rising edge of the TTL was generated (the MW power is changed from 0 W to 40 W), a high voltage was activated immediately to ignite a plasma to generate OH radicals (see Figure 4.17-upper). An example of the timing scheme is depicted in Figure 4.17. OH radical was generated within 0.25 s during the High level of the square waveform and switched off 0.25 s later. OH concentration increased gradually and reached a constant during the haft period of 0.25 s. At the beginning of the second haft period, the MW was turned off, exhibiting a decay of OH concentration. The falling edge of the TTL signal was used to trigger the data acquisition of the DAQ card to record the decay signal within 250 ms at a sampling rate of 200 kS/s.

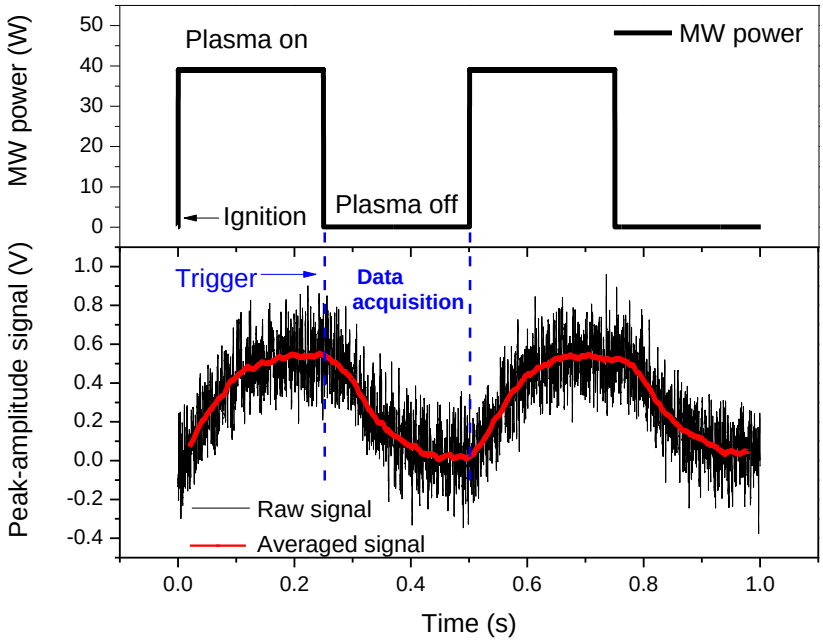

Figure 4.17 An example of the timing scheme of the data acquisition and pulsed generation of OH radicals. Upper – square waveform applied to the MW generator. Lower – experimental 2f peak amplitude signal of OH and its average (red trace). Data acquisition begins at the falling edge of the TTL and lasts for 0.25 s.

As shown in Figure 4.17-lower, the original data (black trace) were rather noisy, thus the data were “smoothed” (red trace) by adjacent averaging of 4000 datapoints. The FRS signal related to OH concentration variations could be easily observed. An exponential function was fitted to the OH decay to extract the decay time related to the OH reactivity.

4.3.2 Measurement of the reaction rate constant of OH with CH_4

In conjunction with the pulses MW discharge device, the performance of the WM-CE-FRS instrument was evaluated through a well-known reaction of OH with CH_4. The measurement of the reaction rate at room temperature was performed based on the pseudo-first-order method where the initial OH concentration $[OH]_0$ was lower than the methane concentration $[CH_4]$ by several orders of magnitude $[OH]_0 << [CH_4]$, such that the methane concentration can be considered constant during its reaction with OH. In the absence of complicated secondary reactions, the relaxation of $[OH]_t$ is then given by the expression [163]:

$$[OH]_t = [OH]_0 \exp[-(k_0 + k[CH_4])t] \tag{4.13}$$

where k is the reaction rate constant of OH with CH_4 to be determined; k_0 is the first-order rate constant in the absence of CH_4 due to the losses of OH on the reactor wall that depend on the experimental conditions. The time-resolved profile of [OH] was obtained by monitoring the peak-amplitude of the 2f-WM-FRS signal $S(t)_{2f}$, as a function of time:

$$S(t)_{2f} = S_0 e^{-(k_0 + k[CH_4])t} + a = S_0 e^{-t/\tau} + a \tag{4.14}$$

where $k_0 + k[CH_4] = k' = 1/\tau$ is the pseudo-first order rate constant related to the decay time obtained from an exponential fit to the measured $S(t)_{2f}$ signal and *a* is the offset of the $S(t)_{2f}$ signal from the lock-in output. The slope of the measured $k'–k_0$ versus CH_4 concentration (in molecule.cm^{-3}) is the reaction rate constant k.

In this work, the CH_4 concentrations were varied in a range of 10^{14}-10^{15} molecule.cm^{-3}, which was 2-3 orders of magnitude higher than the initial OH concentration (of ~1.4×10^{12} molecule.cm^{-3}) produced by the pulsed MW discharge. All the experiments were conducted under flow conditions at a pressure around 0.6 mbar.

4.3.2.1 CH_4 sample reparation

Different CH_4 concentrations were prepared by mixing pure CH_4 (>99.95 %, Airgas) and pure N_2 (99.995 %, Messer) from cylinders in a plastic sampling bag (Figure 4.18-right). The mixing ratio of CH_4 was calculated from the ratio of its volume injected into the bag and the total volume of N_2 and CH_4. Six sampling bags were prepared with CH_4 concentrations of 100, 80, 60, 40, 20, and 0%, respectively. The sampling bags (at 1 atm) were connected to the system via a precision valve, as shown in Figure 4.18-left.

4.3.2.2 Experimental procedure

The diagram for pulse production of OH radical and CH_4 injection is shown in Figure 4.18-left.

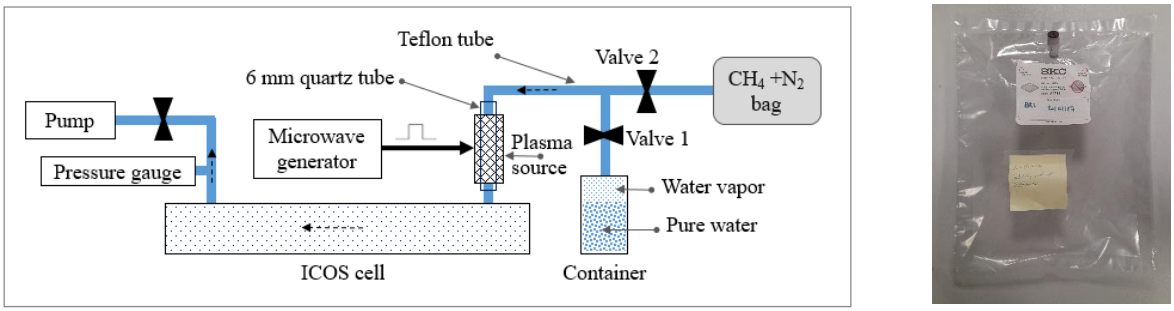

Figure 4.18 Left – schematic diagram of gas injection system used to measure the rate constant of OH in reaction with CH_4. Right – photo of 4-liters gas sampling bag containing a CH_4/N_2 mixture.

The measurement of the pseudo-first order rate constant k' for one CH_4 concentration sample was operated in the following way:

- Valves 1 and 2 were closed and the entire system was evacuated (the reactor ICOS cell and all the connecting components).
- Once the pressure was pumped down to 0.06 mbar, valve 1 was opened to inject H_2O vapor into the microwave cavity for OH production through MW discharge. Valve 1 was then continuously adjusted until the total pressure P_{H2O+OH} was stable at ~0.5 mbar.
- The mixture of CH_4 and N_2 was then added by adjusting valve 2 to increase the pressure up to a $P_{total} \approx 0.6$ mbar.
- When the total pressure was stable, the measurement of OH decay was carried out. Before the decay time measurement, the MW power was set at continuous mode to scan the laser over the full OH spectrum. Then the laser frequency was moved to the center frequency of the OH Q(1.5e) line to monitor the peak-amplitude signal $S(t)_{2f}$ during the full reaction of OH with CH_4. The MW power was then switched to pulse mode to turn on/off the OH production periodically, allowing measurement of the OH decay profile.
- The whole system was cleaned for 2 hours before repeating the measurement for a new CH_4 concentration.

The procedure was repeated for six different CH_4 concentrations. To calculate the concentration of methane, *n*, (in units of [molecule.cm^{-3}]) in the cell, its mixing ratio (C_{ppm})

in the mixture after injection was determined first, based on the initial concentration in the bag $C_{initial}$ [%], as well as the total pressure measurements before and after injecting into the system:

$$C_{ppm} = \frac{C_{initial}}{100} . \frac{P_{total} - P_{H_2O+OH}}{P_{total}} .10^6 \quad (4.15)$$

Then the absolute concentration of CH_4 (n) was obtained using equation (2.12) in **Chapter 2**, taking into account the total pressure P_{total} and room temperature T=293 K. Table 4.6 presents the calculated concentrations of CH_4 injected into the system for six measurements.

Table 4.6 Calculated CH_4 concentrations injected into the reaction cell.

Meas. No.	**[CH_4] in bag**	**Pressure in cell before CH_4 injection**	**Pressure in cell after CH_4 injection**	**Mixing ratio of CH_4 in cell**	**Absolute [CH_4] in cell**[9]
	$C_{initial}$ %	P_{H2O+OH} mbar	P_{total} mbar	C_{ppm} $\times 10^4$ ppmv	n molecule/cm^3
1	0	0.510	0.570	0	0
2	20	0.503	0.581	1.56	3.85E14
3	40	0.505	0.563	2.32	5.92E14
4	60	0.507	0.573	3.96	1.02E15
5	80	0.503	0.579	6.08	1.51E15
6	100	0.5	0.616	11.60	2.70E15

4.3.2.3 Results

The measurement of the reaction rate constant of OH with CH_4 was carried out at room temperature of 293 ± 3 K by measuring the time dependence of [OH] after the MW discharge was turned off. At each pulse microwave discharge event, the recording window spanned 250 ms to acquire 50000 data points and was triggered at the falling edge of the TTL signal for data acquisition. Twenty decays (with the repetition rate of 2 Hz) were averaged within 10 s to obtain a raw OH profile. The noise in the raw data was reduced by applying an average window written by Labview's code, in which each data point was an average of 4000 raw data points around it. The window was scanned across the raw data array with a step size of 400

[9] [CH_4] was determined based on the measurements of pressures according to Eq. (4.13), the uncertainty of CH_4 concentration is mainly dependent on the variations of P_{total} and P_{H2O+OH} measured (~ 0.005 mbar for each). Since the CH_4 injection caused a very small pressure change, $P_{total} - P_{H2O+OH} \approx 0.1$ mbar, the error of [CH_4] was estimated to be ~ 10%. This estimation ignored the drift of P_{H2O+OH} (due to the instability of H_2O injection via valve 1) which could not be monitored after CH_4 injection.

data points, resulting in a time resolution of 2 ms in the final OH profiles (shown in Figure 4.19-upper).

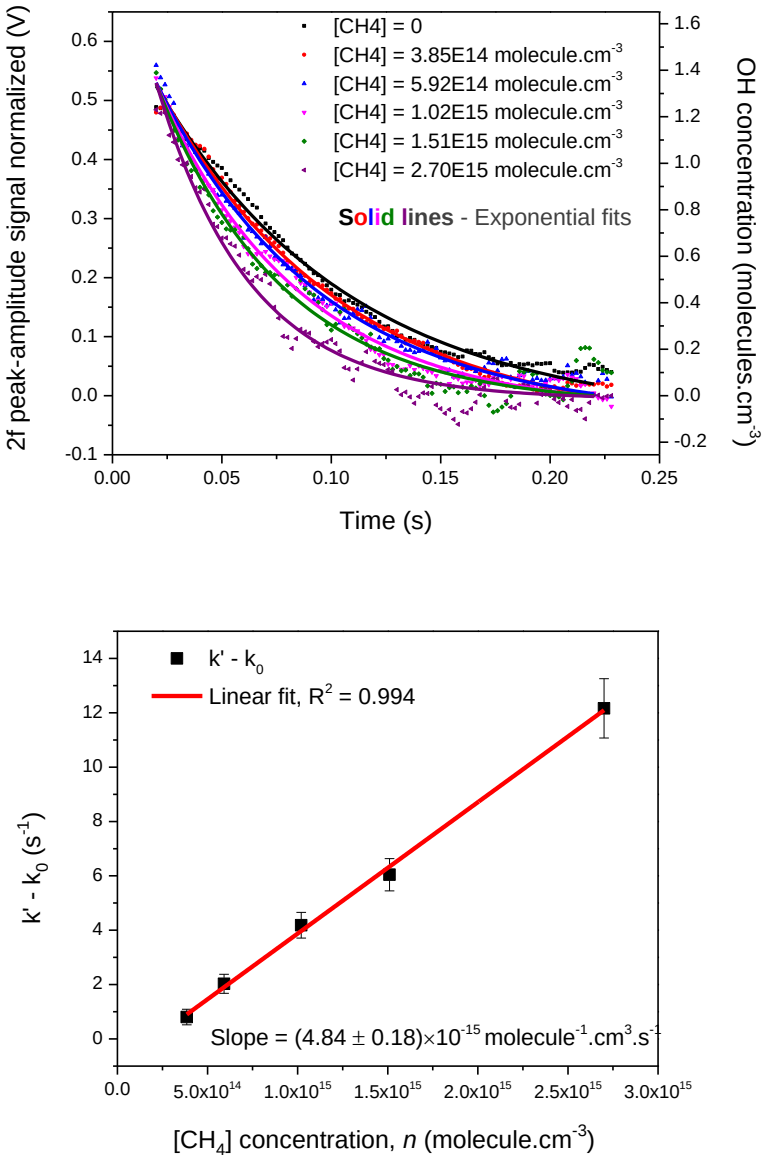

Figure 4.19 Upper – the measured OH decay signals with different CH_4 concentrations. The noise was reduced by applying an average window (size of 4000 data points, step 400 data points) to the raw signal consisting of 50000 data points. Lower – plot of pseudo-first order rate versus CH_4 concentrations. The laser frequency was fixed at the center of the OH line to real time monitor variation of OH concentration due to reaction with CH_4.

The decay time τ was extracted from a single exponential fit to the time dependence of the OH signal, yielding the pseudo-first order constant k' as a function of $[CH_4]$. Figure 4.19-lower shows $(k'-k_0)$ versus the methane number density, in which $k_0 = 1/\tau_0 = 11.2\ s^{-1}$ was determined at zero $[CH_4]$. The slope of the linear fit presents the reaction rate constant of OH

with methane. In this work, the measured rate constant was (4.84 ± 0.52)×10^{-15} $molecule^{-1}.cm^3.s^{-1}$ with an uncertainty of 10.7% resulting from the fitting error (3.7%) and the uncertainty of the calculated [CH_4] (~10%) due to the variation of the measured pressures P_{H2O+OH} and P_{total} (see the footnote of the last column in Table 4.6).

Compared to the reported value of (5.62 ± 0.43)×10^{-15} $molecule^{-1}.cm^3.s^{-1}$ [165], the difference is about 13.9 % between two k values. Possible error sources are discussed as follows. First, CH_4 concentration in our experience was determined based on the measurements of pressures that was manually adjusted without a pressure or mass flow controller. P_{H2O+OH} was only adjusted to a target pressure of 0.5 mbar via valve 1 once before the injection of CH_4 and then was considered stable. After injection of CH_4, the variation of the total pressure P_{total} was reduced by adjusting valve 2 manually with consideration that the continuous injection of H_2O via valve 1 was stable (without drift of P_{H2O+OH}). Thus we could not determine the variation of P_{total} during the decay time measurement, which was due to the unstable CH_4 or H_2O injection. The CH_4 concentration related to the difference pressure, P_{total} - P_{H2O+OH}, might differ to the expected value if there was any drift of P_{H2O+OH}. This potential drift, which could not be measured, contributed to the error of CH_4 concentration. Second, we considered that k was measured at room temperature. In fact, the temperature in the microwave cavity (6-mm quartz tube) where OH was generated, is significantly higher than room temperature. Thus the real temperature of the molecules injected into the reaction cell, by passing through the microwave cavity as well, may be different from the room temperature. The temperature (T) dependent k is expressed as [163]:

$$k(T) = 10^{-16.59\pm0.68} T^{1.83\pm0.17} \exp(-1396 \pm 134/T) \qquad (4.16)$$

According to Eq. (4.14), the variation of T can cause a large uncertainty in the determined k value. Since we could not measure the real temperature of the gas at the outlet of the MW cavity, the influence of T on the uncertainty of k was not included in data evaluation. However, we can consider an example to illustrate the dependence of k on T. In this setup, a 5-cm quartz tube was connected to the optical cavity outside the microwave cavity. It was equipped with a heatsink and a fan for air cooling. The temperature of the gas passing through this part may be lower, compared to the temperature in the microwave cavity. The temperature of the cavity body (outside) was measured by a thermistor sensor with no difference compared to the room temperature (293 K). Thus considering an uncertainty of ΔT = 3 K @ 293 K for the temperature of the gases inside the optical cavity, the relative error of the k value due to the variation of T is estimated to be about 6.8 % using Eq. (4.14). If this

uncertainty is included together with the fit error (3.7 %) and the uncertainty of [CH_4] (10 %), the total uncertainty in k is about 12.6 % which is almost comparable with the difference of 13.9 % between the k values obtained in the present work and from the reference.

4.4 Chapter conclusion

This chapter reported the development of a CE-FRS instrument for OH radical detection. The FRS signal under a static magnetic field was introduced by performing differential detection (BD) scheme. It showed potential in removing the absorption of non-paramagnetic species and suppressing the etalon noise appeared in the signal from each single detector, which allowed significant improvement in the selectivity and detection limit of the instrument. The instrument could be operated in two ways. (A) In the first approach, using a fast scan laser and measuring the differential signal in AC mode provided a LoD of 10^{10} molecule.cm^3 within 20 s averaging time. The corresponding minimum detectable absorption coefficient was 1.5×10^{-7} cm^{-1} which was ~ 9 times better than the OA-ICOS approach. The SNR of the BD-FRS can be further improved by enhancing the cavity transmitted power. (B) wavelength modulation was applied to the differential signal and demodulation was performed using a lock-in amplifier to extract the second harmonic signal. By fixing the laser frequency at the center frequency of the OH absorption line and monitoring the peak-amplitude signal as a function of time, fast measurements of OH were achieved on a milliseconds timescale, allowing real time monitoring of OH time profiles during chemical reactions. Combined with a pulsed microwave discharge device, the WM-BD-FRS was applied successfully to measure the reaction rate constant of OH with CH_4. In order to improve the setup's stability, the laser frequency could be locked to the center of the OH transition.

Chapter 5 Spectral investigation of the ν_2 band of *cis*-HONO near ~ 1660 cm^{-1} using long-path quantum cascade laser (QCL) absorption spectroscopy

This chapter presents the development and evaluation of a quantum cascade laser (QCL) based direct absorption spectrometer to study line parameters of the ν_2 band of *cis*-HONO. The high-resolution quantum cascade laser absorption spectrum of the ν_2 band of *cis*-HONO has been recorded and analyzed, for the first time, in the mid-infrared region of 1659.2–1662.2 cm^{-1} (N=O stretch, *R*-branch). Positions and effective line intensities were determined for about 60 new lines. The absolute absorption frequencies were directly measured during the spectral scan using a wavelength meter with an accuracy of ~0.0017 cm^{-1}. The corresponding simulation spectrum was calculated using the PGOPHER code. The calculated line positions are in a good agreement with the experimentally measured frequencies within the wavelength meter uncertainty. Effective line intensities were determined, with uncertainties of about 17%, by scaling the measured HONO absorption intensities to the previously reported line intensity of a *cis*-HONO line located in the same spectral region near 1659.85 cm^{-1}.

5.1 Introduction

5.1.1 Motivation for studying the spectral features of HONO

Though present in low quantities, typically up to a few parts per billion by volume (ppbv), nitrous acid (HONO) is a key species that plays a central role in tropospheric photochemistry. Several studies have demonstrated that the photolysis of nitrous acid (Eq (5.1)) in the early morning is a significant or even a primary source of hydroxyl (OH) radicals that are known as an atmospheric "cleaner" to remove pollutant trace gases from the atmosphere (CH_4, CO, NO_2, SO_2, …) in urban and rural environments [17–19,166].

$$HONO \xrightarrow{h\nu} OH + NO \quad (300nm < \lambda < 405nm) \tag{5.1}$$

However, the sources and processes leading to the formation of HONO are still not satisfactorily characterized due to the lack of in-situ measurements. There is strong evidence that HONO is mainly formed during the night in the polluted atmosphere via heterogeneous reactions on surfaces, involving NOx, soot, and water vapor [167,168]. For example, the

presently heterogeneous reaction of NO_2 with water on terrestrial surfaces is suspected to be a main HONO source [19]:

$$NO + NO_2 + H_2O \overset{surface}{\rightleftarrows} 2HONO \tag{5.2}$$

$$2NO_2 + H_2O \overset{surface}{\rightleftarrows} HONO + HNO_3 \tag{5.3}$$

Reliable and real-time assessment of HONO concentration changes in the atmosphere is thus crucial to understand its related chemical process, improve air pollution models, and predict environmental changes. Due to its environmental importance, several analytical techniques have been developed for HONO monitoring. These measurement techniques can be classified into two categories: (1) indirect analysis of HONO in the aqueous phase after chemical conversion using wet chemical methods [169]; and (2) direct analysis of HONO in the gas phase using spectroscopic techniques [170].

Table 5.1 Various absorption spectroscopic techniques operating in the ultra-violet (UV) and infrared (IR) regions reported for HONO measurements.

Techniques	**Detection limit[10] and integration time**	**Uncertainty**	**Comments/remarks**	**Ref.**
UV-DOAS	~200 pptv[11] (137 s)	6 %	Measurement of integrated concentration over open optical path length; potential spectral interference.	[171]
UV-IBBCEAS	~40 pptv (1 min)	8.7 %	Measurement of local concentration at atmospheric pressure using cavity; potential spectral interference.	[172], [173]
UV-CRDS	5 ppbv[12] (15 s)	< 10 %	Measurement of local concentration	[174]
IR-TLAS	< 300 pptv (1 s)	10 %	Measurements of local concentration using multi-pass cell at reduced pressure, reduction of spectral interference	[175], [176]
IR-QEPAS	7 ppbv (150 s)		Measurement performed in an ultra-small gas-sample volume, suitable for short-lived species sensing.	[177]

Self-calibrating spectroscopic methods allow the direct measurement of HONO concentrations in the gas phase without the needs for chemical convention. Various techniques based on absorption spectroscopy (described in Table 5.1) have been developed for monitoring HONO concentrations with pptv-level detection limits, such as differential optical absorption spectroscopy (DOAS) [13,171,178], incoherent broadband cavity-enhanced

[10] 1σ detection limit (signal-to-noise ratio = 1)
[11] pptv: parts per trillion by volume
[12] ppbv: parts per billion by volume

absorption spectroscopy (IBBCEAS) [172,179,180], and cavity ring-down spectroscopy (CRDS) [174]. Those spectroscopic instruments exploited the HONO absorptions in the UV range from 300 to 390 nm, influenced by many interfering trace species, thus requiring the identification and correction of the HONO spectrum. In contrast, tunable laser-based measurements of HONO, i.e. tunable laser absorption spectroscopy (TLAS) [175,181] and quartz-enhanced photoacoustic spectroscopy (QEPAS) [177], are performed in the mid-infrared spectral region where this molecule exhibits stronger and narrow absorptions resulting from the fundamental rovibrational transitions, providing higher selectivity for HONO detection. The accuracy of such measurements based on Beer-Lambert law depends strongly on spectroscopic parameters of HONO (line position, line intensity or cross-section) used for quantification and that are needed to be accurately determined.

5.1.2 State of art in HONO spectra investigation in the infrared

The infrared region provides strong rovibrational transitions suitable for optical sensing. The first spectral analysis of HONO in the 1.4 μm region was reported in 1943 [182]. The observation of a double band of HONO in a single path absorption cell, corresponding to the 1st overtone of the O-H stretching vibration ($2\nu_1$), confirmed the existence of two isomers in gas phase. Then, the broad-band spectra of all fundamental vibrational frequencies of both *trans*- and *cis*-HONO were identified from 2 to 14 μm using IR dispersive spectrometers, providing the rotational structures of two isomers despite some disagreements that existed in the assignments [183,184]. However, these studies did not yet report absorption line intensities. In the 1980s and early 1990s, the infrared absorption spectra of the fundamental of *trans*-HONO (ν_1, ν_2, ν_3, and ν_4) and *cis*-HONO (ν_1, ν_2, and ν_4) were measured and analyzed by Fourier transform spectroscopy with an improved spectral resolution of about 0.003 cm^{-1}, yielding an improved set of the corresponding rovibrational parameters [185–189]. Nevertheless, only the band strengths were reported [190,191] instead of the line-by-line intensities, which would be helpful for identification and quantification of the presence of HONO in the atmosphere. Recently, a few studies in the mid-infrared region have been performed based on tunable laser absorption spectroscopy (TLAS) involving quantum cascade laser (QCL) combined with a multi-pass cell, providing high spectral resolution. For instance, Lee et al. [192] reported *trans*- and *cis*-HONO spectra with a resolution of 0.001 cm^{-1} at around 1275 cm^{-1} and 1660 cm^{-1}, respectively, using a dual continuous-wave quantum cascade laser coupled to a 210-m multi-pass absorption cell. The effective line

intensities, along with line positions, were provided to quantify the concentration of HONO [176]. Cui et al. [193] determined the line intensities of the ν_3 band of *trans*-HONO over ~5 cm^{-1} near 1255 cm^{-1} using an external cavity QCL. The absorption spectra were measured in a multi-pass cell with an effective optical path of 152 m. Although serval studies have been reported [194–196], line parameters of the most intense bands in the mid-infrared, such as the ν_2 band of HONO, are not yet available in the common databases like HITRAN [59] or GEISA [60].

5.2 Development of a QCL-based long-path absorption spectrometer in the mid-IR at 6 μm

5.2.1 QCL source

A single-mode continuous-wave distributed feedback quantum cascade laser – DFB-QCL (HHL-795 Alpes Lasers, Inc.) emitting at 6.0 μm was employed to probe HONO absorptions. The laser was driven with a current driver (PLD5K-CH, Wavelength Electronics) and a temperature driver (PCK-5CH, Wavelength Electronics), providing a laser output power of up to 35 mW. The laser frequency was controlled via an interface program. Two voltage signals from the analog output channels, AO1 and AO2, of a National Instrument data acquisition card (NI USB-6361), were applied to the external modulation inputs of the temperature driver and the current driver (15 mA/V), respectively. A frequency tuning range of ~3 cm^{-1} was realized through current scanning (0.0134 cm^{-1}/mA) and temperature tuning (0.122 cm^{-1}/ºC) to cover the infrared range of 1659.2-1662.2 cm^{-1} for *cis*-HONO detection.

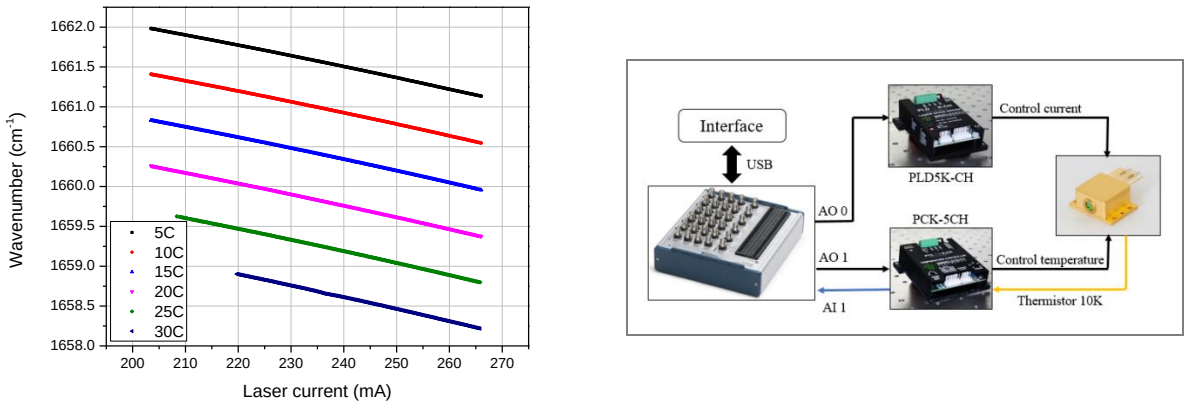

Figure 5.1 Left – mode-hop free tuning of the DFB-QCL to the injection currents and temperatures. Right – schematic diagram of laser controller system.

5.2.2 Optical setup

A QCL-based direct absorption spectrometer (QCL-DAS) associated with a high-resolution wavelength meter has been developed for simultaneous measurements of HONO absorption spectra and the corresponding laser frequencies. Figure 5.2 shows the scheme and the photo of the experimental setup used in the present work.

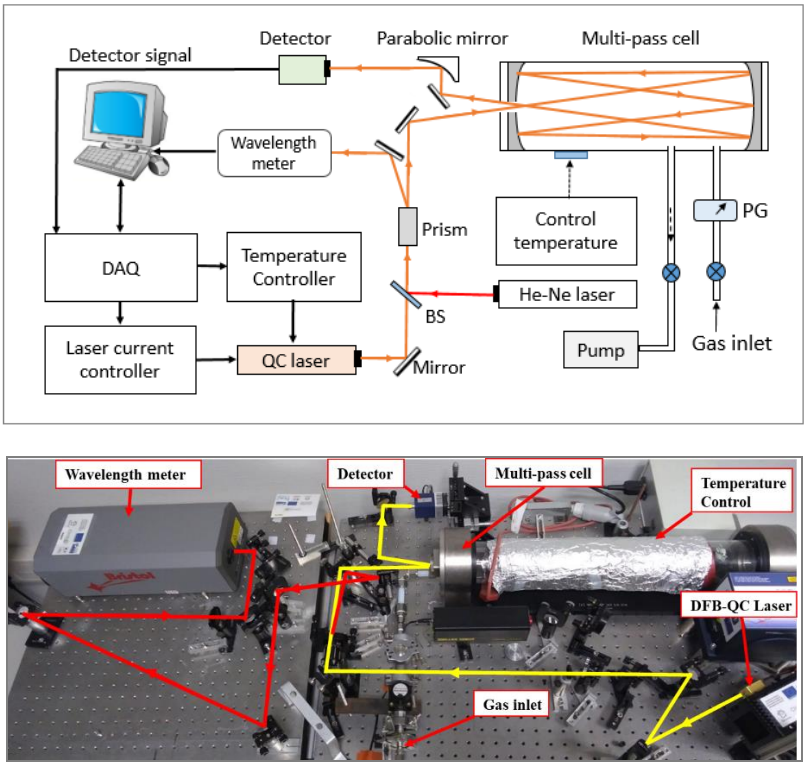

Figure 5.2 Upper – scheme of the QCL-DAS used in the present work. DAQ: data acquisition card, BS: beam splitter, Prism: Rochon prism, PG: pressure gauge. Lower – photo of the complete setup.

The DFB-QCL was placed on a high-power laser mount (model 262-02-06-DB9, Arroyo). The emitted QCL beam was co-aligned with a red He-Ne laser beam via a CaF_2 beam splitter for all optical alignment. The co-aligned laser beams were then split into two beams (50%-50%) with a Rochon prism (RPM10, Thorlabs). The ordinary beam (remaining on the same optical axis as the input beam) was injected into a multi-pass cell (Model 5612 New Focus, Inc.) with a volume of 3.2 L and an effective optical path of 102.9±8.2 m. The emerging laser beam from the multi-pass cell was focused onto a VIGO detector (PVI-4TE-10.6-0.5×0.5) using a 90° off-axis gold parabolic mirror (50 mm focal length) to record the HONO absorption signal. The extraordinary beam deviated by an angle of about 1.5° and was steered to a wavelength meter (671B, Bristol Instrument) for direct measurement of the QCL

frequency with an absolute accuracy of 0.0017 cm^{-1} and a repeatability of 0.0002 cm^{-1}. A Labview program was applied, via the DAQ card, to control the scan of the QCL frequency via current and temperature tuning, to record the absorption spectra, and to real-time read data from the wavelength meter. To control the temperature of the HONO sample and to avoid photolysis of HONO, the multi-pass cell was covered with a heatable mat, which was maintained at 303 K.

5.2.3 Metrology of laser frequency tuning and determination of the line center frequencies

The line positions were determined directly with the wavelength meter. The laser temperature was set at different values for different spectral coverage. For each temperature set point, the injection current of the laser was ramped from 200 to 220 mA to tune the frequency over 0.3 cm^{-1} with a resolution of 0.0001 cm^{-1}, providing 3000 data points for each spectrum scanned. This resolution is suitable for our experimental measurements involving a Doppler-broadened line width of ~0.003 cm^{-1} at 303 K. The laser frequencies were simultaneously recorded together with the absorption signal acquisition. Due to the fast variation of HONO concentrations during the acquisition, discussed in detail in **5.3.3**, the laser frequency scan should be as fast as possible to make a measurement at a quasi-constant, while the sample rate for the wavelength meter is limited at 0.4 s/sample. In order to ensure an acceptable uncertainty in the determined line intensities with a frequency scan as fast as possible, frequency scan at a rate of 0.094 cm^{-1} per minute was performed for the acquisition of HONO absorption signal, while the laser frequency was recorded through interleaved sampling with a ration of 1:20. The measured laser frequency data were then interpolated with a third-order polynomial function (the laser wavenumber vs. the laser current can be described by a third-order polynomial function – see Figure 5.1-left) by a to extract a high-resolution calibration curve of laser frequencies versus the scanning voltage. This approach allows converting time-domain scanned absorption data to a frequency domain spectrum. The line center positions were determined from Voigt profile fits to the experimental absorption lines.

Figure 5.3-a illustrated an ambient water absorption line (located at 1660.4676 cm^{-1}) recorded at 9.2 mbar and at a sample rate of 100 kHz using “point-by-point” frequency tuning. The laser temperature was set at 17 ^{0}C. The absorption spectrum was recorded by scanning the laser current via increasing the voltage applied to the current driver from 1.0 to 2.5 V with a

step of 0.5 mV (corresponding to 0.0001 cm^{-1} in frequency tuning). In order to increase the signal-to-noise ratio (SNR), each data point of the spectral signal (black dot) was averaged 4000 times.

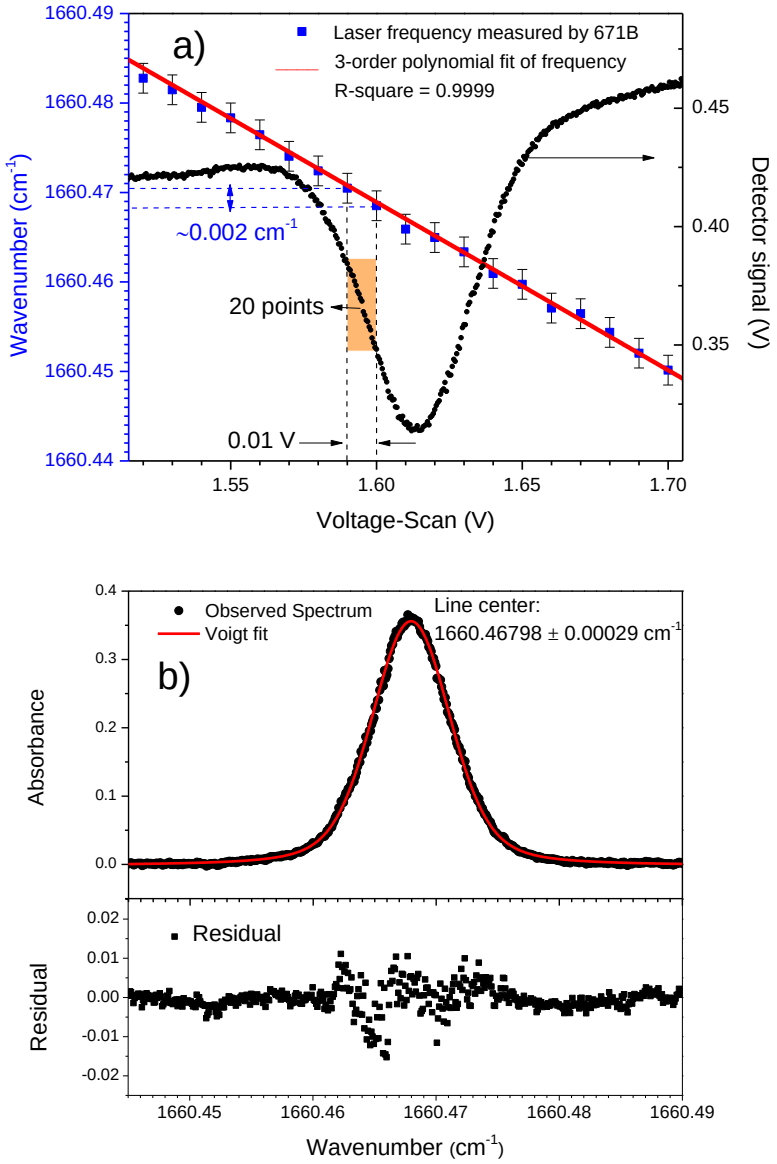

Figure 5.3 Example of the laser frequency measurement: (a) Absorption signal of ambient H_2O vapor at 9.2 mbar and 303 K versus the voltage applied for tuning the laser current (and thus laser frequency) in point-by-point mode with a time interval of 64 ms between two spectral absorption data. The blue dots and the red line were the frequencies directly measured from 671B wavelength meter every 0.002 cm^{-1} (every 10 mV of the scanned voltage) and its polynomial fit, respectively. (b) Upper – absorbance spectrum (black dots) and Voigt fit (red line); Lower – fit residual (experiment-fit).

In order to investigate the measurement accuracy of the wavelength meter as well as the online measurement performance used in the present work, eight lines of water vapor in the

range of 1658.0 to 1663.0 cm^{-1} were measured under the same experimental conditions as for the HONO spectrum measurement (shown in Figure 5.4). The frequencies ν_0^{work} of the measured water absorption lines were determined from Voigt fits to the experimental spectrum. The measured ν_0^{work} were then compared to the corresponding line positions ν_0^{HITRAN} provided by the HITRAN 2016 database [59]. The results are listed in Table 5.2.

As can be seen, the measured and the referenced line positions are in good agreement and the difference $\Delta\nu = \nu_0^{HITRAN} - \nu_0^{work}$ was about 0.0017 cm^{-1} within the wavelength meter uncertainty of 0.0017 cm^{-1} (1 ppm). The measurement uncertainty in frequency in the present work was thus considered to be limited by the fit error (thus the SNR of the spectral lines) and the wavelength meter uncertainty.

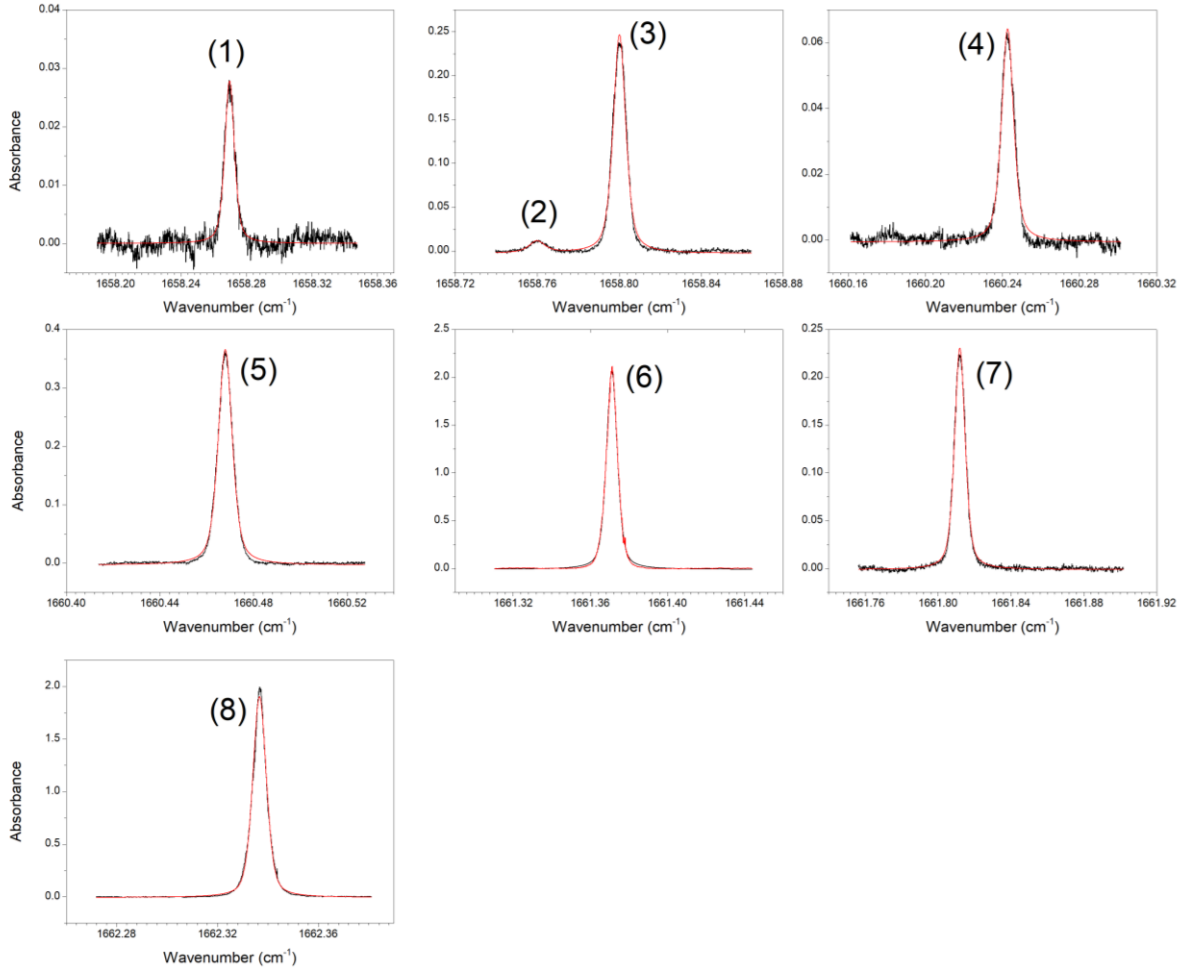

Figure 5.4 Evaluation of the laser frequency tuning method by measuring the line centers of eight water vapor lines in the range from 1658.0 to 1663.0 cm^{-1} under the same experimental conditions as for HONO measurements.

Table 5.2 Measured line positions of water vapor, including three isotopes $H_2{}^{16}O$ (1), $H_2{}^{17}O$ (3) and $H_2{}^{18}O$ (2), in our work in comparison with the data from the HITRAN2016 database [59].

Line		Line intensity $cm^{-1}/(molec.cm^{-2})$	Line Position (cm^{-1})	Uncertainty (cm^{-1})	Difference (cm^{-1})
No.	$J'_{K_a',K_c'} \leftarrow J''_{K_a'',K_c''}$ (isotopologue #)	S	ν_0^{work}	$\Delta\nu_0^{work}$	$\Delta\nu = \nu_0^{HITRAN} - \nu_0^{work}$
1	$6_{2,4} \leftarrow 5_{3,3}$ (1)	3.81E-24	1658.2697	0.0017	0.0017
2	$6_{3,4} \leftarrow 5_{4,1}$ (3)	1.44E-24	1658.7603	0.0018	0.0002
3	$2_{2,1} \leftarrow 2_{1,2}$ (2)	3.21E-23	1658.8002	0.0017	0.0000
4	$7_{3,4} \leftarrow 7_{2,5}$ (1)	1.29E-23	1660.2428	0.0017	0.0016
5	$4_{2,3} \leftarrow 4_{1,4}$ (1)	6.23E-23	1660.4680	0.0017	-0.0003
6	$6_{3,4} \leftarrow 5_{4,2}$ (1)	3.85E-21	1661.3713	0.0017	-0.0002
7	$6_{2,4} \leftarrow 6_{1,5}$ (2)	2.87E-23	1661.8120	0.0017	0.0006
8	$3_{1,3} \leftarrow 2_{0,2}$ (1)	2.06E-22	1662.3367	0.0017	-0.0014

5.2.4 Method for determining the effective line intensity

According to the equation (2.13), the effective line intensity *S* can be determined based on the integrated area from the spectral fitting:

$$S = \frac{A_I}{C_{ppm}.L.N(T,P)} \times 10^6 \tag{5.4}$$

To determine absolute line intensity with high accuracy, the concentration of the target molecule inside the cell generally needs to be known and kept constant during the whole spectrum measurement. Since HONO is an unstable short-lived species, its concentration in the cell declines during a measurement. In the current study, instead of the direct measurements of the concentration of HONO in cell, intensities of new lines were determined, as described in [193,196], by scaling the measured spectral absorption intensities to the previously reported line intensity of $S_{ref} = 6.92\times10^{-21}$ $cm^{-1}/(molecule.cm^{-2})$ of a *cis*-HONO near 1659.85 cm^{-1} [197]. A spectrum of *cis*-HONO containing of the reference line is shown in Figure 5.5. Because the line intensity is proportional to the fitted area, the new line intensity can be determined as:

$$S_{newline} = S_{ref} \cdot \frac{A_{newline}}{A_{ref}} \tag{5.5}$$

with $A_{newline}$ and A_{ref} being the areas under the new line and the reference line to be calculated, respectively.

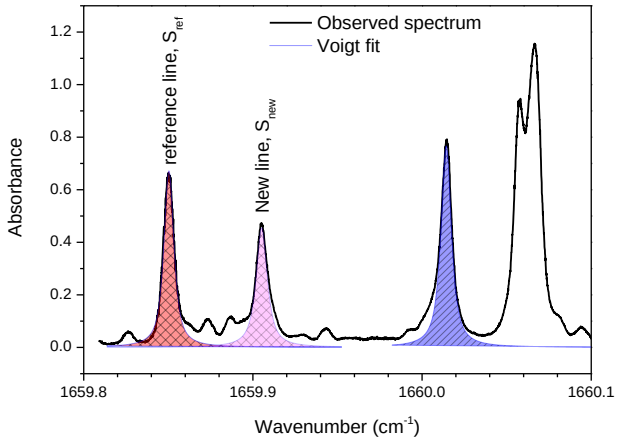

Figure 5.5 HONO spectrum consists of the reference line with the known line intensity used to scale the measured spectral absorption intensities.

In order to minimize the impacts of variation of HONO concentration during the spectral scan, the full spectral region of about 3 cm^{-1} studied in the present work was divided into 12 segments and laser frequency scans for each segment covered about 0.3 cm^{-1}. The HONO sample was renewed for each segment measurement. In addition, as the concentration of HONO injected into the absorption cell for each measurement was difficult to keep the same resulting from each production process, in order to ensure the accuracy of the determined line intensities in different segments, the next scan was performed such that the newly recorded spectrum overlapped with the previous one including at least one absorption line. The previously determined intensity of this line was used for its absorption intensity obtained in the new segment, and used to scale all other lines in the new segment despite the different concentrations in those two measurement segments.

Figure 5.6 shows the decline of the normalized HONO concentration in the 3.2-liters multi-pass cell used in this work. The decay time was determined to be 17.6 ± 0.9 minutes. Based on the decay curve, the variation of HONO concentration was estimated to be around 16 % during 3 minutes for measuring the spectrum in one segment of ~ 0.3 cm^{-1}. This issue makes the largest contribution to the uncertainty in the line intensity determination.

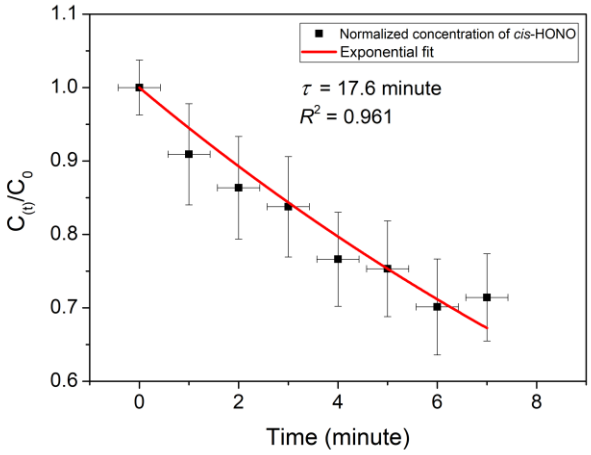

Figure 5.6 Plot of HONO concentration versus time in a closed absorption cell.

5.3 Measurement of line positions and line intensities of the ν_2 band of cis-HONO at 6 μm

5.3.1 HONO sample generation

Gaseous HONO can be generally produced in the laboratory via three methods [170], as summarized in Table 5.3.

Table 5.3 Basic methods producing HONO in laboratory

Method	Chemical reaction	Advantages	Remarks	Ref.
Gas-solid reaction	$HCl(g) + NaNO_2(s) \rightarrow HONO + NaCl$	high purity of HONO	requiring stable high humidity of HCl flow	[176,191,198,199]
Gas-phase reaction	$NO_2 + NO + H_2O \leftrightarrow 2HONO$	nearly pure HONO	significant interference from NO_2, HNO_3, and H_2O	[190,200]
Liquid-phase reaction	$NaNO_2 + H_2SO_4 \rightarrow NaHSO_4 + HONO$	easy to control the production condition	potential interference from NO_2, HNO_3, and H_2O (see reactions R2-R3)	[175,196]

In the present work, the liquid-phase reaction has been chosen since it is easy to control the production condition in the laboratory and high concentrations of HONO can be produced (from a few ppmv to several hundred ppmv). Figure 5.7 shows the experimental arrangement to produce HONO. A dilute solution of 30% H_2SO_4 contained in a dropping funnel was gradually added to a 1% $NaNO_2$ solution in a 3-neck flask placed into an ice-water mixture to reduce the temperature at the liquid surface. The nitrogen was injected into the flask to flush

the generated gases to the spectrometer for recording the absorption spectra. All experiments were carried out in the dark to avoid photolysis. The chemical reaction involved is described in equation R1 [175,196], which can generate by-products such as NO, NO_2, H_2O, and HNO_3 through reactions (R2-R3). These by-products (except for H_2O vapor) do not absorb strongly absorption in the spectral region near 6 µm, and therefore do not affect the HONO measurements. Four water vapor absorption lines appear in this spectral region (at 1660.2443, 1660.4676, 1661.3410, and 1661.8125 cm^{-1}), and they can be easily identified in the recorded HONO spectra.

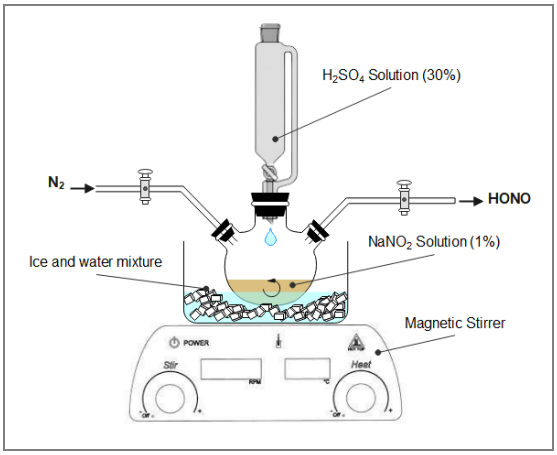

$$NaNO_2 + H_2SO_4 \rightarrow NaHSO_4 + HONO \quad (R1)$$

$$2HONO \leftrightarrow NO + NO_2 + H_2O \quad (R2)$$

$$HONO + NO_2 \rightarrow NO + HNO_3 \quad (R3)$$

Figure 5.7 HONO generation by liquid-phase reaction of $NaNO_2$ solution (1%) with H_2SO_4 solution (30%).

5.3.2 Protocol for measurement of direct absorption spectra of the ν_2 band of cis-HONO

The studied *cis*-HONO spectrum was recorded by direct QCL absorption spectroscopy over 3 cm^{-1} from 1659.2 to 1662.2 cm^{-1} by scanning the laser current at twelve different laser temperatures (25 °C, 22.5 °C, 19.4 °C, 17.3 °C, 15.6 °C, 13.8 °C, 12.0 °C, 9.2 °C, 7.7 °C, 6.0 °C, 5.0 °C, and 4.1 °C, respectively). Before each measurement, the multi-pass cell was cleaned by pumping it down to 0.1 mbar. The cell was then filled with pure nitrogen (N_2) or HONO to 9.2 mbar to record the baseline and the absorption signal, respectively. Figure 5.8 presents a distinct measurement segment at a laser temperature of 15.6 °C. The solid and dashed lines represent the raw HONO absorption signal I(ν) and the polynomial fit of the baseline $I_0(\nu)$ as a function of the voltage scan. The blue dots are the laser wavenumber recorded simultaneously during the scanning process, which allows converting the spectrum in the time domain to the frequency domain, as described in **5.2.3.**

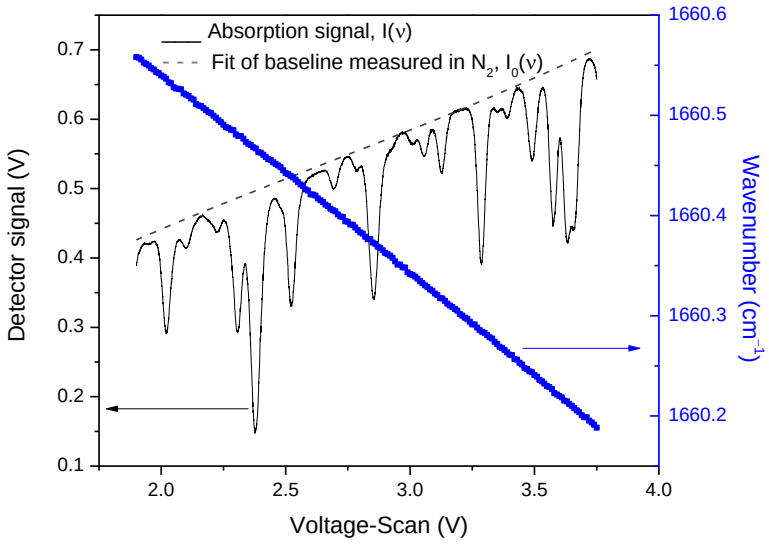

Figure 5.8 A segment of ~ 0.35 cm^{-1} including an experimentally *cis*-HONO raw spectrum (solid) and the polynomial fit (dash) of its baseline in nitrogen, measured at 9.2 mbar and 303 K. The blue dots represent the frequencies directly measured from the wavelength meter.

5.3.3 Spectral processing and determination of effective line intensities of cis-HONO

The absorbance spectrum was calculated from I(ν) and $I_0(\nu)$ according to equation (2.9). The HONO spectrum was recorded at a pressure of P = 9.2 ± 0.1 mbar, where both Doppler- and collisional broadening determine the line width of the absorption features. Voigt profiles were fitted to the lines using "Fityk" software [62], providing the line centers and their integrated areas for the line intensity calculations. The upper panel in Figure 5.9 displays the HONO spectrum (black) after data processing; also shown is the corresponding Voigt fit (red).

As indicated in equations (R2-R3), by-products such as NO, NO_2, water vapor (H_2O), and HNO_3 might also be present in the absorption cell. Besides NO, these by-product molecules have absorption in the target spectral range. Depending on the maximum concentration that we could produce, simulation spectra were calculated with 55000 ppm H_2O, 500 ppm HNO_3, and 500 ppm NO_2 to evaluate potential interferences from these molecules. As shown in the middle panel of Figure 5.9, the absorption of NO_2 was too low to affect the measured HONO spectrum while two H_2O lines were easily observed and identified. Regarding HNO_3, its potential interference may be ignored due to its low concentration from the current way of producing HONO.

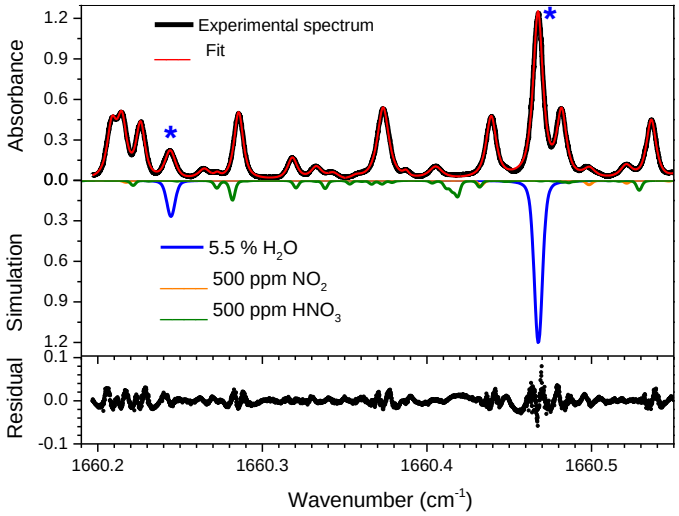

Figure 5.9 Upper panel – a typical experimentally *cis*-HONO absorbance spectrum (black), measured at 9.2 mbar and 303 K, in a segment of ~ 0.35 cm^{-1}, accompanied by a Voigt profile fit (red line). Middle panel – simulation spectrum of 5.5 % H_2O, 500 ppmv HNO_3, and 500 ppmv NO_2. Bottom – residual of the Voigt fit (experiment-fit).

5.4 Simulation of the ν_2 band of *cis*-HONO using PGOPHER code

Table 5.4 Rotational constants of the ground state and the rovibrational constants of the fundamental transitions (from $v'' = 1$ to $v' = 2$) with its ν_2 band of *cis*-HONO taken from [189] for the simulation.

	Ground state rotational constants, in I^r representation, in cm^{-1}	**Ro-vibrational constants of Excited Vibrational Levels,** in cm^{-1}
A	2.80533584(26)	2.79989311(1931)
B	0.439273149(44)	0.438529218(1279)
C	0.379067802(44)	0.378348232(1209)
ΔJ	5.690071(1007). 10^{-7}	5.828410(8763). 10^{-7}
Δ_{JK}	-2.87494(1042). 10^{-7}	-6.6210(3909). 10^{-7}
Δ_K	6.5341569(5301). 10^{-5}	6.53922(4672). 10^{-5}
δJ	9.3669343(7201). 10^{-8}	8.88755(5145). 10^{-8}
δK	2.826896(1574). 10^{-6}	3.4696(1287). 10^{-6}
ΦJ	-8.3979(6731). 10^{-13}	-8.3979. 10^{-13}
Φ_{JK}	--------	0.0
Φ_{KJ}	-6.70840(9638). 10^{-7}	-1.3568(6190). 10^{-8}
Φ_K	5.26274(5914). 10^{-9}	-2.8544(3173). 10^{-8}
φJK	-7.845(2288). 10^{-12}	-7.845. 10^{-12}
φK	1.10254(6113). 10^{-9}	1.10254. 10^{-9}
ν_0		1640.51865

To identify and validate the present experimental results, a simulation of the ν_2 band *cis*-HONO was performed with Watson's *A*-reduced semirigid-rotor Hamiltonian in the I^r representation [201] using the PGOPHER software [202]. The required rotational constants of the ground state and the rovibrational constants of the ν_2 vibrational state of *cis*-HONO were taken from ref. [189] and were shown on Table 5.4.

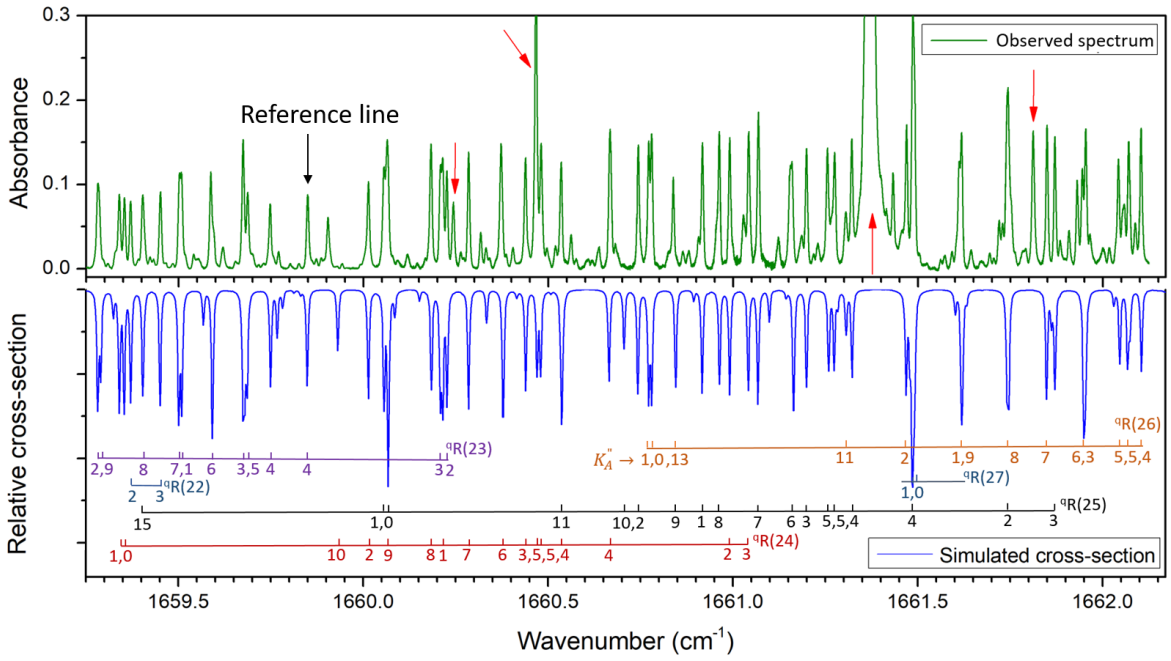

Figure 5.10 Comparison between the experimental and the PGOPHER simulation spectra of *cis*-HONO studied in this work. Upper – absorbance spectrum measured at 9.2 mbar and 303 K. The lines marked with the red arrows are H_2O lines; Lower – simulated relative cross-section spectrum identified with the quantum number using the $qR_{K_A''K_C''J''}$ notation. The relative cross-section spectrum is calculated by scaling it to the experimentally measured absorption intensity.

Figure 5.10 shows the full experimental and simulated spectra of the ν_2 band of *cis*-HONO in the range of 1659.2-1660.2 cm^{-1}. All observed *a*-type *R*-branch transitions are marked, in the simulated spectrum, with the quantum number of the ground state, *J''* using notation *qR(J'')* at different K_c'' values. The *J''* values vary from 22 to 27 over the spectral range of 3 cm^{-1}. The "*point-by-point*" frequency tuning method shows a high spectral resolution in the observed spectrum that resolves the closely spaced lines compared to the simulation. Four H_2O lines were identified in the experimental spectrum. Table 5.5 (see section **5.5**) summarizes the strong lines of *cis*-HONO, confirmed by the simulation. The first and second columns show the quantum number of the transitions of the measured HONO lines. The effective line

intensities reported in this work are either the intensity of one unique transition or the total intensities of some transitions from different quantum number states at the same frequency.

Due to the lack of transition moments, the line intensities could not be directly calculated with the PGOPHER code, only a relative cross-section simulation spectrum σ' is provided. In the present work, the absolute cross-section of the ν_2 band *cis*-HONO was calculated in the following way. Relative band strength $S'_{PGOPHER}$ was calculated based on the simulated cross-section spectrum shown in Figure 5.10:

$$S'_{PGOPHER} = \int \sigma'(\nu) d\nu \tag{5.6}$$

This band strength $S'_{PGOPHER}$ was then scaled to the absolute band strength S'_{Kagann} reported by Kagann et al. [190] and then a scaling factor *k* can be determined:

$$S'_{Kagann} = k \times S'_{PGOPHER} = k \times \int \sigma'(\nu) d\nu \tag{5.7}$$

The determined scaling factor *k* allows calculating the simulated line intensities based on the cross-section from PGOPHER**.**

5.5 Results and discussion

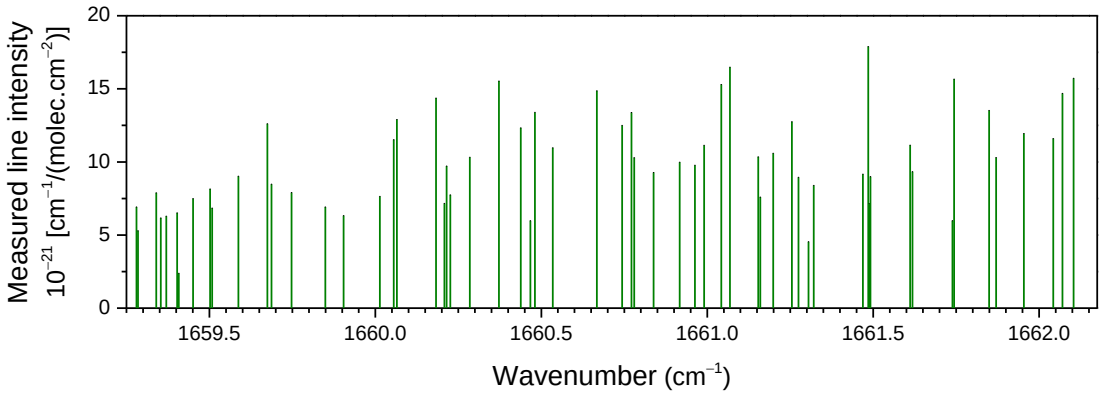

Figure 5.11 Plot of new line positions and their effective line intensities in the ν_2 band of *cis*-HONO in the range of 1659.2 - 1662.2 cm^{-1} (*R*-branch).

About 60 strong-new lines, confirmed by the simulation, of the ν_2 band (N=O stretch) of *cis*-HONO in the range of 1659.2 - 1662.2 cm^{-1} (*R*-branch) are reported here using QCL direct absorption spectroscopy. The line positions and their line intensities are listed in Table 5.5, where they are compared with calculated values. The uncertainties in the line intensities were estimated to be about 17% including a 6% contribution from the reference line used for line

intensity scaling and ~16 % in the determination of the integrated absorbance due to the variation of HONO concentration during the spectrum measurement in each segment

The comparison of the experimental and calculated line intensities through the ratio $S_{calc.}/S_{obs}$, is shown in the 6th column in Table 5.5. As can be seen, the experimental line intensities are usually smaller than the calculated values, which is attributed to the used band strength S'_{Kagann} [190] that was overestimated. In Kagann and Maki [190] formed HONO sample was formed by mixing measured amounts of NO, NO_2 and gaseous H_2O. The spectrum of the mixture was used to determine the equilibrium concentrations of NO, NO_2 and H_2O, and the concentration of HONO formed in the mixture was deduced from the initial concentrations of NO, NO_2, H_2O and the final equilibrium concentrations of these gases. It was thus difficult to accurately determine the HONO band strength based on its broadband absorption spectrum (at 760 torr) interfered by other species, for instance, the strong NO_2 absorptions at the same spectral range of the full ν_2 band of *cis*-HONO. Moreover, the ν_2 band of *cis*-HONO in ref. [190] was measured by a Fourier transform spectrometer with a poor resolution of 0.06 cm^{-1}, which is 60 times larger than our resolution (0.0001 cm^{-1}). Consequently, accurate determine and subtract the absorptions of interfering species from the experimental spectra of HONO is challenged.

It is obvious that the intensity ratios $S_{calc.}/S_{obs.}$ are not constant and vary from 0.7 to 2.9, which indicates that the relative cross-section calculation using the PGOPHER code does not extrapolate all line absorptions very well.

Table 5.5 Line positions and effective line intensities of the strong *cis*-HONO lines measured at 303 K, in comparison with the corresponding simulation values.

Transition		**Line Position** (cm^{-1})	**Difference** (cm^{-1})	**Line intensity** 10^{-21} cm^{-1}/ (molec.cm^{-2})	**Intensity Ratio**
$qR_{K''_A K''_C J''}$		$\nu_0^{obs.}$	$\nu_0^{obs.} - \nu_0^{cal.}$	$S_{obs.}$	$S_{calc.}/S_{obs.}$
qR2,22(23)		1659.2803	-0.0008	6.92	2.5
qR9,15(23)	qR9,14(23)	1659.2849	-0.0047	5.30	2.3
qR1,24(24)		1659.3396	-0.0001	7.89	2.2
qR0,24(24)		1659.3536	-0.0002	6.17	2.9
qR3,19(22)		1659.3702	-0.0005	6.29	2.6
qR8,16(23)	qR8,15(23)	1659.4026	-0.0005	6.52	2.3
qR15,11(25)	qR15,10(25)	1659.4076	-0.0008	2.39	0.7

qR2,20(22)		1659.4509	-0.0005	7.50	2.3
qR7,17(23)	qR7,16(23)	1659.5019	0.0003	8.15	2.3
qR1,22(23)		1659.5084	-0.0007	6.85	2.5
qR6,18(23)	qR6,17(23)	1659.5871	-0.0043	9.03	2.5
qR3,21(23)	qR5,19(23)	1659.6745	-0.0002	12.62	2.3
qR5,18(23)		1659.6869	0.0003	8.48	1.5
qR4,20(23)		1659.7476	-0.0013	7.91	1.8
qR4,19(23)		1659.8492	0.0007	6.92	2.1
qR10,15(24)		1659.9041	-0.0272	6.33	1.4
qR2,23(24)		1660.0136	-0.0007	7.65	2.1
qR1,25(25)		1660.0552	-0.0017	11.53	1.5
qR0,25(25)	qR9,16(24), qR9,15(24)	1660.0648	-0.0032	12.91	2.2
qR8,17(24)	qR8,16(24)	1660.1826	-0.0017	14.37	1.0
qR3,20(23)		1660.2080	-0.0003	7.17	2.2
qR1,23(24)		1660.2147	0.0000	9.72	1.7
qR2,21(23)		1660.2257	-0.0006	7.75	2.1
qR7,18(24)	qR7,17(24)	1660.2847	-0.0007	10.32	1.7
qR6,19(24)	qR6,18(24)	1660.3725	-0.0058	15.54	1.4
qR3,22(24)		1660.4383	-0.0010	12.33	1.2
qR5,20(24)		1660.4671	-0.0025	5.98	2.0
qR5,19(24)		1660.4808	0.0005	13.40	0.9
qR4,21(24)	qR11,15(25), qR11,14(25)	1660.5347	-0.0021	10.97	1.9
qR4,20(24)		1660.6673	0.0016	14.87	0.9
qR2,24(25)		1660.7435	0.0000	12.50	1.2
qR1,26(26)		1660.7717	-0.0002	13.39	1.2
qR0,26(26)		1660.7798	-0.0008	10.30	1.5
qR13,13(26), qR13,14(26),	qR9,17(25), qR9,16(25)	1660.8381	-0.0069	9.28	1.6
qR1,24(25)		1660.9171	-0.0004	9.99	1.5
qR8,18(25)	qR8,17(25)	1660.9629	-0.0011	9.78	1.4
qR2,22(24)		1660.9907	-0.0004	11.14	1.4
qR3,21(24)		1661.0422	0.0001	15.30	1.0
qR7,19(25)	qR7,18(25)	1661.0685	0.0007	16.49	1.0

qR6,20(25)		1661.1536	-0.0105	10.35	1.0
qR6,19(25)		1661.1599	-0.0049	7.60	1.3
qR3,23(25)		1661.1986	-0.0006	10.60	1.3
qR5,21(25)		1661.2551	-0.0039	12.76	0.9
qR5,20(25)		1661.2747	0.0007	8.95	1.3
qR11,16(26)	qR11,15(26)	1661.3050	-0.0016	4.55	1.4
qR4,22(25)		1661.3209	-0.0011	8.40	1.5
qR2,25(26)		1661.4692	0.0002	9.17	1.6
qR1,27(27)		1661.4851	0.0002	17.90	0.8
qR4,21(25)		1661.4881	0.0019	7.16	1.8
qR0,27(27)		1661.4916	-0.0001	9.00	1.7
qR1,25(26)		1661.6112	-0.0069	11.15	1.3
qR9,18(26)	qR9,17(26)	1661.6182	-0.0026	9.34	1.1
qR8,19(26)	qR8,18(26)	1661.7390	-0.0032	5.98	2.2
qR2,23(25)		1661.7438	-0.0017	15.67	0.9
qR7,20(26)	qR7,19(26)	1661.8493	0.0004	13.53	1.2
qR3,22(25)		1661.8706	-0.0001	10.31	1.4
qR6,21(26)	qR6,20(26), qR3,24(26)	1661.9540	0.0052	11.95	2.7
qR5,22(26)		1662.0424	-0.0048	11.60	0.9
qR5,21(26)		1662.0705	0.0024	14.69	0.7
qR4,23(26)		1662.1037	-0.0006	15.73	0.8

To the best of our knowledge, no high-resolution spectral information has been reported on the ν_2 band of *cis*-HONO in the range of 1660.1-1662.2 cm^{-1}. Due to the lack of the studied parameters in the database such as HITRAN or GEISA, the present experimental results are compared with the previous data reported by *Lee et al.* [192] in the spectral region from 1659.2 cm^{-1} to 1659.9 cm^{-1}. Comparisons of the line positions ($\nu_0^{work}, \nu_0^{Lee}$) and the effective line intensities (in terms of the ratio of the line intensities S_{work}/S_{Lee}) between our measurements and *Lee et al.*'s work are summarized in Table 5.6. The spectrum in the present work was recorded with a higher resolution (0.0001 cm^{-1}) than that of *Lee et al.* (0.001 cm^{-1}). The S_{work}/S_{Lee} ratio shows the difference in line intensities between our work and *Lee et al.*, which may be attributed to the different methods used for HONO generation (gas-solid

reaction in *Lee et al.*'s work vs. liquid-phase reaction in our case, see Table 5.3). The HONO concentrations used in our work were significantly higher than that used in Lee's work (a hundred of ppmv vs. a hundred of ppbv), which resulted in a significant improvement in the signal-to-noise ratio in our measured HONO absorption spectrum.

Table 5.6 Comparison of the measured line positions and the line intensities of *cis*-HONO at 303 K between the present work and *Lee at al.*'s data, and between the calculation and *Lee et al.*'s results [192].

Line Position (cm^{-1})		**Difference** (cm^{-1})	**Line intensity** [10^{-21} cm^{-1}/ (molec.cm^{-2})]	**Intensity ratio**	
ν_0^{Lee}	ν_0^{work}	$\Delta\nu_0$	S_{Lee}	$S_{calc.}/S_{Lee}$	$S_{work.}/S_{Lee}$
1659.2817	1659.2803	-0.0014	8.50	2.01	0.81
1659.2869	1659.2849	-0.0020	6.17	1.98	0.86
1659.3405	1659.3396	-0.0009	8.53	2.07	0.92
1659.3548	1659.3536	-0.0012	8.70	2.03	0.71
1659.3714	1659.3702	-0.0012	8.29	1.98	0.76
1659.4043	1659.4026	-0.0017	8.45	1.81	0.77
1659.4523	1659.4509	-0.0014	8.98	1.92	0.83
1659.5031	1659.5019	-0.0012	9.57	1.95	0.85
1659.5099	1659.5084	-0.0015	8.81	1.95	0.78
1659.5887	1659.5871	-0.0016	10.15	2.19	0.89
1659.6770	1659.6745	-0.0025	12.92	2.21	0.98
1659.6886	1659.6869	-0.0017	7.42	1.73	1.14
1659.7496	1659.7476	-0.0020	7.49	1.92	1.06
1659.8507*	1659.8492	-0.0015	6.92	2.08	1.00
1659.9053	1659.9041	-0.0012	4.66	1.96	1.36

* reference line for determination of the effective line intensities of the present work

5.6 Chapter conclusion

A high-resolution spectrum of the ν_2 band of *cis*-HONO (*R*-branch) has been recorded and analyzed in the mid-infrared spectral region of 1659.2-1662.2 cm^{-1}, for the first time, using a lab-developed quantum cascade laser spectrometer. Positions and effective line intensities were determined for ~ 60 new lines. The HONO absorption frequencies were measured using a wavelength meter with an accuracy of ~ 0.0017 cm^{-1}. The experimental spectrum is in good agreement with the PGOPHER simulation. Effective line intensities of the newly measured *cis*-HONO lines were determined by scaling their absorption intensities to the previously

reported line intensity of a *cis*-HONO line located in the same spectral region near 1659.85 cm^{-1}. This method allowed us not only to solve the problem of the evolution of the concentration during the acquisition of the spectrum but also to avoid the need for the parameters involved in the line intensity calculations (χ, L, P, T), as well as the uncertainties of measurement. The maximum uncertainty of ~17% in line intensities is predominantly due to the uncertainty of the reference line intensity at ~ 1659.85 cm^{-1}, and HONO losses in the cell during the measurement. The HONO line located at 1660.6673 cm^{-1} with a line intensity of 1.487×10^{-20} cm^{-1}/molec.cm^{-2} seems useful for high-sensitivity and high-selectivity optical monitoring of HONO with a sub-ppbv detection limit.

Chapter 6 General conclusions and perspective

Hydroxyl free radicals (OH) and nitrous acid (HONO) play a crucial role in atmospheric chemistry. Due to high reactivity and ultra-low concentrations of OH radical in the atmosphere, real-time monitoring of its concentration at ambient levels (sub pptv) is challenging. Though observation of HONO is less challenging and can be carried out by various spectroscopic techniques due to its higher concentration (sub ppbv) and stability than OH. Accurate determination of HONO concentration requires high-quality absorption line intensity (or cross-section) which is not comprehensively listed in the common databases for all spectral ranges, especially in the mid-IR.

In this PhD work, a robust and compact instrument was developed based on off-axis integrated cavity output spectroscopy (OA-ICOS) to determine the absolute concentration of OH. Applying wavelength modulation improved the sensitivity by a factor of 3.4, giving a detection limit of 2.5×10^{10} molecule.cm^{-3} for an integration time of 20 s. A CE-FRS was further developed by coupling the developed OA-ICOS setup to Faraday rotation spectroscopy for interference-free monitoring of OH radicals. A detection limit of 10^{10} OH.cm^{-3} was obtained for an acquisition time of 20 s. The developed WM-CE-FRS was evaluated by measuring the reaction rate constant of OH with CH_4 on a milliseconds timescale.

Below are some considerations for further improvement to obtain higher sensitivity:

(1) As the SNR of the FRS signal is proportional to the transmitted laser power from the cavity, the current SNR is limited by non-resonance coupling of the laser to the cavity resulting in significant loss of laser power injected into the cavity. The SNR can be enhanced by:

- Increasing the coupling efficiency using a re-injection method. A third high reflective mirror is placed in front of the first cavity mirror to re-inject the reflected beam to the cavity [203].
- Isolating the whole system in nitrogen flush to reduce the laser power drop which is due to the strong absorption of ambient H_2O outside of the FRS cell.

(2) The measured FRS signal in the present FRS setup is comparable to the detector noise level. The FRS signal obtained through differential detection scheme is own to noise suppression. As the used two detectors exhibit different performances, the differential

detection scheme could not completely eliminate the noises. Further improvement may be to use two identical detectors or an auto-balanced detection approach.

(3) The CE-FRS performance was inhibited by the low-pressure (< 1 mbar) which is required by the OH production method via a MW discharge. It was difficult and time-wasting to manually control the amount of the gas injected into the cell and keep it stable during OH reactivity measurement. Increasing to higher pressure (OH production by chemical method) allows applying a pressure or mass flow controller and to automatically maintain the total pressure or the gas mixing ratio for a longer time.

Résumé

Les radicaux hydroxyles (OH) et l'acide nitreux (HONO) sont des espèces réactives à courte durée de vie et ils jouent un rôle clé dans la chimie atmosphérique. La surveillance en temps réel de leurs concentrations est cruciale pour étudier la capacité d'oxydation atmosphérique. La spectroscopie d'absorption est un outil efficace pour l'analyse qualitative et quantitative des espèces gazeux à l'état de trace. Selon la loi de Beer-Lambert, l'augmentation de la longueur du *chemin* optique à travers l'échantillon via une cellule multi-passage ou une cavité optique est l'un des moyens plus efficaces d'améliorer la sensibilité de détection. Quant à l'incertitude de mesure, elle dépend fortement de la précision des paramètres de raie spectrale (telles que la position, l'intensité de la raie ou la section efficace) utilisée pour la quantification.

Les travaux de ma thèse portent sur le développement et l'application de trois instruments optiques. Les deux premiers étaient utilisés pour la mesure précise des radicaux OH en laboratoire tandis que le troisième était utilisé pour l'étude spectroscopique des raies spectrales de HONO.

Le premier instrument est un CEAS hors d'axe (appelé Off-axis integrated cavity output spectroscopy, OA-ICOS) qui est destiné à la mesure directe de la concentration d'OH à 2,8 µm. La performance du spectromètre OA-ICOS a été évaluée en mesurant les radicaux OH générés par la décharge micro-onde de vapeur d'eau à basse pression. Deux schémas de détection ont été réalisés et comparés. Tout d'abord, la configuration OA-ICOS a été réalisée pour déterminer la concentration absolue de OH. Ensuite, une modulation de la longueur d'onde (WM-OA-ICOS) a été appliquée pour améliorer la sensibilité.

Le deuxième instrument est un spectromètre de rotation de Faraday amélioré par cavité (CE-FRS) qui est en effet un couplage entre la spectroscopie de rotation de Faraday (FRS) et l'OA-ICOS. Il a été utilisé pour la mesure sans interférence des radicaux OH. En appliquant un champ magnétique externe le long de l'axe de la cavité et en effectuant une détection différentielle pour les deux polarisations de la lumière s'échappant de la cavité, la concentration en OH a été déterminée sur une échelle de temps de l'ordre de la milliseconde. Associé à un dispositif de décharge à micro-ondes pulsées, ce dispositif CE-FRS a été testé et validé en mesurant la constante de vitesse de réaction de OH avec le méthane (CH_4).

Le dernier instrument est un spectromètre d'absorption directe basé sur un laser à cascade quantique (QCL). Il a été développé et utilisé pour déterminer les positions des lignes et leurs

intensités effectives de la bande ν_2 (étirement N=O) du *cis*-HONO dans la gamme de 1659,2-1662,2 cm^{-1} (branche R). Les spectres du *cis*-HONO ont été simulés à l'aide de PGOPHER pour identifier et valider les présents résultats expérimentaux.

(I) Développement d'un instrument basé sur la spectroscopie d'asbsorption en cavité optique (CEAS) pour la détection des radicaux OH

Parmi les différentes techniques de cavité laser, la Spectroscopie d'Absorption en Cavité Résonante Hors d'Axe (OA-ICOS) est un bon candidat pour la détection de gaz à l'état de traces. Utilisant le couplage non résonant d'une source laser à bande étroite dans une cavité, cette approche présente les avantages d'un alignement optique simple et de la robustesse. En particulier, OA-ICOS détermine l'absorption moléculaire en se basant sur la mesure de la lumière intégrée dans le temps qui s'échappe de la cavité, plutôt que sur la décroissance temporelle de l'intensité lumineuse à l'intérieur de la cavité comme dans le CRDS; elle ne nécessite pas de détection à large bande passante. Cette section présente le développement d'un instrument optique pour la détection de OH à 2,8 µm basé sur l'approche OA-ICOS.

I.1. Mise en œuvre d'un système OA-ICOS

L'instrument OA-ICOS, présenté dans la **Figure 3.8**, est développé pour la mesure directe de la concentration d'OH. La source laser utilisée est une diode laser à cascade interbande (ICL) de Nanoplus inséré directement dans un support de type TO66 dont les dimensions sont 50x50x50mm. La diode laser émet un faisceau parallèle de 3 mm de diamètre à l'aide d'une lentille asphérique intégrée juste devant le support. La longueur d'onde d'émission centrale de la source laser est à 3568,5238 cm^{-1} et sa puissance maximale est à 5W. La fréquence du laser peut être accordable sur 14 cm^{-1} en contrôlant l'intensité du courant (0,24 cm^{-1}/mA) et la température (0,36 cm^{-1}/K) du laser. La diode laser est contrôlée en température et en courant par le contrôleur LDC501 de Stanford Reasearch System. Le balayage de longueur d'onde de la diode laser est réalisé par scanner le courant en appliquant une tension de forme sinusoïdale provenant d'un générateur de fonction (Modèle 33120A d'Agilent) à l'entrée du contrôleur LDC501.

Le faisceau ICL collimaté en espace libre a été mélangé avec un laser He-Ne via un séparateur de faisceau CaF_2 pour l'alignement optique. Le faisceau émergeant du séparateur de faisceau a été couplé hors de l'axe à une cavité à l'aide de deux miroirs, M1 et M2. La

cavité est constituée par un tube en acier inoxydable de 50 cm de long et de 3 cm de diamètre extérieur (Los Gatos Research, LGR) et de deux miroirs sphériques (Layertec GmbH). Ces derniers ont un diamètre de 1 pouce et un rayon de courbure de 0,4 m qui sont adaptés à la longueur de la cavité pour former une cavité stable. La réflectivité garantie par le fabricant est supérieure à 99,8 % pour une gamme spectrale allant de 3225 cm^{-1} à 4000 cm^{-1}. La lumière qui s'échappe de la cavité est focalisée sur un détecteur VIGO (PVI-4 TE-3.4/MIPDC-F-1.0) à l'aide d'une lentille dont la distance focale est de 75 mm. Le signal OA-ICOS est ensuite enregistré par une carte d'acquisition de données 16 bits (PCI 6251, National Instrument).

I.2. Calibration de la réflectivité du miroir

Selon l'équation (**3.23**), la mesure quantitative basée sur l'approche OA-ICOS nécessite la connaissance de la réflectivité R du miroir de la cavité. Dans le présent travail, la réflectivité du miroir a été calibrée par la mesure du spectre d'absorption de concentrations connues de CO_2. Les détails du traitement de spectral sont fournis dans la section **3.2.3**. Une longueur de trajet effective a été calculée à 368,6 ± 12,9 m, correspondant à une réflectivité du miroir de (99,864 ± 0,005) %, ce qui donne une finesse de cavité effective d'environ 2308. L'incertitude de la longueur de trajet effective déterminée est d'environ 3,5 %. Elle est estimée par la propagation d'erreur liée à l'incertitude de l'intensité S de raie de CO_2 (2%), de la pente de l'ajustement linéaire (2%), de la concentration de CO_2 (0,3%), et de la température du gaz (2%).

I.3. Performances du système OA-ICOS

Le radical OH est une espèce très réactive dont la durée de vie est très courte (< 1 s). Comme il n'existe pas de source de référence commerciale d'OH, nous devons donc tout d'abord produire une grande quantité d'OH et ensuite les calibrer afin de pouvoir déterminer les performances du système.

Pour effectuer la génération des radicaux OH, un flux de vapeur H_2O pure à moins de mbar est injecté en continu dans la cavité micro-onde. La décharge micro-onde ionise la vapeur d'eau et produit des radicaux OH qui sont envoyés à la cavité ICOS par l'intermédiaire d'un tube en quartz inséré dans la cavité micro-onde.

La **Figure 3.19** montre le spectre d'absorbance de la double raie Q(1,5) de l'état $^2\Pi_{3/2}$ de la transition d'OH qui a été enregistré pendant un temps d'intégration de 60 s. La fréquence de

balayage du laser était de 50 Hz. La concentration d'OH est calculée sur la base de l'équation **(2.11)** en utilisant l'absorbance intégrée déterminée à partir d'un ajustement gaussien du spectre de la transition d'OH Q(1.5e) centré à 3568,5238 cm^{-1}, avec S = $9{,}03\times10^{-20}$ cm^{-1}/(molécule.cm^{-2}). Comme le montre le panneau supérieur de la **Figure 3.19**, l'injection d'un flux de vapeur d'eau pure pour une pression intra-cavité de 0,18 mbar et une puissance de micro-onde de 75 W permet la génération d'une quantité d'OH de $2{,}4\times10^{12}$ molécules.cm^{-3}. Une incertitude de 6,4% sur la concentration d'OH mesurée a été déterminé. Elle dépend de l'incertitude de la longueur de trajet effective (3,5%), de l'intensité de la raie (2%), du signal d'absorption mesuré (5%).

La limite de détection (LoD) peut être estimée à partir de la concentration d'OH mesurée et du signal sur bruit (SNR) du spectre d'absorption. Dans la **Figure 3.19**, le rapport SNR est d'environ 32, ce qui donne une limite de détection de $LoD_{(OA\text{-}ICOS)} = 7{,}5\times10^{10}$ molécules.cm^{-3} avec un temps d'intégration de 60 secondes. Selon l'équation **(3.24)**, le coefficient d'absorption minimal détectable MDAC peut être déterminé à partir du bruit de fond du spectre d'absorption et normalisé par la longueur effective du trajet. Pour cette expérience, $MDAC_{(OA\text{-}ICOS)} = 5{,}8\times10^{-7}$ cm^{-1} en 60 s de temps d'intégration.

Pour étudier les effets du bruit sur la sensibilité de détection de l'instrument développé, la limite de détection en termes de coefficient d'absorption minimal détectable [cm^{-1}] en fonction du nombre de spectres moyennés N (ou en temps d'intégration) a été analysée et représentée par des points rouges dans la **Figure 3.20**. Comme on peut le voir, le bruit de fond a été réduit par un facteur $1/N^{1/2}$ jusqu'à 20000 spectres moyennés (correspondant à 300 s de temps d'intégration), ce qui indique un bon accord avec l'analyse par transformée de Fourier (voir **3.3.5.2**) du signal transmis par la cavité. En raison de la fluctuation de l'intensité du mode cavité, le bruit dans le signal intégré est dominé par le bruit aléatoire, qui peut être réduit par la moyenne spectrale. L'approche OA-ICOS nécessite donc un long temps d'intégration pour réduire le bruit blanc dans le spectre d'absorption. À partir d'un ajustement $\tau^{1/2}$, un $NEAS_{(OA\text{-}ICOS)}$ d'environ $5{,}4\times10^{-6}$ $cm^{-1}.Hz^{-1/2}$ a été obtenu.

Un inconvénient de l'approche OA-ICOS est la nécessité de déterminer et de soustraire un niveau de décalage dû à la contribution ASE du faisceau laser qui est susceptible d'être transmis par la cavité mais sans participer à l'absorption. Dans la section suivante, la modulation de longueur d'onde sera appliquée à l'approche OA-ICOS pour améliorer encore la sensibilité de détection en réduisant le bruit en 1/f du système. De plus, le décalage du

signal OA-ICOS peut être supprimé grâce à la démodulation et à la détection à la seconde harmonique du signal modulé.

I.4. OA-ICOS : amélioration de sensibilité par modulation de longueur d'onde (WM-OA-ICOS)

L'approche WM-OA-ICOS a été réalisé par deux étapes. Tout d'abord, un courant de base (I_b = 120 mA) est imposé à la diode, auquel est ajouté une rampe de courant (I_r = 10 mA) de 50 Hz provenant d'un générateur de fonctions. Cette rampe de courant va engendrer une variation de la longueur d'onde d'émission d'environ de 2 cm^{-1}, à travers les raies d'absorption d'OH et de H_2O situées autour de 3568,52 cm^{-1}. La modulation de la longueur d'onde du laser DFB-ICL a été ensuite effectuée en superposant à cette rampe de courant un signal sinusoïdal, générée par la détection synchrone DSP 7270 d'Ametek (**Figure 3.21**), dont la fréquence (f_m) et l'amplitude sont respectivement de 15,5 kHz et 125 μA_{rms}. Le faisceau laser modulé traversait la cavité et a été capté par un détecteur VIGO (PVI-4TE-3.4). Le signal issu du détecteur a été ensuite envoyé à la détection synchrone pour réaliser une démodulation à la seconde harmonique (2f) en utilisant une constante de temps appropriée. Le signal démodulé à 2f a été enfin enregistré sur l'ordinateur via une carte d'acquisition de données NI PCI-6251.

I.5. Calibration du signal 2f de WM-OA-ICOS

L'intensité du signal 2f est proportionnel à la concentration moléculaire mesurée. Il est néanmoins nécessaire d'effectuer une calibration pour trouver une fonction de conversion. Pour ce faire, le protocole mis en place dans la section **3.2.4.1** a été répété pour déterminer les concentrations absolues d'OH générées, en utilisant la mesure des signaux d'OA-ICOS. Différentes concentrations de OH ont été produites en faisant varier la pression totale de la vapeur d'eau injectée dans la cavité de décharge, de 0,06 à 0,18 mbar. Les spectres d'absorbance mesurés expérimentalement par l'OA-ICOS sont présentés à la **Figure 3.23**. En ajustant du profil de Gaussienne aux spectres enregistrés, les concentrations d'OH ont été calculées et utilisées pour calibrer le pic du signal 2f des lignes OH (**Figure 3.24-droite**) qui est enregistré par l'approche WM-OA-ICOS dans les mêmes conditions que l'OA-ICOS (**Figure 3.23**). Le pic à pic du signal 2f de la transition Q(1,5e) en fonction de la concentration d'OH récupérée par l'approche WM-OA-ICOS est représenté dans la **Figure**

3.24-gauche. Une relation linéaire dont la pente est de $5{,}12\times10^{11}$ molécules.cm^{-3}/volt a été trouvée avec $R^2 = 0{,}995$.

I.6. Performances du système WM-OA-ICOS

En déterminant le rapport entre SNR (~ 32) du spectre 2f à une pression de 0,064 mbar (ligne noire de la **Figure 3.24-droite**) et la concentration d'OH d'environ 8.0×10^{11} molécule.cm^{-3}, un $LoD_{(WM\text{-}OA\text{-}ICOS)}$ a été estimé à 2.5×10^{10} molécule.cm^{-3} pour la mesure WM-OA-ICOS avec un temps d'intégration de 20 s. Cela conduit à un coefficient d'absorption minimum détectable $MDAC_{(WM\text{-}OA\text{-}ICOS)}$ de 2.0×10^{-7} cm^{-1}.

La stabilité du système WM-OA-ICOS développé a été évaluée par une analyse de la variance d'Allan du signal 2f. Comme la concentration d'OH générée par la décharge de H_2O n'est pas suffisamment stable pour mesurer le signal 2f sur une longue période, la mesure de la variance d'Allan a été effectuée en enregistrant le signal 2f d'une ligne H_2O lorsque de la vapeur d'eau pure est injectée dans la cellule sans décharge. Le panneau inférieur de la **Figure 3.26** montre la variance d'Allan du signal 2f (axe de gauche) en fonction du temps d'intégration. Le système est stable avec un temps moyen allant jusqu'à 300 s, ce qui donne une limite de détection de 1.0×10^{10} molécule.cm^{-3}, conduisant à un $MDAC_{(WM\text{-}OA\text{-}ICOS)}$ de 8.0×10^{-8} cm^{-1}.Dans la région < 300 s où le bruit blanc domine la performance du système, l'ajustement du $\tau^{1/2}$ (ligne rouge) a permis une estimation de la $NEAS_{(WM\text{-}OA\text{-}ICOS)}$ d'environ 1.3×10^{-6} cm^{-1}.Hz$^{-1/2}$, ce qui est ~ 4 fois mieux que celle correspondante par l'approche OA-ICOS.

I.7. Conclusion

Un instrument optique compact et robuste basé sur la technique CEAS a été développé pour la détection des radicaux OH à 2.8 μm. En utilisant une cavité à haute finesse (F = 2300), la longueur effective du chemin optique a été augmentée à 368,6 m par rapport à la longueur physique de 0,5 m. Deux schémas expérimentaux : OA-ICOS et WM-OA-ICOS, ont été introduits pour détecter les radicaux OH générés par la décharge de vapeur d'eau par micro-ondes à basse pression (~0,1 mbar). L'approche OA-ICOS permet de déterminer directement la concentration absolue d'OH générée en se basant sur la mesure des spectres d'absorption de la double ligne Q(1,5) de l'état $^2\Pi_{3/2}$ de la transition OH. La mise en œuvre de la modulation de la longueur d'onde WM-OA-ICOS et la détection à seconde harmonique (2f) du signal

d'absorption permettent d'améliorer la LoD d'un facteur 3,4 par rapport au système OA-ICOS, avec un $NEAS_{(WM\text{-}OA\text{-}ICOS)} = 1.3\times10^{-6}$ $cm^{-1}.Hz^{-1/2}$. Le système WM-OA-ICOS permet une limite de détection de 2.5×10^{10} molécules.cm^{-3} pour un temps d'intégration de 20 s et peut être encore amélioré par un moyennage continu.

La principale limite de la sensibilité des deux approches est le bruit optique provenant de la fluctuation de l'intensité de la lumière transmise due au bruit des modes de la cavité. Les LoDs des deux approches n'ont pas pu atteindre le niveau atmosphérique des radicaux OH (10^6 - 10^7 molécules.cm^{-3}). Cependant, l'instrument peut être utilisé pour des applications de combustion et des études de laboratoire où la concentration en OH est plus élevée.

II. Développement d'un instrument basé sur la spectroscopie de rotation de Faraday améliorée par cavité pour la détection sans interférence du radical OH

Cette section présente le développement d'un spectromètre de rotation de Faraday améliorée par cavité (CE-FRS) pour la détection de OH. Cette méthode repose sur la mesure des signaux intégrés dans le temps de deux différentes polarisations résultant de l'effet Faraday. L'approche CE-FRS basé sur la détection différentielle présente l'avantage d'une grande sélectivité en éliminant l'interférence spectrale des espèces diamagnétiques (comme H_2O et CO_2) par rapport aux approches OA-ICOS et WM-ICOS présentées précédemment. L'application à la mesure de la constante de vitesse de réaction de OH avec CH_4 a été démontrée pour évaluer ses performances.

II.1. Mise en œuvre d'un système CE-FRS

Le schéma du spectromètre CE-FRS est présentée dans la **Figure 4.5**. Le principe de cette approche est basé sur la mesure de l'intensité lumineuse intégrée de deux différentes polarisations à la sortie de la cavité. L'approche OA-ICOS utilisée dans l'expérience précédente a été ré-utilisée pour coupler le montage FRS dans le présent travail.

Le faisceau laser collimaté est passé à travers un polariseur P1 (GLP8010, Focteck Photonics) en espace libre pour établir un axe de polarisation du laser incident, et puis a été mélangé avec un laser He-Ne via un séparateur de faisceau CaF_2 pour l'alignement optique. Le faisceau sortant de la cavité a été focalisé sur un polariseur de type Rochon P2 (RPM10, Thorlabs) à l'aide d'une lentille de focalisation dont longueur focale est de 75 mm. L'analyseur P2 a été tourné à 45^o par rapport au polariseur P1 pour convertir la rotation de la polarisation du laser

en changeant d'intensité pouvant être détectés à l'aide de photodétecteurs. Ainsi, le faisceau existant a été divisé en deux polarisations orthogonales s et p. La composante de polarisation s fait un angle de 1,5^{o} par rapport à l'axe de propagation optique. Les rapports d'extinction des deux polariseurs, P1 et P2, sont respectivement $< 5\times10^{6}$ et $< 10^{5}$. Un miroir a été placé à une distance de 10 cm de P2 pour séparer deux sorties de polarisation. Les faisceaux séparés ont ensuite été focalisés sur deux détecteurs, D1 et D2 (PVI-4 TE-3.4 et PVI-4 TE-3, respectivement), à l'aide de deux miroirs paraboliques hors de l'axe OAPM, avec une distance focale de 5 mm et 3,5 mm, respectivement. Les miroirs paraboliques ont été placés de manière à ce que la distance entre le second polariseur P2 et chaque détecteur soit la même, de sorte que les signaux de bruit communs basés sur l'absorption de la vapeur d'eau à l'extérieur de la cavité soient approximativement égaux pour les deux canaux. Par conséquent, le bruit total, y compris les bruits provenant de la source laser et les bruits optiques (c'est-à-dire les effets d'étalon et l'absorption d'eau), contribuera aux deux canaux de détection avec les mêmes caractéristiques qui peuvent être idéalement supprimées autant que possible.

Les signaux des détecteurs D1 et D2 ont été transmis à un préamplificateu (EG&G 5113, Signal Recovery) via les entrées A et B. Le choix du mode d'amplification et de la bande passante du filtre dépend des exigences de l'expérience. Par exemple, un couplage en DC, une sortie en mode A, un gain G de 250 et une bande passante de 0,03 Hz à 3 kHz ont été utilisés pour mesurer l'absorption directe pour 1 canal de détecteur selon l'approche OA-ICOS. Le couplage AC, le mode (A-B), un G de 250, et une largeur de bande de 300 Hz à 10 kHz ont été utilisés pour la mesure du signal différentiel. Le signal amplifié a été envoyé à une carte DAQ (PCI 6251) pour enregistrer les spectres d'absorption et le signal différentiel.

Le balayage de la fréquence du laser d'environ de 0,33 cm^{-1} a été réalisé en appliquant une tension de forme triangulaire (V_s = 0,8 V_{pp} à 510 Hz) provenant d'un générateur de fonctions à l'entrée de modulation externe du contrôleur de laser (LDC 501, Stanford Research). Cette tension triangulaire est converti en courant ave une variation de 20 mA autour de sa valeur centrale de 152,42 mA, correspondant à un accord de fréquence d'environ 0,33 cm^{-1} à travers la ligne d'absorption OH Q(1,5e). Les bobines ont été alimentées par une source de courant continu (72-13330, Tenma), fournissant un courant continu constant jusqu'à 3 A. Un nouveau générateur (GMS200W, Sairem) d'une puissance maximale de 200 W a été appliquée à une cavité micro-onde (S-wave, Sairem) pour la génération de OH (voir **Figure 4.15-en bas**).

II.2. Optimisation et caractérisation du système CE-FRS

Intensité du champ magnétique

Pour maximiser le signal FRS équilibré, l'intensité du champ magnétique B a été optimisée par la mesure de l'amplitude du signal FRS équilibré pour la transition OH Q(1.5e) avec différents valeurs de B. Ces dernières ont été obtenu en modifiant le courant de la bobine avec un pas de 0,3 A (voir **Figure 4.10**).

Comme on peut le voir sur la **Figure 4.10**, l'amplitude crête à crête de la ligne OH Q(1,5e) augmente linéairement avec B pour des intensités de champ magnétique relativement faibles (< 170 Gauss). Une augmentation continue de l'intensité du champ ne peut pas augmenter de manière significative l'amplitude du signal BD-FRS alors que la largeur des lignes OH devient plus grande et se chevauche. De plus, l'utilisation d'un courant plus élevé peut provoquer un auto-échauffement plus rapide des bobines. Une intensité de champ optimale $B_{opt} \approx 318$ Gauss (à $I_{coil} = 1,7$ A) a été sélectionnée pour la caractérisation ultérieure de l'instrument CE-FRS. Comme la largeur de la ligne d'absorption dépend de la pression qui influence la valeur de B_{opt}, toutes les expériences ultérieures ont été réalisées à la même pression dans les mêmes conditions expérimentales.

Vitesse de balayage du laser

Pour l'approche CE-FRS, le signal FRS équilibré s'échappant d'une cavité optique très haute réflectivité est mesuré dans laquelle le bruit optique qui sont des modes aléatoires de la cavité est dominé. Alors que la détection équilibrée utilisant deux détecteurs non identiques ne peut pas éliminer complètement ces bruits communs. Il est nécessaire de faire la moyenne des spectres pour obtenir un bon SNR. Un balayage rapide de la longueur d'onde du laser permet d'augmenter le nombre de moyennes dans un temps d'intégration fixé en conservant une réponse temporelle rapide. Par conséquent, la suppression du bruit en fonction de la vitesse de balayage du laser a été étudiée.

D'après les résultats de la **Figure 4.11**, le SNR est amélioré lorsque la vitesse de balayage du laser augmente. Un taux de balayage plus élevé est donc souhaitable. En revanche, ce dernier est limité par le taux d'échantillonnage de la carte DAQ utilisée et la performance de l'interface Labview. Le taux de balayage maximal réalisable pour cette expérience CE-FRS a été limité à 510 Hz. Une largeur de bande de filtre de 300 Hz - 10 kHz a été ajustée pour minimiser l'effet de "skew" dû aux distorsions de la forme des lignes spectrales par le filtre lors du balayage du laser à 510 Hz.

Signal FRS en fonction de la puissance du laser

Plusieurs études ont souligné que le SNR du signal FRS est proportionnel à la puissance incidente sur le second polariseur P2, qui est la puissance transmise par la cavité dans le présent montage. Une étude du SNR du signal FRS en fonction de la puissance transmise par la cavité a été réalisée avec différentes puissances transmises P_t en atténuant la puissance incidente P_0. La **Figure 4.12-droite** illustre le rapport signal sur bruit (SNR) calculé comme la moyenne quadratique de la puissance d'entrée ou de la puissance transmise par la cavité P_t. Dans ce travail, P_t est bien inférieur à la puissance incidente P_0 (environ 1000 fois) en raison du couplage sans résonance. Ainsi, les performances de l'approche CE-FRS impliquant la détection différentielle ont été limitées par la faible puissance transmise à travers la cavité.

II.3. Performances de l'instrument CE-FRS

La dépendance du MDAC par rapport au temps d'intégration de la mesure, à la précision de la mesure et à la stabilité du système CE-FRS ont été évaluées à l'aide de l'analyse de la variance d'Allan. Comme la concentration d'OH produite était instable pour une mesure de longue durée et que l'absorption de H_2O ne pouvait pas être observée sur le signal FRS (contrairement à l'utilisation du signal d'absorption de H_2O dans un WM-OA-ICOS pour son analyse d'Allan), une série de mesure temporelle (sur 3,8 heures) du "signal FRS" sans génération d'OH a été effectuée lorsqu'on utilise N_2 pour remplir la cavité.

Le résultat est illustré à la **Figure 4.14-b** et comparé aux approches OA-ICOS et WM-OA-ICOS. Le système CE-FRS présente un fonctionnement dominé par le bruit aléatoire pour des temps de moyennage allant jusqu'à 2000 s. Pour un temps de moyennage de 20 s, le coefficient d'absorption détectable minimal est de $1{,}5\times10^{-7}$ cm^{-1}, ce qui est neuf fois meilleur que l'approche OA-ICOS.

II.4. Application à la mesure de la réactivité OH

L'instrument CE-FRS développé a été utilisé par la suite pour l'étude de la réactivité d'OH. Dans une telle étude, la concentration d'OH doit être surveillée en temps réel (voir section **4.3.2**) en fonction du temps à l'aide de l'instrument CE-FRS. Le temps de décroissance de la diminution de la concentration d'OH due à sa réaction avec l'espèce chimique cible peut être déterminé expérimentalement, ce qui permet de déterminer la constante de vitesse de réaction d'OH avec cette espèce cible.

Le mode de balayage rapide et la mesure de la composante AC du signal différentiel représentent une meilleure sensibilité par rapport aux schémas OA-ICOS et WM-OA-ICOS. En raison de la courte durée de vie d'OH, la méthode de balayage avec un temps de moyennage de 20 s a rendu très difficile le suivi en temps réel des changements de concentration d'OH. Pour l'étude de la réactivité des OH, il semble plus simple de fixer la fréquence du laser au pic du signal FRS et de simplement suivre l'amplitude du signal en fonction du temps. Cependant, le FRS détecté en mode AC par la méthode différentielle ne peut être utilisé sans balayage laser. Par conséquent, une extension du CE-FRS pour la mesure de la réactivité OH a été mise en œuvre en effectuant une modulation et une démodulation de la longueur d'onde à l'aide d'une détection synchrone (WM-CE-FRS). Une observation rapide de la concentration d'OH pendant sa réaction avec d'autres espèces peut être réalisée en mesurant le signal WM-CE-FRS.

L'instrument WM-CE-FRS

Le schéma de l'installation WM-CE-FRS est présenté à la **Figure 4.15**. La fréquence du laser a été incrémenté point par point en appliquant un signal de tension provenant de la sortie analogique (AO0) de la carte NI-PCI 6251 à la modulation externe du contrôleur laser via un circuit additionneur. Cela a permis de contrôler le courant du laser à la longueur d'onde cible. Pour la détection WM, une modulation sinusoïdale avec une fréquence f_m de 17,5 kHz (amplitude de modulation de 50 mV_{rms}) provenant d'une détection synchrone a été ajoutée au courant laser. Les signaux détectés par deux détecteurs ont été envoyés à un préamplificateur pour extraire le signal différentiel (A-B) avec un gain de 250 et filtré par une bande passante de 10-30 kHz. La composante AC du signal différentiel a ensuite été démodulée (détection de la seconde harmonique, 2f) par la détection synchrone avec une constante de temps de 200 s pour obtenir le signal WM-FRS.

Mesure du temps de vie de l'OH à l'aide de la décharge micro-onde pulsée

Pour effectuer la mesure du temps de vie de l'OH, il est crucial de produire l'OH avec une concentration constante dans la cellule de réaction et de caractériser le taux de perte (dû à la perte de paroi) sans réaction avec l'espèce cible. Avec une décharge MW continue (CW-MW), l'OH peut être facilement généré et contrôlé par CE-FRS et même OA-ICOS ou WM-ICOS si la concentration est suffisamment élevée. Cependant, cette méthode ne permet pas de distinguer la perte d'OH due à sa réaction avec la molécule étudiée ou à d'autres pertes. Par conséquent, il est nécessaire d'arrêter la production d'OH et d'observer la décroissance d'OH sans et avec la présence de la molécule cible. Malheureusement, la concentration d'OH tombe

rapidement à zéro après l'arrêt de la décharge micro-onde (moins d'une seconde). La détermination d'un profil de concentration en OH à haute résolution temporelle nécessite un temps exact lors de la génération et une mesure synchronisée de sa concentration après l'arrêt de la production, à l'échelle de la milliseconde. Par conséquent, une génération pulsée est plus adaptée à la mesure du temps de vie de l'OH.

Mesure de la constante de vitesse de réaction de OH avec CH_4.

La mesure de la vitesse de réaction à température ambiante a été effectuée en suivant la méthode du pseudo-premier ordre où la concentration initiale d'OH, $[OH]_0$, était inférieure à la concentration de méthane $[CH_4]$ de plusieurs ordres de grandeur ($[OH]_0 << [CH_4]$) de sorte que la concentration de méthane peut être considérée comme constante pendant sa réaction avec OH. Dans ce travail, les concentrations de CH_4 ont varié dans une gamme de 10^{14}-10^{15} molécules.cm^{-3}, ce qui était supérieur de 2 à 3 ordres de grandeur à la concentration initiale d'OH (de $1{,}4\times10^{12}$ molécules.cm^{-3}) produite par la décharge MW pulsée. Toutes les expériences ont été mesurées à une pression d'environ 0,6 mbar.

En l'absence de réactions secondaires compliquées, la relaxation de $[OH]_t$ est donnée par l'équation **(4.13)** et peut être mesurée en surveillant l'amplitude du pic du signal 2f-WM-FRS $S(t)_{2f}$, en fonction du temps, selon l'équation **(4.14)**. À partir du temps de décroissance obtenu par l'ajustement exponentiel, on peut déterminer k' et le soustraire à k_0 qui a été mesuré en l'absence de méthane. La pente de k'-k_0 mesurée en fonction de la concentration de CH_4 (en molécules. cm^{-3}) est la constante de vitesse de réaction k.

La mesure de la constante de vitesse de réaction d'OH avec CH_4 a été effectuée à la température ambiante de 293 ± 3 K. Comme le montre la **Figure 4.19**, la constante de vitesse mesurée d'OH avec le méthane était de (**$4.84\pm0.52)\times10^{-15}$** molécule^{-1}.cm^3.s^{-1} avec une incertitude de 10,7 %, résultant de l'erreur d'ajustement (3,7 %) et de l'incertitude du $[CH_4]$ calculé (~10 %) due à la variation des pressions mesurées.

II.5. Conclusion

Un instrument CE-FRS a été développé pour la détection des radicaux OH. En réalisant un schéma de détection différentielle (BD), le signal FRS sous un champ magnétique statique montre un potentiel pour éliminer l'absorption des espèces non paramagnétiques et supprimer le bruit d'étalon apparaissant dans le signal de chaque détecteur individuel, ce qui permet une amélioration significative de la sélectivité et de la limite de détection de l'instrument.

L'instrument peut être réalisé selon deux approches. Dans la première approche, le laser à balayage rapide et la mesure du signal différentiel en mode AC ont permis d'obtenir une limite de détection de 10^{10} molécules.cm^3 en 20 s de temps de moyennage. Le coefficient d'absorption minimal détectable correspondant était de $1{,}5\times10^{-7}$ cm^{-1}, soit 9 fois mieux que l'approche OA-ICOS. Le rapport signal/bruit de la BD-FRS peut être encore amélioré en augmentant la puissance transmise par la cavité. Dans la deuxième approche, la modulation de la longueur d'onde a été appliquée au signal différentiel et la démodulation a été effectuée à l'aide d'une détection synchrone pour extraire le signal de la seconde harmonique. En fixant la fréquence du laser à la fréquence centrale de la ligne d'absorption de l'OH et en surveillant le signal d'amplitude de crête en fonction du temps, on a obtenu une mesure rapide de l'OH avec une échelle de temps de quelques millisecondes, ce qui permet de surveiller en temps réel le profil temporel de l'intensité de l'OH pendant la réaction chimique. Combiné à un dispositif de décharge micro-onde pulsée, le WM-BD-FRS a été appliqué avec succès pour mesurer la constante de vitesse de réaction d' OH avec CH_4. Pour améliorer la stabilisation à long terme, la fréquence du laser a pu être verrouillée au centre de la transition OH.

III. Étude spectrale de la bande ν_2 du *cis*-HONO près de ~ 1660 cm^{-1} à l'aide d'une spectroscopie d'absorption à laser à cascade quantique (QCL) à long trajet.

Cette section présente le développement et l'évaluation d'un spectromètre d'absorption directe basé sur un laser à cascade quantique (QCL) pour étudier les paramètres de ligne de la bande ν_2 du *cis*-HONO dans la région de l'infrarouge moyen de 1659,2-1662,2 cm^{-1} (étirement N=O, branche R).

III.1. Développement d'un spectromètre d'absorption à long trajet basé sur un QCL dans l'infrarouge moyen à 6 µm

Spectromètre QCL

Un spectromètre d'absorption directe basé sur d'un QCL (QCL-DAS) associé à un compteur de longueurs d'onde haute résolution a été développé pour mesurer simultanément les spectres d'absorption de HONO et les fréquences laser correspondantes. La **figure 5.2** montre le schéma du dispositif expérimental utilisé dans le présent travail. Un laser monomode à onde continue et à rétroaction distribuée - DFB-QCL (HHL-795 Alpes Lasers, Inc.) émettant à 6 µm a été utilisé pour sonder les raies d'absorption de HONO. Un accord de fréquence a été

réalisé par un balayage de courant (0,0134 cm^{-1}/mA) et un accord de température (0,122 cm^{-1}/ºC) pour couvrir la gamme infrarouge de 1659,2-1662,2 cm^{-1} pour la détection du *cis*-HONO.

Le faisceau infrarouge du QCL a été mélangé avec un faisceau laser He-Ne rouge via un séparateur de faisceau CaF2 pour l'alignement optique. Les faisceaux laser mélangés ont ensuite été divisés en deux parties (50%-50%) avec un prisme de Rochon (RPM10, Thorlabs). Le faisceau ordinaire (restant sur le même axe optique que le faisceau d'entrée) a été injecté dans une cellule multipassage (modèle 5612 New Focus, Inc.) d'un volume de 3,2 L et d'un chemin optique effectif de 102,9±8,2 m. Le faisceau laser émergeant de la cellule multipassage a été focalisé sur un détecteur VIGO (PVI-4TE-10,6-0,5×0,5) à l'aide d'un miroir parabolique métallique désaxé à 90° (longueur focale de 50 mm) pour enregistrer le signal d'absorption de HONO. Le faisceau extraordinaire dévié d'un angle d'environ 1,5° a été dirigé vers un mesureur de longueur d'onde (671B, Bristol Instrument) pour une mesure directe de la fréquence du QCL avec une précision absolue de 0,0017 cm^{-1} et une répétabilité de 0,0002 cm^{-1}. Un programme Labview a été appliqué, via une carte d'acquisition de données National Instrument (NI USB-6361), pour contrôler le balayage de la fréquence QCL via le réglage du courant et de la température, et pour enregistrer les spectres d'absorption, ainsi que pour lire en temps réel les données du compteur de longueur d'onde. Afin de contrôler la température de l'échantillon HONO et d'éviter la photolyse de l'HONO, la cellule multipasage a été recouverte d'un tapis chauffant et maintenu à 303 K.

Métrologie de l'accord de la fréquence laser et détermination des fréquences centrales des lignes

Les positions des lignes ont été déterminées directement avec le compteur de longueur d'onde. Une démonstration est présentée à la **figure 5.3**. La température du laser a été réglée à différentes valeurs pour une couverture spectrale différente. Pour chaque point de réglage de la température, le courant d'injection du laser est passé de 200 à 220 mA pour accorder la fréquence sur 0,3 cm^{-1} avec une résolution de 0,0001 cm^{-1}, fournissant 3000 points de données pour chaque spectre balayé. Cette résolution est adaptée à nos mesures expérimentales impliquant une largeur de raie élargie par effet Doppler de ~ 0,003 cm^{-1} à 303 K. Les fréquences laser ont été enregistrées simultanément avec l'acquisition du signal d'absorption. En raison de la variation rapide de la concentration de HONO pendant l'acquisition, discutée en détail dans la section **5.3.3**, le balayage de la fréquence laser doit être aussi rapide que possible pour effectuer une mesure à une quasi-concentration, alors que le

taux d'échantillonnage pour le compteur de longueur d'onde est limité à 0,4 s/échantillon. Afin de garantir une incertitude acceptable dans les intensités de raies déterminées avec un balayage de fréquence aussi rapide que possible, un balayage de fréquence à un taux de 0,094 cm^{-1} par minute a été effectué pour l'acquisition du signal d'absorption HONO, tandis que les données de fréquence laser mesurées ont ensuite été enregistrées par échantillonnage entrelacé avec une gamme de 1:20. Les données de fréquence laser mesurées ont ensuite été ajustées avec une fonction polynomiale de troisième ordre pour extraire une courbe d'étalonnage à haute résolution des fréquences laser en fonction de la tension de balayage. Cette approche permet de convertir le spectre d'absorption dans le domaine temporel en spectre dans le domaine fréquentiel. Les positions centrales des lignes ont été déterminées à partir des ajustements de Voigt aux lignes d'absorption expérimentales.

Méthode de détermination de l'intensité effective des raies

Dans l'étude actuelle, au lieu des mesures directes de la concentration de HONO dans la cellule, les intensités des nouvelles raies ont été déterminées en mettant à l'échelle les intensités d'absorption spectrale mesurées par rapport à l'intensité de raie précédemment rapportée de $6{,}92\times10^{-21}$ cm^{-1}/(molécule.cm^{-2}) d'un *cis*-HONO près de 1659,85 cm^{-1} (voir **Figure 5.5**)

III.2. Simulation de la bande ν_2 du *cis*-HONO à l'aide du code PGOPHER

Afin d'identifier et de valider les présents résultats expérimentaux, une simulation de la bande ν_2 du *cis*-HONO a été réalisée avec l'hamiltonien semi-rigide-rotatif réduit en A de Watson dans la représentation I^r en utilisant le logiciel PGOPHER. Les constantes vibrationnelles requises de l'état vibratoire ν_2 du *cis*-HONO sont indiquées au **tableau 5.4**.

La **figure 5.10** montre les spectres complets expérimentaux et simulés de la bande ν_2 du *cis*-HONO dans la plage de 1659,2-1660,2 cm^{-1}. Toutes les transitions de branche R de type a observées sont marquées, dans le spectre simulé, avec le nombre quantique de l'état fondamental, *J''*, en utilisant la notation *qR(J'')* pour différentes valeurs de K_c''. Les valeurs de *J''* varient de 22 à 27 sur la plage spectrale de 3 cm^{-1}. La méthode d'accord de fréquence "point par point" montre une haute résolution spectrale dans le spectre observé qui résout les lignes étroitement espacées par rapport à la simulation.

En raison de l'absence de moments de transition, les intensités des lignes n'ont pas pu être calculées directement avec le code PGOPHER, seul un spectre de simulation de section

transversale relative σ' est fourni. Dans le présent travail, la section transversale absolue de la bande ν_2 du *cis*-HONO a été calculée en mettant à l'échelle l'intensité de bande relative S'PGOPHER simulée par PGOPHER à la valeur expérimentale rapportée selon les équations **(5.6)** et **(5.7)**. Ensuite, les intensités des lignes simulées peuvent être calculées à partir de la section transversale déterminée.

III.3. Résultats

Environ 60 nouvelles lignes fortes intensités, confirmées par la simulation, de la bande ν_2 (étirement N=O) du *cis*-HONO dans la gamme de 1659,2 - 1662,2 cm^{-1} (branche R) ont été rapportées en utilisant la spectroscopie d'absorption directe. Les positions des raies et leurs intensités ont été listées dans le **tableau 5.5**, comparées aux valeurs calculées. Les incertitudes dans les intensités de raie déterminées ont été estimées à environ 17%, y compris une contribution de 6% de la raie de référence utilisée pour la mise à l'échelle de l'intensité de raie et ~16% dans la détermination de l'absorbance intégrée en raison de la variation de la concentration de HONO pendant la mesure du spectre dans chaque segment.

La ligne HONO située à 1660.6673 cm^{-1} avec une intensité de ligne de 1.487×10^{-20} $cm^{-1}/(molec.cm^{-2})$ semble utile pour la surveillance optique de HONO à haute sensibilité et haute sélectivité avec une limite de détection sub-ppb.

III.4. Conclusion

Un spectre haute résolution de la bande ν_2 du *cis*-HONO (branche R) a été enregistré et analysé dans la région spectrale de l'infrarouge moyen de 1659.2-1662.2 cm^{-1}, pour la première fois, en utilisant un spectromètre à laser à cascade quantique développé par le laboratoire. Les positions et les intensités effectives des lignes ont été déterminées pour environ 60 nouvelles lignes. Les fréquences d'absorption de HONO ont été mesurées à l'aide d'un compteur de longueur d'onde avec une précision de ~ 0,0017 cm^{-1}. Les intensités effectives des raies cis-HONO nouvellement mesurées ont été déterminées en mettant à l'échelle leurs intensités d'absorption par rapport à l'intensité d'une raie cis-HONO précédemment rapportée et située dans la même région spectrale près de 1659.85 cm^{-1}. Cette méthode nous a permis non seulement de résoudre le problème de l'évolution de la concentration pendant l'acquisition du spectre, mais aussi d'éviter le recours aux paramètres

impliqués dans les calculs d'intensité des raies (χ, L, P, T), ainsi que les incertitudes de mesure.

References

[1] R. G. Prinn. *Atmospheric Chemistry in a Changing World: An Integration and Synthesis of a Decade of Tropospheric Chemistry Research*. Springer Science \& Business Media, 2003.

[2] D. E. Heard and M. J. Pilling. Measurement of OH and HO_2 in the Troposphere. Chem. Rev. 2003, **103**, 5163–5198.

[3] D. R. Bates and A. E. Witherspoon. The Photo-Chemistry of Some Minor Constituents of the Earth's Atmosphere (CO_2, CO, CH_4, N_2O). Mon. Not. R. Astron. Soc. 1952, **112**, 101–124.

[4] S. I. Rasool and S. H. Schneider. Normal atmosphere: Large radical and formaldehyde concentrations predicted. Science. 1971, **173**, 141–143.

[5] J. P. Abram, D. J. Creasey, D. E. Heard, J. D. Lee and M. J. Pilling. Hydroxyl radical and ozone measurements in England during the solar eclipse of 11 August 1999. Geophys. Res. Lett. 2000, **27**, 3437–3440.

[6] G. P. Smith and D. R. Crosley. A photochemical model of ozone interference effects in laser detection of tropospheric OH. Meas. Atmos. Gases 1990, **95**, 16427–16442.

[7] S. Lou, F. Holland, F. Rohrer, K. Lu, B. Bohn, T. Brauers, C. C. Chang, H. Fuchs, R. Häseler, K. Kita, Y. Kondo, X. Li, M. Shao, L. Zeng, A. Wahner, Y. Zhang, W. Wang and A. Hofzumahaus. Atmospheric OH reactivities in the Pearl River Delta - China in summer 2006: Measurement and model results. Atmos. Chem. Phys. 2010, **10**, 11243–11260.

[8] O. Forberich, T. Pfeiffer, M. Spiekermann, J. Walter, F. J. Comes, R. Grigonis, K. C. Clemitshaw and R. A. Burgess. Measurement of the diurnal variation of the OH radical concentration and analysis of the data by modelling. J. Atmos. Chem. 1999, **33**, 155–181.

[9] B. Alicke, U. Platt and J. Stutz. Impact of nitrous acid photolysis on the total hydroxyl radical budget during the Limitation of Oxidant Productioh/Pianura Padana Produzione di Ozono study in Milan. J. Geophys. Res. Atmos. 2002, **107**, 8196.

[10] V. Sinha, J. Williams, J. Lelieveld, T. M. Ruuskanen, M. K. Kajos, J. Patokoski, H. Hellen, H. Hakola, D. Mogensen, M. Boy, J. Rinne and M. Kulmala. OH reactivity measurements within a boreal forest: Evidence for unknown reactive emissions. Environ. Sci. Technol. 2010, **44**, 6614–6620.

[11] A. R. Ravishankara, G. Hancock, M. Kawasaki and Y. Matsumi. Photochemistry of ozone: Surprises and recent lessons. Science. 1998, **280**, 60–61.

[12] G. Lammel and J. N. Cape. Nitrous acid and nitrite in the atmosphere. Chem. Soc. Rev. 1996, **25**, 361–369.

[13] D. Perner and U. Platt. Detection of nitrous acid in the atmosphere by differential optical absorption. Geophys. Res. Lett. 1979, **6**, 917–920.

[14] J. G. Calvert, G. Yarwood and A. M. Dunker. An evaluation of the mechanism of nitrous acid formation in the urban atmosphere. Res. Chem. Intermed. 1994, **20**, 463–502.

[15] G. W. Harris, W. P. L. Carter, A. M. Winer, J. N. Pitts, U. Platt and D. Perner. Observations of Nitrous Acid in the Los Angeles Atmosphere and Implications for Predictions of Ozone—Precursor Relationships. Environ. Sci. Technol. 1982, **16**, 414–419.

[16] A. R. Reisinger. Observations of HNO_2 in the polluted winter atmosphere: Possible heterogeneous production on aerosols. Atmos. Environ. 2000, **34**, 3865–3874.

[17] X. Zhou, K. Civerolo, H. Dai, G. Huang, J. Schwab and K. Demerjian. Summertime nitrous acid chemistry in the atmospheric boundary layer at a rural site in New York State. J. Geophys. Res. Atmos. 2002, **107**, 1–11.

[18] X. Ren, H. Harder, M. Martinez, R. L. Lesher, A. Oliger, J. B. Simpas, W. H. Brune, J. J. Schwab, K. L. Demerjian, Y. He, X. Zhou and H. Gao. OH and HO_2 chemistry in the urban atmosphere of New York City. Atmos. Environ. 2003, **37**, 3639–3651.

[19] K. Acker, D. Möller, W. Wieprecht, F. X. Meixner, B. Bohn, S. Gilge, C. Plass-Dülmer and H. Berresheim. Strong daytime production of OH from HNO_2 at a rural mountain site. Geophys. Res. Lett. 2006, **33**, 2–5.

[20] V. Michoud, A. Kukui, M. Camredon, A. Colomb, A. Borbon, K. Miet, B. Aumont, M. Beekmann, R. Durand-Jolibois, S. Perrier, P. Zapf, G. Siour, W. Ait-Helal, N. Locoge, S. Sauvage, C. Afif, V. Gros, M. Furger, G. Ancellet, *and others*. Radical budget analysis in a suburban European site during the MEGAPOLI summer field campaign. Atmos. Chem. Phys. 2012, **12**, 11951–11974.

[21] K. D. Lu, A. Hofzumahaus, F. Holland, B. Bohn, T. Brauers, H. Fuchs, M. Hu, R. Häseler, K. Kita, Y. Kondo, X. Li, S. R. Lou, A. Oebel, M. Shao, L. M. Zeng, A. Wahner, T. Zhu, Y. H. Zhang and F. Rohrer. Missing OH source in a suburban environment near Beijing: Observed and modelled OH and HO_2 concentrations in summer 2006. Atmos. Chem. Phys. 2013, **13**, 1057–1080.

[22] N. Carslaw, D. J. Creasey, D. E. Heard, A. C. Lewis, J. B. McQuaid, M. J. Pilling, P. S. Monks, B. J. Bandy and S. A. Penkett. Modeling OH, HO_2, and RO_2 radicals in the marine boundary layer 1. Model construction and comparison with field measurements. J. Geophys. Res. 1999, **104**, 30241–30255.

[23] D. H. Ehhalt. Gas phase chemistry of the troposphere. Glob. Asp. Atmos. Chem. 1999, **6**, 21–110.

[24] P. S. Monks. Gas-phase radical chemistry in the troposphere. Chem. Soc. Rev. 2005, **34**, 376–395.

[25] K. D. Lu, F. Rohrer, F. Holland, H. Fuchs, B. Bohn, T. Brauers, C. C. Chang, R. Häseler, M. Hu, K. Kita, Y. Kondo, X. Li, S. R. Lou, S. Nehr, M. Shao, L. M. Zeng, A. Wahner, Y. H. Zhang and A. Hofzumahaus. Observation and modelling of OH and HO_2 concentrations in the Pearl River Delta 2006: A missing OH source in a VOC rich atmosphere. Atmos. Chem. Phys. 2012, **12**, 1541–1569.

[26] U. Platt, M. Rateike, W. Junkermann, J. Rudolph and D. H. Ehhalt. New tropospheric OH measurements. J. Geophys. Res. 1988, **93**, 5159–5166.

[27] D. Perner, D. H. Ehhalt, H. W. Piitz, U. Platt, E. P. Roth and A. Volz. OH-Radicals in the lower troposphere. Geophys. Res. Lett. 1976, **3**, 466–468.

[28] H. P. Dorn, U. Brandenburger, T. Brauers and M. Hausman. A new in situ laser long-

path absorption instrument for the measurement of tropospheric OH radicals. Amercian Meteorol. Soc. 1995, **52**, 3373–3380.

[29] W. J. Bloss, T. J. Gravestock, D. E. Heard, T. Ingham, G. P. Johnson and J. D. Lee. Application of a compact all solid-state laser system to the in situ detection of atmospheric OH, HO_2, NO and IO by laser-induced fluorescence. J. Environ. Monit. 2003, **5**, 21–28.

[30] P. Di Carlo, N. L. Hazen, I. C. Faloona, W. H. Brune, H. Harder, M. Martinez and et al. A Laser-induced fluorescence instrument for detecting tropospheric OH and HO_2 : characteristics and calibration. J. Atmos. Chem. 2004, **47**, 139–167.

[31] W. Armerding, J. Walter and F. J. Comes. A White cell type multiple reflection system for tropospheric research. Fresenius. J. Anal. Chem. 1991, **340**, 661–664.

[32] W. Armerding, M. Spiekermann, R. Grigonis, J. Walter, A. Herbert and F. J. Comes. Fast Scanning Laser DOAS for Local Monitoring of Trace Gases, in Particular Tropospheric OH Radicals. Phys. Chem. 1992, **96**, 314–318.

[33] M. Hausmann, U. Brandenburger, T. Brauers and H. P. Dorn. Detection of tropospheric OH radicals by long-path differential-optical-absorption spectroscopy: Experimental setup, accuracy, and precision. J. Geophys. Res. Atmos. 1997, **102**, 16011–16022.

[34] A. E. Parker, C. Jain, C. Schoemaecker, P. Szriftgiser, O. Votava and C. Fittschen. Simultaneous, time-resolved measurements of OH and HO_2 radicals by coupling of high repetition rate LIF and cw-CRDS techniques to a laser photolysis reactor and its application to the photolysis of H_2O_2. Appl. Phys. B Lasers Opt. 2011, **103**, 725–733.

[35] A. Parker, C. Jain, C. Schoemaecker and C. Fittschen. Kinetics of the reaction of OH radicals with CH_3OH and CD_3OD studied by laser photolysis coupled to high repetition rate laser induced fluorescence. React. Kinet. Catal. Lett. 2009, **96**, 291–297.

[36] F. Halland, M. Hessling and A. Hofzumahaus. In situ measurement of troposhere OH radicals by Laser-Induced Fluorescence - A description of the KFA instrument. Amercian Meteorol. Soc. 1995, **52**, 3393–3400.

[37] T. M. Hard, L. A. George and R. J. O'Brien. FAGE determination of tropospheric HO and HO_2. J. Atmos. Sci. 1995, **52**, 3354–3372.

[38] P. S. Stevens, J. H. Mather and W. H. Brune. Measurement of tropospheric OH and HO_2 by laser-induced fluorescence at low pressure. J. Geophys. Res. 1994, **99**, 3543–3557.

[39] Y. Matsumi, M. Kono, T. Ichikawa, K. Takahashi and Y. Kondo. Laser-induced fluorescence instrument for the detection of tropospheric OH radicals. Bull. Chem. Soc. Jpn. 2002, **75**, 711–717.

[40] I. C. Faloona, D. Tan, R. L. Lesher, N. L. Hazen, C. L. Frame, J. B. Simpas, H. Harder, M. Martinez, P. Di Carlo, X. Ren and W. H. Brune. A laser-induced fluorescence instrument for detecting tropospheric OH and HO_2: Characteristics and calibration. J. Atmos. Chem. 2004, **47**, 139–167.

[41] T. M. Hard, R. J. O'Brien, C. Y. Chan and A. A. Mehrabzadeh. Tropospheric Free Radical Determination by FAGE. Environ. Sci. Technol. 1984, **18**, 768–777.

[42] D. Stone, L. K. Whalley, T. Ingham, P. M. Edwards, D. R. Cryer, C. A. Brumby, P. W.

Seakins and D. E. Heard. Measurement of OH reactivity by laser flash photolysis coupled with laser-induced fluorescence spectroscopy. Atmos. Meas. Tech. 2016, **9**, 2827–2844.

[43] D. Amedro, K. Miyazaki, A. Parker, C. Schoemaecker and C. Fittschen. Atmospheric and kinetic studies of OH and HO_2 by the FAGE technique. J. Environ. Sci. 2012, **24**, 78–86.

[44] M. Martinez, H. Harder, D. Kubistin, M. Rudolf, G. Eerdekens, H. Fischer, T. Klüpfel, C. Gurk, R. Königstedt, U. Parchatka, C. L. Schiller, A. Stickler, J. Williams and J. Lelieveld. Hydroxyl radicals in the tropical troposphere over the Suriname rainforest: Airborne measurements. Atmos. Chem. Phys. 2010, **10**, 3759–3773.

[45] K. K. Lehmann, G. Berden and R. Engeln. An Introduction to Cavity Ring-Down Spectroscopy. Blackwell Publishing, 2009 1–26 doi:10.1002/9781444308259.ch1.

[46] S. Cheskis, I. Derzy, V. A. Lozovsky, A. Kachanov and D. Romanini. Cavity ring-down spectroscopy of OH radicals in low pressure flame. Appl. Phys. B Lasers Opt. 1998, **66**, 377–381.

[47] X. Mercier, E. Therssen, J. F. Pauwels and P. Desgroux. Cavity ring-down measurements of OH radical in atmospheric premixed and diffusion flames.: A comparison with laser-induced fluorescence and direct laser absorption. Chem. Phys. Lett. 1999, **299**, 75–83.

[48] C. Wang, N. Srivastava and T. S. Dibble. Observation and quantification of OH radicals in the far downstream part of an atmospheric microwave plasma jet using cavity ringdown spectroscopy. Appl. Phys. Lett. 2009, **95**, 3–6.

[49] C. Wang, F. J. Mazzotti, S. P. Koirala, C. B. Winstead and G. P. Miller. Measurements of OH radicals in a low-power atmospheric inductively coupled plasma by cavity ringdown spectroscopy. Appl. Spectrosc. 2004, **58**, 734–740.

[50] W. Zhao, G. Wysocki, W. Chen, E. Fertein, D. Le Coq, D. Petitprez and W. Zhang. Sensitive and selective detection of OH radicals using Faraday rotation spectroscopy at 2.8 μm. Opt. Express 2011, **19**, 2493.

[51] W. Zhao, G. Wysocki, W. Chen and W. Zhang. High sensitivity Faraday rotation spectrometer for hydroxyl radical detection at 2.8 μm. Appl. Phys. B Lasers Opt. 2012, **109**, 511–519.

[52] G. Litfin, C. R. Pollock, R. F. Curl and F. K. Tittel. Sensitivity enhancement of laser absorption spectroscopy by magnetic rotation effect. J. Chem. Phys. 1980, **72**, 6602–6605.

[53] J. Pfeiffer, D. Kirsten, P. Kalkert and W. Urban. Sensitive magnetic rotation spectroscopy of the OH free radical fundamental band with a colour centre laser. Appl. Phys. B Photophysics Laser Chem. 1981, **26**, 173–177.

[54] W. Zhao, B. Fang, X. Lin, Y. Gai, W. Zhang, W. Chen, Z. Chen, H. Zhang and W. Chen. Superconducting-Magnet-Based Faraday Rotation Spectrometer for Real Time in Situ Measurement of OH Radicals at 10^6 Molecule/cm^3 Level in an Atmospheric Simulation Chamber. Anal. Chem. 2018, **90**, 3958–3964.

[55] N. Wei, B. Fang, W. Zhao, C. Wang, N. Yang, W. Zhang, W. Chen and C. Fittschen. Time-Resolved Laser-Flash Photolysis Faraday Rotation Spectrometer: A New Tool

for Total OH Reactivity Measurement and Free Radical Kinetics Research. Anal. Chem. 2020, **92**, 4334–4339.

[56] M. N. Fiddler, I. Begashaw, M. A. Mickens, M. S. Collingwood, Z. Assefa and S. Bililign. Laser spectroscopy for atmospheric and environmental sensing. Sensors 2009, **9**, 10447–10512.

[57] C. Li, L. Dong, C. Zheng and F. K. Tittel. Compact TDLAS based optical sensor for ppb-level ethane detection by use of a 3.34 μm room-temperature CW interband cascade laser. Sensors Actuators B Chem. 2016, **232**, 188–194.

[58] T. Le Barbu, I. Vinogradov, G. Durry, O. Korablev, E. Chassefière and J. L. Bertaux. TDLAS a laser diode sensor for the in situ monitoring of H_2O, CO_2 and their isotopes in the Martian atmosphere. Adv. Sp. Res. 2006, **38**, 718–725.

[59] I. E. Gordon, L. S. Rothman, C. Hill, R. V. Kochanov, Y. Tan, P. F. Bernath, M. Birk, V. Boudon, A. Campargue, K. V. Chance, B. J. Drouin, J. M. Flaud, R. R. Gamache, J. T. Hodges, D. Jacquemart, V. I. Perevalov, A. Perrin, K. P. Shine, M. A. H. Smith, *and others*. The HITRAN2016 molecular spectroscopic database. J. Quant. Spectrosc. Radiat. Transf. 2017, **203**, 3–69.

[60] N. Jacquinet-Husson, N. A. Scott, A. Chédin, L. Crépeau, R. Armante, V. Capelle, J. Orphal, A. Coustenis, C. Boonne, N. Poulet-Crovisier, A. Barbe, M. Birk, L. R. Brown, C. Camy-Peyret, C. Claveau, K. Chance, N. Christidis, C. Clerbaux, P. F. Coheur, *and others*. The GEISA spectroscopic database: Current and future archive for Earth and planetary atmosphere studies. J. Quant. Spectrosc. Radiat. Transf. 2008, **109**, 1043–1059.

[61] D. E. Burch, E. B. Singleton and D. Williams. Absorption Line Broadening in the Infrared. Appl. Opt. 1962, **1**, 359–363.

[62] M. Wojdyr. Fityk: A general-purpose peak fitting program. J. Appl. Crystallogr. 2010, **43**, 1126–1128.

[63] D. W. Allan. Statistics of Atomic Frequency Standards. Proc. IEEE 1966, **54**, 221–230.

[64] A. Yariv and P. Yeh. *Photonics: optical electronics in modern communications*. Oxford University Express, 2007.

[65] J. Ye, L.-S. Ma and J. L. Hall. Ultrasensitive detections in atomic and molecular physics: demonstration in molecular overtone spectroscopy. J. Opt. Soc. Am. B 1998, **15**, 6.

[66] A. L. Chakraborty and A. Roy. Wavelength Modulation Spectroscopy: combined frequency and intensity laser modulation. Appl. Opt. 2021, **42**, 6728–6738.

[67] K. Song and E. C. Jung. Recent developments in modulation spectroscopy for trace gas detection using tunable diode lasers. Appl. Spectrosc. Rev. 2003, **38**, 395–432.

[68] J. A. Silver. Frequency-modulation spectroscopy for trace species detection: theory and comparison among experimental methods. Appl. Opt. 1992, **31**, 707–717.

[69] E. A. Whittaker, M. Gehrtz and G. C. Bjorklund. Residual amplitude modulation in laser electro-optic phase modulation. J. Opt. Soc. Am. B 1985, **2**, 1320–1326.

[70] J. A. Silver and A. C. Stanton. Optical interference fringe reduction in laser absorption experiments. Appl. Opt. 1988, **27**, 1914–1916.

[71] L. D. Turner, K. P. Weber, C. J. Hawthorn and R. E. Scholten. Frequency noise characterisation of narrow linewidth diode lasers. Opt. Commun. 2002, **201**, 391–397.

[72] P. Werle. Laser excess noise and interferometric effects in frequency-modulated diode-laser spectrometers. Appl. Phys. B Lasers Opt. 1995, **60**, 499–506.

[73] O. Wada. Suppression of the e´talon fringe in absorption spectrometry with an infrared tunable diode laser. Opt. Eng. 1997, **36**, 2586.

[74] C. Li, X. Guo, W. Ji, J. Wei, X. Qiu and W. Ma. Etalon fringe removal of tunable diode laser multi-pass spectroscopy by wavelet transforms. Opt. Quantum Electron. 2018, **50**, 1–11.

[75] H. Riris, C. B. Carlisle, R. E. Warren and D. E. Cooper. Signal-to-noise ratio enhancement in frequency-modulation spectrometers by digital signal processing. Opt. Lett. 1994, **19**, 144–146.

[76] J. M. Nicely, T. F. Hanisco and H. Riris. Applicability of neural networks to etalon fringe filtering in laser spectrometers. J. Quant. Spectrosc. Radiat. Transf. 2018, **211**, 115–122.

[77] W. Chen, A. A. Kosterev, F. K. Tittel, X. Gao and W. Zhao. H_2S trace concentration measurements using off-axis integrated cavity output spectroscopy in the near-infrared. Appl. Phys. B Lasers Opt. 2008, **90**, 311–315.

[78] W. Zhao, X. Gao, W. Chen, W. Zhang, T. Huang, T. Wu and H. Cha. Wavelength modulated off-axis integrated cavity output spectroscopy in the near infrared. Appl. Phys. B Lasers Opt. 2007, **86**, 353–359.

[79] J. Wang, X. Tian, Y. Dong, G. Zhu, J. Chen, T. Tan, K. Liu, W. Chen and X. Gao. Enhancing off-axis integrated cavity output spectroscopy (OA-ICOS) with radio frequency white noise for gas sensing. Opt. Express 2019, **27**, 30517.

[80] E. J. Moyer, D. S. Sayres, G. S. Engel, J. M. St. Clair, F. N. Keutsch, N. T. Allen, J. H. Kroll and J. G. Anderson. Design considerations in high-sensitivity off-axis integrated cavity output spectroscopy. Appl. Phys. B Lasers Opt. 2008, **92**, 467–474.

[81] P. Malara, P. Maddaloni, G. Gagliardi and P. De Natale. Combining a difference-frequency source with an off-axis high-finesse cavity for trace-gas monitoring around 3 μm. Opt. Express 2006, **14**, 1304.

[82] D. Romanini, I. Ventrillard, G. Méjean, J. Morville and E. Kerstel. Introduction to Cavity Enhanced Absorption Spectroscopy. Springer Berlin Heidelberg, 2014 1–60 doi:10.1007/978-3-642-40003-2_1.

[83] A. O'Keefe, J. J. Scherer and J. B. Paul. Cw Integrated cavity output spectroscopy. Chem. Phys. Lett. 1999, **307**, 343–349.

[84] D. S. Baer, J. B. Paul, M. Gupta and A. O'Keefe. Sensitive absorption measurements in the nearinfrared region using off-axis integrated-cavityoutput spectroscopy. Appl. Phys. B Lasers Opt. 2002, **75**, 261–265.

[85] Y. A. Bakhirkin, A. A. Kosterev, C. Roller, R. F. Curl and F. K. Tittel. Mid-infrared quantum cascade laser based off-axis integrated cavity output spectroscopy for biogenic nitric oxide detection. Appl. Opt. 2004, **43**, 2257–2266.

[86] J. B. Paul, L. Lapson and J. G. Anderson. Ultrasensitive absorption spectroscopy with a

high-finesse optical cavity and off-axis alignment. Appl. Opt. 2001, **40**, 4904.

[87] R. Centeno, J. Mandon, S. M. Cristescu and F. J. M. Harren. Sensitivity enhancement in off-axis integrated cavity output spectroscopy. Opt. Express 2014, **22**, 27985.

[88] T. K. McCubbin and R. P. Grosso. A White-Type Multiple-Pass Absorption Cell of Simple Construction. Appl. Opt. 1963, **2**, 764–765.

[89] J. Altmann, R. Baumgart and C. Weitkamp. Two-mirror multipass absorption cell. Appl. Opt. 1981, **20**, 995–999.

[90] J.-F. Doussin, R. Dominique and C. Patrick. Multiple-pass cell for very-long-path infrared spectrometry. Appl. Opt. 1999, **38**, 4145–4150.

[91] J. B. Mcmanus, P. L. Kebabian and M. S. Zahniser. Cells for Long-Path-Length Spectroscopy. Appl. Opt. 1995, **34**, 3336–48.

[92] J. B. McManus and P. L. Kebabian. Narrow optical interference fringes for certain setup conditions in multipass absorption cells of the Herriott type. Appl. Opt. 1990, **29**, 898–900.

[93] G. Berden and R. Engeln. *Cavity Ring-Down Spectroscopy: Techniques and Applications*. Blackwell Publishing, 2010.

[94] M. González-Cardel, P. Arguijo and R. Díaz-Uribe. Gaussian beam radius measurement with a knife-edge: A polynomial approximation to the inverse error function. Appl. Opt. 2013, **52**, 3849–3855.

[95] M. Mazurenka, A. J. Orr-Ewing, R. Peverall and G. A. D. Ritchie. Cavity ring-down and cavity enhanced spectroscopy using diode lasers. Annu. Reports Prog. Chem. - Sect. C 2005, **101**, 100–142.

[96] D. Z. Anderson. Alignment of resonant optical cavities. Appl. Opt. 1984, **23**, 2944–2949.

[97] A. E. Parker, C. Jain, C. Schoemaecker, P. Szriftgiser, O. Votava and C. Fittschen. Simultaneous, time-resolved measurements of OH and HO_2 radicals by coupling of high repetition rate LIF and cw-CRDS techniques to a laser photolysis reactor and its application to the photolysis of H_2O_2. Appl. Phys. B Lasers Opt. 2011, **103**, 725–733.

[98] A. Schocker, A. Brockhinke, K. Bultitude and P. Ewart. Cavity ring-down measurements in flames using a single-mode tunable laser system. Appl. Phys. B Lasers Opt. 2003, **77**, 101–108.

[99] D. J. Hamilton, M. G. D. Nix, S. G. Baran, G. Hancock and A. J. Orr-Ewing. Optical feedback cavity-enhanced absorption spectroscopy (OF-CEAS) in a ring cavity. Appl. Phys. B 2010, **100**, 233–242.

[100] R. Van Zee, J. Hodges and J. Looney. Pulsed, signal-mode cavity ring down spectroscopy. Appl. Opt. 1999, **38**, 3951–3960.

[101] J. J. Scheret, J. B. Paul, A. O'Keefe and R. J. Saykally. Cavity ringdown laser absorption spectroscopy: History, development, and application to pulsed molecular beams. Chem. Rev. 1997, **97**, 25–51.

[102] C. P. Letters, D. Romanini, A. Kachanov and N. Sadeghi. CW cavity ring down spectroscopy. Chem. Phys. Lett. 1997, **14**, 316–322.

[103] B. A. Paldus, C. C. Harb, T. G. Spence, R. N. Zare, C. Gmachl, F. Capasso, D. L. Sivco, J. N. Baillargeon, A. L. Hutchinson and A. Y. Cho. Cavity ringdown spectroscopy using mid-infrared quantum-cascade lasers. Opt. Lett. 2000, **25**, 666.

[104] R. Engeln, G. Von Helden, G. Berden and G. Meijer. Phase shift cavity ring down absorption spectroscopy. Chem. Phys. Lett. 1996, **262**, 105–109.

[105] J. H. Van Helden, D. C. Schram and R. Engeln. Phase-shift cavity ring-down spectroscopy to determine absolute line intensities. Chem. Phys. Lett. 2004, **400**, 320–325.

[106] J. Morville, S. Kassi, M. Chenevier and D. Romanini. Fast, low-noise, mode-by-mode, cavity-enhanced absorption spectroscopy by diode-laser self-locking. Appl. Phys. B Lasers Opt. 2005, **80**, 1027–1038.

[107] D. J. Hamilton and A. J. Orr-Ewing. A quantum cascade laser-based optical feedback cavity-enhanced absorption spectrometer for the simultaneous measurement of CH_4 and N_2O in air. Appl. Phys. B Lasers Opt. 2011, **102**, 879–890.

[108] N. Lang, U. Macherius, M. Wiese, H. Zimmermann, J. Röpcke and J. H. van Helden. Sensitive CH_4 detection applying quantum cascade laser based optical feedback cavity-enhanced absorption spectroscopy. Opt. Express 2016, **24**, A536-543.

[109] A. O. Keefe. Integrated cavity output analysis of ultra-weak absorption. Chem. Phys. Lett. 1998, **293**, 331–336.

[110] R. Engeln, G. Berden, R. Peeters and G. Meijer. Cavity enhanced absorption and cavity enhanced magnetic rotation spectroscopy. Rev. Sci. Instrum. 1998, **69**, 3763–3769.

[111] J. B. Paul, J. J. Scherer, A. O'Keefe, L. Lapson, J. R. Anderson, C. F. Gmachl, F. Capasso and A. Y. Cho. Infrared cavity ringdown and integrated cavity output spectroscopy for trace species monitoring. SPIE 2001, **4577**, 1.

[112] B. Bakowski, L. Corner, G. Hancock, R. Kotchie, R. Peverall and G. A. D. Ritchie. Cavity-enhanced absorption spectroscopy with a rapidly swept diode laser. Appl. Phys. B Lasers Opt. 2002, **75**, 745–750.

[113] F. Schmidt. Development of NICE-OHMS towards ultra-sensitive trace species detection. Umeå University, 2007.

[114] G. S. Engel, W. S. Drisdell, F. N. Keutsch, E. J. Moyer and J. G. Anderson. Ultrasensitive near-infrared integrated cavity output spectroscopy technique for detection of CO at 1.57 μm: New sensitivity limits for absorption measurements in passive optical cavities. Appl. Opt. 2006, **45**, 9221–9229.

[115] D. Perner, U. Platt, M. Trainer, G. Hübler, J. Drummond, W. Junkermann, J. Rudolph, B. Schubert, A. Volz, D. H. Ehhalt, K. J. Rumpel and G. Helas. Measurements of tropospheric OH concentrations: A comparison of field data with model predictions. J. Atmos. Chem. 1987, **5**, 185–216.

[116] P. Bruggeman, G. Cunge and N. Sadeghi. Absolute OH density measurements by broadband UV absorption in diffuse atmospheric-pressure He-H_2O RF glow discharges. Plasma Sources Sci. Technol. 2012, **21**, 035019.

[117] W. R. Stockwell and J. G. Calvert. The absorption spectrum of nitrous acid in caseous NxOy and water mixtures. J. Photochem. 1978, **8**, 193–203.

[118] J. Orphal. A critical review of the absorption cross-sections of O_3 and NO_2 in the ultraviolet and visible. J. Photochem. Photobiol. A Chem. 2003, **157**, 185–209.

[119] J. A. Davidson, C. A. Cantrell, A. H. Mcdaniel, R. E. Shetter, S. Madronich and J. G. Calvert. Visible-Ultraviolet Absorption Cross Sections for NO_2 as a Function of Temperature. J. Geophys. Res. 1988, **93**, 7105–7112.

[120] W. Schneider, G. K. Moortgat, G. S. Tyndall and J. P. Burrows. Absorption cross-sections of NO_2 in the UV and visible region (200 - 700 nm) at 298 K. J. Photochem. Photobiol. A Chem. 1987, **40**, 195–217.

[121] H. Telfah, A. C. Paul and J. Liu. Aligning an optical cavity: with reference to cavity ring-down spectroscopy. Appl. Opt. 2020, **59**, 9464.

[122] V. L. Kasyutich, P. A. Martin and R. J. Holdsworth. An off-axis cavity-enhanced absorption spectrometer at 1605 nm for the $^{12}CO_2/^{13}CO_2$ measurement. Appl. Phys. B Lasers Opt. 2006, **85**, 413–420.

[123] G. Berden and R. Engeln. *Cavity Ring-Down Spectroscopy: Techniques and Applications*. 2010 doi:10.1002/9781444308259.

[124] G. Pesce, G. Rusciano and A. Sasso. Detection and spectroscopy of OH fundamental vibrational band based on a difference frequency generator at 3 μm. Chem. Phys. Lett. 2003, **374**, 425–431.

[125] P. Malara, M. F. Witinski, F. Capasso, J. G. Anderson and P. De Natale. Sensitivity enhancement of off-axis ICOS using wavelength modulation. Appl. Opt. 2012, **108**, 353–359.

[126] K. Niemax, A. Zybin, C. Schnürer-Patschan and H. Groll. Semiconductor diode lasers in atomic spectroscopy. Anal. Chem. 1996, **68**, 351A-356A.

[127] P. Kluczynski, J. Gustafsson, Å. M. Lindberg and O. Axner. Wavelength modulation absorption spectrometry - An extensive scrutiny of the generation of signals. Spectrochim. Acta - Part B At. Spectrosc. 2001, **56**, 1277–1354.

[128] S. Neethu, R. Verma, S. S. Kamble, J. K. Radhakrishnan, P. P. Krishnapur and V. C. Padaki. Validation of wavelength modulation spectroscopy techniques for oxygen concentration measurement. Sensors Actuators, B Chem. 2014, **192**, 70–76.

[129] K. Sun, X. Chao, R. Sur, C. S. Goldenstein, J. B. Jeffries and R. K. Hanson. Analysis of calibration-free wavelength-scanned wavelength modulation spectroscopy for practical gas sensing using tunable diode lasers. Meas. Sci. Technol. 2013, **24**, 125203.

[130] T. Asakawa, N. Kanno and K. Tonokura. Diode laser detection of greenhouse gases in the near-infrared region by wavelength modulation spectroscopy: Pressure dependence of the detection sensitivity. Sensors 2010, **10**, 4686–4699.

[131] K. Niemax, A. Zybin and D. Eger. Tunable deep blue light for laser spectrochemistry. Anal. Chem. 2001, **73**, 135–139.

[132] E. I. Moses and C. L. Tang. High-sensitivity laser wavelength-modulation spectroscopy. Opt. Lett. 1977, **1**, 115–117.

[133] C. Lengignon, X. Cui, W. Zhao, T. Wu, E. Fertein, C. Coeur and W. Chen. RAM-free wavelength modulated off-axis integrated cavity output spectroscopy to OH radical monitoring. Proc. Imaging Appl. Opt. 2014, JTu4A.36 doi:10.1364/aio.2014.jtu4a.36.

[134] G. Litfin, C. R. Pollock, R. F. Curl and F. K. Tittel. Sensitivity enhancement of laser absorption spectroscopy by magnetic rotation effect. J. Chem. Phys. 1979, **72**, 6602–6605.

[135] R. Lewickia, J. H. Doty, R. F. Curl, F. K. Tittela and G. Wysocki. Ultrasensitive detection of nitric oxide at 5.33 μm by using external cavity quantum cascade laser-based Faraday rotation spectroscopy. Proc. Natl. Acad. Sci. U. S. A. 2009, **106**, 12587–12592.

[136] K. Liu, R. Lewicki and F. K. Tittel. Development of a mid-infrared nitrogen dioxide sensor based on Faraday rotation spectroscopy. Sensors Actuators, B Chem. 2016, **237**, 887–893.

[137] S. G. So, E. Jeng and G. Wysocki. VCSEL based Faraday rotation spectroscopy with a modulated and static magnetic field for trace molecular oxygen detection. Appl. Phys. B Lasers Opt. 2011, **102**, 279–291.

[138] B. Brumfield and G. Wysocki. Faraday rotation spectroscopy based on permanent magnets for sensitive detection of oxygen at atmospheric conditions. Opt. Express 2012, **20**, 29727.

[139] C. C. Teng, C. Yan, H. Zhong, A. Rousso, T. Chen, J. Westberg, Y. Ju and G. Wysocki. HO_2 radical measurements in a photolysis reactor using line-locked faraday rotation spectroscopy. Opt. InfoBase Conf. Pap. 2018, **Part F118-**, 3–4.

[140] C. C. Teng, C. Yan, A. Rousso, H. Zhong, T. Chen, E. J. Zhang, Y. Ju and G. Wysocki. Time-resolved HO_2 detection with Faraday rotation spectroscopy in a photolysis reactor. 2021, **29**, 2769–2779.

[141] H. Zhong, C. Yan, C. C. Teng, G. Ma, G. Wysocki and Y. Ju. Kinetic study of reaction C_2H_5+ HO_2 in a photolysis reactor with time-resolved Faraday rotation spectroscopy. Proc. Combust. Inst. 2021, **38**, 871–880.

[142] W. Zhao, G. Wysocki, W. Chen, E. Fertein, D. Le Coq, D. Petitprez and W. Zhang. Shot-noise limited sensitive detection of OH radicals by faraday rotation spectroscopy at 2.8 μm. Opt. InfoBase Conf. Pap. 2011, **19**, 2493–2501.

[143] J. Westberg, L. Lathdavong, C. M. Dion, J. Shao, P. Kluczynski, S. Lundqvist and O. Axner. Quantitative description of Faraday modulation spectrometry in terms of the integrated linestrength and 1st Fourier coefficients of the modulated lineshape function. J. Quant. Spectrosc. Radiat. Transf. 2010, **111**, 2415–2433.

[144] M. Gianella, T. H. P. Pinto, X. Wu and G. A. D. Ritchie. Intracavity Faraday modulation spectroscopy (INFAMOS): A tool for radical detection. J. Chem. Phys. 2017, **147**, 054201.

[145] X. Cui, C. Lengignon, W. Tao, W. Zhao, G. Wysocki, E. Fertein, C. Coeur, A. Cassez, L. Croize, W. Chen, Y. Wang, W. Zhang, X. Gao, W. Liu, Y. Zhang and F. Dong. Photonic sensing of the atmosphere by absorption spectroscopy. J. Quant. Spectrosc. Radiat. Transf. 2012, **113**, 1300–1316.

[146] K. Liu, R. Lewicki and F. K. Tittel. Development of a mid-infrared nitrogen dioxide sensor based on Faraday rotation spectroscopy. Sensors Actuators, B Chem. 2016, **237**, 887–893.

[147] E. J. Zhang, D. M. Sigman and G. Wysocki. In-line optical subtraction using a

differential Faraday rotation spectrometer for $^{15}NO/^{14}NO$ isotopic analysis. arXiv Prepr. arXiv2103 2021, **12196**, 1–4.

[148] H. Adams, D. Reinert, P. Kalkert and W. Urban. A differential detection scheme for Faraday rotation spectroscopy with a color center laser. Appl. Phys. B Photophysics Laser Chem. 1984, **34**, 179–185.

[149] W. Zhao, B. Fang, X. Lin, Y. Gai, W. Zhang, W. Chen, Z. Chen, H. Zhang and W. Chen. Superconducting-Magnet-Based Faraday Rotation Spectrometer for Real Time in Situ Measurement of OH Radicals at 10^6 Molecule/cm^3 Level in an Atmospheric Simulation Chamber. Anal. Chem. 2018, **90**, 3958–3964.

[150] Y. Wang, M. Nikodem, E. Zhang, F. Cikach, J. Barnes, S. Comhair, R. A. Dweik, C. Kao and G. Wysocki. Shot-noise Limited Faraday Rotation Spectroscopy for Detection of Nitric Oxide Isotopes in Breath, Urine, and Blood. Sci. Rep. 2015, **5**, 1–8.

[151] C. Yan, C. C. Teng, T. Chen, H. Zhong, A. Rousso, H. Zhao, G. Ma, G. Wysocki and Y. Ju. The kinetic study of excited singlet oxygen atom O(1D) reactions with acetylene. Combust. Flame 2020, **212**, 135–141.

[152] R. C. Jones. A New Calculus for the Treatment of Optical Systems VI. Experimental Determination of the Matrix*. J. Opt. Soc. Am. 1947, **37**, 110.

[153] C. L. Patrick, J. Westberg and G. Wysocki. Cavity Attenuated Phase Shift Faraday Rotation Spectroscopy. Anal. Chem. 2019, **91**, 1696–1700.

[154] J. Westberg and G. Wysocki. Cavity ring-down Faraday rotation spectroscopy for oxygen detection. Appl. Phys. B Lasers Opt. 2017, **123**, 1–11.

[155] M. Gianella, S. A. Press, K. M. Manfred, H. C. Norman, M. Islam and G. A. D. Ritchie. Sensitive detection of HO_2 radicals produced in an atmospheric pressure plasma using Faraday rotation cavity ring-down spectroscopy. J. Chem. Phys. 2019, **151**, 124202.

[156] D. Jacob, M. Vallet, F. Bretenaker, A. Le Floch and R. Le Naour. Small Faraday rotation measurement with a Fabry-Perot cavity. Appl. Phys. Lett. 1995, **66**, 3546–3548.

[157] C.-Y. Chang and J.-T. Shy. Cavity-enhanced Faraday rotation measurement with auto-balanced photodetection. Appl. Opt. 2015, **54**, 8526.

[158] R. J. Brecha, L. M. Pedrotti and D. Krause. Magnetic rotation spectroscopy of molecular oxygen with a diode laser. J. Opt. Soc. Am. B 1997, **14**, 1921.

[159] F. Nadeem, J. Mandon, S. M. Cristescu, A. Khodabakhsh and F. J. M. Harren. Experimental-based comparison between off-axis integrated cavity output spectroscopy and multipass-assisted wavelength modulation spectroscopy at 7.7 μm. OSA Contin. 2019, **2**, 2667.

[160] W. Zhao, L. Deng, X. Xu, W. Chen, X. Gao, W. Huang and W. Zhang. Static magnetic faraday rotation spectroscopy for OH radical detection at 2.8 μm. Opt. InfoBase Conf. Pap. 2014, 84–86 doi:10.1364/aio.2014.jtu4a.31.

[161] E. J. Zhang, B. Brumfield and G. Wysocki. Hybrid Faraday rotation spectrometer for sub-ppm detection of atmospheric O_2. Opt. Express 2014, **22**, 15957.

[162] W. Zhao, G. Wysocki, W. Chen, E. Fertein, D. Le Coq, D. Petitprez and W. Zhang.

Shot-noise limited sensitive detection of OH radicals by faraday rotation spectroscopy at 2.8 μm. Opt. InfoBase Conf. Pap. 2011, **19**, 2493–2501.

[163] S. Madronich and W. Felder. Direct measurements of the rate coefficient for the reaction $OH+CH_4 \rightarrow CH_3+H_2O$ over 300-1500 K. Symp. Combust. 1985, **20**, 703–713.

[164] H. Yi, L. Meng, T. Wu, A. Lauraguais, C. Coeur, A. Tomas, H. Fu, X. Gao and W. Chen. Absolute determination of chemical kinetic rate constants by optical tracking the reaction on the second timescale using cavity-enhanced absorption spectroscopy. Phys. Chem. Chem. Phys. 2022, **24**, 7396–7404.

[165] J. R. Dunlop and F. P. Tully. A Kinetic Study of OH Radical Reactions with Methane and Perdeuterated Methane. J. Phys. Chem. 1993, **97**, 11148–11150.

[166] X. Zhou, H. Gao, Y. He, G. Huang, S. B. Bertman, K. Civerolo and J. Schwab. Nitric acid photolysis on surfaces in low-NOx environments: Significant atmospheric implications. Geophys. Res. Lett. 2003, **30**, 10–13.

[167] M. Ammann, M. Kalberer, D. T. Jost, L. Tobler, E. Rössler, D. Piguet, H. W. Gäggeler and U. Baltensperger. Heterogeneous production of nitrous acid on soot in polluted air masses. Nature 1998, **395**, 157–160.

[168] G. Lammel and D. Perner. The atmospheric aerosol as a source of nitrous acid in the polluted atmosphere. J. Aerosol Sci. 1988, **19**, 1199–1202.

[169] C. Xue, C. Ye, Z. Ma, P. Liu, Y. Zhang, C. Zhang, K. Tang, S. Tong, M. Ge and Y. Mu. Development of stripping coil-ion chromatograph method and intercomparison with CEAS and LOPAP to measure atmospheric HONO. Sci. Total Environ. 2019, **646**, 187–195.

[170] W. Chen, R. Maamary, X. Cui, T. Wu, E. Fertein, D. Dewaele, F. Cazier, Q. Zha, Z. Xu, T. Wang, Y. Wang, W. Zhang, X. Gao, W. Liu and F. Dong. Photonic sensing of environmental gaseous nitrous acid (HONO): Opportunities and challenges. Wonder Nanotechnol. Quantum Optoelectron. Devices Appl. 2013, 693–737 doi:10.1117/3.1002245.Ch27.

[171] J. Kleffmann, J. C. Lörzer, P. Wiesen, C. Kern, S. Trick, R. Volkamer, M. Rodenas and K. Wirtz. Intercomparison of the DOAS and LOPAP techniques for the detection of nitrous acid (HONO). Atmos. Environ. 2006, **40**, 3640–3652.

[172] K. Tang, M. Qin, W. Fang, J. Duan, F. Meng, K. Ye, H. Zhang, P. Xie, Y. He, W. Xu, J. Liu and W. Liu. Simultaneous detection of atmospheric HONO and NO_2 utilising an IBBCEAS system based on an iterative algorithm. Atmos. Meas. Tech. 2020, **13**, 6487–6499.

[173] S. Dixneuf, A. A. Ruth, R. Häseler, T. Brauers, F. Rohrer and H. Dorn. Detection of nitrous acid in the atmospheric simulation chamber SAPHIR using open-path incoherent broadband cavity-enhanced absorption spectroscopy and extractive long-path absorption photometry. Atmos. Meas. Tech. 2022, **15**, 945–964.

[174] L. Wang and J. Zhang. Detection of nitrous acid by cavity ring-down spectroscopy. Environ. Sci. Technol. 2000, **34**, 4221–4227.

[175] Y. Q. Li, J. J. Schwab and K. L. Demerjian. Fast time response measurements of gaseous nitrous acid using a tunable diode laser absorption spectrometer: HONO emission source from vehicle exhausts. Geophys. Res. Lett. 2008, **35**, 1–5.

[176] B. H. Lee, E. C. Wood, M. S. Zahniser, J. B. McManus, D. D. Nelson, S. C. Herndon, G. W. Santoni, S. C. Wofsy and J. W. Munger. Simultaneous measurements of atmospheric HONO and NO_2 via absorption spectroscopy using tunable mid-infrared continuous-wave quantum cascade lasers. Appl. Phys. B Lasers Opt. 2011, **102**, 417–423.

[177] H. Yi, R. Maamary, X. Gao, M. W. Sigrist, E. Fertein and W. Chen. Short-lived species detection of nitrous acid by external-cavity quantum cascade laser based quartz-enhanced photoacoustic absorption spectroscopy. Appl. Phys. Lett. 2015, **106**, 101109.

[178] J. Stutz, H. J. Oh, S. I. Whitlow, C. Anderson, J. E. Dibb, J. H. Flynn, B. Rappenglück and B. Lefer. Simultaneous DOAS and mist-chamber IC measurements of HONO in Houston, TX. Atmos. Environ. 2010, **44**, 4090–4098.

[179] T. Gherman, D. S. Venables, S. Vaughan, J. Orphal and A. A. Ruth. Incoherent broadband cavity-enhanced absorption spectroscopy in the near-ultraviolet: Application to HONO and NO_2. Environ. Sci. Technol. 2008, **42**, 890–895.

[180] H. Yi, T. Wu, G. Wang, W. Zhao, E. Fertein, C. Coeur, X. Gao, W. Zhang and W. Chen. Sensing atmospheric reactive species using light emitting diode by incoherent broadband cavity enhanced absorption spectroscopy. Opt. Express 2016, **24**, A781.

[181] C. L. Schiller, S. Locquiao, T. J. Johnson and G. W. Harris. Atmospheric measurements of HONO by tunable diode laser absorption spectroscopy. J. Atmos. Chem. 2001, **40**, 275–293.

[182] E. J. Jones. Equilibrium Measurements by Infrared Absorption for the Formation of Nitric Acid from Oxygen, Water Vapor and Nitrogen Dioxide. J. Am. Chem. Soc. 1943, **65**, 2274–2276.

[183] L. H. Jones, R. M. Badger and G. E. Moore. The Infrared Spectrum and the Structure of Gaseous Nitrous Acid. J. Chem. Phys. 1951, **19**, 1599–1604.

[184] G. E. Mcgraw, D. L. Bernitt and I. C. Hisatsune. Infrared spectra of isotopic nitrous acids. J. Chem. Phys. 1966, **45**, 1392–1399.

[185] C. M. Deeley and I. M. Mills. The infrared vibration-rotation spectrum of trans and cis nitrous acid. J. Mol. Struct. 1983, **100**, 199–213.

[186] A. G. Maki and R. L. Sams. Diode laser spectra of cis-HONO near 850 cm^{-1} and trans-HONO near 1700 cm^{-1}. J. Mol. Struct. 1983, **100**, 215–221.

[187] A. G. Maki. High-resolution measurements of the ν_2 band of HNO_3 and the ν_3 band of trans-HONO. J. Mol. Spectrosc. 1988, **127**, 104–111.

[188] J. M. Guilmot, M. Carleer, M. Godefroid and M. Herman. The ν_1 fundamental band of trans-HNO_2. J. Mol. Spectrosc. 1990, **143**, 81–90.

[189] J. M. Guilmot, F. Mélen and F. Herman. Rovibrational Parameters for cis-Nitrous Acid. J. Mol. Spectrosc. 1993, **160**, 401–410.

[190] R. H. Kagann and A. G. Maki. Infrared absorption intensities of nitrous acid (HONO) fundamental bands. J. Quant. Spectrosc. Radiat. Transf. 1983, **30**, 37–44.

[191] W. S. Barney, L. M. Wingen, M. J. Lakin, T. Brauers, J. Stutz and B. J. Finlayson-Pitts. Infrared absorption cross-section measurements for nitrous acid (HONO) at room

temperature. J. Phys. Chem. A 2000, **104**, 1692–1699.

[192] B. H. Lee, E. C. Wood, J. Wormhoudt, J. H. Shorter, S. C. Herndon, M. S. Zahniser and J. W. Munger. Effective line strengths of trans-nitrous acid near 1275 cm^{-1} and cis-nitrous acid at 1660 cm^{-1}. J. Quant. Spectrosc. Radiat. Transf. 2012, **113**, 1905–1912.

[193] X. Cui, F. Dong, M. W. Sigrist, Z. Zhang, B. Wu, H. Xia, T. Pang, P. Sun, E. Fertein and W. Chen. Investigation of effective line intensities of trans-HONO near 1255 cm^{-1} using continuous-wave quantum cascade laser spectrometers. J. Quant. Spectrosc. Radiat. Transf. 2016, **182**, 277–285.

[194] R. A. Cox and R. G. Derwent. The ultra-violet absorption spectrum of gaseous nitrous acid. J. Photochem. 1976, **6**, 23–34.

[195] K. H. Becker, J. Kleffmann, R. Kurtenbach and P. Wiesen. Line strength measurements of trans-HONO near 1255 cm^{-1} by tunable diode laser spectrometry. Geophys. Res. Lett. 1995, **22**, 2485–2488.

[196] R. Maamary, E. Fertein, M. Fourmentin, D. Dewaele, F. Cazier, C. Chen and W. Chen. Effective line intensity measurements of trans-nitrous acid (HONO) of the ν_1 band near 3600 cm^{-1} using laser difference-frequency spectrometer. J. Quant. Spectrosc. Radiat. Transf. 2017, **196**, 69–77.

[197] B. H. Lee, E. C. Wood, J. Wormhoudt, J. H. Shorter, S. C. Herndon, M. S. Zahniser and J. W. Munger. Effective line strengths of trans-nitrous acid near 1275 cm^{-1} and cis-nitrous acid at 1660 cm^{-1}. J. Quant. Spectrosc. Radiat. Transf. 2012, **113**, 1905–1912.

[198] A. Febo, C. Perrino, M. Gherardi and R. Sparapani. Evaluation of a High-Purity and High-Stability Continuous Generation System for Nitrous Acid. Environ. Sci. Technol. 1995, **29**, 2390–2395.

[199] T. Wu, W. Chen, E. Fertein, F. Cazier, D. Dewaele and X. Gao. Development of an open-path incoherent broadband cavity-enhanced spectroscopy based instrument for simultaneous measurement of HONO and NO_2 in ambient air. Appl. Phys. B Lasers Opt. 2012, **106**, 501–509.

[200] A. Dehayem-Kamadjeu, O. Pirali, J. Orphal, I. Kleiner and P. M. Flaud. The far-infrared rotational spectrum of nitrous acid (HONO) and its deuterated species (DONO) studied by high-resolution Fourier-transform spectroscopy. J. Mol. Spectrosc. 2005, **234**, 182–189.

[201] J. K. G. Watson. in Vibrational Spectra and Struture. ed. J. R. Durig, Elsevier, New York 1977, **6**, 1–89.

[202] C. M. Western. PGOPHER: A program for simulating rotational, vibrational and electronic spectra. J. Quant. Spectrosc. Radiat. Transf. 2017, **186**, 221–242.

[203] F. Nadeem, J. Mandon, S. M. Cristescu, A. Khodabakhsh and F. J. M. Harren. Experimental-based comparison between off-axis integrated cavity output spectroscopy and multipass-assisted wavelength modulation spectroscopy at 7.7 μm. OSA Contin. 2019, **2**, 2667.

[204] T. A. Kovacs and W. H. Brune. Total OH loss rate measurement. J. Atmos. Chem. 2001, **39**, 105–122.

[205] R. A. Cox, K. F. Patrick and S. A. Chant. Mechanism of Atmospheric Photooxidation

of Organic Compounds. Reactions of Alkoxy Radicals in Oxidation of n-Butane and Simple Ketones. Environ. Sci. Technol. 1981, **15**, 587–592.

[206] Y. Sadanaga, A. Yoshino, K. Watanabe, A. Yoshioka, Y. Wakazono, Y. Kanaya and Y. Kajii. Development of a measurement system of OH reactivity in the atmosphere by using a laser-induced pump and probe technique. Rev. Sci. Instrum. 2004, **75**, 2648–2655.

[207] J. Gao, P. Zuo, T. Zhu, Q. Gong and H. Jiang. Study of the Formation Dynamics of OH from the Photolysis of O_3 by Ultrashort Laser Pulses. J. Phys. Chem. Lett. 2020, **11**, 6482–6486.

[208] A. J. Hynes and P. H. Wine. Kinetics of the OH + CO reaction under atmospheric conditions. J. Phys. Chem. 1987, **91**, 3672–3676.

[209] Z. W. Liu, X. F. Yang, A. M. Zhu, G. L. Zhao and Y. Xu. Determination of the OH radical in atmospheric pressure dielectric barrier discharge plasmas using near infrared cavity ring-down spectroscopy. Eur. Phys. J. D 2008, **48**, 365–373.

[210] N. Srivastava and C. Wang. Effects of water addition on OH radical generation and plasma properties in an atmospheric argon microwave plasma jet. J. Appl. Phys. 2011, **110**, 053304.

[211] L. Chen, S. Kutsuna, K. Tokuhashi and A. Sekiya. New technique for generating high concentrations of gaseous OH radicals in relative rate measurements. Int. J. Chem. Kinet. 2003, **35**, 317–325.

[212] G. L. Vaghjiani and A. R. Ravishankara. Kinetics and mechanism of OH reaction with CH_3OOH. J. Phys. Chem. ca 1989, **93**, 1948–1959.

[213] G. Dilecce, P. F. Ambrico, M. Simek and S. De Benedictis. LIF diagnostics of hydroxyl radical in atmospheric pressure He-H_2O dielectric barrier discharges. Chem. Phys. 2012, **398**, 142–147.

[214] S. Yonemori, Y. Nakagawa, R. Ono and T. Oda. Measurement of OH density and airhelium mixture ratio in an atmospheric-pressure helium plasma jet. J. Phys. D. Appl. Phys. 2012, **45**, 225202.

[215] X. Pei, S. Wu, Y. Xian, X. Lu and Y. Pan. On OH density of an atmospheric pressure plasma jet by laser-induced fluorescence. IEEE Trans. Plasma Sci. 2014, **42**, 1206–1210.

Appendix

Appendix A – Production of OH radicals

Measurement uncertainty, precision, specificity and limit of detection are essential features that are used for the characterization of spectroscopic instrument's performance. They generally rely on well calibrated reference samples. The difficulty in characterizing instrument dedicated to OH measurement lies in the fact that there is no commercial reference source for OH radicals. It is necessary to produce OH radicals in suitable quantities. There are several methods usually used for the production of OH radicals, which can be divided into two techniques: chemical process combined with photolysis technique [204–208], and plasma discharges [48,116,209,210].

A.1 Chemical processes with photolysis of gas sample by UV sources

Photolysis can be performed in different approaches, depending on the photolytic sample and the UV source. For instance, OH radicals are generated in a flow tube at the tip of a sliding injector by photolysis of water vapor using a mercury vapor lamp [204]:

$$H_2O + h\nu\ (184.91\ nm) \rightarrow H + OH \qquad (R\ 0.1)$$

$$H + O_2\ (+M) \rightarrow HO_2\ (+M) \qquad (R\ 0.2)$$

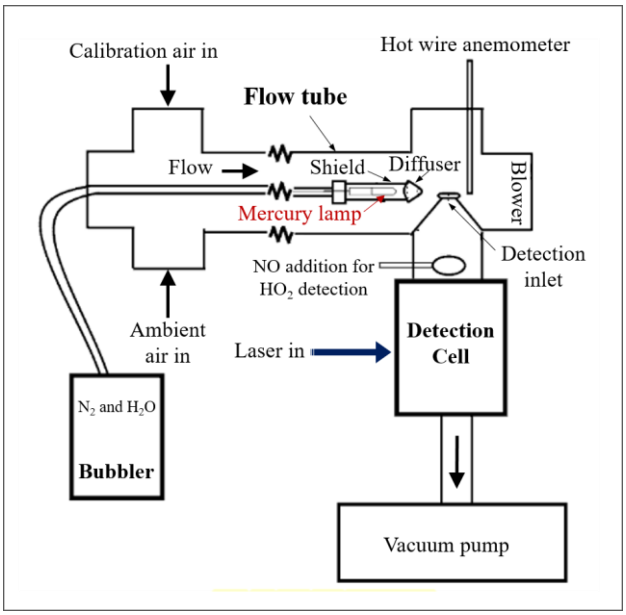

Figure A.1 A scheme of a flow tube equipped with an injector and detection system for the OH loss rate measurement [204].

The OH signal is monitored downstream of the injector after mixing with ambient airflow in the main tube. A significant disadvantage of the flow tube method is the generation of equal concentrations of OH and HO_2, leading to the potential of uncontrolled reaction of HO_2 with other ambient gases, such as NO and other. This makes it difficult to calibrate the generated OH concentration [42].

UV lasers, typically at a wavelength of 266 nm [55,206–208,211], are widely used to photolyze different OH precursors, i.e., HONO [205], O_3/H_2O mixture, or H_2O_2. For example, the photolysis of O_3 generates $O(^1D)$ that then reacts with H_2O to form OH:

$$O_3 + h\nu\ (266\ nm) \rightarrow O_2 + O(^1D) \quad \text{(R 0.3)}$$

$$O(^1D) + H_2O \rightarrow 2OH \quad \text{(R 0.4)}$$

$$H_2O_2 + h\nu\ (266\ nm) \rightarrow 2OH \quad \text{(R 0.5)}$$

The OH produced in this way is usually measured using laser-induced fluorescence (LIF) [42,43,212]. Flash-photolysis in conjunction with LIF measurements is also a suitable method to generate OH for real-time observation of OH concentration decay and OH reactivity. In addition, laser flash photolysis has the advantage to produce uniform OH concentrations throughout the reaction cell. This method minimizes the risk of poor mixing, which is potentially problematic in flow tubes. However, it requires a coupling and expanding of the UV laser beam to overlap with the optical axis of the detection system, which, in some cases, makes the design of the absorption cell and the optical system more complicated [140,141]. Table A.1 lists several OH production methods and some experimental details.

A.2 Plasmas discharges

OH radicals can be also produced from various plasma discharges of water vapor for continuous/pulse production, such as DC discharges [209], dielectric barrier discharges (DBD) [210], and radio frequency (MHz) powered atmospheric plasma jets (APJs) [116] or microwave (2.45 GHz) discharges [48]. The principle is based on the dissociation of H_2O molecules via two distinct mechanisms that take place in the plasma:

$$H_2O + e^- \rightarrow OH + H + e^- \quad \text{(R 0.6)}$$

$$H_2O + M \rightarrow OH + H + M \quad \text{(R 0.7)}$$

Figure A.2 illustrates three approaches based on plasma discharges: (a) dielectric barrier discharge (DBD), in which the OH radicals are generated between two electrodes covered by a dielectric material and powered with a high voltage (HV) waveform source (in the order of

kV). The main advantage of the DBD in general is that non-thermal plasmas can be generated in a simple and efficient way at atmospheric pressure [209]. Both (b) and (c) are atmospheric plasma jets (APJs) powered by microwave and high electrical voltage sources, respectively. By injecting the mixture of H_2O (from hundreds of ppm to a few percent) and carrier gas (Helium or Argon) into a quartz tube inserted through the plasma cavity, OH radicals are generated at atmospheric pressure and distributed along the axis of the plasma flame. Several studies found that the OH density depends strongly on the water vapor content in the Helium flow but weakly on the discharge current [213,214].

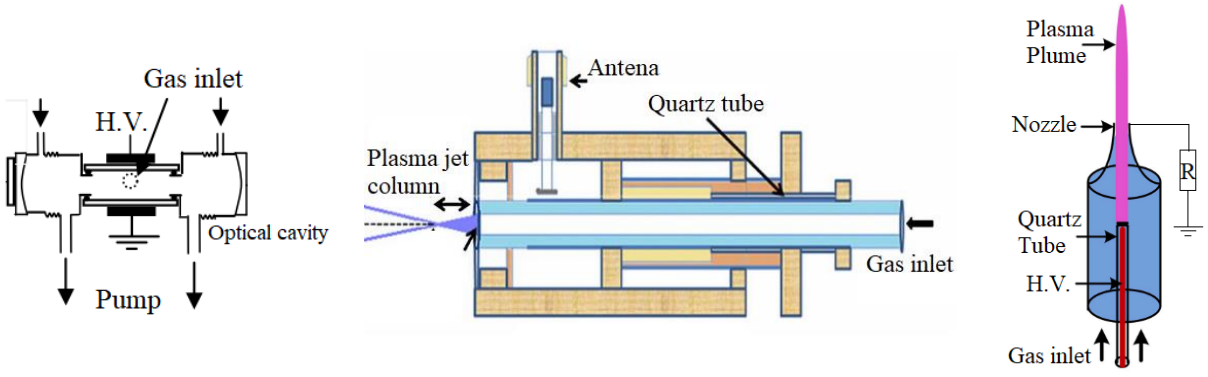

a) b) c)

Figure A.2 Various approaches to plasma discharge of OH production. (a) Dielectric barrier discharge with a high voltage source [209]. (b) Atmospheric plasma jet [48] powered with a 2.45 GHz microwave source. (c) High voltage (HV) electrode of atmospheric plasma jet device [215].

Table A.1 Various approaches for OH production using photolysis processes and plasma discharges.

Laser flash photolysis				
Photolysis source	***Photolytic source***	***[OH]*** *molecule.cm^{-3}*	***Pressure***	***Refs***
Flash-lamp-pumped Nd: YAG laser (266 nm, 20 ns pulse duration)	O_3/H_2O mixture	10^9	300 Pa	[206]
Pulse laser (282.2 nm, 250 fs pulse duration)	O_3/H_2O mixture	10^{11}	1 atm	[207]
Hg lamp (254 nm)	O_3/H_2O mixture	$(0.53–1.2)\times10^{11}$	300-500 torr	[211]
Nd: YAG laser (266 nm, 25 ns pulse duration)	O_3/H_2O mixture	$(0.1–2.0)\times10^9$	50 mbar	[55]
Nd: YAG laser (266 nm, 25 ns pulse duration)	H_2O_2	1×10^{12}	700 torr	[208]

Plasma discharge				
Method and power supply source	***Sample***	***[OH]*** *molecule.cm^{-3}*	***Pressure***	***Refs***
Continuous WM discharge (2.45 GHz microwave source, 75 W)	H_2O	2.2×10^{12}	0.6 mbar	[51,142]
Continuous – APJ (2.45 GHz microwave source, 104 W)	H_2O/Ar mixture ratio (0.0 – 1.9%)	[13]$(0.2–2.8)\times10^{16}$	1 atm	[210]
Pulse – APJ (HV source, 7 kV peak voltage pulse, frequency of 8.4 kHz, 35 μs duration, 2.5 W)	H_2O/He mixture ratio (0.0–0.1%)	$(0.6–6.0)\times10^{13}$	1 atm	[214]
DBD (HV – sine wave source with 6 – 10.4 kV peak–to–peak voltage, frequency of 70 kHz)	H_2O/He mixture ratio (0.67%)	$(2.1–3.7)\times10^{13}$	1 atm	[209]
Continuous – APJ (2.45 GHz microwave source, 12 W)	Ar (99.99%)	[14](7.2×10^{12})	1 atm	[48]
Pulse – APJ (HV source with 8 kV peak voltage pulse, 8 kHz repetition rate)	Pure He	[15](2.4×10^{13})	1 atm	[215]

In this thesis, the generation of OH radicals is realized by dissociating H_2O molecules via a microwave discharge at 2.45 GHz at reduced pressure in order to reduce line broadening. In that way the spectral overlap of absorption features can be minimized especially in the spectral region around the detection wavelength. More details of the experimental conditions are presented in sections **3.3** & **4.3**.

[13] OH concentration was measured along the jet axis at locations near the quartz tube nozzle.
[14] OH concentration was measured down to 28 mm away from the plasma orifice.
[15] OH concentration was measured at 5 mm away from the plasma jet nozzle.

Appendix B – Publications and Conferences

Publications

[1] **Minh-Nhut Ngo**, Yang Zheng, Qian Gou, Nicolas Houzel**,** Tong Nguyen-Ba, Cécile Coeur, Weidong Chen, "New line positions and effective line intensities of the ν_2 band cis-HONO near 1661 cm^{-1} from quantum cascade laser absorption spectroscopy", Journal of Quantitative Spectroscopy and Radiative Transfer, 2022, **278**, 108012. https://doi.org/10.1016/j.jqsrt.2021.108012.

[2] **Minh-Nhut Ngo**, Tong Nguyen-Ba, Fabrice Cazier, Weixiong Zhao, Lars Nähle and Weidong Chen. Wavelength modulation enhanced Off-axis integrated cavity output spectroscopy for OH radicals measurement at 2.8 μm. In revision.

Conferences

[1] **Minh-Nhut Ngo**, Qian Gou, Nicolas Houzel**,** Tong Nguyen-Ba, Cécile Coeur, Weidong Chen, "Investigation of new line positions and line intensities of cis-HONO around 1660 cm^{-1} using direct quantum cascade laser absorption spectroscopy", The 5th Asian Workshop on Molecular Spectroscopy, March 9-10, 2021, online.

[2] **Minh-Nhut Ngo**, Tong Nguyen-Ba, Denis Petitprez, Fabrice Cazier, Weidong Chen, "Measurement of OH radicals using off-axis integrated output spectroscopy (OA-ICOS) at 2.8 μm", European Geosciences Union General Assembly 2021, April 19-30, 2021, Online. https://doi.org/10.5194/egusphere-egu21-16416

[3] **Minh-Nhut Ngo**, Qian Gou, Nicolas Houzel**,** Tong Nguyen-Ba, Cécile Coeur, Weidong Chen, **"**Measurements of new line positions and effective line intensities of cis-HONO of the ν_2 band around 1660 cm^{-1} using quantum cascade laser absorption spectroscopy**"**, International Symposium on Molecular Spectroscopy, June 21-25, 2021, online. https://doi.org/10.15278/isms.2021.TF10.

[4] **Minh-Nhut Ngo**, Tong Nguyen-Ba, Weixong Zhao, Weidong Chen, "Off-axis integrated cavity output spectroscopy enhanced Faraday rotation techniques for OH detection at 2.8 μm", European Geosciences Union General Assembly 2022, May 22-28, 2022, Vienna, Austria. https://doi.org/https://doi.org/10.5194/egusphere-egu22-1929.

[5] **Minh-Nhut Ngo**, Tong Nguyen-Ba, Nicolas Houzel, Cécile Coeur, Weixiong Zhao, Weidong Chen, "Off-axis integrated cavity output spectroscopy enhanced Faraday

rotation approach for measurements of total OH reactivity", The international workshop: New Developments in High Resolution Molecular Spectroscopy and outreach to modern applications, May 29th to June 3rd, 2022, Les Houches school of physics, Haute Savoie, France.

[6] **Minh-Nhut Ngo**, Qian Gou, Nicolas Houzel**,** Tong Nguyen-Ba, Cécile Coeur, Weidong Chen, "Measurements of new line positions and effective line intensities of cis-HONO of the ν_2 band around cm^{-1} using quantum cascade laser absorption spectroscopy", Half-day for doctoral students - CAPPA, September 7, 2021, University of Lille, Villeneuve-d'Ascq, Lille, France.

[7] **Minh-Nhut Ngo**, Tong Nguyen-Ba, Weixiong Zhao, Weidong Chen, "Optical monitoring of OH radicals using Faraday rotation measurement enhanced by off-axis integrated cavity output spectroscopy at 2.8 μm (poster)", The 2022 plenary days, June 14-17, 2021, Dunkerque, France.

[8] **Minh-Nhut Ngo**, Tong Nguyen-Ba**,** Nicolas Houzel**,** Cécile Coeur, Weixiong Zhao, Weidong Chen, "Optical monitoring of OH radicals using Cavity-enhanced Faraday rotation spectroscopy at 2.8 μm (poster)", Day of doctoral students of the MTE pole, July 12, 2022, University of the Littoral Opal Coast, Dunkerque, France.

[9] **Minh-Nhut Ngo**, Tong Nguyen-Ba**,** Weixiong Zhao, Weidong Chen, "Cavity-enhanced Faraday Rotation measurement for OH monitoring (poster)", Journée Scientifique 2022 du Labex CaPPA, March 10, 2022, University of Lille, Villeneuve-d'Ascq, Lille, France.

Abstract

Are reported in this PhD thesis the developments and applications of optical instruments dedicated to accurate measurements of OH radical mixing ratios and to investigations of spectral line parameters of HONO. The first instrument operating near 2.8 µm was developed for direct measurement of OH concentration, based on **off-axis integrated cavity output spectroscopy (OA-ICOS)**. Wavelength modulation was then applied to further enhance the detection sensitivity. **Faraday rotation spectroscopy** combined with the OA-ICOS setup was developed to establish a **cavity-enhanced Faraday rotation spectrometry** approach (CE-FRS) for interference-free monitoring of OH radicals. The CE-FRS setup was tested via measuring the reaction rate constant of OH with CH_4 on a milliseconds timescale. The second setup based on a quantum cascade laser spectrometer (6 µm) was developed and employed to measure the high-resolution spectrum of the ν_2 band of *cis*-HONO (*R*-branch) in a region of 1659.2-1662.2 cm^{-1}. Positions and effective line intensities were determined, for the first time, for ~ 60 new lines.

***Keywords**: OH radicals, off-axis integrated cavity output spectroscopy, Faraday rotation spectroscopy, wavelength modulation spectroscopy, quantum cascade laser spectroscopy, ν_2 band* cis*-HONO, effective line intensity.*

Résumé

Nous reportons dans ces travaux de thèse le développement et l'application d'instruments optiques pour des mesures directes de concentration des radicaux OH et pour l'étude des paramètres spectraux des raies d'absorption de HONO. Le premier instrument fonctionnant à 2,8 µm a été développé pour la mesure directe de la concentration d'OH, basée sur la **Spectroscopie d'Absorption en Cavité Résonante Hors d'Axe (OA-ICOS)**. La modulation de longueur d'onde a ensuite été appliquée pour améliorer la sensibilité de détection. Ensuite, le dispositif OA-ICOS est couplé à un champ magnétique afin de réalisé un spectromètre de **rotation de Faraday en cavité** (CE-FRS) dédié pour la surveillance sans interférence des radicaux OH. Le dispositif CE-FRS a été validé en mesurant la constante de vitesse de réaction de OH avec CH_4 sur une échelle de temps de quelques millisecondes. D'ailleurs, un spectromètre à laser à cascade quantique (6 µm) a été développée et utilisée pour mesurer les spectres d'absorption de la bande ν_2 de *cis*-HONO (branche R) à haute résolution dans la région de 1659,2-1662,2 cm^{-1}. Les positions et les intensités effectives des lignes ont été déterminées, pour la première fois, pour une soixantaine de nouvelles raies d'absorption.

***Mots-clés** : radicaux OH, OA-ICOS, spectroscopie de rotation de Faraday, spectroscopie de modulation de longueur d'onde, cis-HONO ν_2 bandes, intensité de raie efficace, spectroscopie laser à cascade quantique.*